TECHNISCHE UNIVERSITÄT ILMENAU
Fakultät für Maschinenbau

Dissertation

HIGH PRECISION FORCE MEASUREMENTS IN HORIZONTAL DIRECTION IN COMBINATION WITH HIGH DEAD LOADS: NON-CONTACT FLOWMETER FOR LOW CONDUCTING ELECTROLYTES

Zur Erlangung des akademischen Grades
Doktoringenieur (Dr.-Ing.)

von Herrn
M.Sc. Suren Vasilyan
geboren am 18. 03. 1986 in Yerevan/Armenia

Tag der Annahme durch den Fakultätsrat: 27.11.2015
Tag der Verteidigung: 23.02.2016

Erstgutachter: Univ.-Prof. Dr.-Ing. habil. Thomas Fröhlich (TU Ilmenau)
Zweitgutachter: Dr.-Ing. Dorothea Knopf (PTB)
Drittgutachter: Prof. Dr.-Ing. habil. Tino Hausotte (Erlangen-Nürnberg)

URN: urn:nbn:de:gbv:ilm1-2016000136

Kurzfassung

Die Lorentzkraftanemometrie ist ein berührungsloses Verfahren zur Messung der Durchflussgeschwindigkeit elektrisch leitfähiger Fluide. Sie basiert auf der Wirkung der Lorentzkraft, die vom leitfähigen Fluid beim Durchströmen eines von außen angelegten Magnetfeldes entsteht. Die Stärke der Lorentzkraft ist linear proportional zur Fließgeschwindigkeit und Leitfähigkeit sowie quadratisch proportional zur magnetischen Feldstärke.

Die Arbeit konzentriert sich hauptsächlich auf die Entwicklung geeigneter Kraftmesssysteme zur hochauflösenden Erfassung der in horizontaler Richtung wirkenden Lorentzkraft, in einem Messbereich von etwa 1 µN. Die zur Erzeugung des Magnetfeldes benötigten Permanentmagneten sind beweglich mittels einer Aufhängung am Messsystem (1 kg schwer) angebracht. Durch sie wirkt eine nicht zu vermeidende Kraftkomponente von ca. 10 N in vertikaler Richtung.

Ein besonderer Fokus dieser Arbeit liegt auf der Erhöhung der relativen Auflösung der Kraftmessung, d. h. dem Quotienten der kleinsten in horizontaler Richtung auflösbaren Kraftkomponente und der Totlast (Aufhängung mit Magnetanordnung)—$\mathrm{std}(F_L)/F_g$.

Zunächst werden umfangreiche Messungen mit bestehenden Kraftmesssystemen vorgenommen. Die äußeren Störeinflüsse (z. B. thermische Drift und Vibrationen) wurden untersucht und ihre Auswirkungen auf Messergebnisse identifiziert.

Darauf basierend wird ein Konzept vorgestellt, um diese Störeinflüsse mithilfe von Differenzmessungen zu reduzieren und damit die relative Auflösung zu erhöhen. Anschließend wird ein neues Verfahren zur Messung der Lorentzkräfte auf Grundlage der elektromagnetischen Kraftkompensation präsentiert. Eine allgemeine theoretische Beschreibung und Analyse für die vorgeschlagene Methode auf Basis der verwendeten Messsysteme erfolgt mithilfe eines analytischen Modells.

Die Funktionsfähigkeit für alle drei neu entwickelten Kraftmesssystemen wurden vorgestellt. Neue experimentelle Untersuchungen dieser Arbeit an zwei verschiedenen Salzwasserkanälen zeigen die signifikanten Verbesserungen bei der Bestimmung der F_L.

Im Vergleich zu den vorherigen Systemen konnte eine Erhöhung der Auflösung der Kraftmessung von 1 µN auf 20 nN erreicht werden, mit einem Verbesserungsfaktor 50. Dies erlaubt rechnerisch die Messung der Strömungsgeschwindigkeit von Fluiden mit einer um 2 Größenordnungen geringeren elektrischen Leitfähigkeit, bis zu 0,059 S m^{-1}. Praktische Messungen mit Flüssigkeiten mit einer Leitfähigkeit von 0,005 S m^{-1} to 0,059 S m^{-1} werden präsentiert und die unerwarteten neune Ergebnisse diskutiert.

Abstract

The Lorentz Force Velocimetry (LFV) is a non-contact technique to measure flow rate of an electrically conducting fluid exposed to an externally applied magnetic field. The flow measurement is enabled by measuring the Lorentz force (F_L), generated in the flow and linearly proportional to the mean flow velocity, electrical conductivity and magnetic field in the second power, with application specific force measurement systems (FMS).

This work is mainly devoted to the development of suitable FMSs for LFV applications in a special case when the measurand force acts horizontally on the magnet system and ranges about 1 µN. The magnet system, weighing 1 kg and suspended from FMS, is an essential component of the LFV application. Thus, they produce an unavoidable force on FMSs in vertical direction due to the gravity force ($F_g \approx 10\,\mathrm{N}$). A special focus of this work is to increase the relative resolution of the force measurements, i.e. the ratio of the horizontally directed force measurement resolution over the total weight of the dead load (magnet system and suspension mechanism)- $\mathrm{std}(F_L)/F_g$.

Initially, a set of extensive measurements are made using previously developed FMSs. Environmental influences are studied and their impact on measurement results are identified (thermal drift and vibration noise). The work then progresses to address how the relative resolution of the measurements can be increased using the difference method of force measurements to reduce the influence of these errors. Then, a new approach to measure F_L in LFV applications is presented, based on electromagnetic force compensation method directly applied on LFV magnets. Generalized theoretical description of the proposed method is provided based on the design of the existing LFV application and the complete analytical model and analysis. Overall, the performances of three newly developed FMSs are presented. Further, the practical measurements of F_L on two different salt-water channels are made showing several significant improvements achieved by this work.

In comparison with previous works the resolution of force measurements from 1 µN to 20 nN are increased, providing a factor of 50 improvement. By this, improved performance of the LFV application is validated and the flow rate measurements according to LFV theory are enabled for 2 orders of magnitude lower values of electrical conductivity, until $0.059\,\mathrm{S\,m^{-1}}$. Finally, measurements for lower ranges of the electrical conductivity $0.005\,\mathrm{S\,m^{-1}}$ to $0.059\,\mathrm{S\,m^{-1}}$ are presented and some remarks on unexpected new results are discussed.

Contents

Abkürzungsverzeichnis

1DoF	1-Degree-of-Freedom
3DoF	3-Degree-of-Freedom
A/D	Analog to Digital conversation
D/A	Digital to Analog conversation
dFMS	differential Force Measurement System
EMFC	Electromagnetic Force Compensation
FFT	Fast Fourier Transform
FIR	Finite Impulse Response
FMS	Force Measurement Systems
GPIB	General Purpose Interface Bus
IPK	International Prototype of the Kilogram
LDA	Laser Doppler Anemometry
LFV	Lorentz Force Velocimetry
MDoF	Multi-Degree-of-Freedom
MID	Magneto-Inductive flow meter
PC	Personal Computer
PID	Proportional–Integral–Derivative
RS-232	Serial port, standard for serial communication transmission of data
SDoF	Single-Degree-of-Freedom
USD	Ultrasound flowmeter

1 Introduction

> *Many measurements are made to provide an objective basis for decisions about a product or a process.*
>
> Novel mathematical and statistical approaches to uncertainty evaluation.
> Trevor Esward

In this chapter the basic physics of the Lorentz Force Velocimetry (LFV) and the character of measurand force is introduced, namely the Lorentz force F_L. A brief overview on applications using LFV technique is discussed. Further, the State-of-the-Art of the force measurement systems (FMS) are provided for two different experimental facilities. Initially, in 1.2.1 it is discussed the first FMS for the prototype channel which uses the laser interferometric measurements of deflection, then in 1.2.2 the second FMS for advanced channel using a commercially available State-of-the-Art balance. Finally, the main problems will be identified around which overall objectives and the structure of current work will be defined 1.3.

1.1 Overview on Lorentz Forces Velocimetry

1.1.1 Basic physics

Over the last decade, a number of reports have been dedicated to the development of various contactless flowmeters [1–16] based on the LFV technique. The necessity of this kind of contactless flowmeters is crucial when the liquid is not directly accessible for conventional methods such as magneto-inductive flowmeters, ultrasound flowmeters, and optical flowmeters. For instance, in the glass or chemical industry to control the production processes of various aqueous solutions or glass melts which have $10^{-6}\,\mathrm{S\,m^{-1}}$ to $10^{2}\,\mathrm{S\,m^{-1}}$ electrical conductivity sometimes become challenging for all conventional methods. Usually, pipes are opaque and hot, whereas the substance also can be chemically aggressive for immersed electrodes of the inductive flowmeters. There are several other fields of interest where this type of flowmeters may be applied, e.g. to measure molten salts in solar thermal power plants or in high temperature reactors. An alternative technique to overcome some of these challenges was previously presented as Lorentz Force Velocimetry (LFV). The LFV technique was first described by *Shercliff* [2] in the framework of magneto-hydrodynamics [1, 3] and was recently reintroduced by Thess et al. [4]. The working principle of LFV is based on measurements of electromagnetic forces F_L that are induced due to the transverse interaction of a magnetic field and a moving, electrically conducting medium. This work addresses a special case of liquid flow with low electric conductivity. The working fluid is chosen the ordinary tap water for economical convenience. The electrical conductivity of the tap water is relatively easy to manipulate in the range of $10^{-3}\,\mathrm{S\,m^{-1}}$ to $10^{2}\,\mathrm{S\,m^{-1}}$.

Hence, when the flow is exposed to the magnetic field, an electric current $\vec{j}_i$ is induced by virtue of the Ohm's law. The interaction of this electric current with the primary magnetic field $\vec{B}$ generates a Lorentz force that breaks the flow (cf. figure 1.1, due to the weak electrical conductivity of the fluid and the low velocity of the flow the magnetic flux density of the secondary magnetic field is negligibly small). In the absence of an externally applied electrical current, the equation reads as

$$\vec{F}_L = \int\limits_V \left(\vec{j}_i \times \vec{B}\right) dV = \int\limits_V \left(\sigma \vec{v} \times \vec{B}\right) \times \vec{B}\; dV, \tag{1.1}$$

where $\vec{v}$ is the velocity field of the fluid flow, σ is the electrical conductivity of the fluid and $\vec{B}$ is the flux density of the primary magnetic field over the interaction V volume with the fluid.

The force F_L is directed opposite to the mean flow, and at the same time an equivalent but downstream directed force is acting on the magnetic field generating source due to the reciprocity principle. In turn, as suggested by theory and confirmed by experimental measurements [3, 4] for the stationary case, F_L depends linearly on the electrical conductivity, mean flow velocity (v_0) and magnetic flux density in the second power (B^2)

$$F_L \sim \sigma\, v_0\, B^2, \tag{1.2}$$

or

$$F_L = c_{cf} \cdot \sigma\, v_0\, B^2. \tag{1.3}$$

where c_{cf} is the calibration coefficient of this type of flowmeters, mostly dependent from geometrical factors of particular setup.

Therefore, by measuring the reaction force induced for a given magnetic flux density, it is possible to estimate the mean flow velocity of the fluid when the value of its electrical conductivity is known. This statement should be considered under the kinematic theory of LFV [17], which assumes no back reaction of the Lorentz force on the flow. In this work the conductivity will be treated as a constant. However, the inverse problematics is also of great interest to several authors when the velocity is being considered as a known parameter and determination of the conductivity is the target parameter. In these cases LFV is a method to detecting impurities (defects) [18] in the bulk of the material or to determine the conductivity (sigmometry) [19]. In addition, if the magnets are small compared to the duct size, LFV can be applied to determine the local velocity of the flow profile [12].

This method for most of industrial applications provides reasonable accuracy and

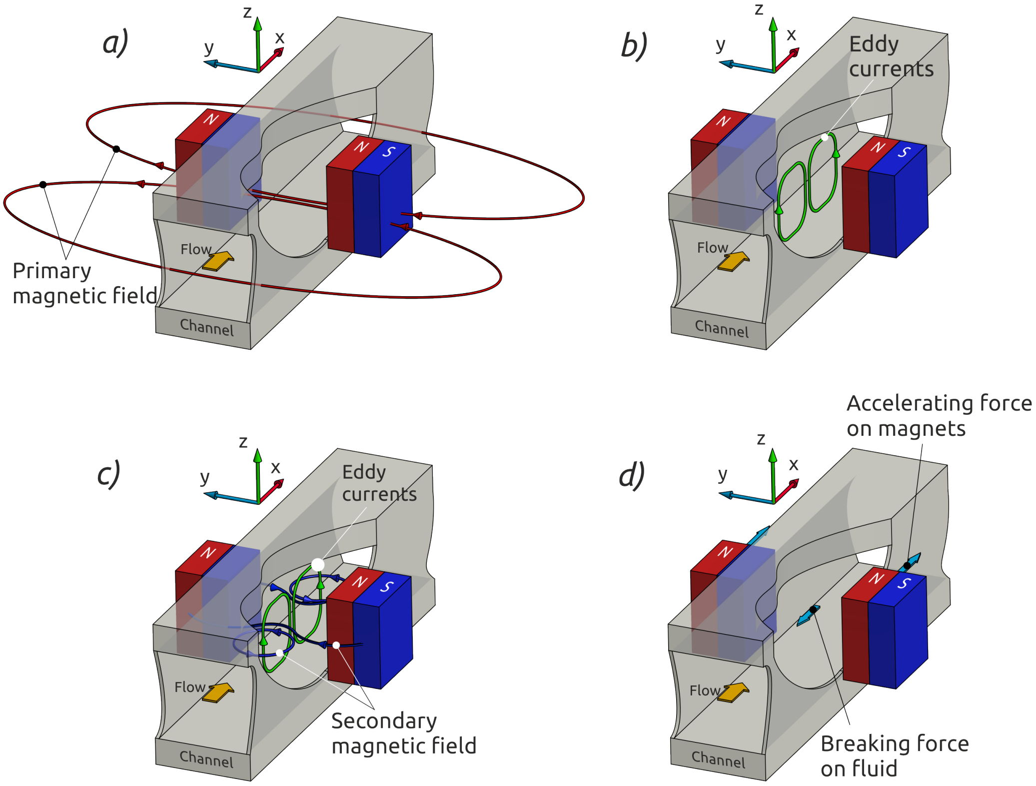

Figure 1.1: 3-D sketch representing working principle of the LFV. a) The flow of the fluid is exposed to the magnetic field of permanent magnets, b) the primary magnetic field (red-extended) induces eddy currents (green) inside the fluid, c) the eddies are the source of a secondary magnetic field (blue), d) interaction of superimposed magnetic field with eddy currents result in a braking force on the fluid that is matched by an accelerating force on magnets.

sufficient measurement resolution, nevertheless a basic research is required as systematical studied to uncover the full dynamic model of LFV. Recent experimental investigation, see Ref. [20], provides some answers on the character of Lorentz force response when back reaction on moving conductor is considered. More specifically, in the study the time dependent distortions of primary magnetic field line due to generated secondary magnetic fields are considered (cf. figure 1.1). In order to systematize all these effected may be considered the generalized non-dimensional parameter which is the magnetic Reynolds number. It is defined as $R_m = \tilde{U}\tilde{L}/\tilde{\eta}$, where $\tilde{U}$ is a typical velocity scale of the flow, $\tilde{L}$ is a typical length scale of the flow and $\tilde{\eta}$ is the magnetic diffusivity. This parameter presents the magneto-hydrodynamic effects in-

ducing in the flow. In other words it is the ratio of the magnetic effects induced in the fluid over the magnetic field applied externally. Sokolov et al. [20] studied the response of LFV in the case of finite and low Re_m cases for solid bodies, $Re_m \sim 1$. However, in the limit of $R_m \ll 1$ effects that are inducing in low electrically conducting fluids (the secondary magnetic field) can be neglected which is considered in the current work.
Also, in order to define the character of the Lorentz force it is important to consider the hydrodynamic interactions inducing due to the flow of the fluid. It is the hydrodynamic Reynolds number Re which is also a generalized non-dimensional parameter providing a measure of the hydrodynamic effects inducing non-linearly in the flow. The $Re = \tilde{U}\tilde{L}/\tilde{\nu}$, where the $\tilde{\nu}$ is the kinematic viscosity ($\nu = \mu/\rho$, μ is the dynamic viscosity of the fluid and ρ, is the density of the fluid). In other words, the Reynolds number presents the ratio of the momentum forces over the viscous forces in the fluid. In this study the $Re \approx 10^4$ to $2 \cdot 10^5$, however the measured flow rate of the fluid has very good relative stability (below 1%), therefore the only factor to be associated with the induced and measured Lorentz force is the standard deviation of the velocity value.

1.1.2 Application overview

The LFV has been implemented in a wide variety of conditions and applications. It has been already tested for various material substances, subdivided in to three main groups, in terms of their value of the electrical conductivity. Particularly, ***(i)*** for high conductive *liquid metals* or *molten salts* the performance of LFV is tested in industry [5, 6] and under laboratory [7–12] conditions. The typical electrical conductivity for this case is ranging in order of $10^4\,\mathrm{S\,m^{-1}}$ to $10^6\,\mathrm{S\,m^{-1}}$. For ***(ii)*** *electrolytes* [13–16] whose electrical conductivity is typically ranging in order of $10^{-6}\,\mathrm{S\,m^{-1}}$ to $10^2\,\mathrm{S\,m^{-1}}$, the applicability of LFV have been tested only recently and only for limited range of the electrical conductivity $2\,\mathrm{S\,m^{-1}}$ to $20\,\mathrm{S\,m^{-1}}$ specifically for salt water, however among the electrolytes should be considered material substances such as blood, acids, glass melts and etc.. The applications based on LFV are also applied for ***(iii)*** *solid materials* where value of the electrical conductivity reaches up to $10^7\,\mathrm{S\,m^{-1}}$.
In the aforementioned groups the induced Lorentz forces, which needs to be measured to characterize the flow of the substance, have different magnitudes. This difference is strongly conditioned by geometry of designed application in respect to strength of the magnetic field, the electrical conductivity of the fluid and the flow velocity, and generally can be explained by equation 1.2. To discuss each of this parameter separately one may distinguish that, in most of the practical applications the velocities are not exceeding $5\,\mathrm{m\,s^{-1}}$, and the magnetic field is in range of $0.1\,\mathrm{T}$ to $1.5\,\mathrm{T}$, whereas the most wide spread range has the electrical conductivity $10^{-6}\,\mathrm{S\,m^{-1}}$ to $10^7\,\mathrm{S\,m^{-1}}$ (cf. figure 1.2).
The current work deals with the Lorentz force measurements for *electrolytes* whose electrical conductive ranges from 10 down to $10^{-3}\,\mathrm{S\,m^{-1}}$. This is done based on ear-

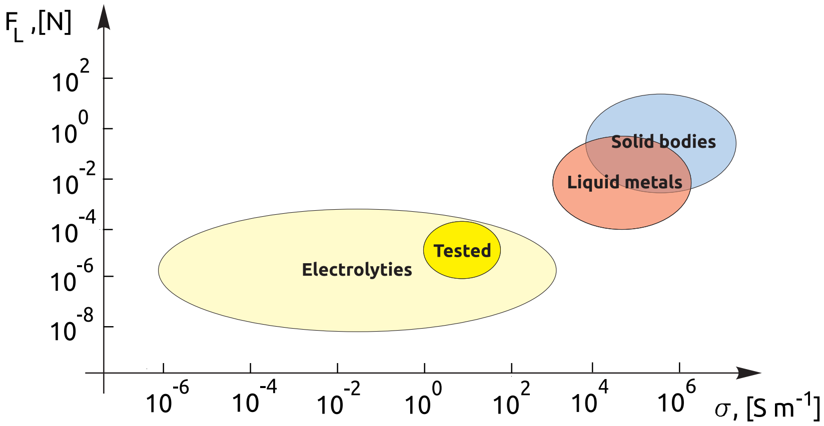

Figure 1.2: Diagram showing scaling relation between F_L and σ in LFV applications (cf. equations 1.2 and 1.3). All data are collected based on [5–16, 20], the tested region for electrolytes from [13–16].

lier developed two experimental facilities. Both facilities consisting two main parts, namely the force measurement setup (FMS) and fluid loop channel (channel). Initial development of the FMSs have been done by *Diethold et al.* [13, 14, 21], whereas the channels and magnets have been developed by *Wegfrass et al. and Werner et al.* [13, 15, 22–24].

It is important to mention that the choice of material properties and geometrical design of this LFV was only based on initial guess in order to generate measurable order of magnitude Lorentz forces. In contrast to other LFV based flowmeters this one is yet only know non-contact flowmeter to be able to address flow measurements on electrolytes.

There are LFV based flowmeters that are know to use time-of-flight method. This method states the necessity of the significant turbulent fluctuations in the flow. Since, the turbulent fluctuations are generating signals (either a force or a voltage) they are possible to measure by separate sensors and to calculate the velocity of flow by principle of auto- or cross-correlation (cf. numerical investigation [7]). In these systems the magnetic field is generated by applying current to the coil(s) that is winded around channel. Similarly, an experimental study showing feasibility of the time-of-flight method is presented in [8] or [25]. For this case the magnetic field is generated by conventional permanent magnets and the Lorentz force is measured by strain gauge based force sensors. Assumed advantage of this method is that these flowmeters are working independent of the value of the electrical conductivity. However, experiments and computations have been only performed for high conductive substances (order of $10^6\,\mathrm{S\,m^{-1}}$ and higher) where induced forces are in order of some mN and above.

Other examples of LFV based flowmeter are using rotation rate of magnet systems which are set into motion by induced F_L. In the one case it is the rotation rate of the flywheel with several permanent magnets on it [10] and in the second case it is freely rotating single magnet which is magnetized perpendicularly to the rotary axle [9]. In both cases, among other advantages the elegant theoretical descriptions constituting the fact that the flow rate measurements become independent of the electrical conductivity of the liquid metal. However, here a general assumption is made, namely calculations are done only for the limiting case of vanishing frictional losses between the magnet(s) and their supporting mechanical system(s). As it is seen from the experiments, this frictional contact mechanics play the key role in resolving accurate flow measurements. Also, the measurements were performed only for substances with high electrical conductivity (for instance, above $10^6\,\mathrm{S\,m^{-1}}$ electrical conductivity has molten Na at 200 °C temperature or GaInSn at the room temperature).

In this work, in both facilities the flow measurements are particularly enabled by measuring induced Lorentz forces with specially developed FMSs (discussed in section 1.2.1 and 1.2.2). The common principle of force measurements is done using deflection measurements of dead loads. Due to the design of LFV, here the Lorentz forces are acting in horizontal direction and are ranging from µN to sub-µN. The dead load in these systems is the weight of the magnets which are suspended from FMSs. The magnets are chosen such to provide a realistic electromagnetic and mechanical configuration of the application in order to generate measurable order of magnitude Lorentz force. The magnets are weighing about 1 kg and producing unavoidable force on FMSs in vertical direction due to the gravity force (F_g =10 N). Due to these unusual requirements a specific FMSs are desirable.

1.2 State-of-the-Art in force measurements

In this section a short overview on State-of-the-Art of FMSs is given. The general requirement of the FMSs is, to measure horizontally directed forces acting on the ≈ 1 kg magnets. The magnets are producing onto the FMS an unavoidable vertically directed force in order of 10 N. Thus, the relative resolution of force measurements is somewhat about $std(F_L)/F_g \sim 10^{-7}$ and below. It is important to mention beforehand, that such a FMSs are not available on commercial bases or in research, therefore a completely new FMS should be developed. This was the general motivation of the work done by *Diethold et al.*, and of the current work, respectively. Thus, a portable and robust setup resolving stable and high precision force measurements is desirable.

In research on precision force measurements there are a number of techniques and State-of-the-Art sensors to conduct force measurements down to pN resolution/precision [21, 26–38], however without supporting high dead loads. The common principle employed in most of them is deflection measurements of dead loads, either by torsional or pendulum-based balances. Typically, the measurements are taken from open-loop mode or compensating it to zero in closed-loop mode. Among all different principles used to measure forces, a remarkable precision is achieved in measurements of deflection by electrostatic forces on cylindrical [26, 27, 31] or flat capacitive transducers [28, 29] with measurement resolution below 50 pN. Also, a laser interferometric measurements of deflections [30] is known and an attempt to adopt the method for LFV application have been already reported [13, 14] (see subsection 1.2.1). There are also developments as pendulum-like setups in the field of micro-electric propulsion systems. Although these systems are supporting high dead loads for the thrust calibration and characterization [32, 33, 35], their reports are discussing measurements only in the µN to mN range.

1.2.1 Prototype channel with Pendulum FMS

The experimental facility on which the pendulum FMS was developed is that from Ref. [13, 14], which is the first prototype model of LFV. The magnet system is arranged on a pendulum which is realized by four point suspension system with parallel tensioned tungsten wires. The wires have a diameter of 175 µm and a free pendulum length of 560 mm. The pendulum is free to oscillate in horizontal plane, thus having 3 components of motion (3DoF) 2 translational in x, y direction, and 1 rotational in the xy plane (cf. figure 1.3). Earlier the force measurements were made by tracking the deflection of the pendulum by means of a 1D laser interferometer [39] with 1 nm measurement resolution (see item 4 in figure 1.3).

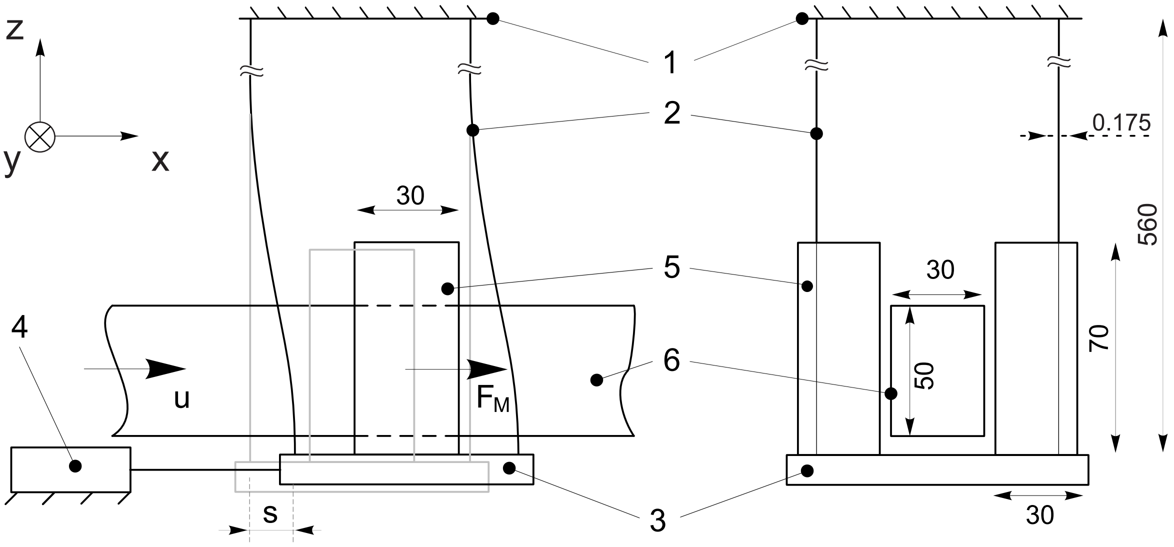

Figure 1.3: Sketch of the pendulum FMS. Left: side view of the deflected magnet system. By grey color is indicates the undeflected state. Right: front view. (1) support, (2) four point suspension system (tungsten wires), (3) coupling element, (4) interferometer, (5) magnet system, (6) channel.

The force measurements F_M are considered only for single axis. The force is calculated in accordance with Hook's law by multiplying the effective deflection s of the pendulum with the stiffness of the system (K_s) (cf. equation 1.4). This is greatly simplified approach since the pendulum is considered as a point mass and its deflection only as a single degree freedom motion. The circular motion of the pendulum is also neglected in this computations. In practice, this is achieved using a special suspension method known as parallel beam suspension (in the figure 1.3 item 2).

$$F_M = s \cdot K_s. \tag{1.4}$$

The stiffness of the system may be determined experimentally or by theoretical computation. Theoretically, the accuracy of the measurements is greatly restricted by the variation and/or exact distinction of the length of the wires, since the uncertainty contribution of the length of the wire is 2 orders of magnitude greater than any other parameter of the system (see item 2 in figure 1.3 and table 1 in [13]). The calibration of the measurements has been carried out by means of an electromagnetic force compensation voice coil [13]. In the calibration procedure, the magnets (item 5 in figure 1.3) were replaced by an equivalent dummy weight to avoid magnetic interactions with the voice coil actuator.

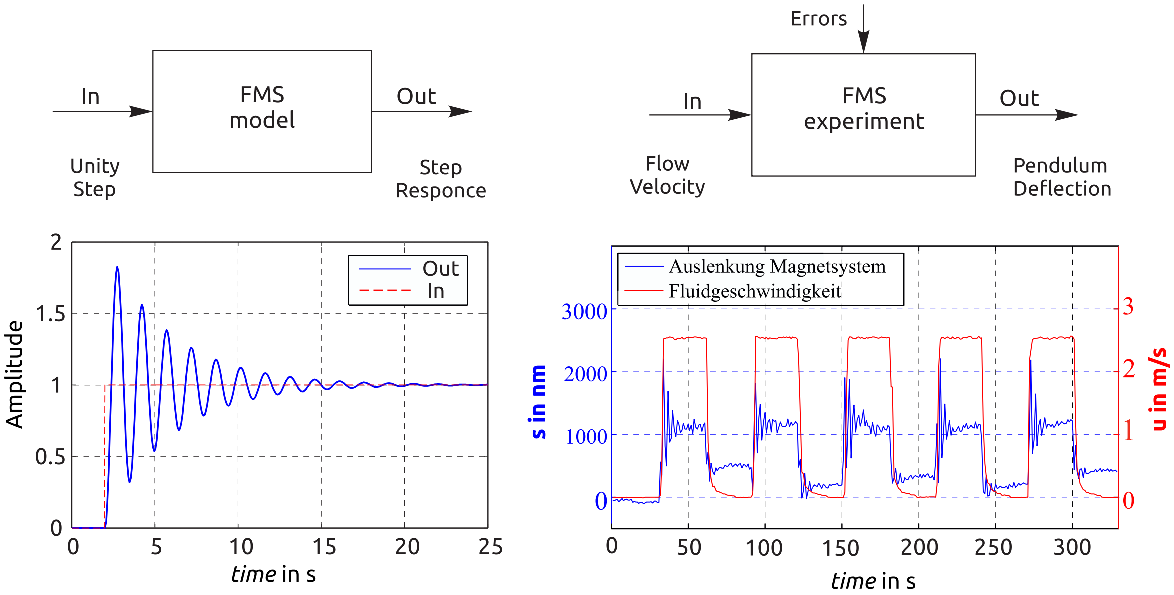

Figure 1.4: Comparison of the theoretical 1DoF FMS model (left) with measurement result (right) of the pendulum FMS.
Left: the system response (blue) to the unity step (red) based on a theoretical 1DoF model, obtained by equation 3.15 using parameters provided in table 3.1 (see section 3.4.1).
Right: Typical experimental results of the Lorentz force measurements. Adapted from [22] with several minor editing changes. On the right-hand axis (red), the flow velocity (m/s) represents an input parameter, on the left-hand axis (blue), the deflection of the pendulum (nm) as a result of acting F_L, measured by interferometer.

In practice, the measurements of the Lorentz force F_L during the experiments revealed several largely unidentified effects. These effects were generalized as other experimental errors occurring in measurements. These errors may be classified as follows:

- The F_L is the averaged effective force over the volume of the electromagnetic interaction of the magnets and the flow of the fluid (volume integral of $\vec{B}$ and $\vec{j}$ vector multiplication, cf.equation 1.1). However, the measurements were made assuming that the reaction force on magnets has only one component and acts in x direction. Therefore, the translation in y direction and/or the rotation in the xy plane of the pendulum were neglected.
- All measurements were made under room temperature and the temperature effects on the experimental facility, on the FMS and during the measurement process of F_L, were largely left out of consideration. There are three types of temperature dependent effects originating a considerable amount of measurement error,
  - the thermal expansion of the supporting mechanical construction that leads to a thermal drift (deterioration) of the zero-point stability,
  - the change of the temperature of the fluid changes its value of the electrical conductivity that leads to a change of the actual value of the generated F_L during the measurement process,
  - the change of the temperature is also known to affect the stability of the magnetic field distribution (flux density) of magnet systems. Therefore, the latter can also change the stability of F_L during the measurement process.
- Random vibrations (by their magnitude and frequency) obstruct the measurement signal, and the actual acting forces become indistinguishable. The main sources of these are the ground-born vibrations and convective air fluxes.
- The magnetic interaction of the magnets with the parasitic strays of magnetic fields existing in the laboratory is the most indistinguishable error. In general, the main disadvantage of LFV flowmeters depends exactly from this error.

The cumulative effect of all these errors and the calibration results leads to the actual F_L measurements with a resolution of about $\approx 2.5\,\mu\text{N}$. The working range of the Pendulum FMS was calibrated for around $\pm 100\,\mu\text{N}$ forces. However, aforementioned errors exclude the possibility of discussing the performance of the Pendulum FMS in terms of its measurement accuracy and stability. The F_L measurements presented in figure 1.4 (right) illustrate part of these effects, such as the unstable zero point and the drift of the force signal. Furthermore, for the continuous flow measurements, the F_L measurements should not only present an acceptable accuracy and stability, but also certain dynamic capabilities. From the theoretical model given in figure 1.4 it can be seen that the settling time of the Pendulum FMS within 5 % is about 12 s, whereas from experimental measurements it is hardly distinguishable. Despite all these distinguished problems the solid body experiments and quasi-static finite element simulations (COMSOL) show considerable agreement, as reported in [13],

thereby providing means to conclude that the measurement system generally works under laboratory conditions for metering the flow of the fluid in the channel.
This first prototype facility and the Pendulum FMS constitutes the basis for the development of an extended setup for a more sophisticated and refined facility with other FMS (at an earlier stage developed by A. Wegfrass, C. Diethold and M. Werner).

1.2.2 Extended setup, use of EMFC balance

Based on the progress in F_L measurements with pendulum FMS, discussed in subsection 1.2.1, a FMS was developed by *Diethold et al.* [21] for an extended LFV facility. This FMS uses a single State-of-the-Art high-precision balance (provided by Sartorius AG – Göttingen) working on the basis of the principle of electromagnetic force compensation balances [40] (hence, EMFC balance for short).

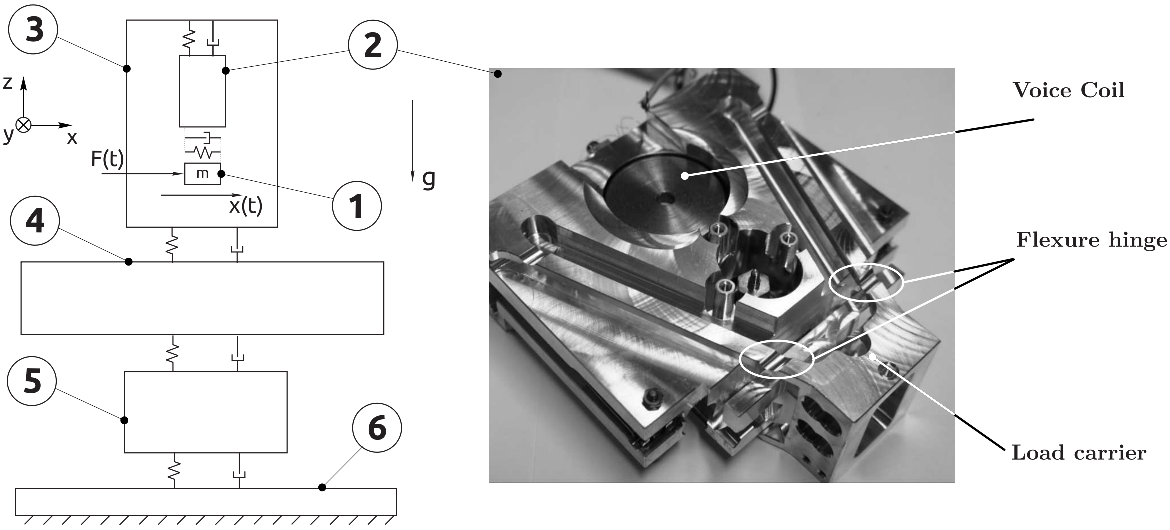

Figure 1.5: Mechanical diagram of the experimental setup (left), the image of EMFC balance (right). The mechanical diagram is presented as MDoF system. (1) - dead load ≈ 1.35 kg, (2) – EMFC balance with suspension system ≈ 3 kg, (3) – supporting frame ≈ 40 kg, (4) – granite stone ≈ 800 kg, (5) – supporting structure of the stone, (6) – fixed base, physically decoupled from building foundation. Force measurements are taken as $x(t)$ signal against horizontal acting $F(t)$ forces on item 1.

The mechanical configuration of the experimental setup is presented in figure 1.5 as Multi-Degree-of-Freedom System (MDoF). The force $F(t)$ acting on the dead load is to be measured in horizontal direction, that is, perpendicular to the gravitational force (mg). For practical measurement purposes, the setup is treated as a Single-Degree-of-Freedom (SDoF) deterministic linear dynamic system. As shown in the mechanical diagram of the construction (cf. figure 1.5 left) the EMFC balance is

assembled inside the supporting aluminium frame, which rests on a 800 kg granite stone. To minimize random mechanical vibrations, the whole system is mounted on a fixed base, which is physically decoupled from the building foundation.
The working principle of the EMFC balance and its use in combination with high dead loads have already been reported in detail in [21]. In that report a measurement resolution smaller than 1 µN was obtained, and some general comments on increasing the resolution further were presented.
A typical measurement by EMFC balance is made when it is aligned horizontally in order to match the measured quasi-static forces in vertical direction with the local gravity. An example employing such configuration in bigger scales is used in the research of mass comparators [41, 42] or for redefining the unit of mass from the international prototype of the kilogram (IPK) in terms of fundamental constants as the Planck constant [34, 36, 37] or the Avogadro number [43]. The EMFC balance used in this research has a measurement readability given by the manufacturer of around 1 µg, which approximates as ≈ 10 nN depending on the local gravity value on the site of the measurements. The working range is given as ±5.5 g (≈ 55 mN).

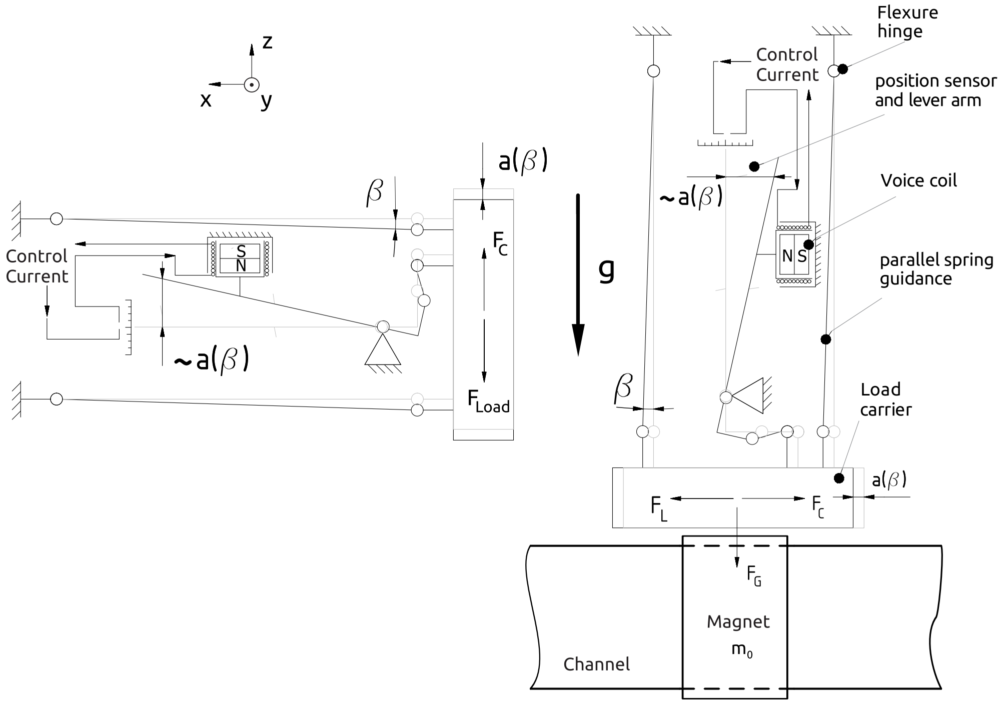

Figure 1.6: Schematic diagram of the EMFC measurement principle (grey undeflected). Left: conventional usage of EMFC balance aligned horizontally, measuring the deflection a(β) in vertical direction. Right: usage in modified vertical alignment, measuring the deflection in horizontal direction. F_C - total force measured as EMFC compensation force, F_G - gravity force, F_L – horizontally acting force.

The EMFC balance is arranged in rotated 90° orientation relative to its common usage in a horizontal alignment. The load carrier is pointing downwards as depicted in the illustrations (cf. figure 1.6, right). The resulting special orientation of the EMFC balance assumes a naturally achievable zero stable condition, which provides an advantage of using high dead loads suspended from EMFC balance. Moreover, the offset correction for counterbalancing the proportional lever arm of the EMFC balance is no longer necessary. The only limiting factor for using high dead loads is the elastic properties of the inner construction of the EMFC balance, particularly mechanical linkages, flexure hinges and parallel spring beams [44]. The load carrier is guided by linked parallelogram beams and series of flexure hinge pivots, therefore the measurements are solely directed along one axis (x). The measurements are made in the air. The effects such as air buoyancy correction or nonuniform temperature distribution are not considered.

The control loop of the measurement system uses a digital PID controller. The settling time is less than 1.4 s. The output variable of the measurement system is the compensation current which is proportional to the measured Lorentz force. To get the relation between the measured Lorentz force and the compensation current, the measurement system was calibrated by means of an electromagnetic force compensation voice coil. The magnet system was replaced by a dummy weight (made of non-ferromagnetic material) with equivalent mass. The calibration measurements have shown that there is no influence of the mass of the magnet system on the calibration factor which is $5.1075\,\mathrm{mA\,N^{-1}} \pm 0.0012\,\mathrm{mA\,N^{-1}}$. The measured reproducibility is less than $s(F)$=0.5 µN [15].

Despite some improvements achieved for F_L measurements by this EMFC balance in comparison with Pendulum FMS, this system also is subjected to certain type of errors that are involved in the Pendulum FMS. In particular, there are undefined systematic errors such as force drift and random noise appearing either as ground/seismic vibrations or electromagnetic influences due to parasitic strays of the magnetic field from external sources. An example showing these errors is presented in figure 1.7 when only the zero-point stability (no forces applied in horizontally directed) was measured.

This is one of the first attempts made in this work to quantify the effect of a temperature variation on the force measurement. In the first step, the force signal of the zero point stability as well as the temperature and humidity of the surrounding environment were monitored over a relatively steady and long period. Figure 1.7 shows a typical long-term measurement over a 12 h period. Among measured signals, a stronger correlation of the force signal with the temperature signal can be distinguished. Furthermore, it can be observed that a change of about 0.1 K induces an error higher than 5 µN, while a vibration of the system leads to an oscillation of 2 µN to 4 µN. On the other hand, changes in humidity affect the measurement indirectly, since they are closely related to changes of the temperature.

The state of both FMSs described in this and previous subsections was the starting point of the current work. This initial analysis presents a ground for further improvements and possible new developments of FMSs. In the next section (1.3) the target problems of the current work are identified around which the overall structure of this study is described.

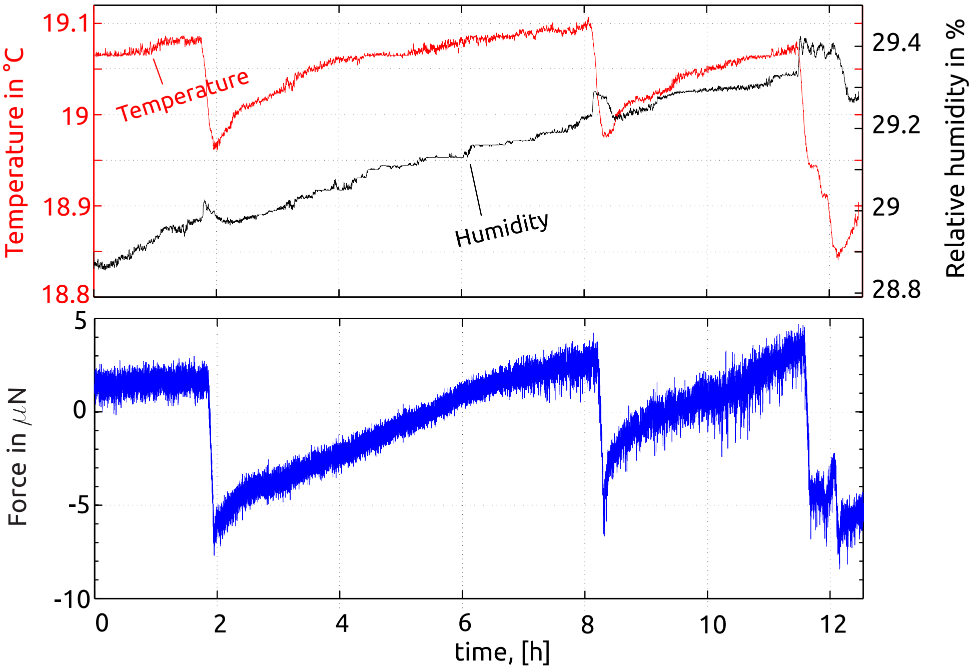

Figure 1.7: An example of force measurements on zero-point stability. Change of temperature and humidity over a 12 hour measurement period (top). Monitoring of the zero point stability force signal by single EMFC balance [21] (bottom). The linear correlation of force and temperature signals is above 95 %.

1.3 Objectives and structure of the work

In previous reports it have been already presented the feasibility of LFV technique. The measurements of the flow rate of low electrically conductive fluid is enabled by measuring the F_L by two FMSs (Pendulum and EMFC balance).

In this work the general objective is to increase the resolution and the accuracy of F_L measurements. Preliminary, the goal was set to increase the relative force measurement resolution of about $\mathrm{std}(F_L)/F_g \approx 10^{-8}$ ($\approx$ 10 ppb), which suggests that the actual F_L measurements should have at least 100 nN resolution. Compared to performance of previous FMSs this target value is 1 order of magnitude smaller. Another goal was set to resolve the stability problem of the force measurements for long-term measurement periods. It is identified, in section 1.2.2, that the temperature of the surrounding environment strongly affects the stability of the force measurements in both FMSs. Besides this, the resolution of force measurements is obstructed by random vibration errors.

From technical point of view, it is desirable to simplify both the measurement process of F_L and construction of the FMSs. Previously, this problem was mostly neglected in favor of the research experiences which was necessary to aggregate before any possible modifications to be made. The prove of the working concept of the LFV flowmeter for low electrically conducting electrolytes was the main motivation in developing two main LFV setups (FMS by *Diethold et al.*, salt water channel by *Wegfrass et al.*, and magnet systems by *Werner et al.*). Several aspects, such as the geometry and the material properties of the supporting mechanical construction were not addressed critically before actual constructions was developed. Due to this reason the vibration noise and temperature influence (e.g. figure 1.7) were mostly hidden and treated as unknown systematic errors. Thus, the work presented in this Dissertation is mainly devoted to improvements of FMSs, while all other components of the LFV application remain in their initial state of development (details of salt water channels can be found in [22] and magnets systems in [23]).

Nevertheless, the FMSs have been based/constructed on the separated ground and were passively isolated from ground/seismic vibrations (see item 4 and 6 in figure 1.5), it was mostly indefinite whether the noise (about 1 µN to 4 µN, which also defines the resolution of FMSs) in the measured force signal were originated from the electronics of the EMFC or from randomly accruing processes, such as mechanical noises. Moreover, the electric setup of measurements is guided by a digital controller which provides only 18 Hz to 20 Hz sampling rate for the smallest achievable resolution of the measurements.

In regard with the general objectives described above several improvements are made towards fulfilling main task of the current work. In particular, it will be shown a combination of extensive measurements on old FMSs and continuous developments of three new FMSs. Diagrammatic representation of the structure and evolution of these developments is shown in figure 1.8.

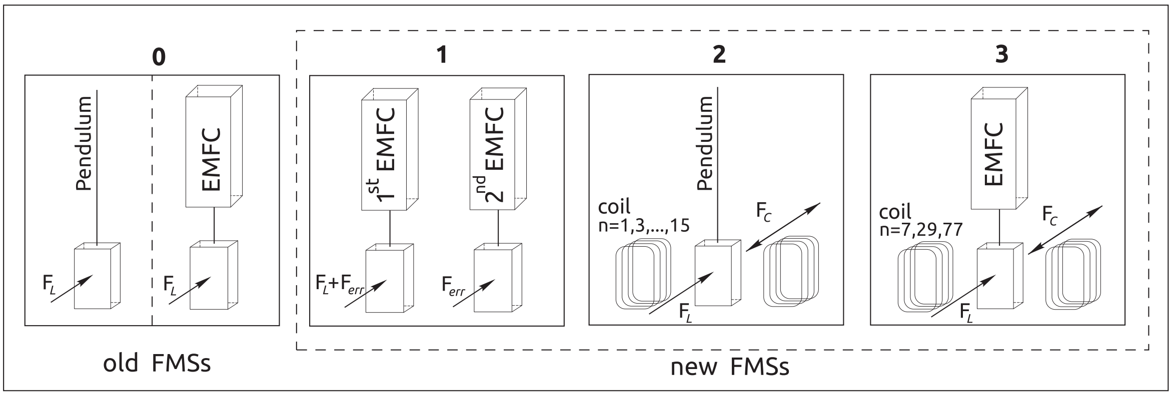

Figure 1.8: Structure of the FMS developments.

0. Old – FMSs
   - Pendulum (section 1.2.1),
   - Single EMFC balance (sections 1.2.2, and 2.1 to 2.1.3),
1. New – double EMFC balance *d*FMSs (chapter 2 starting from section 2.2),
2. New – direct compensation Pendulum FMS (chapter 3),

3. New – direct compensation single EMFC balance FMS (chapter 4),

Each newly developed FMSs are discussed in 2^{nd}, 3^{rd} and 4^{th} chapters separately. Each chapter is structured based on common logical sequence, namely,

a) **introduction** of the FMS

b) **design** of the FMS and measurement infrastructure

c) **measurement results**, in which the following steps are considered

  - measurements of deflection of the LFV magnets (or dummy weights) in the **open-loop** operation mode for **static and dynamic forces**, based on which

  - **dynamic characteristics** of FMSs are identified in order to estimate their **transfer functions**. In chapter 3 this is derived based on theoretical computations of the measured signal for static forces. In chapters 2, 4 it is obtained from extensive measurements and data analyses for dynamic forces,

  - using the dynamic characteristics of each FMS the **closed-loop** operation regime and measurement scheme will be set up for compensation measurements of the deflection,

  - **calibration results** and **summary**.

Initially, the old (single) EMFC balance, developed by *Diethold et al.* [21], will be used for the extensive measurements and for characterization of several error factors which were not discussed previously in depth. Then, in chapter 2 the work progresses to address the design and the measurement capabilities of a newly developed differential force measurements setup (dFMS) which uses two new and identical EMFC balances (without any in-house modifications). Next in chapter 3, on the basis of the Pendulum FMS a new concept of Lorentz force measurements will be presented. Further, this new concept will be reexamined and the improvements will be shown in chapter 4.

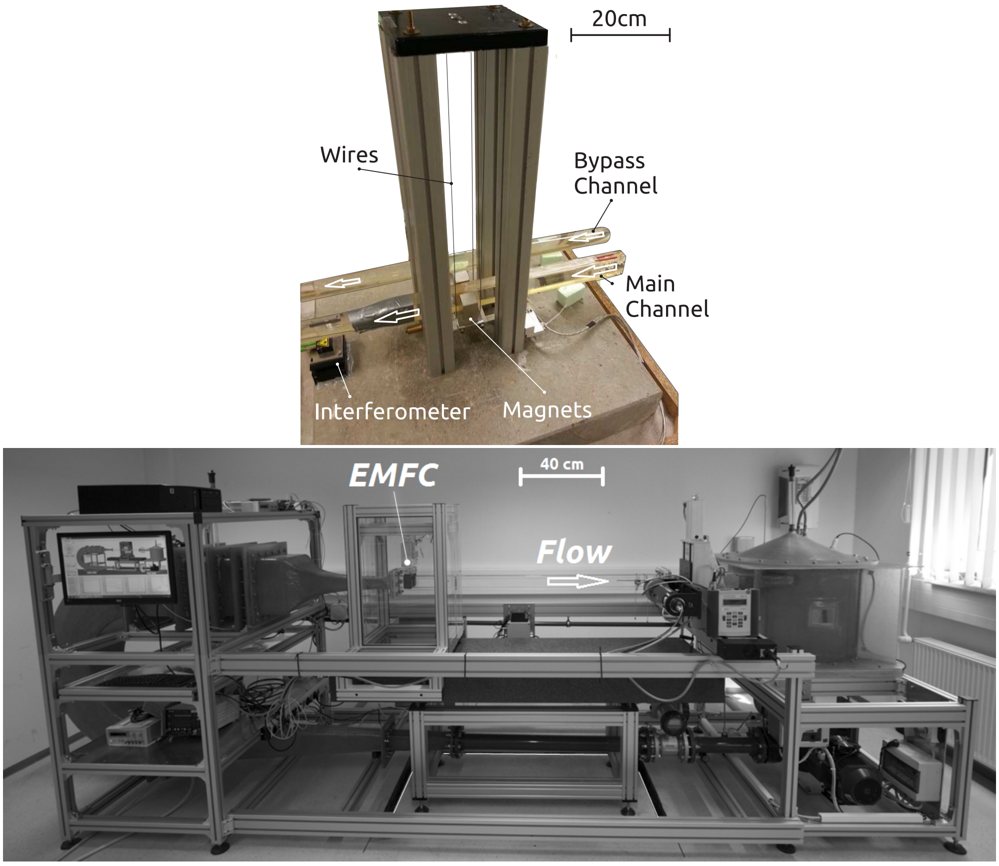

Figure 1.9: Image of prototype (top) and extended (bottom) salt water channels.

After development and checking the performance capabilities of the FMSs, they are applied for practical measurements (chapter 5) of the flow rate on two different salt water channels (cf. figure 1.9).
In section 5.1 will be shown the measurement results of Lorentz forces by the Direct Compensation Pendulum FMS which is arranged to prototype channel. Then, in section 5.2, an extensive measurement will be shown by the dFMS which is arranged to the extended channel. In section 5.3 will be shown briefly some unexpected measurements results that suggests some general open research problem for future studies.
In final chapter 6, the work will be concluded and future improvements will be discussed.

2 Advancement in EMFC Balance measurements

Motto of 3-year doctoral program:
a day without result is a lost day

from private talk
Univ. Prof. Christian Karcher

In this chapter a differential force measurement setup dFMS that uses two identical EMFC balance is presented. The development of dFMS is a continuation of earlier work of *Diethold et al.* [21], where the setup consist of single EMFC balance. Therefore an analyzes of the performance of the single EMFC balance will be initially provided. Further, the main characteristics of the new dFMS is presented as portable and robust system for force measurements in LFV application. The actual setup can support high dead loads (up to 13.5 N), and measure horizontal acting forces with resolution of 20 nN. The stability of measurements is evaluated considering the thermo-mechanical properties of the supporting construction and the noise due to random mechanical vibrations.

This chapter is organized as follows: in section 2.1 the main environmental effects persisting in the laboratory are determined. It is done by using single EMFC balance (old FMS by Diethold et al. [21]) and monitoring the force signal for short- and long-term measurement periods. The temperature dependency of FMS will be discussed (2.1.1) in terms of the chosen mechanical construction. Then, the newly developed (dFMS) will be shown in sections 2.2 and 2.3, with the calibration results and filtering considerations for force measurements in static- and quasi-static cases. Further, for applied quasi-dynamic calibration forces the dynamic characteristics of the setup is exemplified. All measurements were conducted in the air and only minimal usage of passive thermal insulation is considered for shielding the setup, therefore improvement of force measurements in vacuum is yet being expected. The final section (2.4) will briefly discuss the future developments and conclude the chapter by providing main achievements on force measurements by dFMS[1].

---

[1] A significant portion of the results obtained in this chapter are compressed in the peer-reviewed journal publication [45] **S. Vasilyan, et al. High-precision horizontally directed force measurements for high dead loads based on differential electromagnetic force compensation system. 05.10.2015 submitted, 15.02.2016 accepted by Measurement Science and Technology http://iopscience.iop.org/0957-0233.**

2.1 Investigation on the old FMS

Herein, an error analysis of environmental effects on to measurement setup are presented. To characterize behavior of the existing single EMFC balance FMS a short- and long-term measurements have been done at room temperature. Through the measurement analysis the hypothesis expressed in [21] that the main influence on the measurements is due to tilting angle of the FMS have been confirmed. The tilt of the FMS originates due to thermo-mechanical properties of supporting construction. It has been observed that, besides the randomly directed continuous drift of the force signal, the FMS is influenced also by sudden change of the surrounding temperature. The temperature change of ±0.1 °C (over few minutes) leads to over 5 µN to 6 µN force measurement error. The quality of the measurement signal has been improved by thermal isolation.

2.1.1 Temperature and tilt

The simplified schematics presented in figure 2.1 show the basic principle of measurements. In the ideal case the measurements consider no influence from gravity force, when the axis of the system is perfectly aligned in vertical direction (cf. figure 2.1a). Under the actual laboratory conditions several external disturbances affect the measurements. The total measured force is the combination of the acting force (F_L), the tilt force (F_T) and vibration induced forces (F_{err}). Resulting total force, given as F_C, is the addition of the deflection β plus the tilting angle α. The tilt which appears in on-axis direction can be eliminated by measuring it with an equivalent system aligned on the same axis (a detailed description will be given in section 2.3). However, the tilt can be also computed theoretically from zero point measurements as tilt forces (F_T) (cf. figure 2.1b) from

$$F_T = F_C = m_0 \cdot g \cdot \sin(\alpha), \tag{2.1}$$

in so called tiltmeter mode of measurements [46]. In equation 2.1 m_0 is the mass of the dead load, g the local gravity acceleration, α the tilt angle and F_C the applied compensation force to maintain the system in the zero position.

In the system the tilt appears as an error in force signal and it is strongly related to thermal drift of supporting construction. In order to quantify the tilt effect, force measurements in parallel with tilt measurements of the upper plane of the supporting construction were performed by reference tiltmeter [47]. Further, to illustrate random character of this error a simple experiment have been set up along with simulation model. It is intended to estimate the magnitude of the tilt error, as a result of the non-uniform distributed temperature gradients in the supporting aluminum frame. Based on the estimation done in previous work [21] which states that for a dead load of $m_0 \approx 1\,\mathrm{kg}$, the tilt angle has to be less than $\alpha \leq 0.1 \cdot 10^{-6}\,\mathrm{rad}$, otherwise the measured tilt error F_T is higher than the resolution of system $10^{-6}\,\mathrm{N}$ (cf. equation 2.1 and figure 2.1). In the preset work, it is aimed to achieve a resolution at least one order of magnitude better, and thus smaller errors caused by tilt forces has

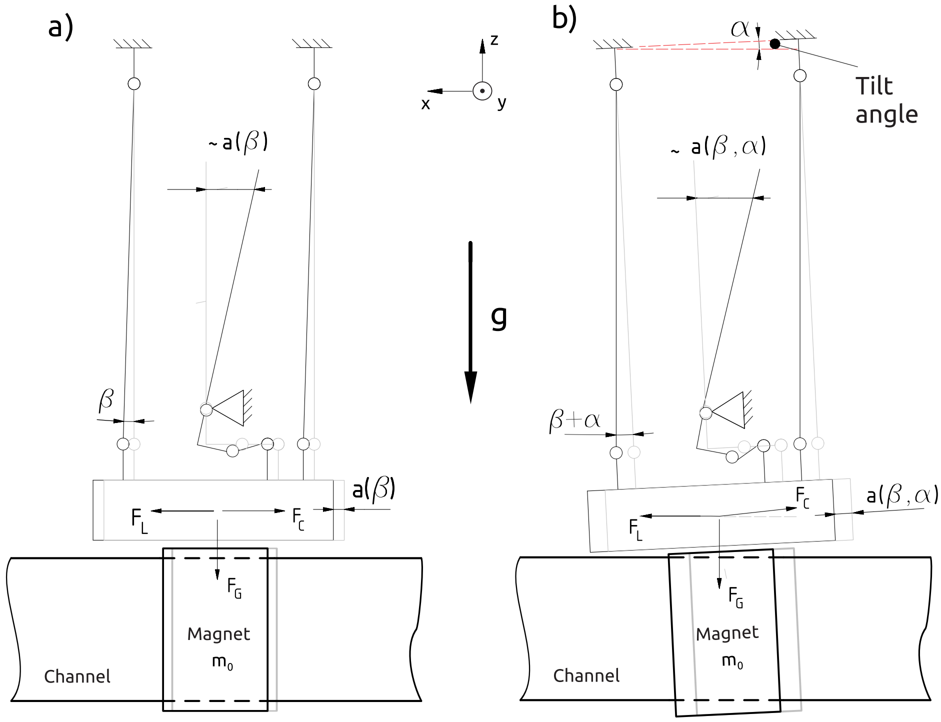

Figure 2.1: Schematics diagram showing the tilt error of the EMFC balance, in grey undeflected state. Deflection: a) in ideal case - a(β), b) impaired with α tilt angle error - a(α+β). F_C - total force measured as EMFC compensation force, F_G - gravity force, F_L – horizontally acting force.

to be correctly resolved.

As preliminary discussed in section 1.2.2 the measurements showed that force signal and temperature change of surrounding environment are strongly correlated. In figure 1.7 is presented one of many consecutive measurements of zero-point stability signal which are influenced by the thermal drift.

These observations allow to identify that thermal expansion of the supporting structure leads to a significant change in tilting angle of the measurement system and thus on the force signal. To demonstrate this fact, an external and controllable point heat source were imposed to the system, particularly attached to the one of the feet of supporting frame (4 in total, all construction is made of aluminum). The heating will induce a thermal expansion of the support, as shown in figure 2.2a.

The control of the heat source is done by a temperature sensor on the contact surface between heating resistor and the aluminum profile. The system response was recorded for repetitive scenarios of temperature change and for different test locations of the heat source. In figure 2.2b is presented an example of measurements of the force signal of zero-point stability by single EMFC balance system (blue curve), change of tilt angle by a reference tiltmeter (red dotted) and the temperature difference from initial (ambient temperature) value on thermocouple (inset right) as function of time. Tilting angle of horizontal upper plane has been monitored by reference device 2.2c, model of inclinometer: Nivel 210 (Leica Geosystems AG) which has

1 µrad measurement resolution [47]. Linearly increasing heat flux during 5 minutes is considered with a maximum temperature change of approximately 4 K. The control of the power dissipation of heating resistor has been done manually by observing the change of temperature. The change in temperature leads to a local thermal expansion of aluminum bar producing a maximum angle change of approximately 2 µrad and a force change of ≈ 15 µN respectively. The value can be used for rough estimation of the error due to tilt force by plugging it into equation 2.1.

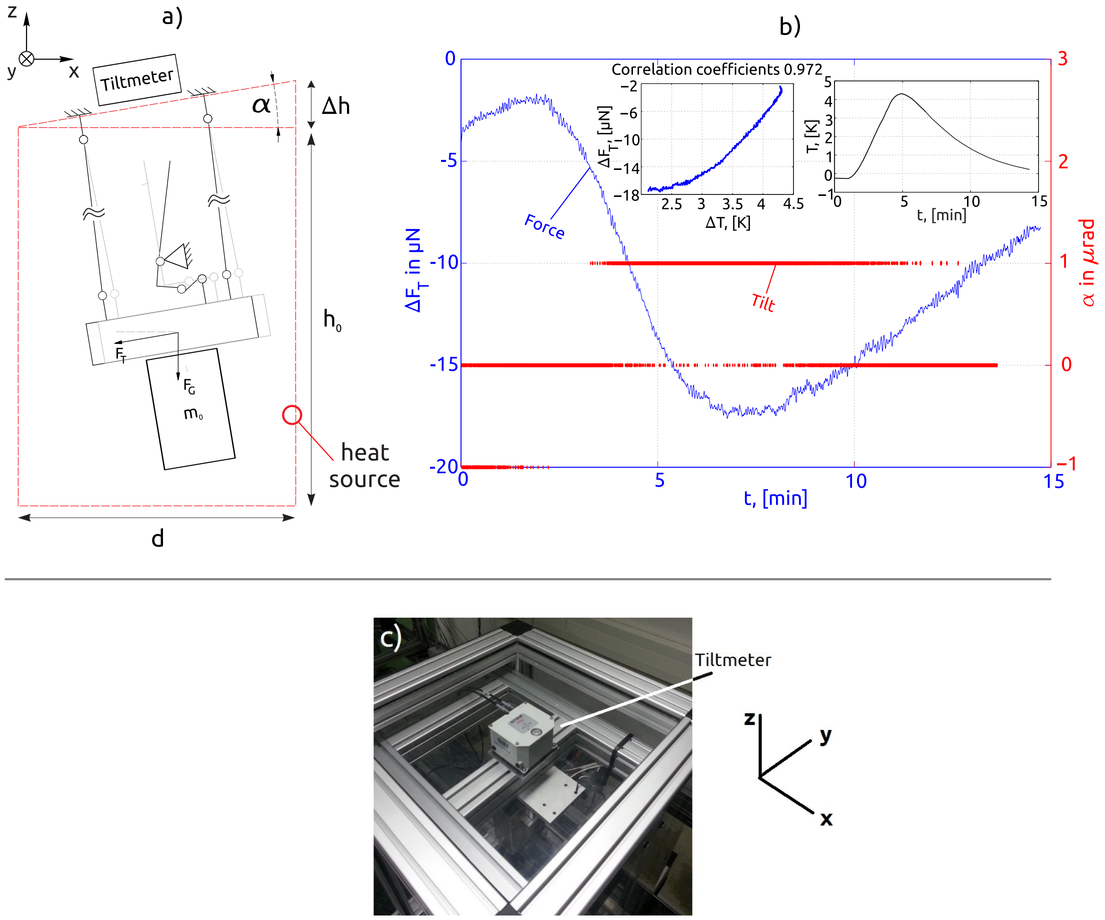

Figure 2.2: Schematics of the experiment and an example of tilt error measurement. a) Exaggerated sketch of tilting angle development, b) measurement of zero-point stability force signal in µN (solid line) over 15 minutes. Tilt angle of force setup in µrad (horizontal dotted lines, right axis). Inset right: change of temperature, left: correlation of the force signal and change of the temperature during first 5 minutes. c) Image of the upper plane of the supporting construction with tiltmeter.

It is possible to estimate the unidimensional deformation of the aluminum profile from the supporting frame when assume a uniform temperature change and considerably simplified construction of the setup. The simplified-model of tilt angle for the linear thermal expansion case can be calculated analytically, analogous to sketch in figure 2.2a, using the following relation

$$\alpha \approx \frac{\Delta h_0}{d} \approx \tan^{-1}\frac{\Delta h_0}{d} = \tan^{-1}\frac{h \cdot \alpha_{\mathrm{Al}} \cdot \Delta T}{d}, \tag{2.2}$$

here the small angle approximation has been used, d and h_0 are dimensions of the base and height of the construction frame, in this case 50 cm and 70 cm respectively. The α_{Al} is the thermal expansion coefficient of aluminum (α_{Al}=$23.1 \cdot 10^{-6}\,\mathrm{K}^{-1}$) and ΔT is the temperature change. It should be notice that equation 2.2 is valid only under simplifying assumptions, that is when the heating is homogeneous and construction has two supporting bars, thus it is expected an overestimation of the thermal expansion for real cases. As mentioned previously, the tilt error can be also calculated analytically by equation 2.1 when change of the tilt angle is measured by high precision reference tiltmeter.

In order to determine full field of deformations of the supporting aluminum frame when point heating source is attached onto one of its bars, a 3-D numerical simulation of the problem was done using COMSOL Multiphysics of the steady state when the temperature reach the maximum (4 K above the ambient temperature)[2]. The lower bases of the four long vertical supports are fixed, namely, their total displacements are zero. Additionally, the connections between the different aluminum bars are considered as rigid. The heat source is modeled as a surface of 2 cm × 5 cm at 296 K temperature and located on the surface of one of the vertical bars at 30 cm from its base, similar to experiment. Also a natural convection over all surfaces was considered. The cross-section of the bars is non-monolithic, as can be observed in figure 2.3. Additionally, the mass m_0 hanging in the middle of the connection horizontal profile is modeled (≈ 4 kg). Due to non-symmetrical defined 3-D problem and a special feature of the support bars an extremely fine mesh with more than 25 million of elements was implemented in simulations.

In figure 2.3 a-c are shown the temperature and total vertical displacement distributions for the described problem. Under simulated conditions heat is completely dissipated in the supporting bar and produces a maximum vertical displacement of ≈ 20 µm at its upper extreme. Notice that rigid connections lead to negative displacements in the opposite side of construction due to ≈ 4 kg weight of upper construction block and the weight of the systems. This can be observed in the 2-D vertical displacement plot in the middle cut plane of the supporting bars, depicted in figure 2.3a. To ensure visualization of vertical displacement it is scaled and presented according to color-code, whereas initial horizontal position of the bars is indicated in black color. Simulation show a change of height in $\Delta h_0 \approx 3\,\mu\mathrm{m}$ that agrees with calculations based on experimental observations and the simple model described by equation 2.2.

Although degrees of the temperature change used in simulation model and test experiments are far to be realistic compared to real temperature fluctuations in the laboratory, they confirm the hypothesis that the thermal expansion effect is the dominant cause of the drift in force measurement signal under stable conditions. In

---

[2] Results of the numerical simulations were obtained in collaboration with Michel Rivero.

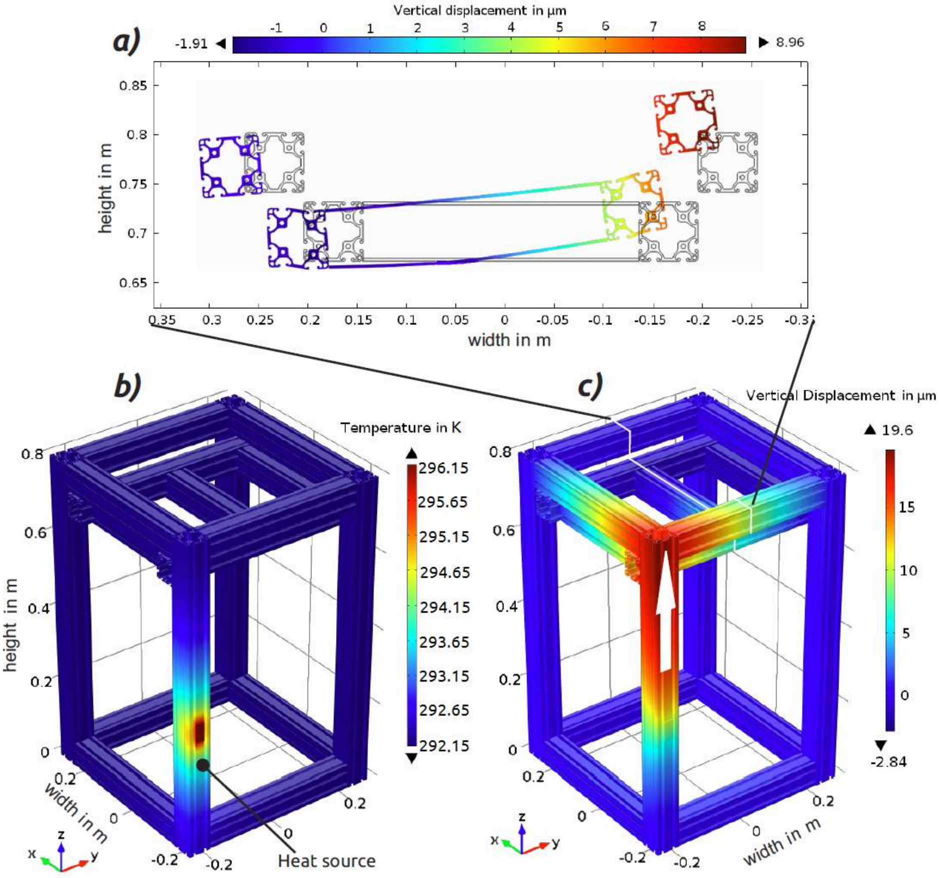

Figure 2.3: Simulation results showing the mechanical deformation of supporting construction. a) Vertical displacement of the support bar shown on symmetry cut plane in µm with initial horizontal position (black line) (scaled by factor of 5000 to ensure visualization). b) Temperature field distribution for simulated a point heat source in K. c) Total vertical displacement in µm.

fact, the same rate of temperature change during independent measurements leads to random drift due to other undefined and imbalanced mechanical stresses existing in supporting construction, which partially explain the force jump shown in figure 1.7. Moreover, reference tiltmeter shows random orientation of supporting construction after settling of the temperature influences.

Analysis summarized above provides an overview on dominant temperature effects causing the drift of force signal due to complex thermo-mechanical stresses, aside (yet being) insignificant temperature dependent variations of the magnetic field strength of the magnet inside of the voice coil of EMFC balance.

2.1.2 Stability of the mechanical construction

As discussed in the previous subsection, the force signal (under the current laboratory conditions) is mostly sensitive to the change of the tilt angle of the FMS. Therefore, the general stability of the overall mechanical construction (FMS together with the supporting structure of the stone, cf. items 3, 4 and 5 in figure 1.5) should be investigated. In order to verify that the force signal is sensitive also to the change of the tilt angle of the stone a simplified experiment is performed. In figure 2.4 the supporting construction of the FMS and the stone (cf. items 3, 4 in figure 1.5) is shown. At the points indicated in the figure (*a)*, *b)* and *c)*) a 2 kg mass piece is applied to influence the construction to tilt. At each point, the mass piece is loaded and unloaded alternately. The force signal from FMS is recorded in parallel with the reference tiltmeter (cf. figure 2.2). The tiltmeter is arranged such that one of its measurement axis coincides with the force measurement direction (x), whereas the second measurement axis of the tiltmeter makes the tilt measurement of the same horizontal plane but perpendicular (y) to the FMS measurement axis.

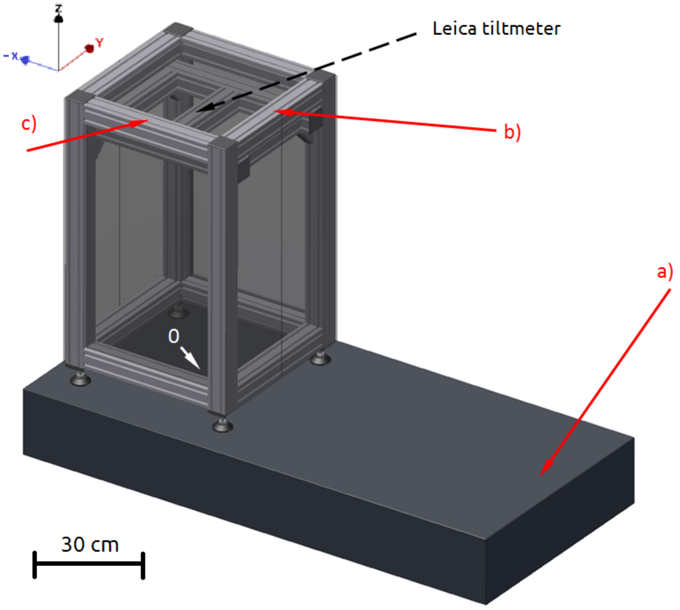

Figure 2.4: Configuration of the experiment showing the influence of the tilt angle of the stone on the force signal (left). The position of a) is chosen to be 150 cm away from the center base point of the FMS, refer to side view in 2.5 *a)* and *b)*.

The force signal is inserted into equation 2.1, and the resulting α tilt angle is compared with the measurements of the tiltmeter. These comparative measurements are made for each individual *a)*, *b)* and *c)* loading point separately, the examples are being shown in figure 2.5. At point *a)* the change of the α tilt angle can be measured by FMS and tiltmeter, revealing the best correspondence with each other. When the load is placed on the top of the supporting construction, point *b)*, other tilting angles are developing (α_1 and α_2), due to mechanical deformations of the supporting constructions (of the FMS and of the stone). At point *c)*, only the change in the y angle is measurable with the tiltmeter, whereas the FMS still measures some other parasitic tilt angle changes. The magnitude of the force change is: *a)* ≈ ±11.8 µN, *b)* ≈ ±10.2 µN and *c)* ≈ ±8 µN.

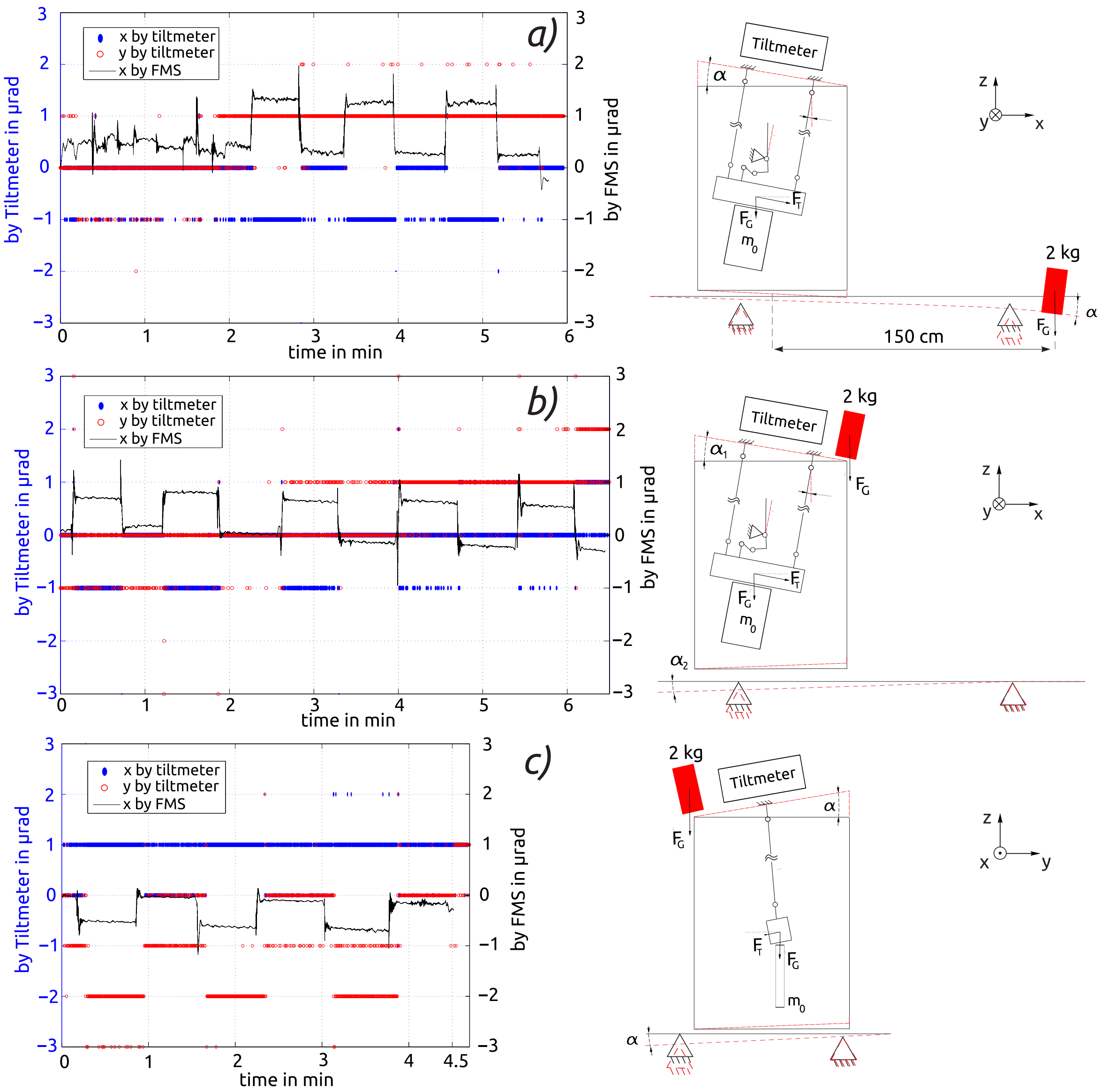

Figure 2.5: Test measurements of the tilt angle, developing due to the load influence by a 2 kg mass piece. The x- and y-axis measurements of the tiltmeter (symbols), the FMS measurements considered to be sensitive only for x direction changes (solid). It is presented for three different cases (as in 2.4). For a) and b) the change of the tilt angle is observable in x direction (side view), for c) in y direction (front view).

In order to verify a further development of the tilt angle, a set of mass pieces of higher weight m_{Load}=1, 3, 5, 10, 15 and 20 kg are applied on the stone at position *a)*. For each m_{Load}, a loading and unloading procedure is repeated three times. The readings from the FMS and the tiltmeter are taken once the settling time is reached.

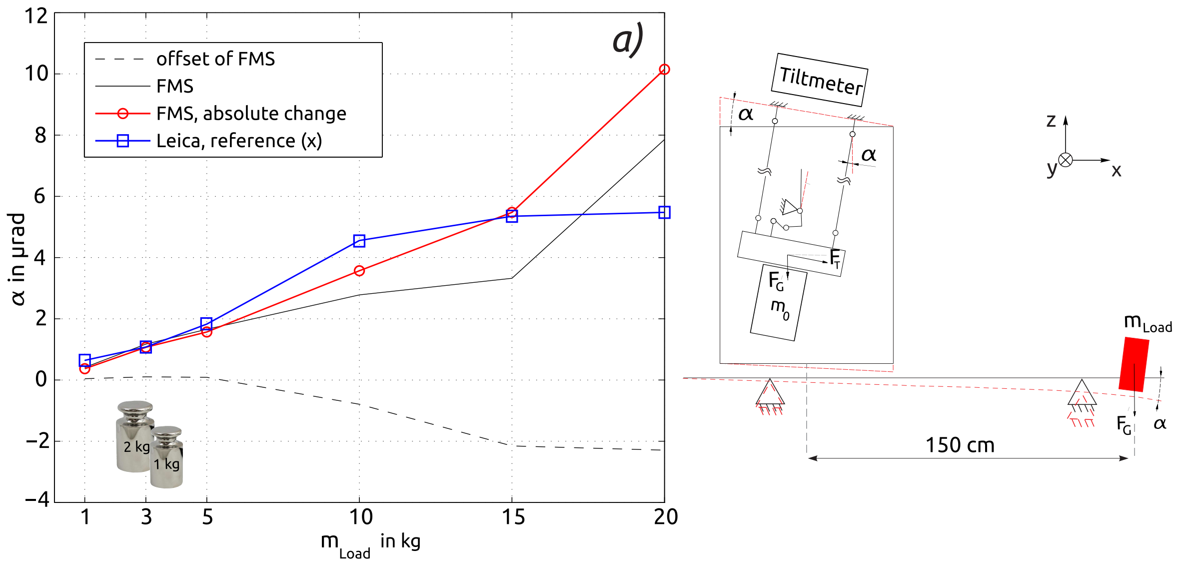

Figure 2.6: Comparison of the tilt angle measurements by FMS and tiltmeter against the loads applied to the stone. The change in the tilt angle is developed due to applied loads on the stone. Right: the tilt angle offset drift due to loading and unloading measured by FMS (—), the absolute change of the tilt angle measured by FMS (○—), reference measurements by tiltmeter (□—). Left: the sketch of the tilt measurement experiment shown in side view (cf. figure 2.4).

The measurements of the tilt angle (converted from the force value cf. equation 2.1) with FMS provides a better resolution in comparison with the tiltmeter. Therefore, the offset drift is presented on the basis of measurements of FMS (cf. figure 2.6 dashed line). The comparison of these measurements shows the direct correspondence of the force signal drift with the developed tilt angle. Moreover, when the supporting construction of the FMS is re-positioned to the center (or to the opposite edge) of the stone the behavior and the magnitude of the force drift are changed. Thus, it is possible to conclude that the stability of the force signal is strongly obstructed by the temperature-dependent tilt angle developments, due to the greatly imbalanced mechanical stresses existing in the supporting constructions (items 3 and 5 in figure 1.5). These errors, however, may be corrected using a high-precision tiltmeter once the supporting construction is reduced towards a simpler and well-defined mechanical assembly.

In order to avoid these tilt effects and to validate given reasoning, an identical second EMFC balance with an equal dummy weight is introduce on-axis of the first EMFC balance. In the next section, a newly developed differential force measuring system provided with mechanically simplified suspension elements is described. By this configuration one of the EMFC balance measures the forces which are applied in horizontal direction combined with noise effects, whereas the second EMFC balance measures only the noise effects. By using this method, it is expected that - when considering the difference of both signals - only the forces which are acting in horizontal direction will be detected.

2.1.3 Spectral analysis of the force signal

In this subsection, a brief characterization of the force signal is presented with regard to its spectral distributions over the frequency domain. The time-dependent force signal is exploited in the following by means of its frequency and amplitude. In figure 2.7 (left) a typical signal of the force measurements at the zero-point stability over a period of 4 hours is presented. The response time of the old FMS is ≈ 1.4 s [15]. The amplitude of the force signal on the time domain shows pick-to-pick values of about 2 µN. The signal can be sampled at a maximum frequency of ≈ 18 Hz to 20 Hz (for the maximum achievable resolution), therefore, in the frequency domain only below ≈ 10 Hz frequencies of the force signal are observable, in accordance with the Nyquist theorem.

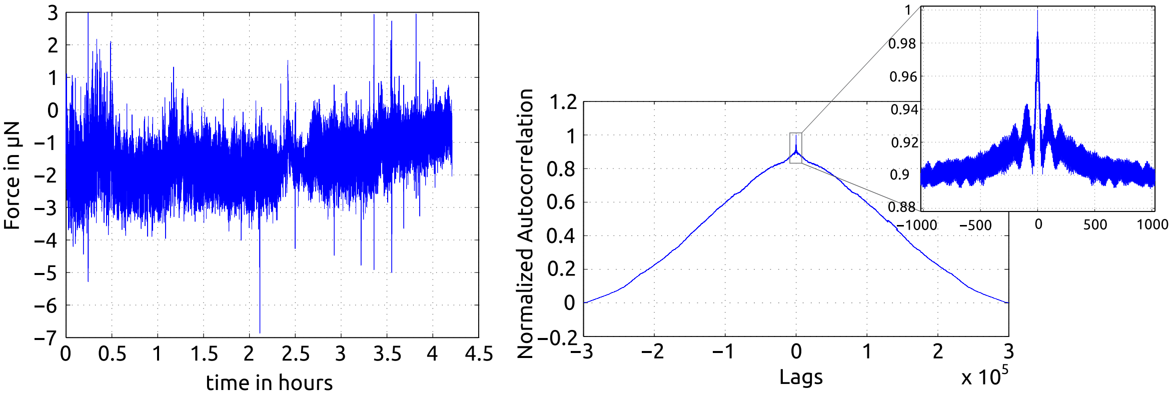

Figure 2.7: Typical force signal measured at the zero-point stability over a period of 4 hours (left) and the plot of normalized autocorrelation (right).

The randomness in a data set is ascertained by computing autocorrelations for data values at varying time lags. From the plot of the autocorrelation in figure 2.7 (right) it can be observed that the signal does not entirely consist of white noise, but rather has some weak degree of autocorrelation between the adjacent and near-adjacent time lags.

To reveal more information about the dominant frequencies (of non-random origin) which are developing the noise, the power spectral density and the distribution of the amplitude spectrum of the force signal in the frequency domain are plotted. The force signal is converted from the original time domain and shown in the frequency domain, using the discretized computation of the fast Fourier transform (FFT).

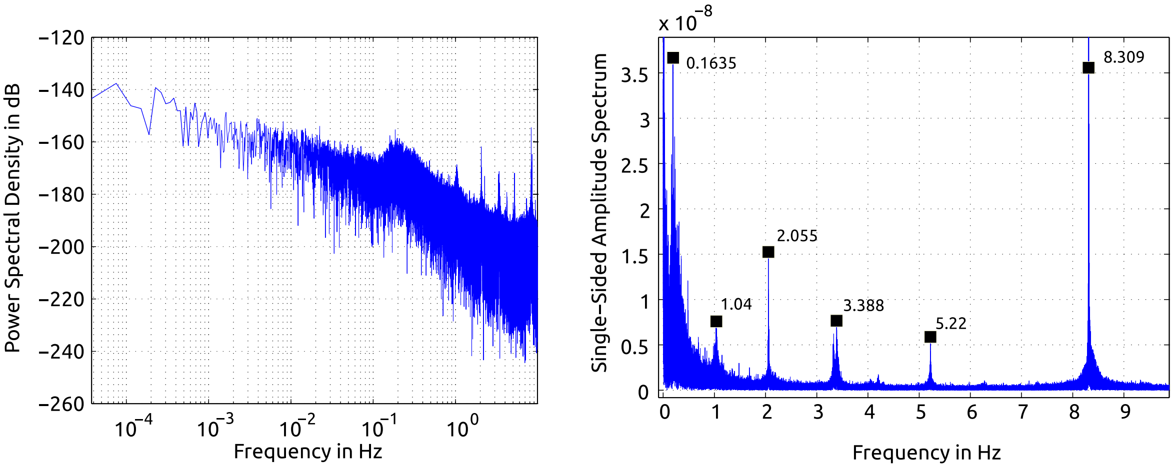

Figure 2.8: The power spectral density (left) and the amplitude spectrum distribution (right) of the typical force signal over the frequency domain. The peak values of dominant frequencies in the amplitude spectrum plot are indicated in Hz.

The power spectral density presented in figure 2.8 (left) illustrates the fact that the signal is strongly obscured within frequency band of 0.1 Hz to 0.4 Hz, aside the slower processes which are becoming influential below 10^{-2} Hz frequency. From the signals' amplitude spectrum distribution, presented in figure 2.8 (right), the resulting peak value in this frequency region amounts to 0.1639 Hz for this particular force signal (this value varies within 0.15 Hz to 0.18 Hz for all other measurement signals). There are few more dominant frequencies whose influence can be neglected (cf. figure 2.8). However, these frequencies exist in all measurements made with the old FMS [21]. In section 2.3.5, a more detailed discussion of the origin of these frequencies is provided.

2.2 Details of the new EMFC balance

In this section, the details and basic properties of the new model of EMFC balances are presented. New EMFC balances are to be used to develop differential FMS. In comparison to old FMS, where an older version of similar EMFC balance was used, no modifications concerning their mechanical structure, electric circuit or data processing method were made here. Due to some commercial and authorship regulations, the EMFC balances and their electronics they will be treated, to a certain extent, as a black box[3]. Similarly, the old EMFC balance used in single FMS was

---

[3] Most of the commercial equipment, instruments, or materials are identified in this dissertation in order to characterize the experimental and measurement procedure adequately, solely with the intention to provide legal grounds for comparison or as a reference for any of potential development/research to be made in the future. Thus, such identification is neither intended to imply recommendation/endorsement by the author, nor is it intended to imply that the materials or equipment

grossly treated as a black box, and all of the initial measurements made in this work (section 1.2.2 and 2.1) were intended to reveal the measurement characteristics of the system. Therefore, most of the investigations presented in 1.2.2 and 2.1 were accompanied/compared with some reference devices (tiltmeter, temperature sensors, etc.) in order to estimate the magnitude of changes and the general behavior of the system.

2.2.1 Basic properties of the balance

Only few reports are known which deal with such high-precision EMFC balances in detail, for example [21] and [48]. In this work, special attention is focused on several behavioral characteristics of the EMFC balance which are critical when adapting it for the LFV application. Later in this chapter, the comparison of the new EMFC balances with the old EMFC balance will be presented, see in section 2.3.5, and section 2.4, and table 2.1.

The EMFC balance is provided by *Sartorius - AG (Göttingen)* [40], the model according to the electronics is of a *WZA16-LC* model. Some of the EMFC balance details are available in the datasheet. The balance has a working range of ±5.5 g with a readability of 1 µg, therefore, the range of force measurements (F=mg) may be approximated as ±55 mN and the readability of ≈ 10 nN. Depending on the site of the measurements the value of the local gravity acceleration g is different. According to publicly available information system [49] provided by PTB, the value of g reads $9.810\,131\,\mathrm{m\,s^{-2}} \pm 0.000\,041\,\mathrm{m\,s^{-2}}$ within the level of confidence of approximately 95 % (i.e. coverage factor k=2).

The complete EMFC balance consists of an actual mechanical part and its corresponding electronic device, some components of the electronics are integrated inside the mechanical part.

The mechanical part of the balance is made of a monolith block of an aluminum brick and has a complex inner structure. The main parts of the balance may be simplified as follows: a load carrier is connected to the frame of the balance by flexure hinges and four parallel beams, constructing a 1DoF parallelogram guidance for the load carrier. The load carrier is additionally connected to a lever arm (leverage 1:≈5.41 proportionality factor). A coil is connected at the longer side of the lever arm (opposite side of the load carrier), whereas the permanent magnet assembly is firmly mounted on the balance's frame. At the top end of the longer side of the lever arm is located an ensemble of the photoelectric positioning sensor. The sensor consist of two components a) LED facing to a differential photodiode, both fixed to the frame of the balance, and b) rectangular aperture mask, fixed to the lever arm. The rectangular aperture mask obstructs the path of the photo transmission between LED and differential photodiode, therefore, the effective deflection of the lever arm (load carrier) exerts a proportional photoelectric signal in the sensor. The signal is a voltage, which is converted from the generated electric current difference in the differential photodiode. Further, this voltage is passing through a PID controller of

---

identified are the only and/or necessarily the best available for the purpose.

the balance's electronics is converted to an electric current. It is the necessary compensation current to be applied to the coil to control the position of the lever arm. This is done by the well-known electromagnetic interaction between the coil carrying certain amount of electrical current and the magnet. The force is measured by multiplying the compensation current with some force constant, defined by the manufacturer. Thus, the measurements made by means of the EMFC balance consider the method of balancing at the zero point. This method is known as closed-loop operation, however, when the coil is disconnected from the electric circuit of the EMFC balance electronics, the open-loop measurements may be made. In the open-loop regime, the measurement signal is simply the measured voltage from the positioning sensor.

When the EMFC balance is arranged in vertical position (cf. figure 1.6) the lever arm and the load carrier are resting in a naturally achievable stable zero position. By measuring the signal (voltage of the positioning sensor) of the EMFC balance in the open-loop mode, it is possible to determine the zero position and adjust the balance mechanically. Thus, an offset correction to keep the lever arm at the virtual zero position is no longer necessary.

2.2.2 Electronics and software

The data processing is carried out by the electronic part of the EMFC balance, designed by *Sartorius*. For each EMFC balance the electronics is unique, since in the control scheme some temperature and non-linearity compensation aspects are taken into considerations.

The complete electronic part consists of a photo-positioning sensor, a microelectronic unit and the coil. The voltage from the photo-positioning sensor serves as an input parameter for the microelectronic unit, whereas the output is the electric current (being applied to the coil) generated by an analog PID controller inside the microelectronic unit. The electronic unit can be connected to a personal computer (PC) for retrieving the measurement results using various types of connections (RS-232, USB, etc.). None of these types of connections has shown a considerable advantage against another one (in the scope of this work), therefore, a USB connection type is used for simplicity.

Figure 2.9: Scheme of the filter adaptation regimes of the EMFC balance (short).

According to the datasheet [40], the microelectronic unit provides a maximum data output rate of around 150 Hz (values per second) for a certain filter adaptation regime. Unfortunately, as discussed earlier, neither a complete documentation nor the source code of the microprocessor was available in order to test this property. Despite the value given in the datasheet as maximum data output rate, in reality only 80 Hz to 100 Hz were maximally achievable during the test measurements using different software environments (LabVIEW, C++)[4] with different implementation algorithms. Therefore, a new custom *C++* code was developed to maintain data acquisition between the PC and the microelectronic unit.

The microelectronic unit has various settings which are possible to choose optionally. In this work, however, a considerable part of them were turned off. Only several filtering options were critical and of practical interest (cf. figure 2.9). It is provided multilevel options to choose necessary mode for the data filtering. In order to receive data readouts continuously at a maximum data output rate, none of the built-in filters or operation regimes should be used. It is of a particular importance to mention that all of them are specially designed by the manufacturer on the assumption that the mechanical part of the balance is aligned horizontally. When the usage of the mechanical part of the balance (in this work, rotated by 90°) varies from defined recommendations given by the manufacturer, special care should be taken to assure the proper behavior of the balance and its measurement results obtained by built-in filters. In this work, although in the calibration procedure all possible combinations of the built-in filters are tested (cf. section 2.3.3), most of the measurements have been made without using the built-in filters, thereby the measurement signal is received directly from the PID-loop (cf. figure 2.19 bottom row “OFF OFF”).

2.3 Differential force measurement method

To compensate the drift of the force signal and to reduce the vibration errors a reference system is required. An identical EMFC balance with an equivalent mass of the dead load is used for direct referencing the calibration (or the Lorentz) force measurements. Below, in this section the measurement principle of newly developed differential force measurement setup (dFMS) is presented. The border value in measurements of horizontally directed forces with earlier developed FMS is assumed to be 1 µN [21], as it is discussed in section 2.1. In this regard, the goals to be achieved by the dFMS are to define and increase the temporal stability of measurements and to increase the force measurement resolution at least by one order of magnitude (0.1 µN).

2.3.1 Measurement principle and mechanical construction

The addition of a second EMFC balance with the same dynamic behaviour on-axis of the first EMFC balance allows a simpler treatment of the force signal. The dFMS system can be described as two free swinging simple pendulums having one degree of freedom and 13.5 N dead load each. Thus, the complete dFMS consists of two identical but independent working EMFC balances, two equal masses which are suspended

---

[4] Also tested by MATLAB and Python, yet the maximally achievable data readout rate is $\lesssim$10 Hz

from each EMFC balance, and correspondingly identical mechanical suspension components which are fastening both EMFC balances to the common bearing plate. The functional diagram of the dFMS is presented in figure 2.10 a) in side view and the sketch of the suspension construction in b).

In order to minimize the effects originating from thermo-mechanical stresses, the suspension system is designed under the consideration to provide minimal surface contact between the different parts of the construction. For this reason, the common bearing plate and two elbows (items 1 and 2 in figure 2.10) are made of restrained monolithic aluminium blocks and fastened together with minimal surface contact, as it is the case for the contact between EMFC balances and elbows. Additionally, this design provides the possibility of fine tuning of both EMFC balances to common axes, as shown in figure 2.10 b), where the reference axis for the two elbows (2) and the common bearing plate (1) are depicted in dashed red and grey, respectively.

A horizontally directed calibration force F_L is applied to the system, particularly to the dead load. The force deflects the lever arm of the EMFC balance (the diagram is an exaggerated representation) which is possible to measure directly by an internal photo-positioning sensor of the EMFC balance in the open-loop mode. In the closed-loop mode, the EMFC balance compensates deflection of the lever arm by balancing it at vertical zero position using a compensation current applied to the internal voice coil. In this case the current is proportional to the applied calibration force. In the diagram, both configurations of the calibration element are shown (item 6 in figure 2.10). In the first case, the calibration element is mechanically fixed to one of the EMFC balances and to the external fixed point. In this configuration, only one of the EMFC balances is sensitive to the calibration force. In the second case, the calibration element is fixed to both EMFC balance, therefore, both EMFC balances are subjected to a forces which have the same magnitude but opposite direction. Also, when the whole system is tilted both EMFC balances are sensitive to the common error, namely a tilting force (F_T) which is originating due to the gravitational force F_g.

Considering that the force measurements of the reference EMFC balance is $F_{1M} = F_{err}$ and the force measurements with an actively used EMFC balance is $F_{2M}=F_{err}+F_L$, then the difference $F_{diff}=F_{2M}$-$F_{1M}=F_L$ in the ideal case would be equal to the calibration force. Under this consideration the common error is assumed to be measured by both EMFC balances. Thus, any discrepancy between the applied F_L and measured F_{diff} forces may represent parasitic forces from other error sources. Complete image of the dFMS presented in figure 2.11.

Both EMFC balances are aligned together to the x-axis by their natural zero stable positions. This offset position is defined experimentally by unplugging the PID controller and measuring the natural zero position of the EMFC balance directly by the voltage signal of positioning sensor in the open-loop mode. However, to avoid unforeseen angular errors which may develop during the actual force measurement processes, one should consider to align both EMFC balances by their absolute angles for each individual axis.

Beside this, it should be also considered a special type of coupling between the dead loads and the EMFC balance. For experimental proposes in measurements of

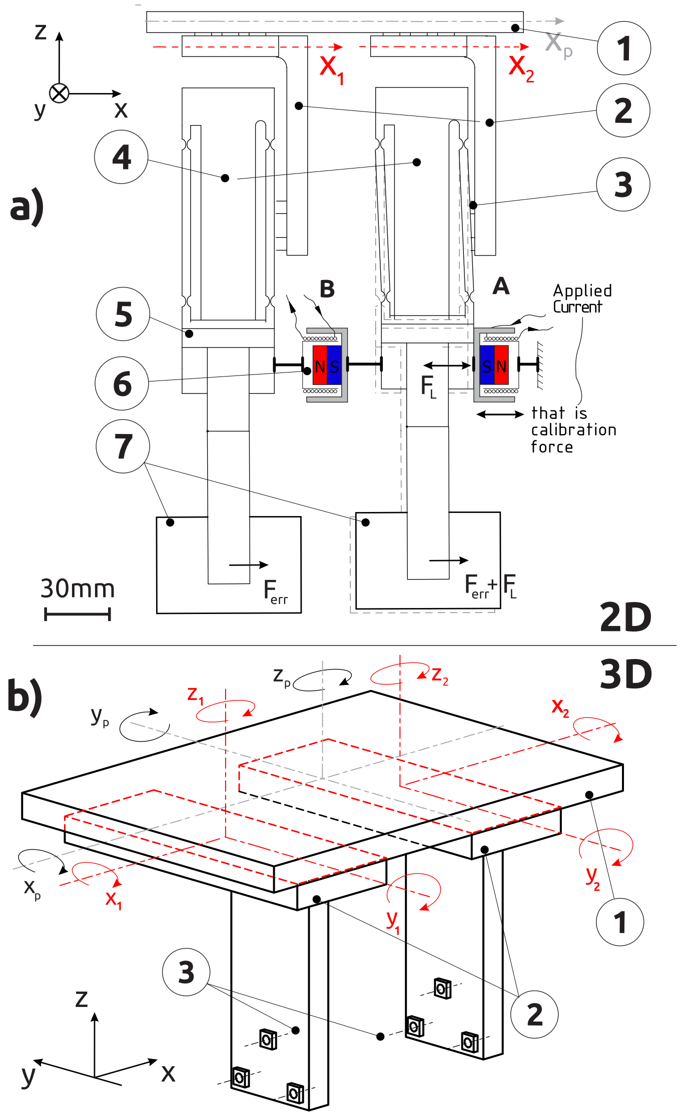

Figure 2.10: Functional diagram and geometrical configuration of the EMFC dFMS. a) Side view presented as two independent pendulum, dashed line in the right EMFC balance indicates initial state. b) Sketch of suspension construction. (1) common bearing plate, (2) separate elbows for tuning EMFC balances in horizontal plane, (3) clearance holes for fixing EMFC balances, (4) EMFC balance, (5) load carrier, (6) voice coil actuator for generating calibration forces on the dummy weight. It is fixed in two different configurations; position A - external ground and dummy weight, position B - dummy weight and dummy weight, (7) dummy weights. $x_{p,1,2}$; $y_{p,1,2}$; $z_{p,1,2}$ - represent axes for fine tuning each suspension block, items (2) and (1). Subindexes $-_1$, $-_2$ (red) are designating axes of each individual elbows and $-_P$ for common plate.

Lorentz forces the dead load (or the magnets) should be handled and adjusted man-

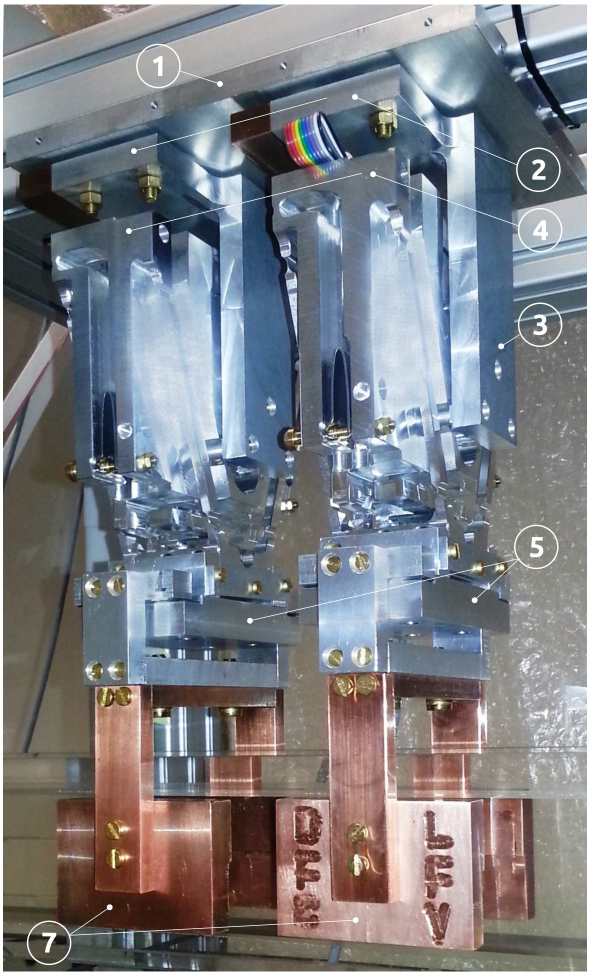

Figure 2.11: Image of the *d*FMS. Designation of the component parts similar to figure 2.10.

ually. Due to fragility of the EMFC balances it is necessary to assure the coupling of load carrier and dead load with high precaution. In the old FMS (*Diethold et al.* [21]) a solidly fixed mechanical contact was used. This type of coupling imposes several technical complications during the adjustment process of the dead load to the load carrier. Another, a restriction based complication is due to the safety tolerance which is given for the position of the dead load in respect to the electrolyte channel (less than ±1 mm along y axis). Also, this type of coupling neither prevents the EMFC balances from the sudden mechanical shocks nor the high stresses on its flexure hinges which might appear due to unexpected mechanical contact between the electrolyte channel and the dead load. By trial and error a new type of coupling is developed for the *d*FMS, it is based on method of quasi-kinematic coupling constraint using a sphere and groove geometries with some additional considerations.

Since the forces (maximum $F_L \approx 100\,\mu\mathrm{N}$) which should be measured are acting in horizontal direction are negligibly small to overcome the friction forces produced by dead load (item 7) of $\approx 13.5\,\mathrm{N}$ it is possible to suspend the dead load from the load

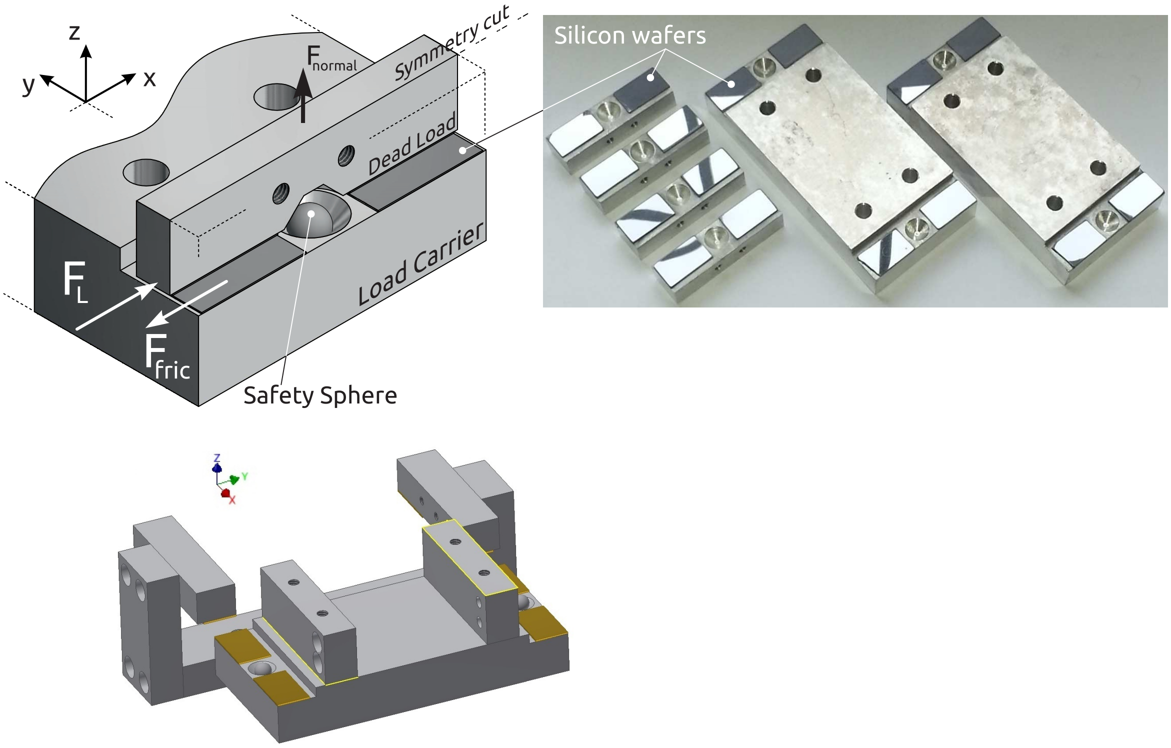

Figure 2.12: Friction based coupling (left), and the image of the components (right). The silicon wafers are used as a contact surface.

carrier without mechanical fixation.

$$F_L \ll F_{friction} \tag{2.3}$$

$$F_{friction} = \mu_0 \cdot F_{normal} = \mu_0 \cdot F_g = \mu_0 \cdot m_0 \cdot g \tag{2.4}$$

where $\mu_0 \approx 0.1$ to 0.4 is the friction coefficient between two silicon wafers, $F_{friction} \approx 1\,\mathrm{N}$ to $5\,\mathrm{N}$. Thus, only in case when $F_L \geq F_{friction}$ the dead load will slide on the surface. This provides means to set the dead load on a flat surface of the load carrier and adjust it in accordance with given requirements. In figure 2.12 (left) the sketch of the friction based coupling and the image of the components (right) are presented. The manufactured parts are providing adjustable position tolerance of the dead load in respect to load carrier as $\pm 2.5\,\mathrm{mm}$ in x and y directions, and approximately $\pm 7°$ in xy plane in respect to the nominal zero position (cf. figure 2.12 (left) rotation about z axis).

2.3.2 Data treatment and filtering

Since the EMFC balance is arranged in an unusual configuration and its application differs from the designed commercial mode, the built-in filters of the electronics cannot be applied directly. However, in the calibration procedure all combinations of built-in filters are tested, a moving average filter is chosen for raw data filtering. This digital filter is designed based on an external software model. A standard feed backward FIR (finite impulse response) filter is considered with the z-transform of first difference $(1 - z^{-1}) \cdot X(z)$. The numerical formulation simplifies to

$$F_L^{(j)} = h \cdot F_{Lf}^{(j)} - (h-1) \cdot F_{Lf}^{(j-1)}, \tag{2.5}$$

where F_L and F_{Lf} are raw and filtered signals at measured point j while h is the coefficient of the filter. To choose the value of this coefficient, a statistical estimation is performed on the typical measured raw data having t=1 hour duration, analogous to the Allan Deviation method.

$$f(t,h,\tau) = \frac{\left[\displaystyle\sum_{i=1}^{n} \mathrm{std}(F_{Lf}(h,\tau))\right]}{n} \geq 10\,nN, \tag{2.6}$$

here n=1,2,⋯, max(t/τ).

The estimation procedure is based on two main considerations; *i)* when the dead load is removed, m_0=0 kg, the EMFC balance should measure its natural stable point that is a static zero force, *ii)* the limit of measuring static force is preset by the manufacturer as minimal readability value ≈ 10 nN and response time of τ_0=1.4 s. To be conservative, the general criterion is chosen such to not exceed the limit given by *(ii)* while filtering the static zero force signals for minimal τ duration. The first value is chosen as $\tau_0 < \tau_1$=1.8 s, which leads to integration over j=45 samples (f_s=25 Hz). This value is continuously increased for each iteration up to 20 minutes. The signal is filtered with h=2,3,...,70,... for each subsequent τ time interval during the whole measurement period. Finally, the mean value (cf. equation 1.3, $f(t,h,\tau)$) of the standard deviation is computed as a function of τ and h.

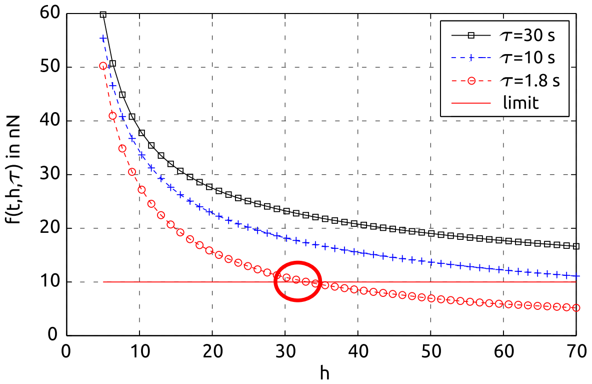

Figure 2.13: Estimation criterion as a function of h filtering coefficient and τ integration time window, (cf. equation 1.3).

In figure 2.13 the estimated force resolution is shown as a function of the filter coefficient and the integration time window. The optimal value for h is chosen from the graph when the curve converges with the border of the readability limit. In this case τ=1.8 s, which is slightly above the settling time of the EMFC balance, the filter coefficient is h=30. Thus, this filtering model with the obtained coefficient is used to compute the resolution of differential force measurements.

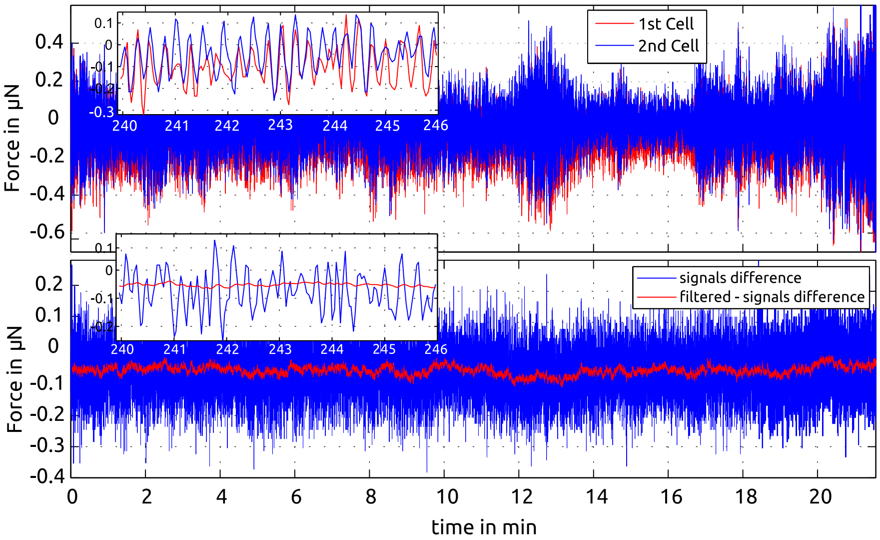

Figure 2.14: Force signal from dFMS of zero-point stability measurements. Top: Raw signal of both EMFC balance over 20 minutes, Bottom: difference of signals and filtered difference of signals (h=30). Insets: magnified measurements over 6 s time window of the signals presented in μN and s.

Figure 2.14 shows the force measurement signal when m_0=0 kg and the sampling frequency is 25 Hz. In the upper figures (in minutes) and insets (in seconds), the raw signals of both systems are plotted. The standard deviation of both signals over the whole measuring time (20 min) is 0.134 μN and 0.136 μN. The difference of both signals leads to a resolution of 82 nN, as can be observed in the lower figures. When the difference signal is filtered by the previously defined filter with coefficient h=30, a resolution of approximately 14.9 nN over 20 min is obtained.

2.3.3 Calibration: *in case of quasi-static forces*

2.3.3.1 Position A

For the calibration procedure, a voice coil linear actuator is used in order to generate horizontally directed forces. As depicted in figure 2.10 the voice coil actuator is assembled in two different configurations. In the first configuration the voice coil is fixed to the external point and to the suspended dummy weight (cf. figure 2.10 a) position A). In this state the calibration force is applied to one EMFC balance and, therefore, the calibration force is the difference between both signals, namely F_L=F_{diff}.

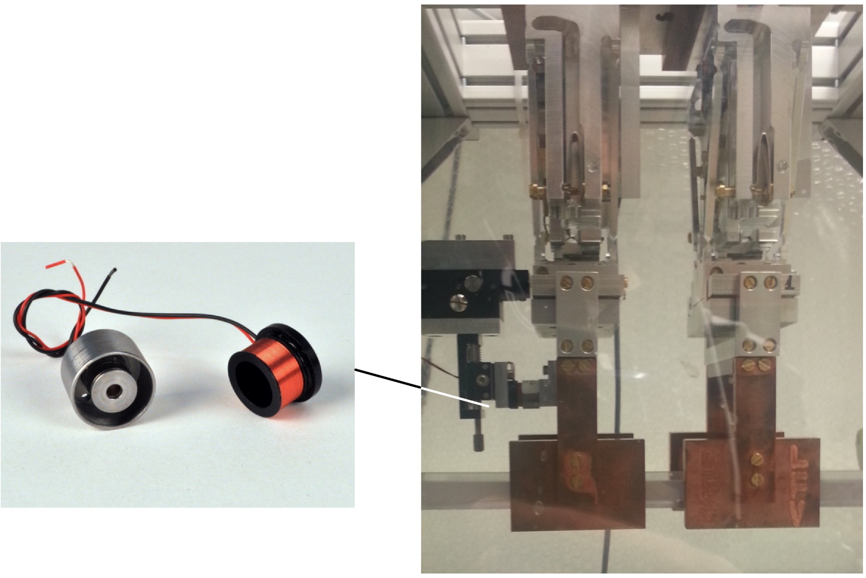

Figure 2.15: Image of the dFMS calibration setup at position A.

In the second configuration, each element of the voice coil is fixed to each suspended dummy weight (cf. figure 2.10 a) position B), therefore, the same force is measured by two EMFC balances as oppositely directed calibration forces $F_{1M} = F_L + F_{err}$, $F_{2M} = -F_L + F_{err}$, thus $F_L = F_{diff}/2$. The force constant (or $l \cdot B$) of the voice coil is given as 0.9 N A^{-1} with 5 % accuracy, depending on the adjustment and immersion depth. With all available data it is possible to compute this constant experimentally.

A precision current source [50] is used to apply 100 nA DC current steps to the voice coil. In order to verify the measurement range of both EMFC balances within the limits of interest of ±100 µN, the current is applied step-wise in multiples of ΔI=100 nA or in the form of a square wave of different magnitudes. The same procedure is carried out while the EMFC balance is operating in different regimes of the built-in filters. Examples of typical calibration measurements within a force range of ±25 µN and ±1 µN are presented in figure 2.16 and 2.17, respectively. In these figures, the raw signals and their difference are plotted. In both cases the calibration voice coil is located in position A. From the figures it can be observed that forces larger than 1 µN can be accurately resolved by both systems. On the other hand, for measurements below 1 µN the force steps can be hardly distinguished from the raw signal. When the difference of the signal is taken, ≈ 93 nN steps can be resolved even without special treatment of the signal. The same results were obtained when the calibration voice coil is is arrange at position B. Data analysis are carried out in agreement with the recommendations given by GUM [51]. The calibration measurements presented in figures 2.16 and 2.17 are only illustrative examples of many similar measurements for two different measurement ranges. Figure 2.18 shows the complete range of calibration measurements, tested over the range of ±100 µN. The slope of the linear fit computes as ≈ 93 µN µA^{-1}, which is the force constant of the

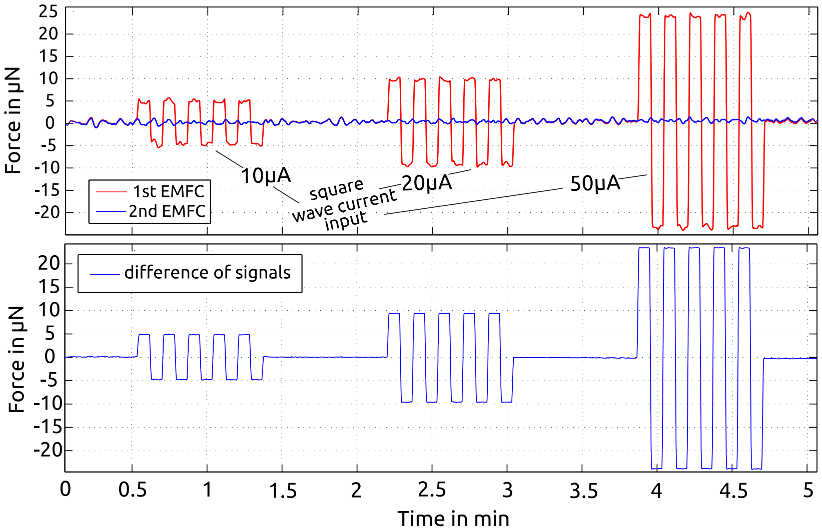

Figure 2.16: Calibration measurements of dFMS against quasi-static forces in the range of ±1 µN to ±25 µN, when the voice coil actuator is arranged at position A. The calibration force is produced by a electrical current which is applied to the voice coil (see Figure 2.10a). Raw measurement signal from both balances (top), and difference of signals (bottom).

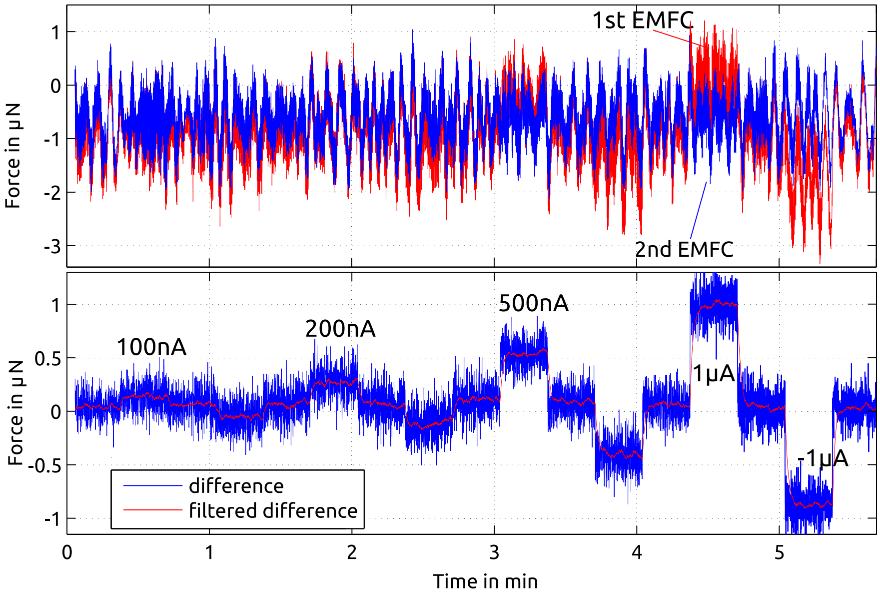

Figure 2.17: Similar description as in figure 2.16 for the range of ±0.1 µN to ±1 µN forces.

voice coil actuator (cf. figure 2.10 position A). The measurement data points are randomly variate on average with 7 % accuracy. This value is in tolerable agreement with the manufacturer's specifications. In this measurements the measured difference

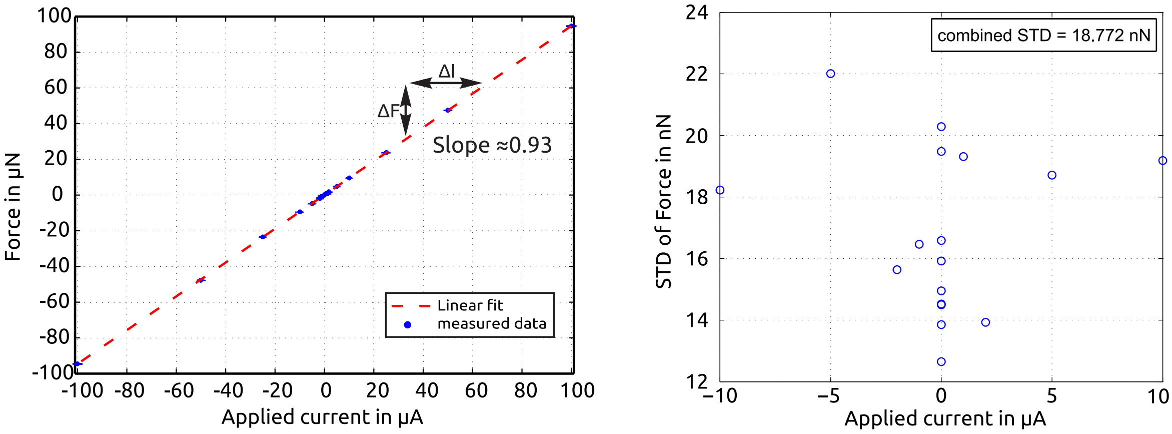

Figure 2.18: The linear slope of the calibration measurements for case of applied quasi-static forces (left), given as measured differential signal of dFMS against applied current to the external linear voice coil actuator arranged at position A. Standard deviation of filtered F_{diff} signal at each step (right).

signal from dFMS can be described as:

$$\Delta F_{diff} = \Delta F_{2M} - (\Delta F_{1M}) = \Delta F_L \tag{2.7}$$

where

$$F_{2M} = F_{err} + F_L, \quad F_{1M} = F_{err} \tag{2.8}$$

Taking in account that both EMFC balances can be used under built-in filtering modes (preset by manufacturer, cf. the scheme provided in figure 2.19) it is possible to test their performance based on this configuration of the calibration measurements.

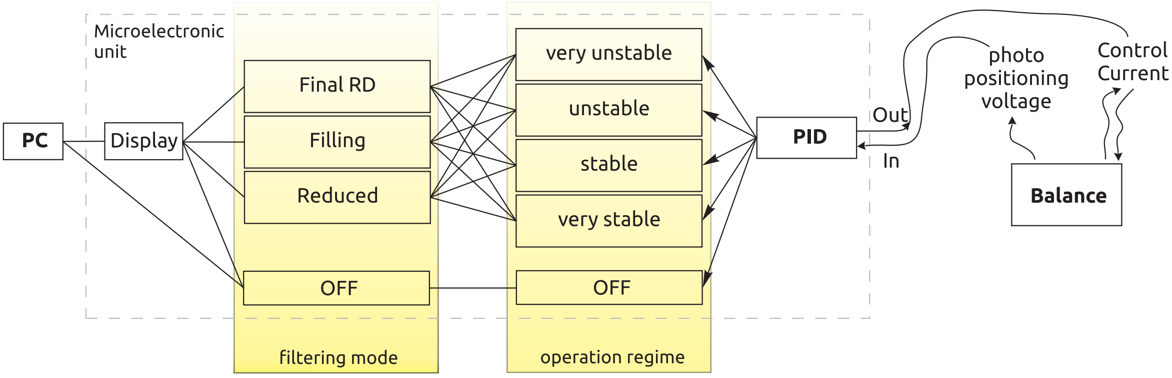

Figure 2.19: Scheme of the filter adaptation regimes of the EMFC balance.

The combined standard deviations is obtained for each filtering mode (the electronics is being pre-adapted before each set of measurements in order to test 12 different configuration of filtering modes), similar to 2.16 and 2.17.
The results are showing that when taking the difference of signals which are obtained by filters OFF-OFF mode then filtering the difference signal with a method described in section 2.3.2 by equation 2.5 a better noise reduction can be achieved. However, under existing laboratory conditions and mechanical arrangement of the experimental setup the *Filling mode* with predefined *very unstable* configuration shows the best possible result to be achieve with the dFMS (see table 2.1 the values in brackets), if 1.2 s settling time is required. Otherwise, the OFF-OFF filtering mode provides 20 nN measurement resolution with 6 s settling time. This resolution can be further increased by increasing the integration time of the filter and as an inevitable consequences it will lead to lost of dynamical capabilities of dFMS.

2.3.3.2 Position B

Additional calibration measurements are performed when the voice coil actuator is arranged at position B (cf. figure 2.10). Same calibration procedure is used as in case of position A. This is done to confirm that the signal of dFMS (difference signal) is also linear when the same calibration force is acting on both EMFC balances simultaneously. In figure 2.20, an example of such a measurement is shown.
In these measurements, the measured difference signal from dFMS can be described as:

$$\Delta F_{diff} = \Delta F_{2M} - (-\Delta F_{1M}) = 2 \cdot \Delta F_L \tag{2.9}$$

where

$$F_{2M} = F_{err} + F_L, \;\; F_{1M} = F_{err} - F_L \tag{2.10}$$

Note that in figure 2.20*b)* the slope is also linear and has two times higher value in comparison with the value obtained in calibration measurements when the voice coil actuator is arranged at position A (figure 2.18). This difference in values is conditioned by the fact that both EMFC balances measure the same magnitude but oppositely directed horizontal forces, as described by equations 2.7 and 2.9. In figure 2.20*c)*, the standard deviation for each step of the measured force is plotted against the electrical current that is applied to the coil for generating that step response. For this particular set of measurements, the combined value of all standard deviations results to be ≈ 23 nN. In figure 2.20*d)* the single-sided amplitude spectrum of all signals in the frequency domain is represented. It is showing more clearly that the force signals from both EMFC balances are grossly identical which provides a greater reduction of vibration noises when considering the difference between them, figure 2.20*d)* below.
Hence, to summarize the results presented in this subsection, on the assumption that both EMFC balances are measuring simultaneously the same mechanical noises (which was the case during all measurements), the resolution of the horizontal force

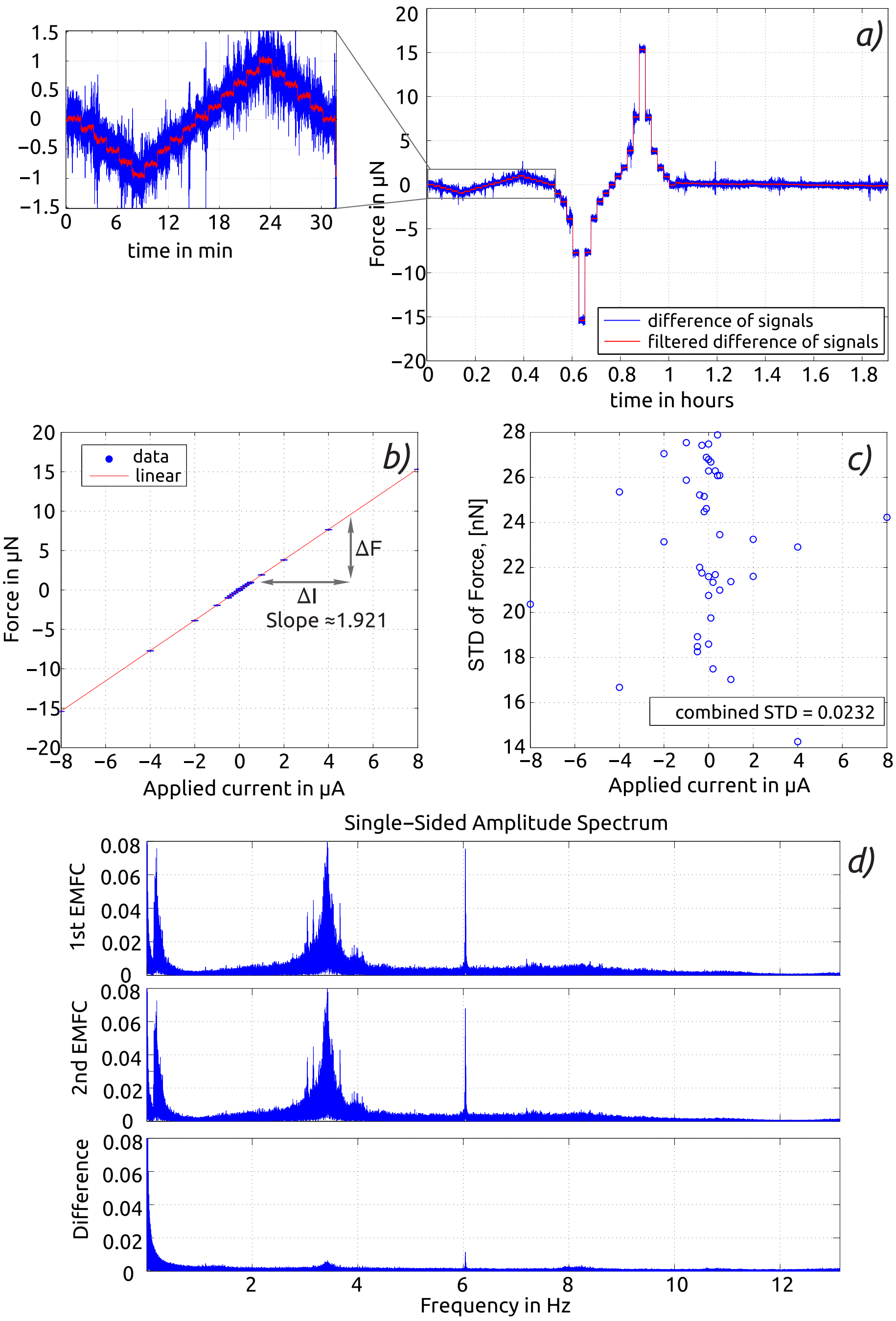

Figure 2.20: Calibration measurements of dFMS against quasi-static forces in the range of ±100 nN to ±15 µN when the voice coil actuator is arranged at position B. *a)* Measured force from dFMS over 2 hours, difference signal F_{diff} and filtered F_{diff} signal. *b)* Linear slope of calibration measurements $F_L = F_{diff}/2$. *c)* Standard deviation of filtered F_{diff} signal at each step. *d)* Single-sided amplitude spectrum of the force signal from 1st EMFC balance, 2nd EMFC balance and the difference signals.

measurements is increased from several hundreds of nN (≈ 400 nN) for the single EMFC balances to 20 nN for the filtered signal of dFMS.

2.3.4 System identification: *in case of dynamic forces*

The results presented in subsection 2.3.3 were obtained assuming the case of horizontally acting quasi-static calibration forces without taking care of the time dependent aspects of EMFC balance behaviors. In all calibration measurements the data are collected and analysed once the settling time of the low pass filter is reached, estimated statistically as ≈6 s. For this reason, an additional set of measurements to reveal dynamic characteristic of EMFC balances are necessary. The force measurements are taken from single EMFC balance for both open- and closed-loop operating modes and without using built-in filters. The system response is examined against sinusoidal excitations, that is horizontally acting calibration forces in the frequency range of 0.06 Hz to 100 Hz. Similar to the force measurements performed in quasi-static case, a linear voice coil actuator is used to generate dynamic forces within the specified range. The external voice coil is fixed at position A (cf. item 6 in figure 2.10 a). In the closed-loop operating mode, the compensation (control) current of the integrated coil inside of the EMFC balance is chosen as an output signal. In the open-loop operating mode the output signal is chosen as the voltage signal of the positioning sensor of the EMFC balance. In both cases the output signal is analysed against the feed-in signal which is the electric current applied to the voice coil. The electric setup consists the following main units; a digital signal processing unit (dSPACE [52]), a voice coil actuator, several analog signal converters from current-to-voltage and from voltage-to-current. Complete electric setup is presented in the figure 2.21. In the measurements the dSPACE is used through MATLAB software environment for both; to generate the input signal through a D/A converter and for sampling the output signal through A/D converters.

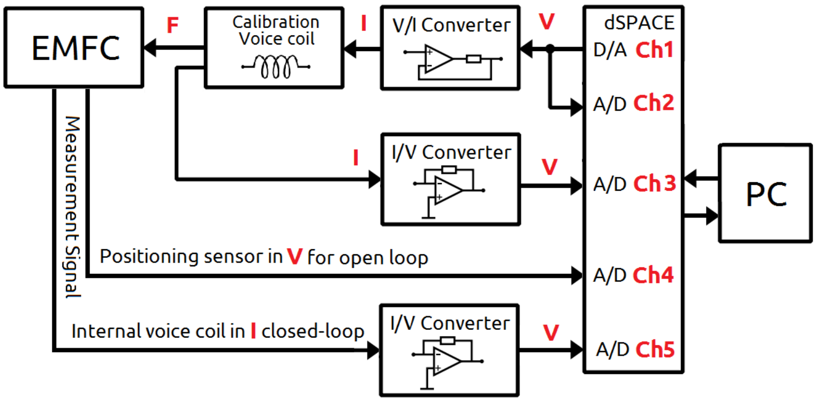

Figure 2.21: Electric setup used in dynamic calibration of EMFC balance.

$$\textbf{Bode plot} \text{ of the open-loop} \quad \sim \quad 20 \cdot \log \frac{V_{Ch4}}{V_{Ch2}} \tag{2.11}$$

$$\textbf{Bode plot}\text{ of the closed-loop} \sim 20 \cdot \log \frac{V_{Ch5}}{V_{Ch2}} \tag{2.12}$$

A linear chirp signal is applied to the voice coil actuator (the voltage is an initial output signal from dSPACE, further being converted to a proportional current signal) whereas the output signal is processed digitally to obtain the characteristic FFT of the measurements [53][5].

$$V(t) = \xi \cdot \sin\left[\phi_0 + 2\,\pi\left(f_0\,t + \frac{f_1 - f_0}{2 \cdot \Delta t} \cdot t^2\right)\right] \tag{2.13}$$

where $V(t)$ is the applied voltage that consists of a sinusoidal signal with the initial phase ϕ_0 (at time t=0), and f_0 starting and f_1 final frequencies of oscillations during Δt=t_{end}−t_0 (sweeping) time period, the ξ is the conditional constant for conversation of the units from radians to voltage.

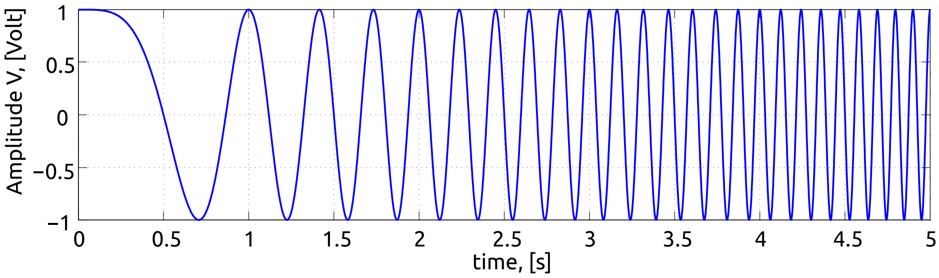

Figure 2.22: Example of a linear chirp signal. f_0=0, f_1=10 Hz, t_0=0, t_{end}=5 s, ϕ_0=0.

The operation for both open- and closed-loop modes is tested and the results are presented in figure 2.23 as bode plot of the EMFC balance (cf. equations 2.11 and 2.12). High oscillations at low frequencies are due to chosen short time period of measurements. Thus, it is only experimentally conditioned measurement artifact which is possible to eliminate by using a logarithmic chirp signal with a sufficiently longer measuring time at lower frequencies. The measurement procedure and the method of the data collection can be optimized further (e.g. using an exponential chirp signal, a longer measurement time, and etc.). However, in the current tests a single set of measurement takes approximately 3 hours due to the actual measurement process and related data processing wait-time, meanwhile it results to a huge data-set which is produced as MATLAB **.mat* file of approximately 250 Mbytes.
The results obtained from dynamic measurements show considerable agreement with the results of calibration measurements for quasi-static forces. Particularly, the low pass filter (6 s response time) used in quasi-static force measurements is identical to the system response obtained from the open-loop dynamic measurements (cf. figure 2.23 cutoff frequency ≈ 0.35 Hz). In the case of the closed-loop operation mode, the cutoff frequency is ≈ 0.7 Hz to 0.8 Hz, demonstrating more clearly the fact that it is

---

[5] Familiarity in using the dSPACE digital signal processing unit and development of the necessary infrastructure of the electric setup are gained in close collaboration with Jan Schleichert.

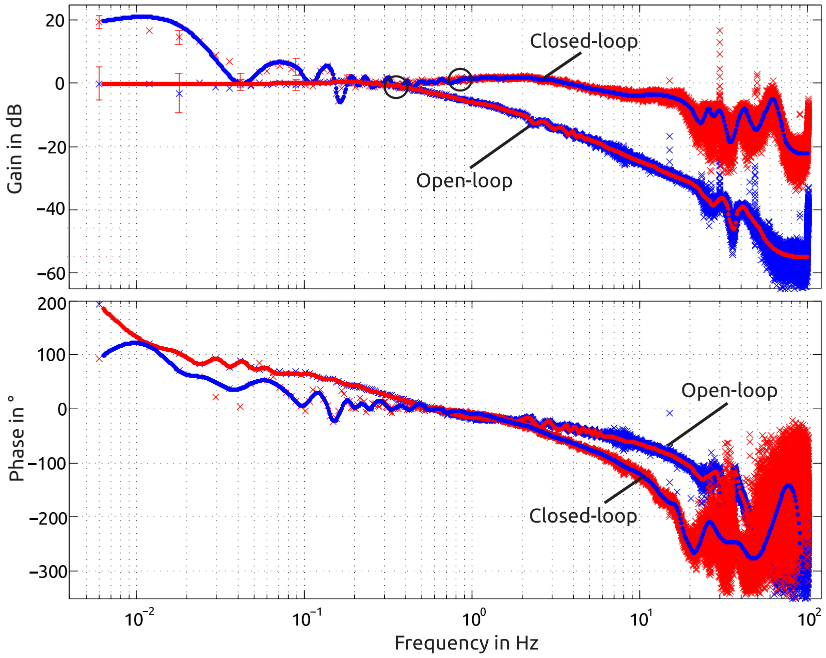

Figure 2.23: Frequency response of EMFC balance in open- and closed-loop operating modes. Interpolated curves are fitted to the measurement results. The results are plotted as the averaged value from 5 independent measurements, for open- and closed-loop operating modes respectively. Circles on each curve are highlighting the frequencies when the value of the magnitude is ≈|3| dB.

identical as the response time of the EMFC balance ≈ 1.2 s to 1.4 s (given by manufacturer) when using the built-in filters.

To summarize, the closed-loop operation mode with built-in filters provides ≈ 0.7 Hz to 0.8 Hz maximum loading frequency, whereas using the low pass filter the system shows 0.18 Hz maximally tested loading frequency. Note that the resolution (≈ 20 nN) of force measurements obtained with developed low pass filter is better than the resolution (≈ 25 nN) obtained with the built-in filters (cf. table 2.1). Moreover, the averaging low pass filter may provide even better force measurement resolution for cases when the loading frequencies is well below 0.18 Hz and the integration time of the filter is much larger than τ_0=1.8 s. The integration time can be further increased once the frequency of the applied loads are defined (cf. figure 2.14 and 2.13).

2.3.5 Analysis of the vibration noise

As discussed, below 1 µN range the force signal measured by new single EMFC balance is mostly obstructed by the vibration noise. From figure 2.17 it can be observed that the vibration noise defines the resolution of the EMFC balance signal as ≈ 400 nN in case of built-in filters, whereas when using only external filter (cf. section 2.3.2) the resolution of the signal results to ≈ 250 nN. The origin of this noise is purely mechanical, which exists identically in raw signals of both EMFC balances (cf. figure 2.20). The dominant frequencies of this noise can be defined from the spectral distribution of the raw signal on the frequency domain. In figure 2.24 two dominant frequencies can be distinguished from the power spectral density (top) and amplitude spectrum distribution (bottom).

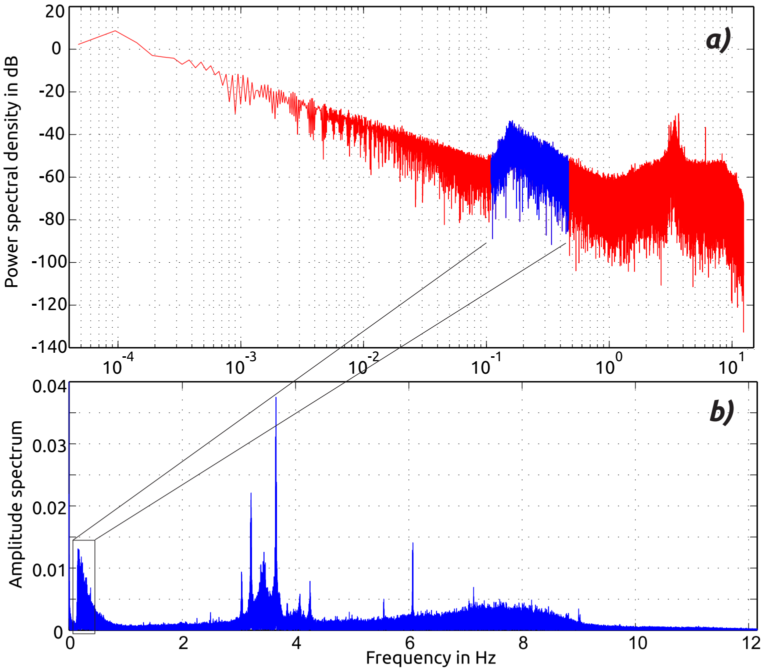

Figure 2.24: a) Power spectral density of the raw force signal from single EMFC balance, b) single sided amplitude spectral distribution of the raw force signal from single EMFC balance, m_0=1.15 kg.

The noise in range of 3 Hz to 3.7 Hz corresponds to the eigenfrequencies of the EMFC balance, which originates as a result of the its complex inner mechanical structure. The second frequency range, spanning from 0.1 Hz to 0.4 Hz, is known as micro-seismic surface waves [46, 54, 55]. The noise at 0.1 Hz to 0.4 Hz grossly influences the EMFC balance and changes the signal-to-noise ratio of the force measurements as the weight of the dead load is changed. The estimation of the character of this noise is presented in figure 2.25 for different dead loads m_0=0 kg, 0.420 kg and 1.150 kg. The behavior of the system is given in terms of signal-to-noise ratio and peak frequency values, both as a function of dead load m_0. Here the signal-to-noise ratio is averaged on the 0.1 Hz to 0.4 Hz window from the power spectra of the zero-point stability measurements, as highlighted in figure 2.24.
It can be observed from figure 2.25 that with increasing the mass of the dead load the noise of the signal also increases. The value of the frequency peak, however, varies randomly within 0.15 Hz to 0.18 Hz independent of the mass of the dead load. In comparison with the vibration noise existing in old EMFC balance [21], discussed in current work from section 1.2.2 to section 2.1.3, the new EMFC balances show

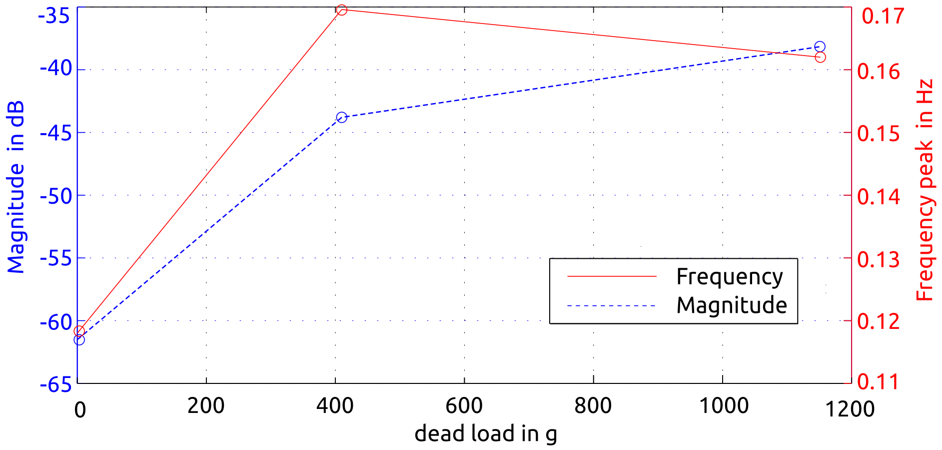

Figure 2.25: Influence of the noise in 0.1 Hz to 0.4 Hz frequency range on the single EMFC balance as a function of weight of the dead load. Averaged magnitude - left axis (dashed), maximum frequency peak - right axis (solid).

some improved characteristics. Particularly, when comparing the single sided amplitude spectral distribution of the measured raw force signal from old and new EMFC balances, an obvious distinction can be made between them (see figure 2.24 and 2.8). However, the common noises in the ranges 0.1 Hz to 0.4 Hz and 3 Hz to 3.7 Hz still exist in the measurement signals of old and new EMFC balances. As shown in section 2.3.3, particularly by figures 2.14, 2.17, 2.20*a)* and *d)*), the noise reduced signal is obtained by taking the difference between force measurement signals from two new EMFC balances. In table 2.1 the comparison is provided between measurement results obtained by new and old EMFC balances.

2.4 Summary

In this chapter, it is presented a differential force measurement setup (dFMS) described as a stand-alone system for high-precision measurements of single axis and horizontally directed forces in combination with high dead loads. The force measurement setup uses two identical high-precision state-of-the-art balances whose working principle is based on a zero point balance by means of electromagnetic force compensation. The setup is capable of resolving horizontally acting quasi-dynamic forces with a resolution of $\approx 20\,\text{nN}$ over the working range of $\pm 100\,\mu\text{N}$. The value of the maximum loading frequency achieved is 0.7 Hz for the minimal measurable forces as $\approx 25\,\text{nN}$ in the closed loop-mode. However, forces acting below 0.18 Hz frequencies are possible to measure with $\approx 20\,\text{nN}$ and below, depending on the chosen filtering method, the integration time of measurements and the operation mode of the balances. Note that in dFMS the EMFC balances are capable of carrying up to 13.5 N dead loads each, which yield a relative force measurement resolution of $\delta F_L/F_g \approx 1.47\,\text{ppb}$. In comparison with the previous work by Diethold et al. [21], the resolution of the force measurements with the current work is increased by about 2 orders of magnitude (cf. table 2.1).

Table 2.1: Details of best achieved measurement results by dFMS.

Force measurement	Units	*new EMFC balances current work*		*old EMFC balance previous work*
		signal of single EMFC balance	*Difference signal*	*signal of single EMFC balance* [21]
Resolution in case				
$m_0 \approx 1.35\,\mathrm{kg}$				$m_0 \approx 1.688\,\mathrm{kg}$
Raw	nN	600	150	< 1000
Filtered		250, (350)[1]	**20**, (25)[1]	-
$m_0 = 0$		quasi-static		-
Raw	nN	200	78.85	
Filtered		85.05	15.7	
Range	µN	±100, available ±5.5 mN		±100
Sampling frequency	Hz	25, available up to 80		< 18
Response time, τ_0				
Raw	s	1.4		1.4
Filtered		6, (1.2)[1]		-
Loading frequency				-
$m_0 = 0$	Hz	quasi-static		
$m_0 \approx 1.35\,\mathrm{kg}$		up to 0.18, (0.7)[1]		
Stable period[2]				-
$m_0 = 0$	min	60		
$m_0 \approx 1.35\,\mathrm{kg}$		30		

[1] numbers in brackets obtained with built-in filters.

[2] dependent from temperature, defined as $\Delta T < 20\,\mathrm{mK}$.

The increase of the relative force measurement resolution broadens the application possibilities of the LFV. Particularly, enabling usage of larger magnet systems and/or high temperature superconductors [56] to generate higher magnetic flux density. Also, for measurements of electrolyte flows in low velocities and low electrical conductivities (e.g. for salt and glass melts). Besides, the dFMS may find potential applications in other research areas, e.g. for the thrust calibration and characterization micro-electric propulsion systems [32, 33, 35].

To define the resolution, range, linearity and stability of the force measurements a calibration measurements were made. In sections 2.3.3 and 2.3.4 are provided the calibration results of the dFMS against static and dynamic forces acting in horizontal direction. Furthermore, it is examined the force measurement stability against influential temperature effects in the case when no measurement force is applied. Particularly, the thermal expansion of the supporting construction is identified as the main reason of force drift. The analysis of the thermo-mechanical effects shows that the small variations of temperature of about 0.3 K lead to force errors in the order of a 1 µN, which was the resolution reached in previous work [21]. Thus, the stability of the force measurements is mainly restricted by the surrounding temperature of the setup. Although the improved shielding of the setup provides a significant passive temperature control, the time limit for stable measurements is estimated experimentally and given as temperature stability of the surrounding environment in ±20 mK range for the current construction. In all measurements the typical time for stable force measurements is estimated as 30 minutes for $m_0 \approx 1.35$ kg, and over 1 hour for $m_0=0$. Due to this fact, random angular misalignments appear between common axes of both EMFC balances (x,y,z).

In order to improve the overall performance of the *d*FMS, different approaches can be considered for future works. A possible method to increase the time of the stable force measurement is to redefine the supporting construction to a simpler configuration where the thermal expansion is negligible. An alternative way to increase the stability of the measurements is to align both EMFC balances by their absolute angles to all common axes (x,y,z). This requires high resolution adjustments of angular errors below 100 nrad. In the last case, the random drift of the whole construction - in theory - should lead to a parallel drift of both EMFC balances along all x,y,z common axes, therefore, the difference signal will be sensitive only to the measurand force. Additionally, a significant improvement in the setup's performance for measurements under vacuum conditions is expect. The use of a vacuum chamber will provide reasonable conditions to refine *d*FMS characteristics [41], particularly to eliminate influences such as convective air currents, non-uniform temperature distribution and air buoyancy effect.

3 Direct compensation of Lorentz forces

> There is only one way to avoid criticism: do nothing, say nothing and be nothing.
>
> Aristotle

In this chapter, a new concept of Lorentz force measurements for LFV applications is described and realized. The magnetic field of the LFV magnet systems is directly employed for setting up a system of force measurements that uses the principle of electromagnetic force compensation. It is shown that the deflection of the magnet system can be directly compensated, therefore measured, to the zero position by an applied electric current to a custom developed coil, which is solidly fixed in the vicinity of the magnet systems. The structure of the coil is determined in relation to the design of the LFV application, but more importantly its arrangement is defined in relation to the magnetic field distribution of the magnet system. The method is tested for practical measurements of electrolyte flows at velocity of $0.4\,\mathrm{m\,s^{-1}}$ to $2\,\mathrm{m\,s^{-1}}$ and a conductivity of $2\,\mathrm{S\,m^{-1}}$ to $20\,\mathrm{S\,m^{-1}}$. Based on a straightforward theoretical description and experimental results, further improvements are discussed. This new concept of flow measurements is called Direct Lorentz Force Compensation flowmeter[1], particularly suitable for metering the flow rate of low electrically conducting electrolytes.

3.1 Outlook on experimental setup

In spite of the progress achieved in force measurements by dFMS (cf. chapter 2), yet a simplified method for force measurements in LFV applications is required. The complex system of dFMS, based on two identical EMFC balances, suggests several improvements that may be made in order to develop an optimized force measurement system. A general concern relates to the usage of two different magnet systems when considering a single EMFC balance LFV measurements. In the schematics of these systems the first magnet systems ($\approx 1\,\mathrm{kg}$) is suspended from the EMFC balance, the second magnet system, much smaller than the first one, is integrated in the EMFC balance. Both magnet systems are mechanically fixed from the EMFC

---

[1] A significant portion of the results obtained in this chapter are compressed in the peer-reviewed journal publication [16] **S. Vasilyan, T. Froehlich. Direct Lorentz force compensation flowmeter for electrolytes. Applied Physics Letters, 105(22), 2014.**

balance and the magnetic interaction between them is greatly indefinite. Despite this fact, each magnet system is treated separately, and each has a certain functional purpose. The first one generates the Lorentz forces in the flow, whereas the second one is used to compensate the deflection of the lever arm to the zero position. Hence, one of the improvements can be made by combining both functions in one magnet systems, particularly in that magnet system which is located around the electrolyte channel and generates the Lorentz forces. Figure 3.1 shows a diagram of this reduction. Such a scheme of the measurements of Lorentz forces in LFV applications is introduced for the first time, and is recognized as a new type of flowmeter based on Direct Lorentz Force Compensation (the basic idea is introduced by T. Fröhlich and formulated in its complete form in [57] independently and in parallel with the progress of this research/work [16]). Note that in the diagram the mechanical construction is shown in a simplified form, which is done only to illustrate the fact that the usage of the internal coil of the EMFC balance can be omitted. Nevertheless, the mechanical construction plays a crucial role in guiding the deflection of the magnet systems. Thus, the mechanical construction should be designed such that the Lorentz forces, which are in the order of µN and below, can deflect the magnet system at least by the resolution of the position measuring sensors.
Initially, the method was realized on the Pendulum FMS (cf. section 1.2.1) and is applied to a small electrolyte channel. In this regard, a brief introduction of the measurement infrastructure of the full facility is given in the following.
The experimental setup is that of described in Ref. [13, 14] where the Lorentz force is generated by the transverse interaction of a turbulent electrolyte flow (salt water inside the glass channel) with a magnetic field of LFV magnet system. For experimental convenience saline water is chosen as a test electrolyte. The rate of conductivity (as provided σ =[2.7, 4.35, 10.01, 17.86, 20.11] $\mathrm{S\,m^{-1}}$) is set by a mixture of regular tap water ($\approx 11\,\mathrm{L}$) and common salt (Sodium chloride) at room temperature. Typical molar concentration of the totally dissolved salt in the water of provided conductivities are $c_M \approx$ [0.23, 0.37, 0.86, 1.53, 1.72] $\mathrm{mol\,L^{-1}}$, assuming a molar weight of ${M_i}^{NaCl}$=$58.44\,\mathrm{g\,mol^{-1}}$, and respectively Promille=[13.49, 21.74, 50.03, 89.28, 100.52]. The Pendulum FMS consists of free oscillatory platform suspended by four thin tungsten wires and magnetically coupled two identical permanent magnets fixed on an aluminum frame with a separation distance of 32 mm. So, the volume between magnets encompasses the channel with minimal air gap of 1 mm from both sides as depicted in figure 3.2, 1.3 and 1.4. The glass channel has rectangular cross section at the test section by 50 mm × 30 mm height and width, while 2 mm thick walls define 46 mm × 26 mm cross section of the electrolyte flow. Interaction of strong magnetic field with the flow (in the transverse directions) resulting in horizontal directed volume force that acts in opposite direction to the volume flow (or velocity vector). The Lorentz force is integrated force over the volume of the interaction region and leads to a reaction force acting on the magnet system in downstream direction.
Earlier, the reaction force was measured through the measurements of the effective deflection (s) of the Pendulum FMS, tracing it by means of a commercial laser interferometer [39]. When the stiffness of pendulum K_s is known (otherwise given as

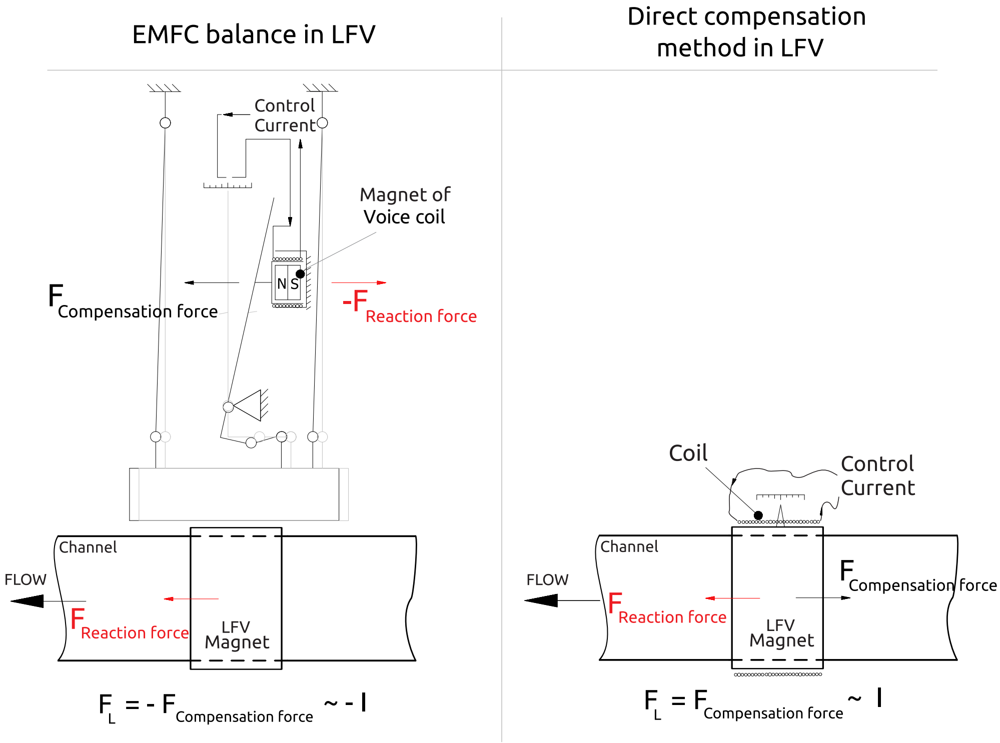

Figure 3.1: Reduced measurement schematics of the LFV applications using direct Lorentz force compensation method. (Left) Measurement principle of Lorentz forces with the EMFC balance, where two different magnet systems are involved in the measurement scheme, (right) measurement principle of Lorentz forces with direct Lorentz force compensation method, the LFV magnet system is used for both, generating Lorentz forces and compensation of the resulting deflection.

calibration factor of the FMS) the reaction force can be computed as

$$F_R = -F_L = s \cdot K_s, \tag{3.1}$$

converting it by the amount of deflection from zero point. In turn, the calibration factor can be obtained [13, 14] by a) computing the stiffness of the Pendulum FMS by Young's modulus and Hooke's law or b) determining experimentally by means of a separately developed calibration setup. In both cases, the methods of determining the calibration factor is indirect, and they both have several disadvantages;
a) Theoretical

- computation neglects the magnetization property of the setup and considers the magnet system as a dead load,
- accurate determination of the parameters of the mechanical construction strongly affects the accuracy of the computations. Furthermore, the uncertainty contribution can become bigger for more complex systems,

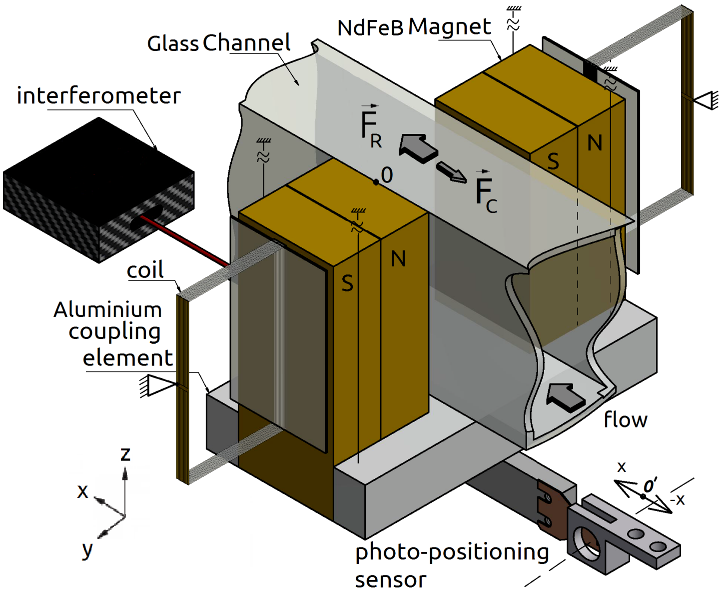

Figure 3.2: Illustration of the noncontact flow meter with direct compensation method for Pendulum FMS. Main components are; Pendulum FMS with magnet system balancing at equilibrium point, channel, positioning sensor and interferometer, fixed rectangular coils carrying I current in order to generate compensation forces.

b) experimental

- measurements also neglect the magnetization property of the setup, the magnet system is replaced from the Pendulum FMS with an equivalent dead load.
- calibration measurements are made by applying calibration forces with an electromagnetic voice coil actuator: consisting of a coil fixed to the support via a micro stage and a solenoid-type magnet that is fixed to the dead load.

The new method of measurements is designed to overcome some of these disadvantages, meanwhile suggesting a direct force calibration procedure along with deriving the model of theoretical computation. Mechanically, the setup is designed under the consideration that two oppositely directed Lorentz forces are acting on the magnet system along one axis, thus the superimposed force should be zero.

$$\vec{F}_R + \vec{F}_C = 0, \tag{3.2}$$

The first one is the reaction force $F_R = -F_L$ (due to electrolyte flow) that acts in the direction of flow, whereas the second one is the necessary compensation force F_C which is produced by an externally applied electric current in the coil that is static fixed in close vicinity of the magnet system. The implementation of the measurements are made through servo-controlling of these two opposing forces (cf. figure 3.2) in a way to keep the combined force vector acting on the magnet system at zero, in other words balancing the magnet system in its equilibrium point. Generally, the compensation force ($\vec{F}_C$) is described by equation 3.3 as integrated force along the path line of the coil, that is imposed in the magnetic field (B) of the magnet system and carries I electric current.

$$\vec{F}_C \sim I \int\limits_{coil} d\vec{l} \times \vec{B}, \tag{3.3}$$

where $d\vec{l}$ is the infinitesimal length of the coil. As mentioned, the geometrical structure of the coil (or simply a current carrying conductor) strongly relates to the design of the LFV application and magnetic field distribution, therefore it should be noted that the effective compensation force (cf. equation 3.3) is the sum of the forces produced by each infinitesimal length of the conductor in the spatially distributed magnetic field $d\vec{F}_C(\vec{I}(\vec{x},\vec{y},\vec{z}),\vec{B}(\vec{x},\vec{y},\vec{z})) = I\,d\vec{l} \times \vec{B}$. In the next section, a detailed derivation of the compensation force is given based on the chosen geometrical arrangement of the coil.

3.2 Coil arrangement and theoretical model

Two spatial arrangement of the current carrying conductor have been considered for the initial test of the concept (see illustrations in figure 3.2 and 3.3); i) two rectangular coils which are fixed at the outer sides of the magnet system, and ii) thin conductor sheets which are placed along the surfaces of the magnets and outer walls of the channel. For both cases each of the counterpart is placed symmetrically along the x axis and carry an equal amount of electric current. This is done to prevent the Pendulum FMS from parasitic rotational motions.

description of the figure 3.3 and notations:

- dimension of the single permanent magnet - $[\,a \times b \times c\,] = [\,30 \times 70 \times 30\,]$ mm,
- distance between the inner surface of the magnets - m =32 mm,
- gap between each side of the channel and magnet - 1 mm,
- gap between the coil and magnets - g=1 mm,
- length of the longer edge of the rectangular coil - l=48 mm,
- thickness of the wire used to manufacture the coil - δ_0=0.2 mm,
- wiring of the coil is symmetric along center line of the magnet system,
- winding error is considered as a distance between two parallel wires - $\eta \approx \pm 0.058$ mm,

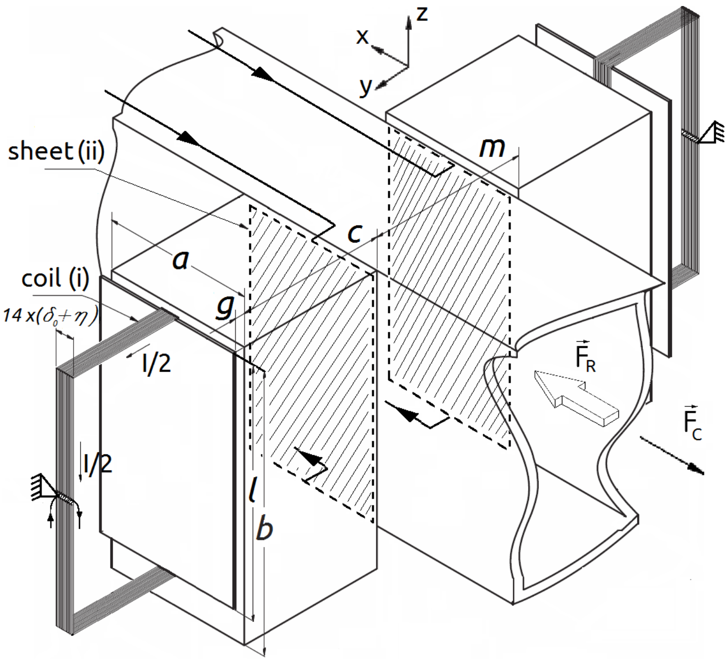

Figure 3.3: 3-D sketch of the noncontact flow meter with direct compensation method for Pendulum FMS. (i) A coil is fixed to an external mechanical ground without contacting the magnet system or the channel, (ii) a thin conductor sheet is fixed on the surface of the channel facing to the inner side of the magnets.

- total number of turns - 15 (the number was chosen arbitrarily for the initial test and proof of the concept),
- magnets are magnetized along y axis, coercivity - M_s=1 050 000 A m^{-1},
- thickness of the thin sheet conductor - 0.15 mm,
- surface of the thin sheet conductor - 28 mm × 50 mm.

Given the magnetization property of magnets and dimensions of system it is possible to calculate analytically the theoretical estimate of the calibration factor (i.e. the force constant lB). In case of the thin sheet conductor *ii)* the flow path of the electric current is indefinite, therefore, only in case of i the derivation of the force, which is produced by applied electric current in the coil, is given in following.
The compensation force is produced by the cross product of magnetic field and electric current in the coil. The electric current flows through the edges of the rectangular coil, that is only in y and z directions. The distribution of the magnetic field is non-uniform in the space and has different values for each components (B_x, B_y, B_z) at each reference point.

$$\vec{I} = [0, I_y, I_z], \quad \vec{B} = [B_x, B_y, B_z], \tag{3.4}$$

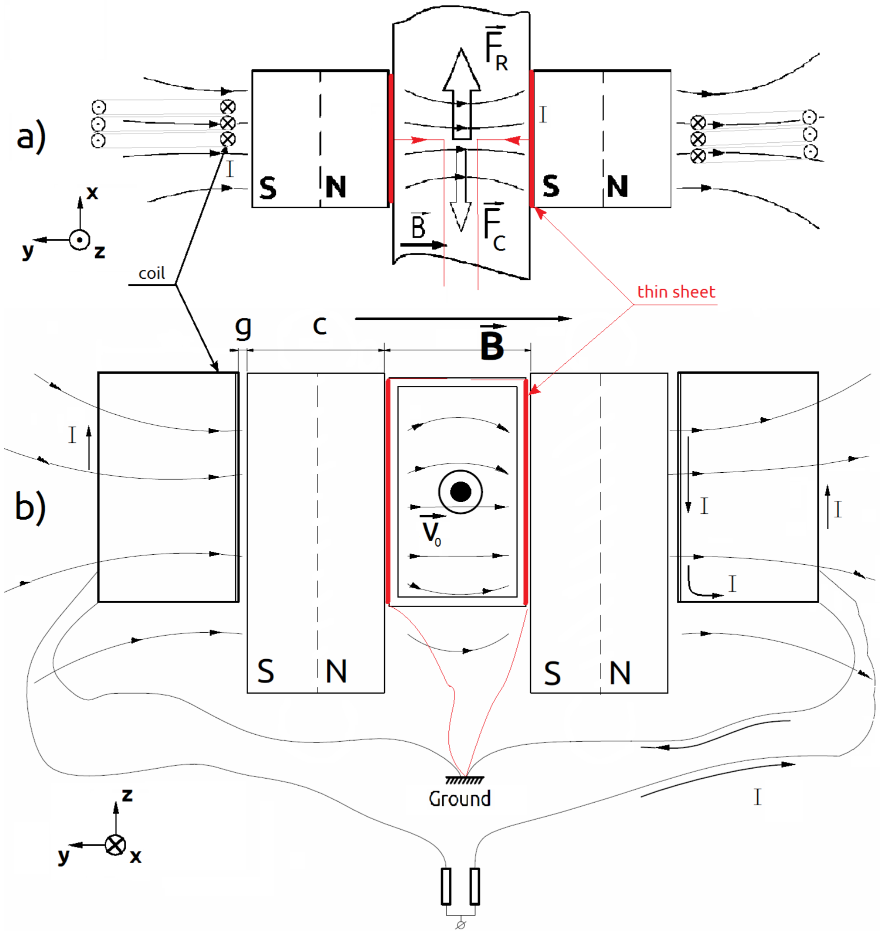

Figure 3.4: 2-D sketch of the noncontact flow meter with direct compensation method for Pendulum FMS. *a)* Top view – x-y plane, *b)* side view – y-z plane (the lateral cross-section).

$$\vec{I} \times \vec{B} = (I_y B_z - I_z B_y)\,\hat{\mathbf{x}} + (I_z B_x - I_x B_z)\,\hat{\mathbf{y}} + (I_x B_y - I_y B_x)\,\hat{\mathbf{z}}, \tag{3.5}$$

because of $I_x = 0$ (cf. equation 3.4) in the right hand side of the equation 3.5 the following terms are zero

$$I_x B_z = 0, \quad I_x B_y = 0, \tag{3.6}$$

thus, the equation 3.5 can be simplified to discuss only the terms which may generate a significant force and therefore a mechanical deflection

$$F_C = (I_y B_z - I_z B_y)\,\hat{\mathbf{x}} + (I_z B_x)\,\hat{\mathbf{y}} + (-I_y B_x)\,\hat{\mathbf{z}}, \tag{3.7}$$

The resulting forces should be considered only in relation to the actual deflection possibilities of the Pendulum FMS, in other word with its degrees of freedom. The motion in positive or negative direction along the z axis is impossible given the F_C which is negligible force to overcome the gravity force of the Pendulum FMS and magnet system for moving it up or down. From which follows, that the last term in equation 3.7 is also zero ($F_C \ll F_g{=}12.8\,\mathrm{N}) \Rightarrow (-I_y\,B_x)\,\hat{k} = 0$. Further, assumptions are used to simplify the equation 3.7, that is in the vicinity of the magnets the field is directed along the normal of the magnet surface in y direction, therefore B_x and B_z components of the magnetic field can be neglected in comparison with the B_y component of the magnetic field ($B_y \gg B_x, B_z$). Thus, only the $(I_z\,B_x)\,\hat{\mathbf{y}}$ term represents a force that leads to a deflection of the Pendulum FMS in y direction , and the term $I_y\,B_z$ of the deflection in x direction can be assumed zero.

$$F_C = -I_z\,B_y(x,y,z)\,\hat{\mathbf{x}}, \tag{3.8}$$

The equation 3.8 represent a force that is produced by a electric current I_z flowing in vertical edge of the rectangular coil and y component of the magnetic field $B_y(x,y,z)$, when coil has single turn. As discussed, only the B_y component of magnetic field can generate the force which deflects the magnet system in x direction (cf. equation 3.8). For deriving the analytical expression of the magnetic field distribution outside of the single rectangular bar magnet a charge model is used [58].

$$B_y(x,y,z) = \frac{\mu_0 M_s}{4\pi}\cdot\sum_{k,p,q=1}^{2}(-1)^{k+p+q}\times\tan^{-1}\left[\frac{(x-x_p)\cdot(z-z_q)\cdot(y-y_k)^{-1}}{\sqrt{(x-x_k)^2+(y-y_p)^2+(x-x_q)^2}}\right] \tag{3.9}$$

here M_s is saturation magnetization, μ_0 is permeability of the air, integers k, p and q are determining computation signature for negative and positive poles within single bar magnet. Note that each coil is imposed in the magnetic field of both (left and right) magnets therefore at each reference point superposition

$$B_y(x,y,z) = B_y^{\mathbf{right}}(x,y,z) + B_y^{\mathbf{left}}(x,y,z) \tag{3.10}$$

of magnetic fields should be assumed. In figure 3.5 presented analytic model of magnetic field calculated by equation 2.3 for existing magnet system. The calculated values of magnetic field differ from measured results in averaged by 3 % (see report in supplementary material of [14]). Besides this a rough measurements of the magnetic field is made to confirm the assumption that at the surface of the magnet the measured total value of the magnetic field agrees the values computed analytically by equations 3.10 and 3.9. Compare the red bold lines highlighted as $B_y[0,\text{-}32,z]$ and $B_y[0,\text{-}30,z]$ in figure 3.5 with the figure 3.6. The other B_x and B_z components are negligibly small compared with B_y component of the magnetic field at the surface of the magnets.

Inserting equation 3.9 into 3.8 it is possible to compute the F_C force for any amount of turns in the coil. In order to increase the effective force that acts to the magnet system, the number of turns of the coil should be increased. A generalized principle to compute the F_C force is given in equations 3.11 for the coil which has following structure:

- number of turns $2\alpha + 1$ in a single row, where α is an integer $\alpha = 0, 1, \ldots, 7$,

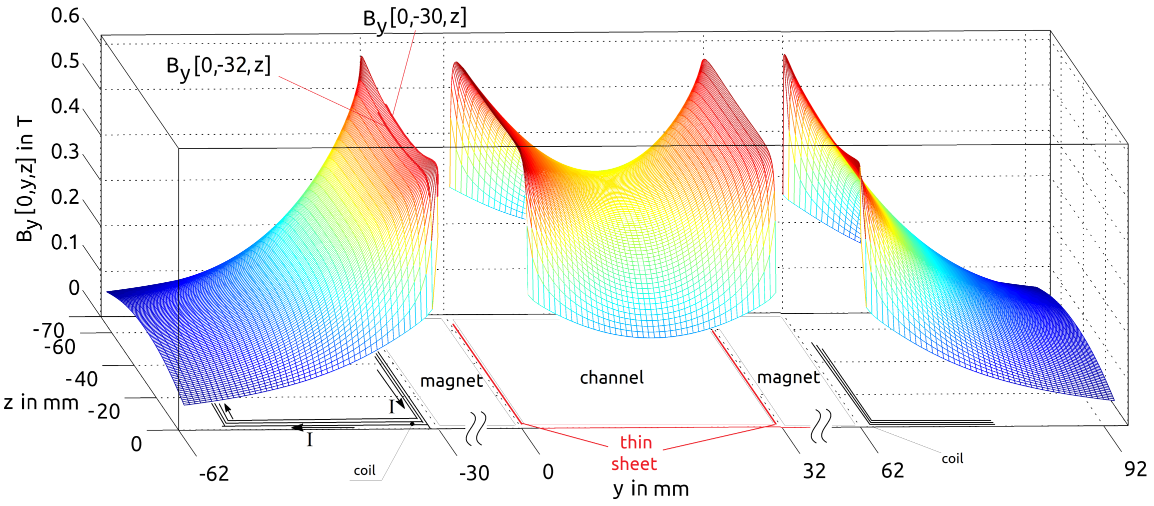

Figure 3.5: Analytically calculated B_y component of the magnetic field as a function of spatial (y, z) dimensions of experimental setup.

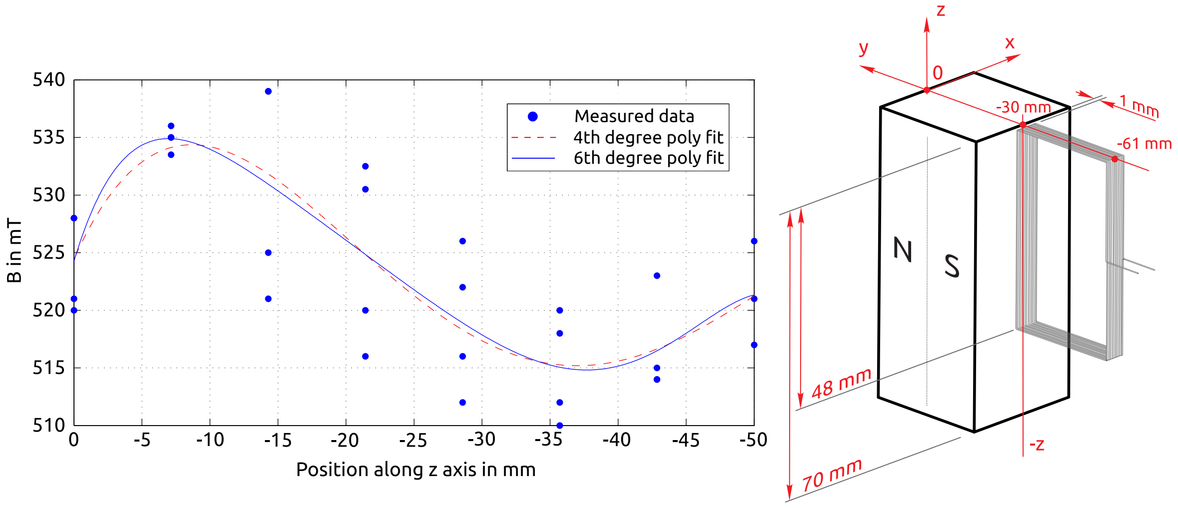

Figure 3.6: Measured magnetic field of the Pendulum FMS magnet system. Measured with [59] along symmetry axis $(x = 0, y = 30, z)$ on the outer surface of the permanent magnet, the accuracy of positioning is ±1 mm.

- length of the vertical edge l,
- diameter of the wire δ_0,
- wires are strictly parallel to each other,
- located along z axis,
- fixed distance from the magnet surface g,

Under defined supply current effective force is the aggregated force which develops by interaction of the same current in each wire by spatially distributed magnetic field.

$$F_C^{2\alpha+1} = \sum_{\alpha=0}^{n} \left[I_z \cdot \int_{z_1}^{z_2} dz\, B_y^{\alpha} \right] = I_z \int_{l_0}^{l_{end}} dz \sum_{\alpha=0}^{n} B_y^{\alpha} \tag{3.11a}$$

$$\begin{aligned} B_y^{\alpha} &= B_y^{\alpha}(\delta_0 + \eta \cdot \alpha, g, z) = \\ &= -(B_y^{0,\,\mathbf{left}} + B_y^{0,\,\mathbf{right}}) + 2 \cdot \sum_{\alpha=0}^{n} (B_y^{\alpha,\,\mathbf{left}} + B_y^{\alpha,\,\mathbf{right}}) \end{aligned} \tag{3.11b}$$

from here the force constant can be computed as

$$\frac{F_C^{2\alpha+1}}{I_z} = \int_{l_0}^{l_{end}} dz \sum_{\alpha=0}^{n} B_y^{\alpha} \tag{3.12}$$

In the next sections the computation results by equation 3.12 in comparison with actual measurements are presented.

3.3 Description of the measurement setup

Initial measurements have been made on the Pendulum FMS (cf. section 1.2.1 and figure 1.3). The simplified infrastructure of the measurement setup is presented in figure 3.7.

The coils are connected to the electric setup with a simple parallel circuit by an equivalent load for each ($R_1 = R_2$). A precision current source [50] is used to apply a single value of electric current (I) to the circuit, as presented in figure 3.8. When applying an electric current to the coil, a deflection results on the Pendulum FMS, that can be measured by laser interferometer. In addition, a photoelectric sensor is introduced to measure the position of the Pendulum FMS during deflection. The positioning sensor is similar to that integrated in the commercial EMFC balance; however, the electronics for maintaining the measurements is different. Here, the commercial laser interferometer is used only to reference the measurements.

Hence, the system can be characterized by the common open- and closed-loop measurement modes. The open-loop operation mode is intended for identifying and self-calibrating the system. In open-loop mode, the input signal is the electric current applied to the coils and the output signal is the voltage of the positioning sensor. Both the measured voltage from the electronics of the positioning sensor (measured by high-precision multimeter [60]) and the electric current applied to the coil are digitized in order to maintain an appropriate data acquisition scheme in the PC be-

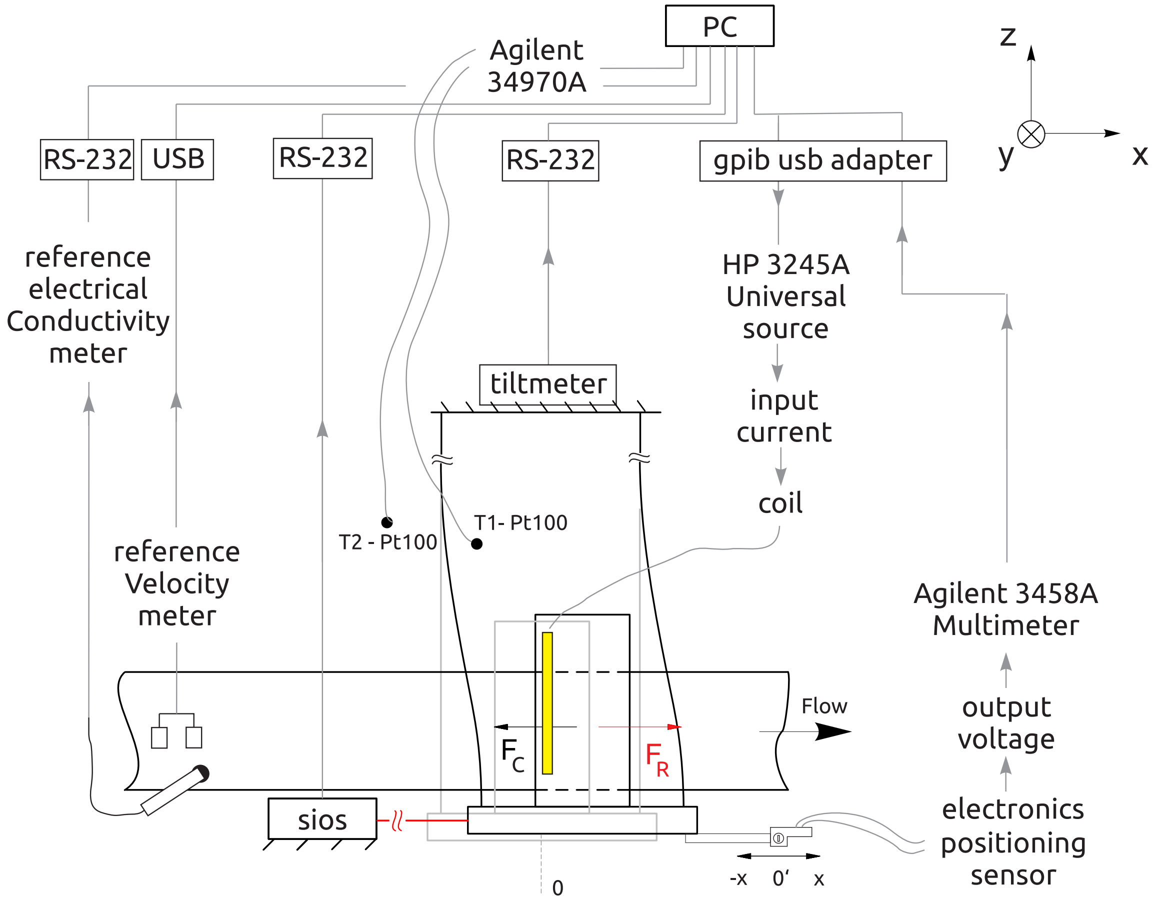

Figure 3.7: Measurement setup for direct compensation scheme applied to the Pendulum FMS, Ref. figure 1.3.

tween analog signals. In addition, several monitoring sensors are installed (and connected to the PC) for later analysis of the complete physical processes that occur in the experimental setup. The most relevant ones are as follows; an ultrasound velocity meter for reference measurements of the flow rate, a conductivity meter for reference measurements of the electrical conductivity of salt water, a tilt meter for reference measurements of absolute offset point of the mechanical construction, and two *Pt100*[2] temperature sensors for reference measurements of the temperature inside and outside of the housing.

---

[2] All temperature sensors used throughout this work were initially calibrated (for absolute values) at fixed-points of the ITS-90 temperature scale. The sensors with four wire connection were set up in combination with Agilent 34970A. Two fixed-points were considered, lower at the ice melting point (ice-bath 0.008 °C ±8 mK, k=2) and upper at Gallium melting point (29.7646 °C ±3 mK, k=2). However, at the later stages of this work, measurements were made only by measuring the relative change of the temperature signal with uncertainty below ±10 mK.

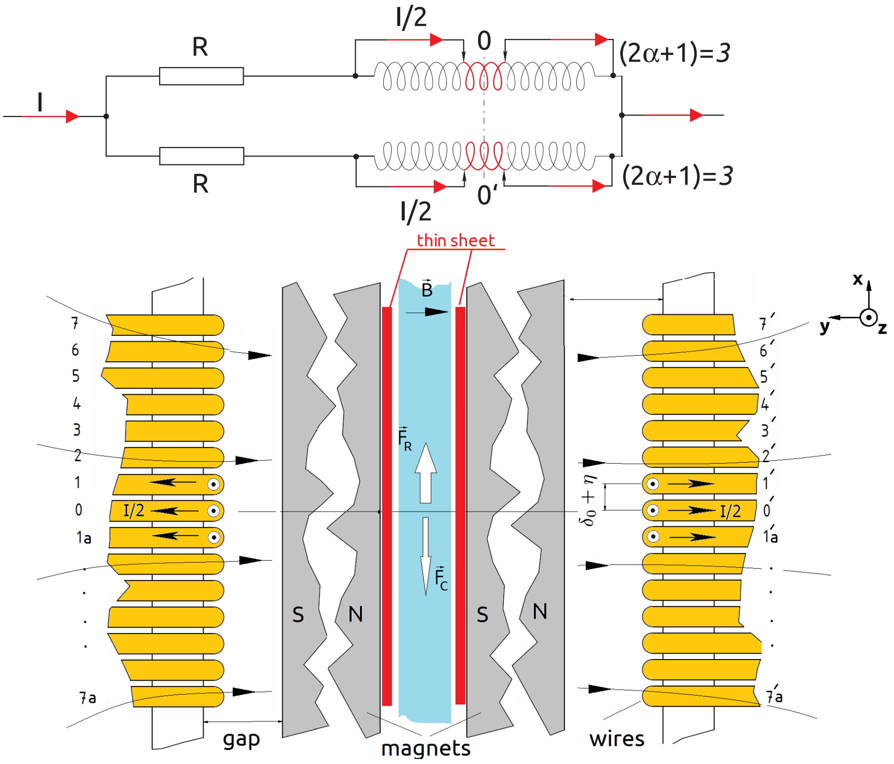

Figure 3.8: Electric connection scheme and sketch of the coil system (top view). Illustrated for $\alpha = 1$ case, when only three turns are connected to the circuit (left-$1, 0, 1a$ and right-$1', 0', 1a'$). The electric current $I/2$ are applied to each coil simultaneously.

3.4 Measurements

In this section, the measurement results on the direct compensation Pendulum FMS are presented using the positioning sensor measurements as replacement to the laser interferometer measurements. However, the measurements of the positioning sensor are still referenced with the simultaneous measurements of the same deflection by the laser interferometer. To identify the performance and dynamic behavior of the direct compensation Pendulum FMS, a reference DC electric current is applied to the coils. Initially, the open-loop operation mode is employed, based on which the closed-loop system is set up.

3.4.1 System identification and open-loop

Setting up the measurements. In order to identify the system characteristics, a DC current I=[0, -10, -5, -2, 0, -2, -5, -10, 0] mA is applied to the coil. Measurements from the positioning sensor and interferometer are recorded. Data obtained from the interferometer is converted by $F = K_s \cdot s$ to plot the values in Newton. One of the typical measurements made in this open-loop operation mode is presented in figure 3.9.

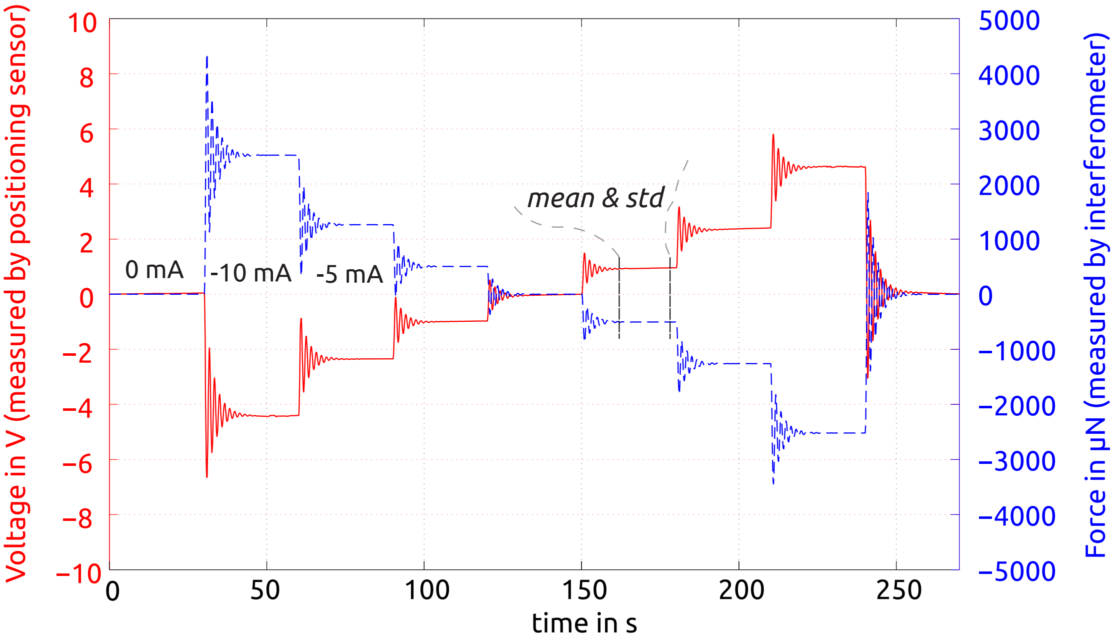

Figure 3.9: Typical response of the Pendulum FMS against the electric current applied to the coil. The coil in this example is connected by all 15 turns. Left axis–deflection measured by positioning sensor; right axis–deflection measured by interferometer.

The measurement signals are symmetrically opposite because the interferometer and positioning sensor measure the motion of the Pendulum FMS from opposite sides. Similar measurements are made for the thin sheet conductor *ii)* and coil *i)* when the latter is connected to the electric circuit by turns 1, 3, 5, 7, 9, 11, and 13 (cf. figure 3.8). For each number of coil turns, the measurements are repeated three times. The mean values and standard deviations at each step are computed once the settling time of the Pendulum FMS is reached (see example in figure 3.9 noted as *mean* & *std*). Figure 3.10 presents a full set of measurements obtained by the positioning sensor and interferometer for the same processes.

As mentioned in section 3.2, the effective force is expected to be higher when the number of turns is large, which can be seen in figure 3.10. The slope of either the voltage over current or force over current is steeper when the coil is connected by its 15 turns (black ◁ —). The summarizing characteristics of the Pendulum FMS response against the applied electric current for each number of turns is presented in figure 3.11.

The figure 3.11 shows the force constant factor $(l \cdot B)$ of the direct compensation Pendulum FMS for each number of turns in the coil in terms of V/I or F_C/I quantities (the slope of each measurement presented in figure 3.10). These expressions, in terms of SI base units, are read as $\mathrm{mV\,mA^{-1}}$ (left) and $\mathrm{\mu N\,mA^{-1}}$ (right). Both the positioning sensor and interferometer are fixed on separate grounds and measure the same deflection process of the Pendulum FMS. The uncertainty of the positioning sensor measurements increases because the data are obtained based on raw signals.

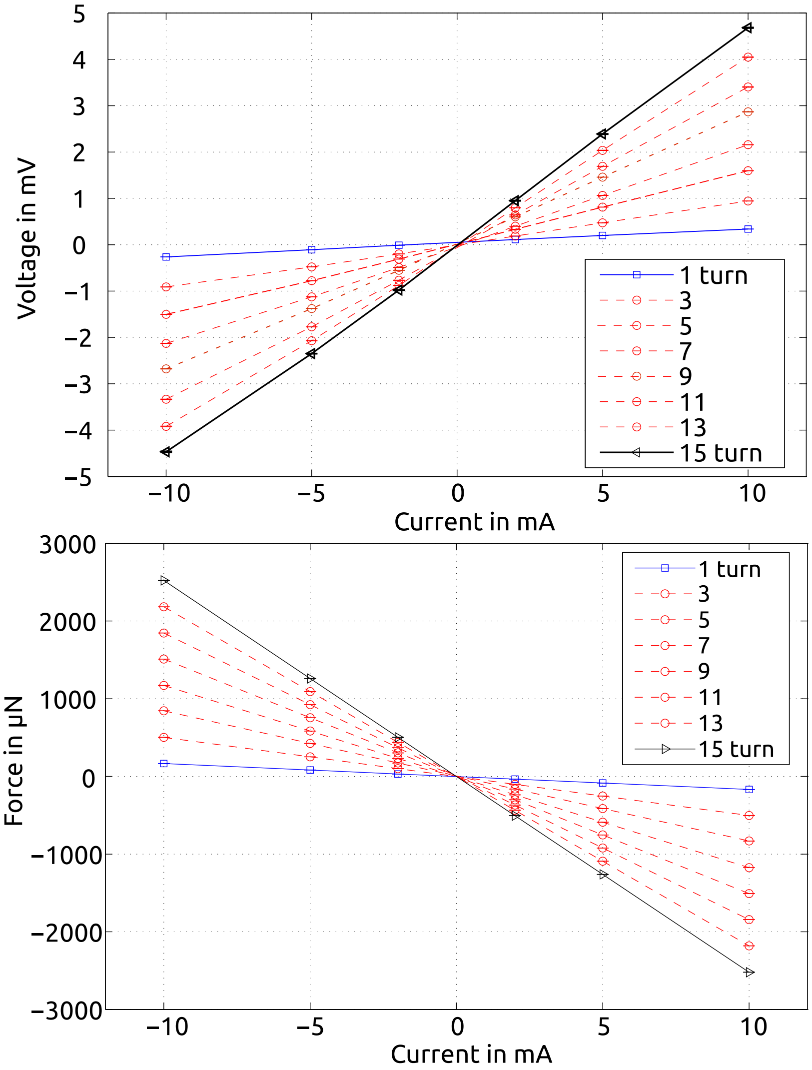

Figure 3.10: Full set of measurements for each number of coil turns showing the response of the Pendulum FMS against the electric current applied to the coil.

The positioning sensor measures the deflection of the Pendulum FMS as a change of voltage from the absolute offset position, whereas the interferometer measures from the relative predefined optical wave front. This is one of the motivating factors for changing the complete measurement scheme from interferometer to positioning sensor.

Estimation of the transfer function. A typical step response of the system as an output voltage signal from the positioning sensor is measured in order to create a second-order linear model. Figure 3.12*a)* presents the example of measurement used to obtain the parameters of the transfer function.
The damping ratio is found using percent overshoot. The percent overshoot for this step response is 80.8 %, which yields a damping ratio of 0.0609. The peak time is

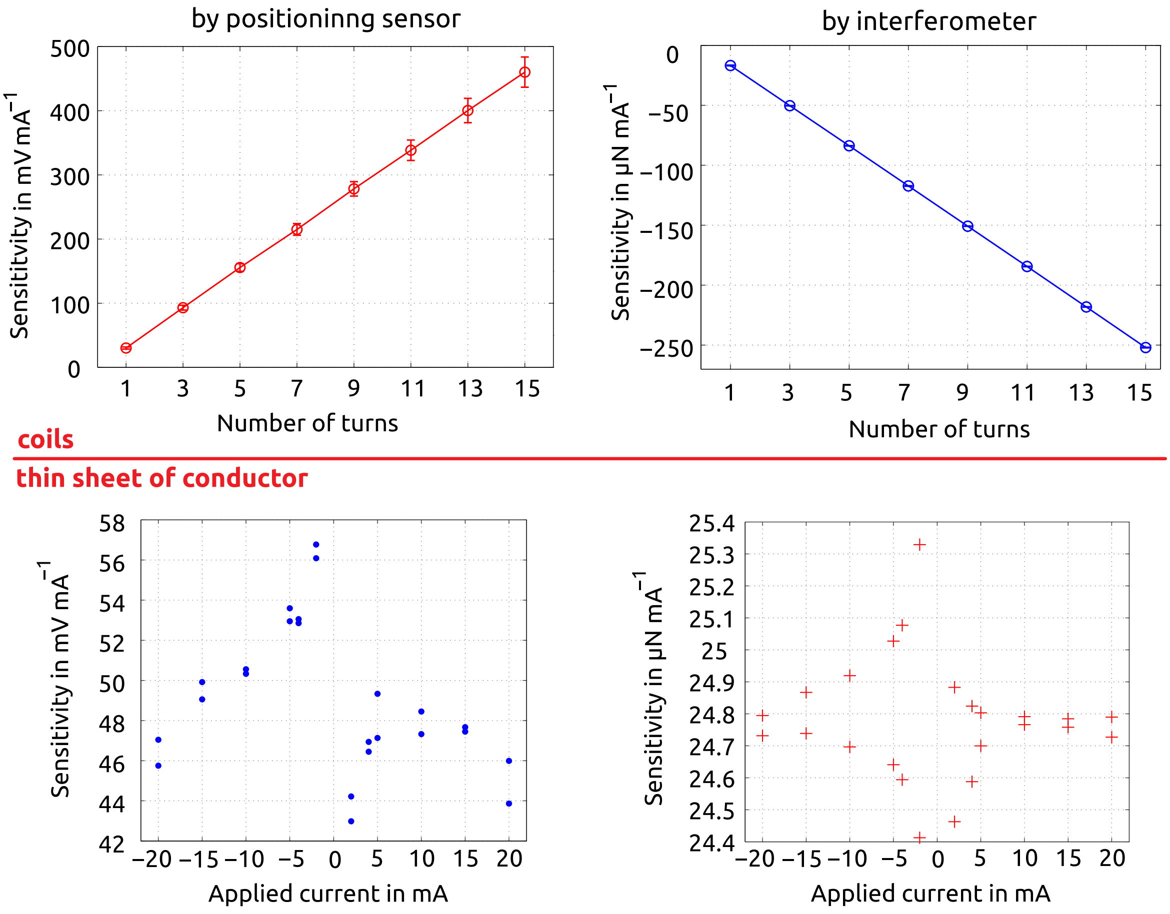

Figure 3.11: Measured sensitivity constant of the direct compensation Pendulum FMS for each number of turns in the coil (top row) and for the thin sheet of conductor (bottom row). Measurements are done by positioning sensor (left column) and by interferometer (right column).

found to be 0.7414 s, which yields a natural frequency of 4.2452 rad s^{-1} and damped natural frequency of 4.2374 rad s^{-1}. Using these values and the median DC gain of 0.6185 and θ=1.5098 rad, the second-order linear model is complete. Table 3.1 presents the parameters used to create the transfer function (ref. to figure 3.12*b)* for a summary of these data).

This is the under-damped case ($0 < \zeta < 1$), and it is assumed that the transfer function has the following form:

$$\frac{Y(s)}{R(s)} = \frac{{\omega_n}^2}{(s^2 + 2\zeta\omega_n s + {\omega_d}^{\ 2})} \tag{3.13}$$

Based on equation 3.13, the model of the transfer function presented in figures

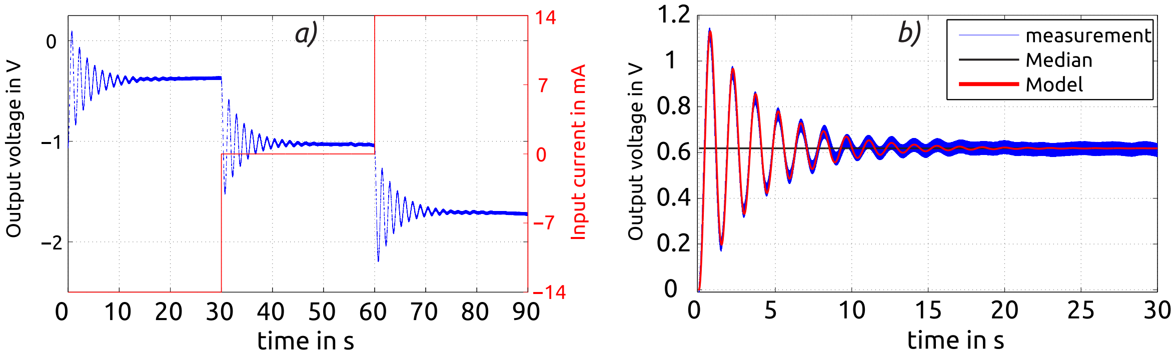

Figure 3.12: a) An example of the step response of the direct compensation Pendulum FMS. The electric current applied to the coil with three turns (right axis), and the response of the Pendulum FMS is measured by the positioning sensor (left axis). b) Comparison of the second-order linear model (plotted by equations 3.14 and 3.15) with measurements.

Table 3.1: Parameters used to obtain the transfer function of the direct compensation Pendulum FMS.

percent overshoot	$\mathrm{PO} = \frac{y_{max} - y_{ss}}{y_{ss}} \cdot 100\,\%$	$\mathrm{PO} = 80.8\,\%$
peak time		$T_P = 0.7414$ s
damping ratio	$\mathrm{PO} = \exp\left[\frac{-\zeta\pi}{\sqrt{1-\zeta^2}}\right]$	$\zeta = 0.0609$
natural frequency $1\,\mathrm{Hz} = 2\pi\,\mathrm{rad\,s^{-1}}$	$\omega_n = \frac{\pi}{T_P\sqrt{1-\zeta^2}}$	ω_n=4.2452 rad s^{-1} or 0.6756 Hz
damped natural frequency	$\omega_d = \omega_n\sqrt{1-\zeta^2}$	ω_d=4.2374 rad s^{-1} or 0.6744 Hz
median dc gain		$G_{dc} = 0.6185\,\mathrm{V}$
θ	$\tan^{-1}\left[\frac{\sqrt{1-\zeta^2}}{\zeta}\right]$	$\theta = 1.5098\,\mathrm{rad}$

3.12*b)* and 1.4 (left) is plotted from:

$$V(t) = 1 - \frac{\exp^{-\zeta\omega t}}{\sqrt{1-\zeta^2}}\sin(\omega_d t + \theta) \tag{3.14}$$

In both equations 3.13 and 3.14, G_{DC} can be multiplied to obtain the same result as that from the sample in figure 3.12*b)*. Equation 3.14 and the parameters presented in table 3.1 yield the following transfer function for the Pendulum FMS:

$$G(s) = \frac{18.0217\ G_{dc}}{s^2 + 0.5171\, s + 17.9556} \tag{3.15}$$

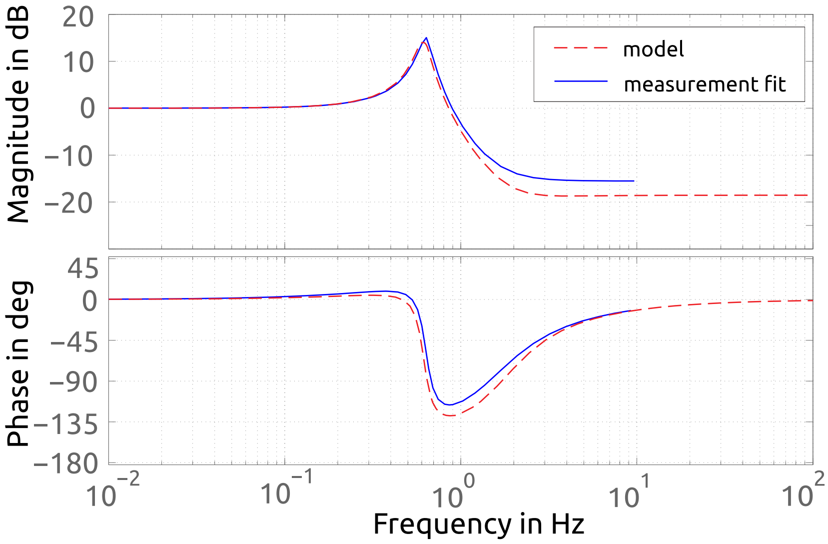

Figure 3.13: Bode diagram of the Pendulum FMS. Comparison of the least square fit and theoretical estimate based on measured data.

Using the parameters obtained above, it is possible to define the settling time. This is the required time for the response to stay within a defined error band $\pm\Delta$ of the final normalized value of unity. An approximation is used to calculate the time at which the response envelope reaches the values within the error band. This approximation is conservative because the response itself never lies outside the envelope. The envelope decays to the final value of unity with an error magnitude of $\exp(-\zeta\omega_d\tau)$, and reaches the tolerance band for

$$\exp(-\zeta\omega_d t\tau)\frac{1}{\sqrt{1-\zeta^2}} = \Delta \tag{3.16}$$

and thus,

$$\tau = -\frac{\ln(\Delta\sqrt{1-\zeta^2})}{\zeta\omega_d} \tag{3.17}$$

Therefore, the *settling time* within the given $\pm\mathbf{1}\,\%$ or $\pm\mathbf{5}\,\%$ error tolerances, remembering that $\exp(2.3) \approx 10 \Rightarrow \ln(0.01) \approx -4.6$, computes as

$$\tau_{\pm 1\,\%} \approx \frac{4.6}{\zeta\omega_d} = \mathbf{17.8004\ s}, \quad \tau_{\pm 5\,\%} \approx \frac{\ln 0.05}{\zeta\omega_d} = \mathbf{11.5794\ s}, \tag{3.18}$$

Furthermore, the Bode diagram is obtained (see figure 3.13) for the measured data using the least square fitting method and for the theoretical estimation (cf. equation 3.15).

Based on these results, a basic servo-system algorithm that uses a standard closed-loop PID digital controller is introduced in the next subsection.

3.4.2 Closed-loop

The proposed implementation of the closed-loop model is shown in figure 3.14. The input signal of the PC-based digital PID controller is the voltage signal from the positioning sensor, which is further converted to the value of an electric current to be applied to the coils of the Pendulum FMS.

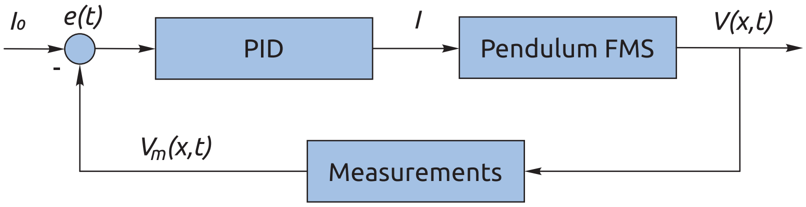

Figure 3.14: Closed-loop measurement scheme used to servo-control the position of the Pendulum FMS at the offset zero position.

The transfer function of the Pendulum FMS (cf. equation 3.15 plant) is inserted into the MATLAB Control System Toolbox in order to generate the optimal tuning parameters (K_i, K_p, and K_d) for the PID controller. To design and implement a digital PID controller in the PC, the standard form of the PID controller is discretized. Approximate solutions for the first-order derivatives are performed using the backward finite difference method.

Initially, the continues time expression of the PID controller in ideal form is considered:

$$u(t) = K_p\left(e(t) + \frac{1}{T_i}\int_0^t e(\tau)\,d\tau + T_d\frac{d}{dt}e(t)\right), \quad T_i = \frac{K_p}{K_i},\, T_d = \frac{K_d}{K_p} \tag{3.19}$$

where $u(t)$ is the controller output, $e(t)$ is the error value in the time domain, and τ is the integration time. The integral term is discretised using trapezoidal approximation, with sampling time Δt as follows:

$$\int_0^{t_k} e(\tau)\,d\tau = \sum_{i=1}^{k} e(t_i)\Delta t \tag{3.20}$$

where, $e(t_i)$ is the error of the continuous time system at the i-th sampling bin.

The derivative term is approximated as,

$$\frac{de(t_k)}{dt} = \frac{e(t_k) - e(t_{k-1})}{\Delta t} \tag{3.21}$$

Thus, the discretized PID controller can be obtained by differentiating $u(t)$ using the numerical approximations of the first- and second-order derivatives. After simplifying and solving equation 3.19 for $u(t_k) = u(t_{k-1}) + \dots$, PID in its final discretized form reads as follows:

$$u(t_k) = u(t_{k-1}) + K_p\left[\left(1 + \frac{\Delta t}{T_i} + \frac{T_d}{\Delta t}\right)e(t_k) + \left(-1 - \frac{2T_d}{\Delta t}\right)e(t_{k-1}) + \frac{T_d}{\Delta t}e(t_{k-2})\right] \tag{3.22}$$

In the numerical algorithm, instead of values $e(t_{k-2})$, $e(t_{k-1})$ and $e(t_k)$, the digitized values of the voltage measured from the positioning sensor is used as $V(t_{end-2})$, $V(t_{end-1})$ and $V(t_{end})$; before the starting loop, $u(t_{k-1})$ is calculated and identified with the same equation 3.22 as the offset current of the coils. Thus, in order to avoid the artificial (numerical) zero offset point the natural zero point of the Pendulum FMS measured by positioning sensor should be identified first.

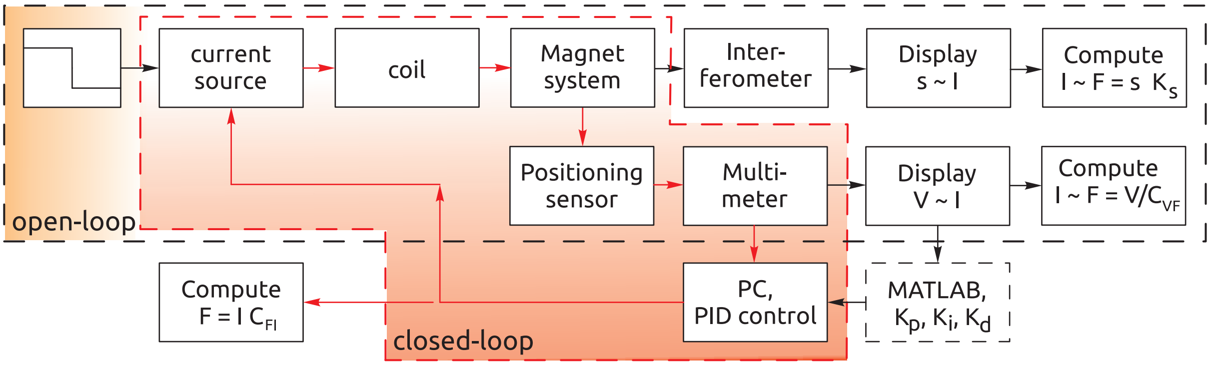

Figure 3.15: Block scheme of the measurement setup.

Because of the time-conditioned limitations of the A/D (analog-to-digital) and D/A conversations between *a)* the signal of the positioning sensor → multimeter 3458A → GPIB-USB-adapter → PC and *b)* and the digital value of the electric current generated from PC (by equation 3.22) → GPIB-USB-adapter → current source HP 3245A → coils, the minimum time (Δt wait time) for the complete cycle of the control loop necessitates 40 ms to 50 ms for the required measurement resolutions. Figure 3.15 presents the complete block diagram of the measurement setup. Initially, the maximum wait time for one loop of measurements (PID controller) is chosen to be 100 ms in order to provide stable and continuous measurements. Thus, in the open-loop operation mode, the output value of the direct compensation Pendulum FMS is the voltage from the positioning sensor, whereas in closed-loop operation mode the output value is the last value of the electric current, generated by the controller and further applied to the coil. A qualitative comparison of these two output quantities is presented in figure 3.16 for open- and closed-loop operation modes. The PID controller effort shows significant reduction of the response time, i.e., $\tau_{open-loop}$>11.5 s and $\tau_{closed-loop}$<3 s.

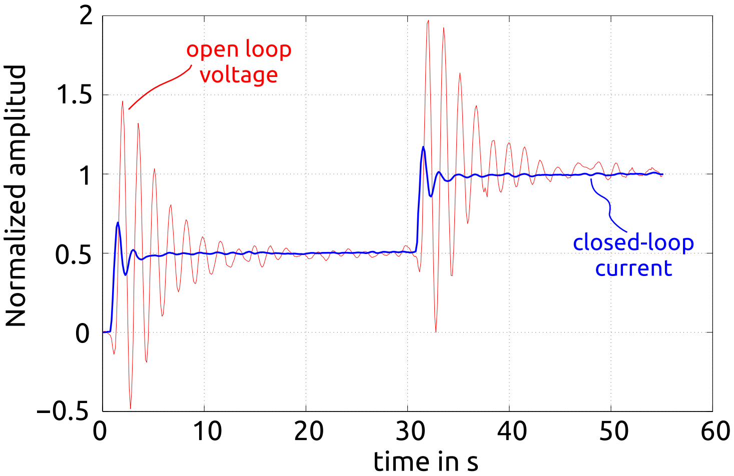

Figure 3.16: Comparison of the direct compensation Pendulum FMS measured responses in the open- and closed-loop operation regimes to the same step input. To ensure visualization, both curves are normalized by their initial and last values and shown as change of the signal amplitude.

Controlling the position at the zero point in the closed-loop operation mode assumes an additional advantage. In theory, it is possible to diminish the nonlinear influences that exist along the full measurement range of the positioning sensor, and to focus on increasing the measurement resolution. However, the vibration noises in the signal are much larger than the actual resolution of the voltage measurements from the positioning sensor (for example, see figure 3.16).
Because the deflection of the Pendulum FMS is already measurable as a proportional value of the electric current applied to the coils, the direct compensation scheme should be calibrated in order to provide traceable measurements of the forces. In the next section, a description and some understanding on the strategy of the calibration concept are presented.

3.4.3 Calibration concept

Open-loop. Earlier, a measurement of the forces that act in the horizontal direction on the Pendulum FMS is calibrated with voice coil actuator and measured by laser interferometer as an effective deflection (cf. Ref. [21]) in the open-loop mode. The positioning sensor can be calibrated based on these interferometric measurements of the deflection. In the open-loop operation mode, the measurement signal of the positioning sensor (in volts) is traceable to the measurements with the interferometer (in meters later converted to Newton, cf. figure 3.9). At the current arrangement of the Pendulum FMS, the calibration factor can be computed as $\mathrm{mV\,\mu N^{-1}}$ from the values presented in figure 3.11, where measurements are obtained separately for each operation regime of the coil(the calibration forces are produced by the electric current applied to the coil connected to the electric circuit for each measurement set by $1, 3, \ldots$,15 turns).

The mean value of the calibration factor for each operation regime of the coil is computed through a division of the mean value of the positioning sensor sensitivity (*V(s)/I*) over the mean value of the interferometer sensitivity (*F(s)/I*). Initially, the combined standard uncertainty of both the voltage measurements from the positioning sensor and force measurements from the interferometer is computed for each operation regime separately. The standard uncertainties from each step response are computed by the summation of the quadrature for addition:

$$\text{Combined } uc(V) = \sqrt{[u(V_1)]^2 + [u(V_2)]^2 + \ldots + [u(V_n)]^2 + \ldots} \tag{3.23}$$

$$\text{Combined } uc(F) = \sqrt{[u(F_1)]^2 + [u(F_2)]^2 + \ldots + [u(F_n)]^2 + \ldots} \tag{3.24}$$

Furthermore, the relative uncertainty of the calibration factor is computed by the method of summation in the quadrature for division as

$$\frac{uc(C_{VF})}{C_{VF}} = \sqrt{\left[\frac{uc(V)}{V}\right]^2 + \left[\frac{uc(F)}{F}\right]^2} \tag{3.25}$$

Equation 3.23 to 3.25 omit the *1/I* factor because both the positioning sensor and interferometer measure the same process simultaneously for the same I electric current applied to the coils.

Finally, the mean value and combined relative uncertainty of the calibration factor from all operation regimes can be estimated (cf. figure 3.17 for C_{VF}^{all}).

The mean value and combined standard uncertainty are computed as

$$\text{mean}(C_{VF}^{\text{all}}) = \frac{\sum_{\alpha=0}^{n} C_{VF}^{2\cdot\alpha+1}}{n} \tag{3.26}$$

$$uc(C_{VF}^{\text{all}}) = \sqrt{\sum_{\alpha=0}^{n} \left[uc(C_{VF}^{2\cdot\alpha+1})\right]^2} \tag{3.27}$$

Measurements are obtained for all connection cases ($\alpha = 7$), thus equations 3.26 and 3.27 become

$$\text{mean}(C_{VF}^{\text{all}}) = \frac{C_{VF}^{1} + C_{VF}^{3} + \ldots + C_{VF}^{15}}{n} \tag{3.28}$$

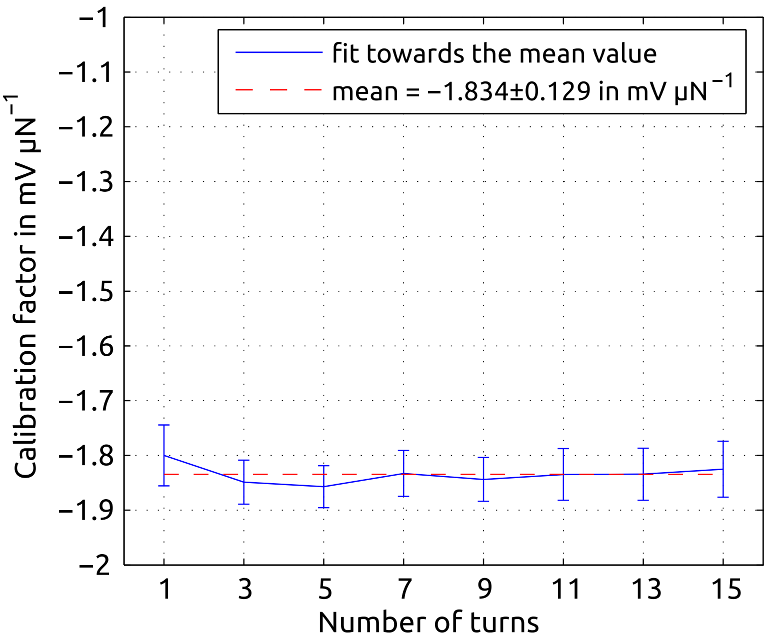

Figure 3.17: Calibration factor of the positioning sensor computed in reference to the interferometer measurements.

$$uc(C_{VF}^{\text{all}}) = \sqrt{\left[uc(C_{VF}^{1})\right]^2 + \left[uc(C_{VF}^{3})\right]^2 + \ldots + \left[uc(C_{VF}^{15})\right]^2} \qquad (3.29)$$

The value of the calibration factor considers all measurement results $-1.834\,\text{mV}\,\mu\text{N}^{-1} \pm 0.129\,\text{mV}\,\mu\text{N}^{-1}$ with a combined standard uncertainty of approximately ±7 % relative to the mean value. Within these numerical values, the uncertainty contribution from the positioning sensor results approximately 6.4 %. In contrast to the positioning sensor, the uncertainty contribution from the interferometer is low: approximately 0.56 %. However, this cannot be considered the final result, yet, because the sampling frequencies of the measurements with the interferometer and positioning sensor are different, and thus provide an incomplete picture of the overall uncertainty budget. Partially, for this reason, the standard uncertainties of the positioning sensor and interferometer for each set of measurements are computed separately (cf. equations 3.23 and 3.24) as the summation of the quadrature for addition. The measurements from the positioning sensor are obtained with a sampling frequency of approximately 20 Hz, which manifests high amplitude and low frequency oscillations in the measurement signal that results from the effects of seismic and other ground-borne mechanical noises. Refer to figure 3.16 for an example: the parasitic oscillations obstruct the signal of the position sensor even when the settling time of the Pendulum FMS is reached. The measurements from the interferometer are obtained with 8 Hz sampling frequency[3].

---

[3] In addition, the measurement data are preprocessed by the electronics of the laser interferometric system using some internal low pass filter (‘black box’ [39]).

Closed-loop. As indicated in the previous paragraph for measurements in the open-loop operation regime, the signal from the positioning sensor is traceable to the signal from the interferometer with a defined calibration factor. In the closed-loop operation regime, the same signal from the positioning sensor is feed to a digital PID controller that generates the compensation current to be applied to the coils. The electric current is generated and applied to the coils such that the Pendulum FMS and the aperture attached to it remain at the zero balance position by an electromagnetic force between the electric current applied to the coils and the magnet system. Thus, the electric current applied to the coil is proportional to the force that acts on the Pendulum FMS. This means that calibration using the interferometer measurements can also be applied here. To obtain the calibration factor (F/I proportionality factor C_{FI}), a known amount of electric current should be applied to the coils and the measurements obtained from the interferometer have to be recorded. As shown in figure 3.10, this procedure is performed for all cases where the coil is connected to the electric scheme and the resulting sensitivity factors for all cases is plotted in figure 3.11 in terms of $\mu\mathrm{N}\,\mathrm{mA}^{-1}$ as a function of the number of turns in the coil. Similar measurements are also obtained for *ii)* the thin sheet conductor. These sensitivity factors can be interpreted as follows: (e.g.) in the closed-loop operation regime the direct compensation Pendulum FMS can compensate approximately 250 µN horizontally acting forces when the coil (connected to the electric circuit with 15 turns) carries 1 mA electric current.

Alternatively, as discussed in section 3.2, using equations 3.11-3.12, the theoretical estimate of the same calibration factors can be computed analytically once all parameters are known. The calibration factors are obtained based on this argument and all available parameters defined earlier for the direct compensation Pendulum FMS system (cf. description of figure 3.3). The values obtained from equations 3.11-3.12 are compared with the measurement results from figure 3.11. Figure 3.18 presents the absolute values of the calibration factors.

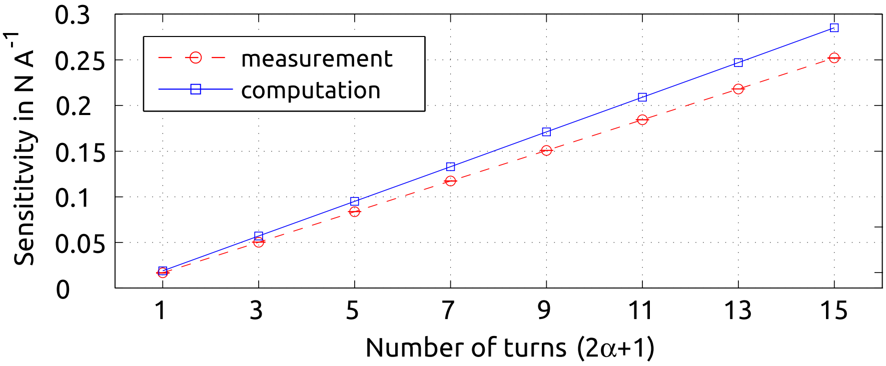

Figure 3.18: Comparison between measured and theoretically computed calibration factors (C_{FI}) of the direct compensation Pendulum FMS as a function of the number of turns in the coil. Given as their absolute values, they should be adapted based on the polarity of the electric current during measurement.

The values differ by approximately 13 % for each $2\alpha + 1$ number of turns in the coil. The origin of this difference is mainly dependent from:

- unrefined positioning of the coil in the magnetic field,
- homogenization of the magnetic field given as a single value for the saturation magnetization M_s of the rectangular bar magnet and its dependence (yet undefined) from the varying temperature of the surrounding environment,
- the assumptions made while deriving the theoretical expression in section 3.2,
- the accuracy of the measurements from the interferometer (the calibration error, cf. table 1 in [13]), that imposes an additional 2-4 % inaccuracy while referencing and calibrating these measurements.

Based on these calibration factors, the direct compensation Pendulum FMS can be applied to the measurements of the Lorentz forces on the electrolyte flow channel. An example of such practical measurements is presented in figure 3.19. In the figure, all necessary measurements are obtained in order to verify the applicability of the developed direct compensation Pendulum FMS and compare the results of flow measurements against the earlier published data presented in [13]. Thus, the Lorentz forces are generated for the given flow velocity (cf. figure 3.19*a)*). These forces act on the Pendulum FMS that attempts to deflect the magnets along the flow direction. At this point, the control loop acts by generating varying compensation electric currents (cf. figure 3.19*b)*) that bring the Pendulum FMS to the offset position (in the example is approximately 64 mV, cf. figure 3.19*c)*). In addition, the laser interferometer measures the same offset position of the Pendulum FMS (cf. figure 3.19*d)*) that serves as reference for the photoelectric positioning sensor that the direct compensation method performs well in terms of controlling the zero position. In all figures, the same running average filter for the last 25 data points is used (green). The amplitude of the Lorentz force measurements generally agree with the measurements published earlier. From here, the values of the electric current presented in figure 3.19*b)* can be readily converted to the force values using the calibration factors given in figure 3.18. In the example, the measurements are obtained for the coils when they are connected with 15 turns, therefore, the mean value and standard deviation at each step of the compensation current should be multiplied by the calibration factor of approximately 250 µN mA^{-1} in order to obtain the force value. Hence, the Lorentz force measurements can be made by the method of the direct Lorentz force compensation.

Note that the measurement response time is reduced greatly (< 3 s) compared with the open-loop measurement employed in earlier measurements [13, 14]. In addition, in all subsequent measurements the response time is further reduced to approximately 2.4 s, by manually tuning the coefficients (K_p, K_i, and K_d) of the PID controller.

At the current state, the system has three main drawbacks that limit the possibilities of characterizing its dynamic measurement performance in depth. The first is

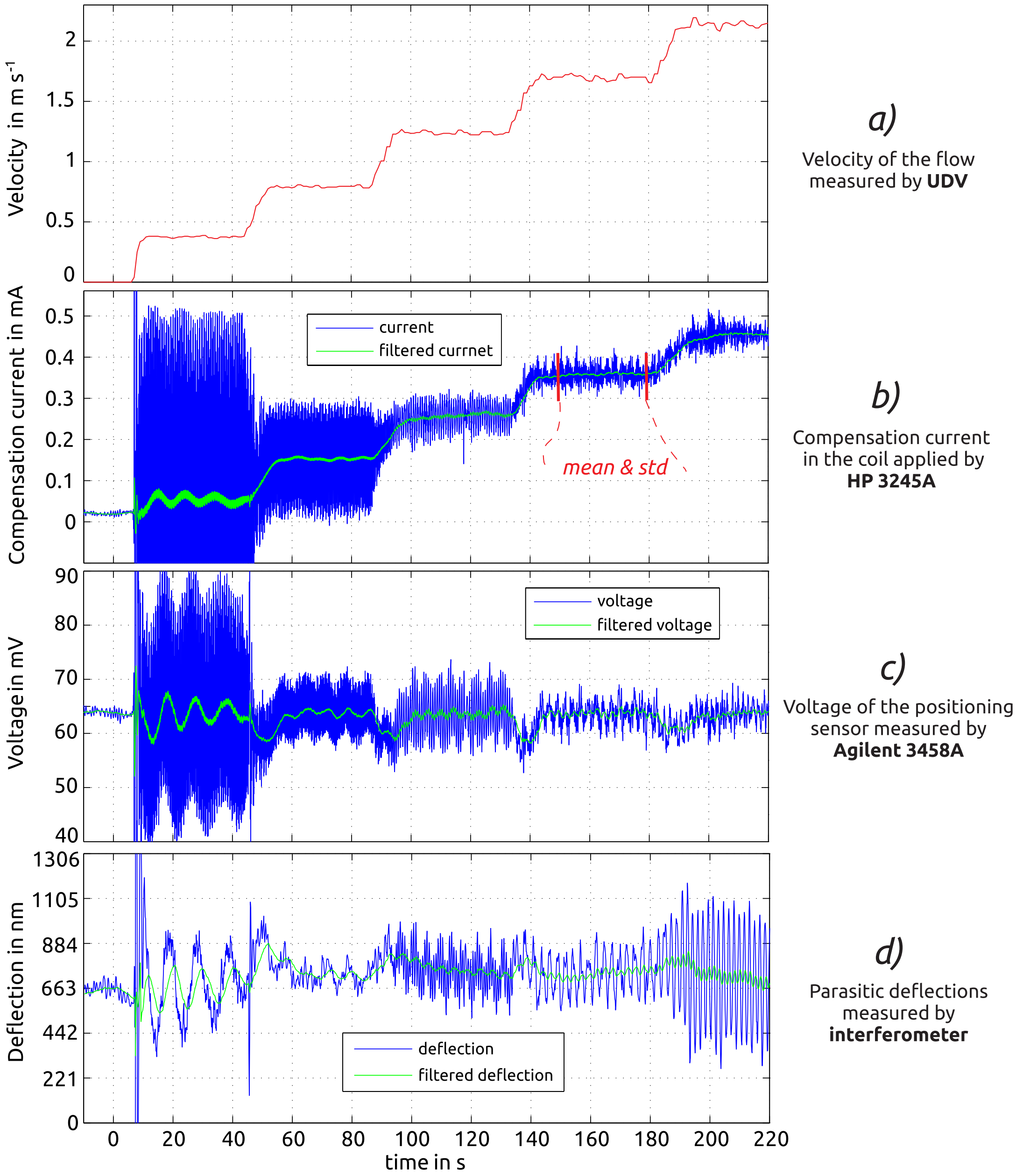

Figure 3.19: Example of the direct compensation Pendulum FMS performance (for coil with 15 turns) applied on the electrolyte flow channel for practical measurements of the Lorentz forces. Here, the electrical conductivity of the fluid is σ =20.11 S m^{-1}, for full set of measurements for different values of electrical conductivity see figure 5.2. a) The given velocity of the flow is measured by the reference UDV flowmeter. b) The compensation current is applied to the coils by a high-resolution digital current source. c) The signal from the position sensor is measured by a high-resolution digital multimeter with initial offset voltage of approximately 64 mV. d) The reference measurements of the offset position by the interferometer.

the unstable offset position of the Pendulum FMS that results in significant force drift during long-term measurements. The force drift is detected as having a similar origin to that identified for dFMS, dependent on the thermo-mechanical effects, discussed earlier in sections 2.1.1 and 2.1.2. The second is the poor sampling frequency $< 20\,\text{Hz}$ of the measurements conditioned only by the performance of the digital PC-based controller (cf. section 3.4.4). The third has a more natural origin, and can be generalized as follows: the inertial forces that act on the Pendulum FMS are much smaller compared with the gravity force, and therefore make the system reluctant to reacting against high-frequency dynamic forces. However, the response time is expected to be improved when considering an analog PID controller. In the case of force drift, an estimation of the character for this error is presented in section 3.4.5.

3.4.4 Spectral distribution of the measurement signals

This subsection presents a brief overview of the dominant frequencies that obstruct measurements. The signals of the measurements of the direct compensation Pendulum FMS (cf. figure 3.19) are obtained with the following sampling rates: *a)* velocity measurements with UDV flowmeter by 1 Hz, *b)* and *c)* applied compensation current and measured voltage by $\leq 17\,\text{Hz}$, and *d)* deflection measurements with interferometer by $\leq 8.5\,\text{Hz}$. These values are estimated based on the data readouts collected on the time domain. All data are synchronized using the PC processor clock. The FFT representations of the signals on the frequency domain are computed. The distribution of power spectral densities of all signals are presented in figure 3.20.

Figure 3.20 shows the typical situation of noise distributions involved in each measurement. Figures 3.20*b)* and 3.20*c)* are interrelated because the power spectral density of figure 3.20*c)* is obtained from the compensation current generated based on the voltage signal; therefore, the peak frequencies in both measurements have the same value. The noise at the lower frequencies obstructs the signal of the positioning sensor, and therefore imposes a considerable amount of artificially created noise in the signal of the electric current (the numerical error is transmitted through the D/A converter to an analog noise). After the initial test measurements, it is determined that this noise is predominant when the flow rate is also low, which can be observed in figure 3.19.

The filtered signal of the applied electric current with standard backward averaging filter (last 25 data) is compared with the actual measured raw signal. Based on this, a result with more systematic representation can be drawn. Figure 3.21 presents a relative standard uncertainty of the applied electric current as a function of the electrolyte flow rate.

At higher velocities, the amplitude of the generated Lorentz forces dominate over the amplitude of the random noise effect, which leads to the process being controlled more vividly by the digital PID controller. The result is that the noise also remains in the measurements when the electrolyte channel operates only by its bypass channel (cf. figure 3.21, △-bypass channel). Use of the bypass channel considers that the main channel is closed and the electrolyte flow does not interact with the magnetic

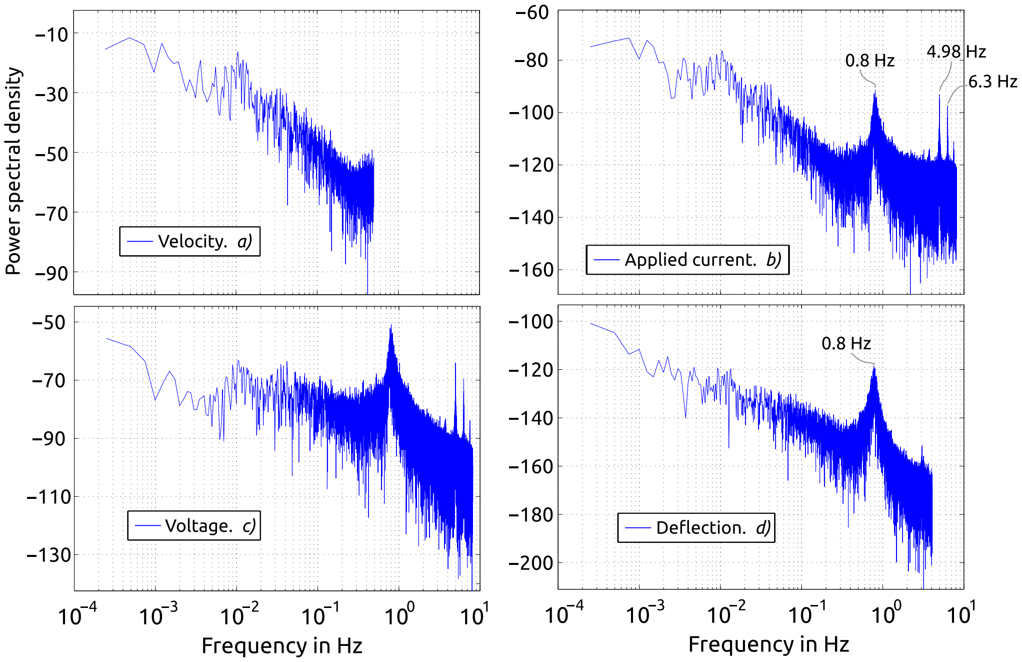

Figure 3.20: Distribution of the power spectral density given on the frequency domain for the measurements obtained with direct compensation Pendulum FMS. See figure 3.19 for comparison. According to the Nyquist theorem, the maximum frequencies are: a) for the velocity - 0.5 Hz, b) for the applied compensation current - 8.14 Hz, c) for the voltage - 8.14 Hz, and d) for the deflection measured by interferometer - 4.2 Hz.

field; therefore, no Lorentz forces can be generated. Thus, the noise is produced only by the flow pump (an integrated part of the electrolyte channel) and transmitted to the direct compensation Pendulum FMS through the ground.

3.4.5 Uncertainty of the force drift

A significant offset position error is identified in the measurements with the direct compensation Pendulum FMS. The offset position drifts because of the thermo-mechanical properties of the supporting construction. This error can be observed when measuring the position of the Pendulum FMS with an additional reference device. As discussed earlier, during the direct compensation process, at least one axis reference measurement is necessary with a laser interferometer in order to verify the behavior of the Pendulum FMS. Figure 3.22 presents an example of long-term measurements obtained simultaneously from the positioning sensor and interferometer. As the figure shows, even when the zero point is controlled very well from the signal of the positioning sensor against any disturbances imposed on the system throughout the measurement period, significant drift from this zero point is evident in the measurements from an independent reference interferometer system. For this, systematic long-term measurements and monitoring of the signal of zero-point stability

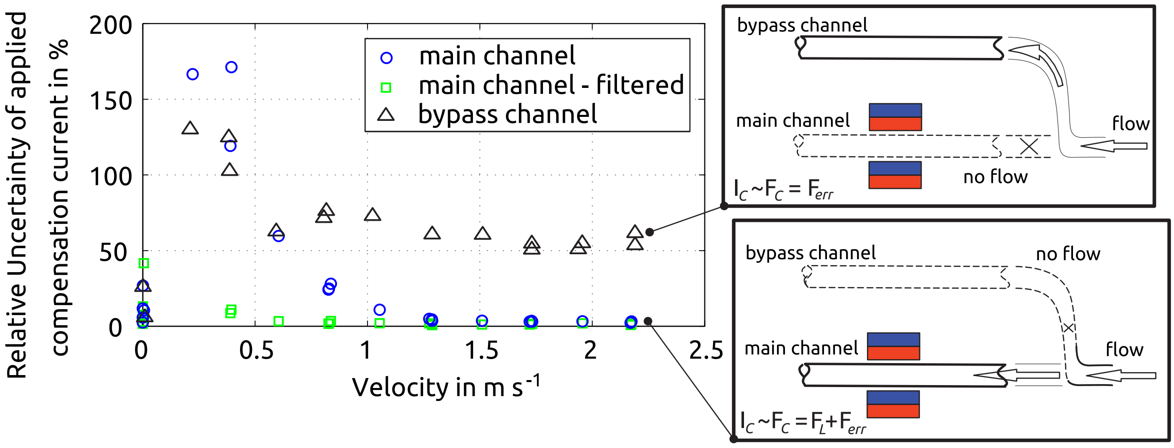

Figure 3.21: Relative uncertainty of the electric current applied to the coils as a function of the flow velocity. Compare figure 3.19*a)* with the figure 3.19*b)* raw and filtered signals of the applied electric current. △-bypass channel shows the relative uncertainty of the applied electric current as an effort of the PID controller to balance the Pendulum FMS at the zero position, when no Lorentz force is measured but the flow pump is operating.

are obtained. A strong correlation is identified between the temperature of the surrounding environment and the signals of the interferometer and compensation current. Furthermore, the thermal expansion and total deformation of the supporting construction is found to be the main reason for this strong correlation.

A tiltmeter is introduced to the mechanical construction in order to measure and provide a quantitative estimate on the magnitude of the tilt error. The thermosensors measure in parallel the temperature of the air outside the insulation box and that of the aluminium-supporting bar of the construction inside the insulation box (cf. figure 3.7 for complete scheme of the measurement setup). The tiltmeter is arranged so that one of the measurement axes coincides with the measurement axis of the positioning sensor and interferometer (x), and the second measurement axis in the perpendicular direction (y). The force drift is measured by the tiltmeter as the tilt angle of all construction. Thus, during the measurements presented in figure 3.22, all necessary data are recorded in parallel. Figure 3.23 presents an example of the change of the setup tilting angle and the temperature change of the surrounding environment.

Further analysis and basic schematic calculations confirm that the system tilt is the dominant cause for the force drift.

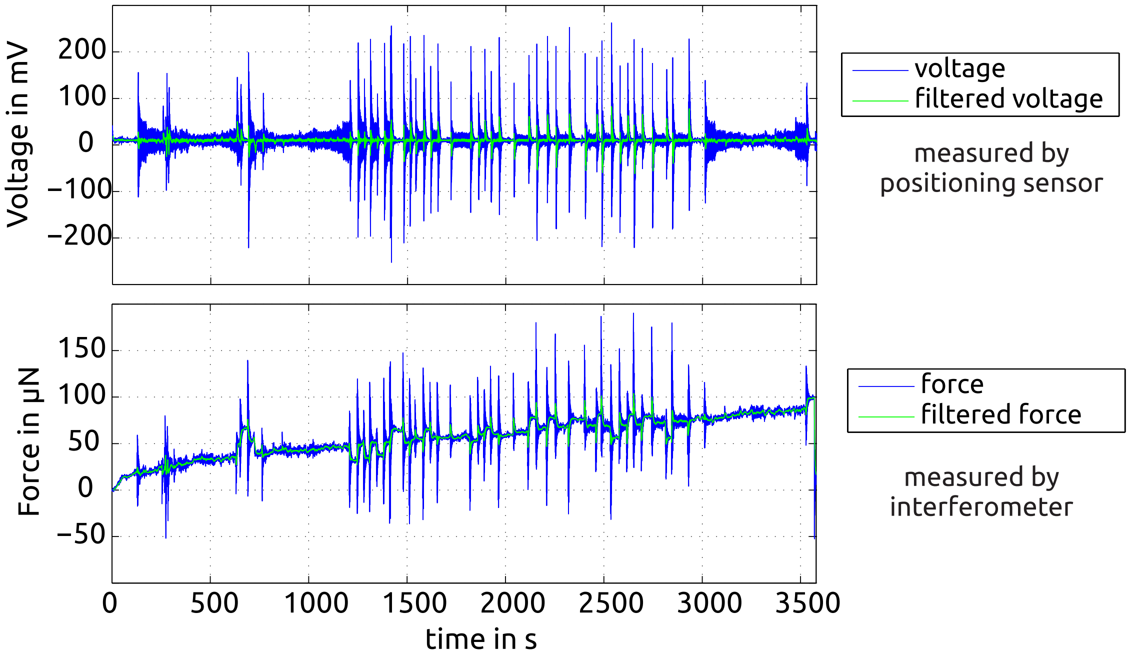

Figure 3.22: Example of long-term measurements on the direct compensation Pendulum FMS that shows the systematic error of the drifting offset point. Voltage from the positioning sensor with the offset voltage of 10.9455 mV (top); reference measurements with interferometer expressed in µN to indicate the force drift (bottom).

3.5 Summary

In this chapter, a general introduction to the direct Lorentz force compensation flowmeter was presented. The new method was implemented on the Pendulum FMS using the prototype electrolyte channel. The essential feature of the flowmeter is that the Lorentz forces, produced by interaction of the electrically conducting flow and magnetic field, and acting on the magnet system, are now measured directly on the magnet system using the principle of electromagnetic force compensation. Compared with earlier methods for measuring the Lorentz forces [7, 14, 15, 61], in the proposed method, reduced complexity for the overall measurement system is introduced. In particular, the current method only requires a magnet system, sufficiently sensitive linear guide to trace the deflection of the magnet system, and current-carrying conductor arranged in close vicinity to the magnet system in order to generate compensation forces. From here, measurements of the compensation forces are the key feature that underlies this method. The compensation force is proportional and directed oppositely to the reaction force that acts on the magnet system. In turn, the reaction force is proportional and has opposite direction to the Lorentz force, and therefore the compensation force is equal to the Lorentz force. The compensation force is produced by electromagnetic interaction between the magnetic field of magnets and electric current applied to the coils. The coils are statically fixed

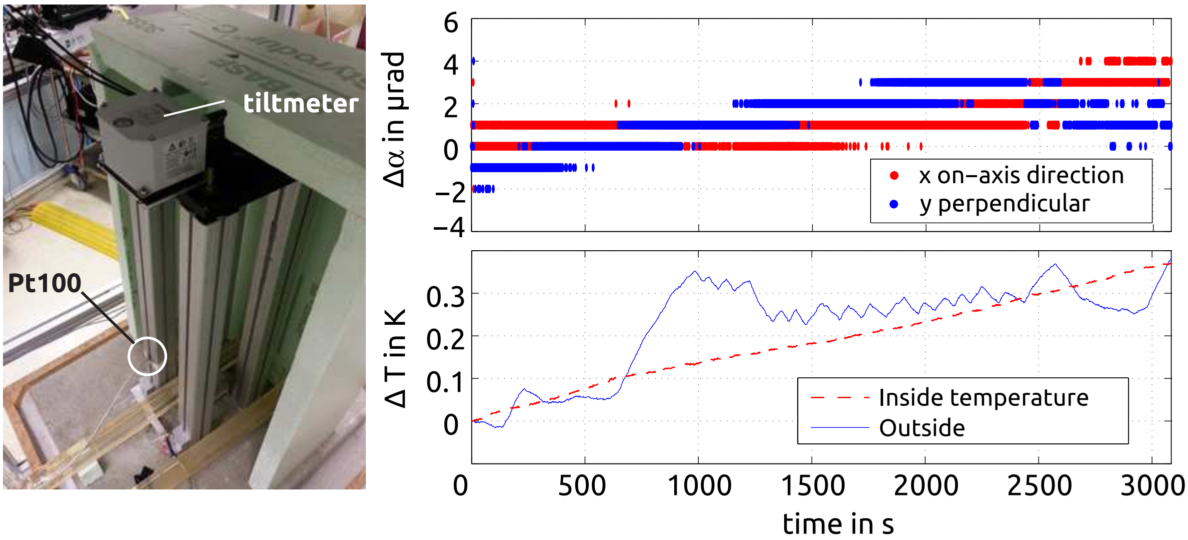

Figure 3.23: Example of long-term measurements on the direct compensation Pendulum FMS (same measurement process presented in figure 3.22) that shows the tilting angle change (top) and the temperature change of the surrounding environment (bottom). Left: image of the tiltmeter installed on the mechanical construction of the setup.

in the vicinity of the magnets so that the produced forces act on the magnet system along the same x-axis. Several different configurations of the coils were employed to test the initial performance of the direct compensation Pendulum FMS. The method of balancing on the zero point was used to perform the measurements. A servo-controlling setup was developed based on a digital PID controller. The input signal to the PID controller was the voltage from the positioning sensor that traces the deflection of the Pendulum FMS. The output signal of the PID controller was the electric current applied to the coils to maintain the vector force, a superimposed force that experiences the magnet system, at zero. Indeed, the preliminary measurements showed that for continuous flow rate measurements, this method suggests an improved stability, reduced response time, and optimised technical and measurement complexity for the setup.

Usually, within the commercially available precision FMS (or developed separately), some magnets and electromagnetic elements are integrated that can introduce unwanted interaction between them and the high-power magnet systems (necessary for LFV application) adjacent to the electrolyte channel. Therefore, these magnetic interactions are completely avoided with the new method, and a natural advantage against those types of FMS is achieved. Thus, instead of using a separately developed or commercially available FMS, the newly developed force measurement system can be directly integrated to an electrolyte channel based only on its design characteristics.

Section 3.1 presented an outlook on the experimental setup and a short discussion

on the proposed force measurement method. Subsequently, section 3.2 derived a theoretical model for the measurements based on the setup parameters and arrangement of the custom manufactured rectangular coils (current-carrying conductors). The theoretical calculation was presented to simplify a further argumentation that the method is suitable for a wide variety of applications. Moreover, setup sensitivity can be calculated in advance and adopted in relation to a particular application design. For instance, can be considered a current-carrying conductors in the form of a coil that have a high number of turns compared with the case presented in this section, or a coil with additional rows of winding (see next section). It can be also considered coils with parallel winding in order to apply a non-linear control mechanism for finer resolution [62]. Section 3.4 showed a number of test measurements by a rectangular-shaped coil winded in a single row with 15 turns that also works with $1, 3, 5, \ldots,$ and 13 turns as an adjustable inductive element (cf. figure 3.8). Sections 3.3 and 3.4 provided a description of the measurement infrastructure.
Based on the linear relationship of the sensitivity (or calibration factors) derived in equations 3.11 and 3.12 and illustrated in figures 3.10, 3.11, 3.17, and 3.18 as a function of the number of turns in the coil, the following quantitative estimate can be made. If a 10^{-3} A current in one turn produces approximately $2 \cdot 10^{-5}$ N compensation force, one can argue that *a)* the same current for a coil with 1000 turns can produces approximately $2 \cdot 10^{-2}$ N compensation force, which is a typical force range in the liquid metal LFV measurements. The electrical conductivity of liquid metals is approximately 10^6 times higher than that of electrolytes [5, 8]; therefore, higher compensation forces will be required. A similar argumentation holds for case *b)* 10^{-6} A electric current in a single turn that can generate 10^{-8} N compensation force that can provide higher resolution of compensation measurements. The last is an estimation based on the sensitivity slope presented in figure 3.18. However, the validity of the above statements can be tested after resolving the problem of zero point stability for case *b)*, and in case *a)* should be consider the influence of an additionally produced magnetic field by coils that can affect the stability of the electrolyte flow. In the measurements presented in this work, in accordance with Faraday's law of induction, the magnetic fields produced by rectangular coils is computed at approximately 10^6 times smaller than the nominal remanence B_r =1.37 T of the magnet systems; therefore, their influence here is mostly negligible.
In summary, the new method for the Lorentz force measurements by the direct compensation principle can be used to facilitate flow measurements of low conducting electrolytes. Figure 3.24 presents the actual state of the measurements; this figure also shows all significant disturbances and limitations identified during the development and operation with the direct compensation Pendulum FMS. However, general advantages and disadvantages should be considered in account in further development and measurements, respectively. The main **advantages** achieved when using this direct compensation method are as follows:

- *measurement stability* is improved using a simple and reliable position-measuring sensor based on LED and differential photodiodes, instead of laser interferometer measurements,

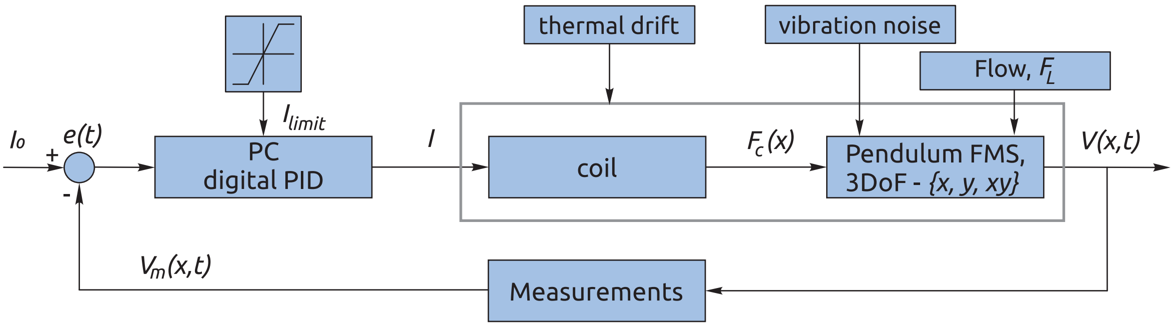

Figure 3.24: The actual state of the closed-loop scheme of the direct compensation Pendulum FMS, including all significant disturbances.

- the *settling time* is reduced by using a servo-system (closed-loop measurements),
- compared with measurement methods established earlier using the interferometer measurements, the new method already provides the possibility for *online and continuous measurements* of the Lorentz forces, and therefore for the measurements of the flow velocities of low electrically conducting electrolytes.

Among the advantages obtained during the development process for the direct compensation method, several **disadvantages** are revealed that are partially dependent on the mechanical properties of the Pendulum FMS. They can be avoided in future designs of the mechanical systems:

- *the zero point stability* is the most influential error involved in measurements,
  - *the overall stability of the zero point* in long-term measurements is attributed to the thermal drift of the supporting construction,
  - *the rotational and perpendicular shift* of the Pendulum FMS is neglected. This is done under the assumption that during measurement of the deflection of the magnet system, the Lorentz and compensation forces are in one direction (x). However, the Pendulum FMS has two other components, translational (y) and rotational (xy), that introduce additional and indefinite noise,
- *combined vibration noises* identified mostly as a result of the effects of seismic and other ground-borne mechanical noises. Among these sources, two are dominant and transmit to the Pendulum FMS significantly:
  - *mechanical vibration of the pump* with different high frequency components at different regimes of its operation. This noise only introduces high disturbance during low rotation regimes for low flow velocities (under $1\,\mathrm{m\,s^{-1}}$ and approximately 100 rpm),

  - *passive ground vibrations* that set the Pendulum FMS in to an oscillatory motion. The resulting parasitic deflections, equivalent to force values, range from approximately 2 µN during the day to approximately 1 µN during the night at approximately 0.8 Hz frequencies,

- *insufficient setup sensitivity* defined by the electromagnetic interaction between the custom manufactured coils and magnetic field (or force factor $l \cdot B$). When the coil is connected with its maximum number of turns, the sensitivity value results at approximately $0.25\,\mathrm{N\,A^{-1}}$ (cf. figure 3.18), which is a relatively good force factor for performing precision measurements compared with all other smaller number of turns or the thin sheet conductor. However, from the practical measurements on the electrolyte channel (cf. figure 3.19*b)*) it was evident that a higher number of turns in the coil is still required. In all measurements presented in this chapter, a numerical limit of 1 mA was set to the applied electric current in order to prevent the coils from overloading. This limitation introduces several disadvantages, such as limiting the range of measurements to ±250 µN, and limiting the dynamic characteristics of the control loop.

The next chapter considers some of these advantages and disadvantages during development of the final (third) type of FMS that uses the direct compensation method combined with an EMFC balance. The EMFC balance is treated only as a linear guide in order to trace the deflection of the magnets with sufficient accuracy. Compared with the Pendulum FMS, the EMFC balance provides better possibilities of avoiding errors, such as the linear force drift and translational (y) and rotational (xy) shifts of the zero-point stability.

4 Direct Compensation with EMFC Balance

> Auch aus Steinen, die Dir in den Weg gelegt werden, kannst Du etwas Schönes bauen.
>
> Erich Kästner

Development presented in this chapter intends to provide confirmation with an additional set of measurements that the direct compensation method is indeed a relatively simple and cost-effective system for Lorentz force measurements, while having the potential for further practical improvements. The old EMFC balance (same from sections 2.1 and 2.1.1 to 2.1.3 and Ref. [21]) is used to develop a new FMS with mechanically predefined single axis sensitivity (1DoF). This is an alternative to the Pendulum FMS used during the initial development and test measurements (with 3DoF, cf. chapter 3). The magnet system is the same that for the direct compensation Pendulum FMS. Several custom manufactured rectangular coils with different number of turns $(7, 29, 77, 255)$ are used to perform the compensation measurements. Coils with n=$7, 29,$ and 77 are winded above each other on a single piece of support forming three rows of independently working coils, whereas the coil with n=255 is winded on a separate piece of support forming a single coil with four rows above each other. Based on this, a variety of connection schemes of the coils are possible for implementing the compensation force measurements. Subsequently, simultaneous use of two different coils with a different number of turns in the measurement scheme is proposed in a double-coil operation regime or double-force compensation method [62], addressed in 4.3.3. The complete FMS is mechanically arranged on the prototype channel such to minimize possible thermo-mechanical influences. FMS performance is tested for all coils through extensive measurements. A calibration procedure is performed against those components integrated into the internal structure of the EMFC balance (positioning sensor and voice coil actuator); in addition, reference measurements with laser interferometer are obtained similar to those presented in the previous chapter.

4.1 Objectives and proposed improvements

The main considerations listed in the summary of the last chapter (section 3.5) are the bases for the possible improvements discussed here. A new setup is constructed

on the prototype channel in order to enhance the performance of the direct compensation method. From the mechanical and electrical perspective, the same experimental infrastructure is used (cf. figure 3.7). The only modifications concern two main components of the setup: the EMFC balance introduced separately instead of the Pendulum FMS, and newly manufactured rectangular coils.
The **EMFC balance** is chosen because it can provide a linear guidance for deflection measurements of the magnet system in the single (x) axis direction. The same magnet system used for the Pendulum FMS is now mechanically fixed (upside down) from the load carrier of the EMFC balance. In addition, a corner cube mirror is fixed to the coupling element of the load carrier and magnet system in order to perform reference measurements of the same deflection with laser interferometer. Although the EMFC balance stiffness is incomparably high compared with that of the Pendulum FMS (see table 4.1), a finer assembly of the inner mechanical structure of the EMFC balance is expected to provide higher measurement stability and resolution.

Table 4.1: Stiffness comparison between the Pendulum FMS and old EMFC balance [21] FMS.

FMSs	Stiffness, $[\mathrm{N\,m^{-1}}]$	comment
old EMFC balance [21]	407.861 ± 24.959	*based on the measurement results presented later in this chapter and the value given in* [21]
Pendulum	20.99 ± 0.24 *or* 22.53 ± 0.24	*the values are given in* [13]

In addition to the aforementioned characteristics of the EMFC balance, the choice is also motivated by the fact that several features of these systems are identical to the setup already tested on the Pendulum FMS, and meet the necessary minimal requirements for implementing the direct compensation measurements. In particular, the following similarities are present: amount of dead load carried; type of positioning sensor based on other electronics (developed by C. Diethold for [21])[1] with only some minor differences compared with that used for the direct compensation Pendulum FMS; and the same PC-based digital PID controller with the existing electrical

---

[1] There are various possibilities for designing the electronics of such positioning sensors. For several reasons (such as the random mechanical noise that highly influences all FMS, high precision of the required voltage measurements, and digital PID controller), the necessity for further investigation on an optimal electric design remains out of scope of the current work. The actual achieved resolution of the voltage measurements with the developed electronics under test is much better than the stability of the zero point measurements, i.e., its performance is satisfactory for measurements proposes considered in this work (see figures 3.12*a)* and 3.16 *open-loop*). However, for future investigation, one possible way of defining the optimal design for the electronics of the positioning sensor can be considered when its measurements are directly linked to an analog PID controller in order to improve the performance of the closed-loop operation regime. In contrast to this, the only advantages using a digital PID controller are freedom of manual/numerical adjustments, and the possibilities of incorporating various non-classical algorithms in the control loop.

setup (high-precision digital multimeter and current source) that can be adapted readily to perform compensation measurements.

The **rectangular coils** are manufactured with a higher number of turns, n=7, 29, 77 and 255, in order to increase the sensitivity factor and range of produced compensation forces. Based on earlier measurements (cf. chapter 3) that show the linear relationship between the number of turns and compensation forces produced for the same range of applied electric current, and the comparison with theoretical calculations, it is expected to improve the range of measurements at least with one order of magnitude. The general parameters and geometrical configuration (in reference to the magnetic field distribution) of the rectangular coil remain the same as those chosen for the earlier coil. However, several minor differences are introduced in order to ensure the performance and accuracy of the direct compensation measurements. The coils with n=7, 29 and 77 are winded above each other on a single piece of mechanical support. Each coil is winded in a single row and can be connected to the electric circuit independently. Based on this feature, combined operations of two (or more) coils are possible. Later in this chapter, the simultaneous use of two different coils with different numbers of turns in the measurement scheme is proposed for a double-coil operation regime or double-force compensation method [62], addressed in section 4.3.3. The coil with n=255 turns is winded on a separate piece of mechanical support. This coil has four rows winded above each other with almost an equal number of turns in each row.

The combination of these two principal components (EMFC balance and rectangular coils) further support the idea that, once a sufficiently sensitive linear guide is provided, it will be possible to *a)* adopt the direct compensation measurement method for a variety of LFV applications, and *b)* reduce the overall complexity of the measurement schematics. The next section briefly describes significant details in the design of the new setup.

4.2 Design of the setup

This section presents the design of the combined mechanical and electrical assembly. The principal operation of the EMFC balance is already known, and it is well described in chapter 2. Here, in order to accomplish similar operational conditions, the EMFC balance is fixed from a bearing plate in the very vicinity of the electrolyte channel (cf. item (3) in figure 4.1). A complete direct compensation EMFC balance FMS occupies a volume of approximately 7 cm × 15 cm × 40 cm in the x, y, and z dimensions, respectively, whereas the lever arm of the EMFC balance is approximately 11.5 cm with overall 1:≈5.41 proportionality ratio. Because the lever arm is attached to the magnet system by the load carrier and coupling element, the deflection of the magnet system can be measured by the positioning sensor integrated within the EMFC balance. The deflection of the magnet system is measured in the x direction; moreover, the measurements can be referenced to the interferometer fixed on a separate ground. Because of the same feature of the mechanical connection between the lever arm and magnet systems, the electromagnetic voice coil actuator of the EMFC balance can be used for applying the calibration forces on the lever arm. The comparison between these calibration forces and compensation forces produced by the rectangular coils (cf. item (1) in figure 4.1) solidly fixed from each side of the magnet system is the procedure for the calibration and redundant cross-check measurements for the direct compensation method. Thus, by applying known electric current either to the coil of the EMFC balance or the rectangular coils, calibrating the system is possible. Based on this particular design of the measurement scheme, the calibration principle differs from that used for the Pendulum FMS; however, a similar procedure is employed for the measurements.

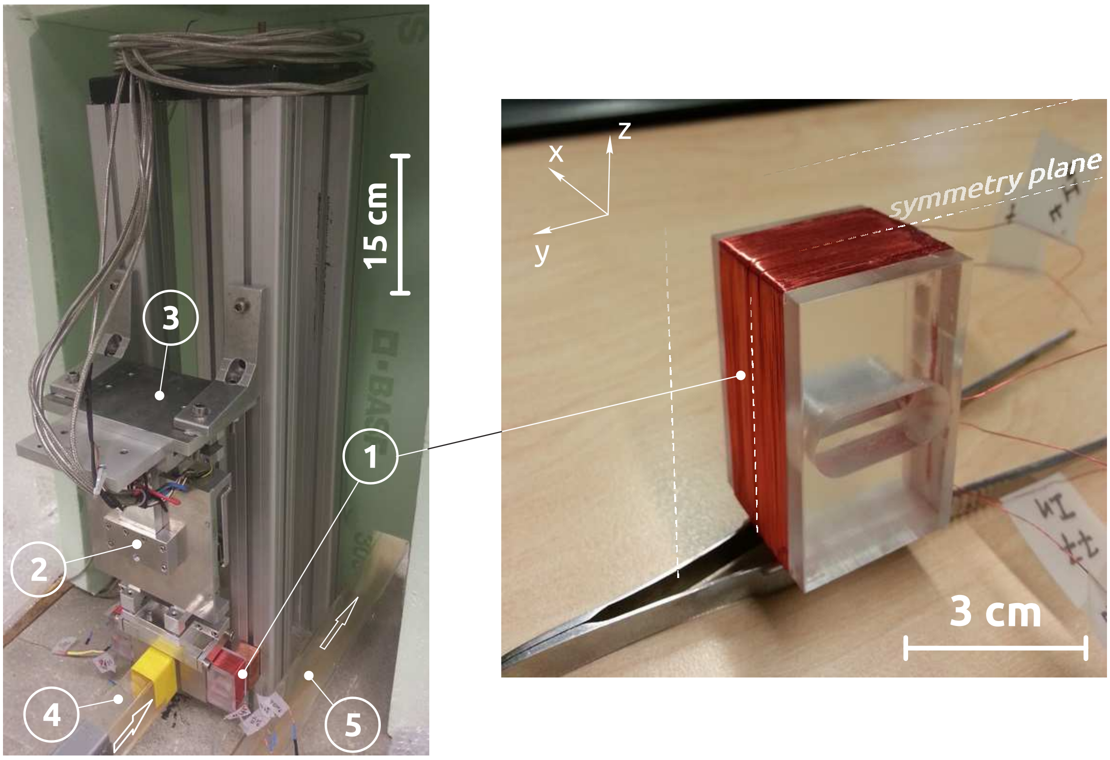

Figure 4.1: Image of the direct compensation EMFC balance FMS integrated on the prototype channel (left) and the sample of the rectangular coil used to generate the compensation forces (right). (1) - rectangular coil, (2) EMFC balance and attached to it magnet system, (3) - bearing plate fixed on the supporting construction, (4) - main channel, and (5) - bypass channel.

As implemented for the direct compensation Pendulum FMS, a similar electrical schematic is tailored for both in order to connect the coils to the high-resolution digital current source and to connect the electronics of the positioning sensor to the high precision digital multimeter. To simplify the mechanical adjustment procedure and achieve finer symmetrical positioning, the coils are winded on the mechanical support assuming a symmetry cut plane along both magnets, so that the starting turn of each coil coincides with each other and with this symmetry plane (cf. figures 3.8 and 4.1 right), and every subsequent turn is spread consecutively on both sides of the symmetry plane. Thus, the rectangular coils fixed from both sides of the magnet system face each other symmetrically. The rectangular coils with an equivalent number of turns are connected in parallel and share a single value of the applied electric current from one channel of the current source. Based on such design, a similar connection can be provided to any other pair of rectangular coils or to the single coil of the EMFC balance.

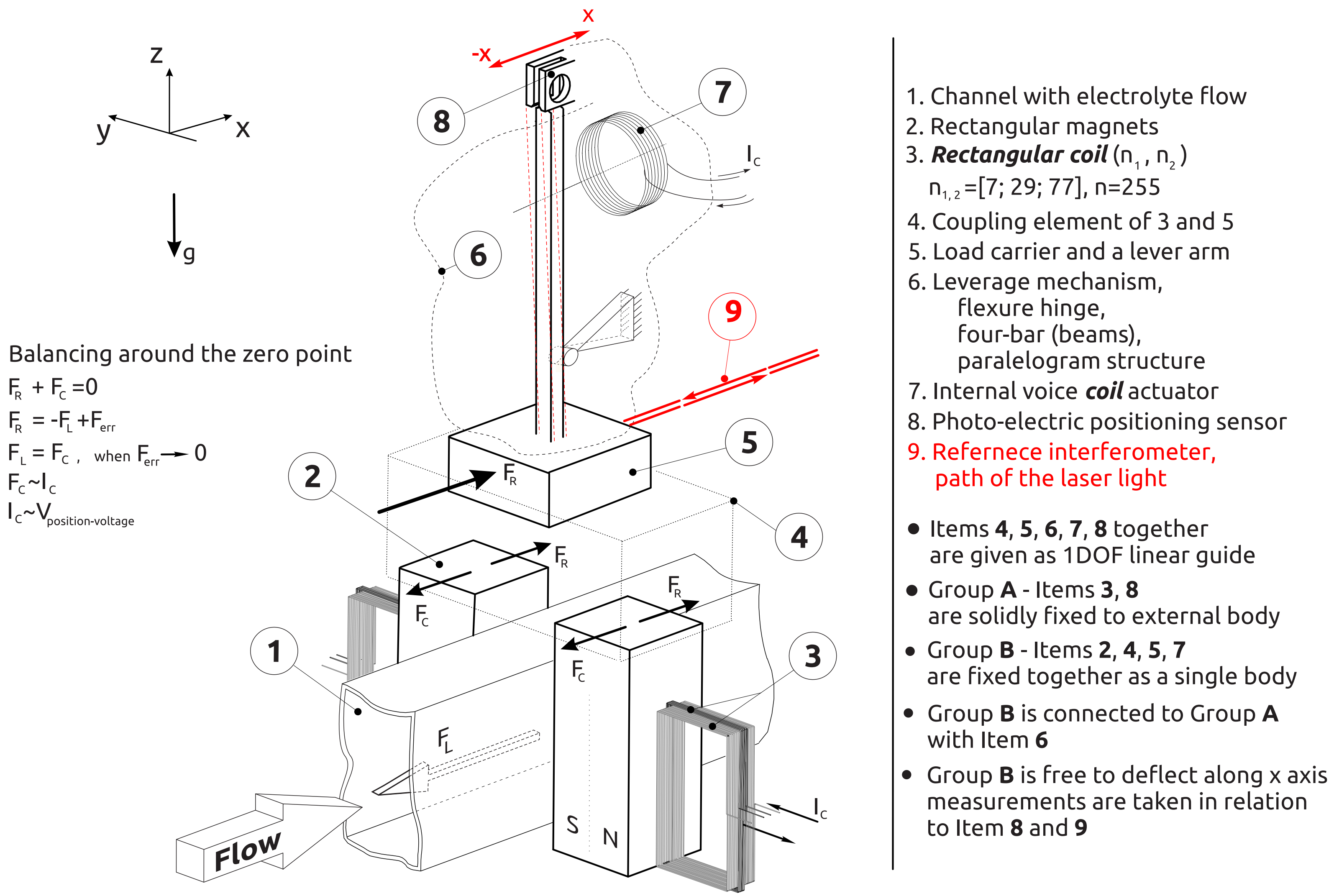

Balancing around the zero point

$F_R + F_C = 0$

$F_R = -F_L + F_{err}$

$F_L = F_C$, when $F_{err} \longrightarrow 0$

$F_C \sim I_C$

$I_C \sim V_{position\text{-}voltage}$

1. Channel with electrolyte flow
2. Rectangular magnets
3. ***Rectangular coil*** (n_1, n_2)
   $n_{1,2}$=[7; 29; 77], n=255
4. Coupling element of 3 and 5
5. Load carrier and a lever arm
6. Leverage mechanism,
   flexure hinge,
   four-bar (beams),
   paralelogram structure
7. Internal voice ***coil*** actuator
8. Photo-electric positioning sensor
9. Refernece interferometer,
   path of the laser light

- Items **4**, **5**, **6**, **7**, **8** together are given as 1DOF linear guide
- Group **A** - Items **3**, **8** are solidly fixed to external body
- Group **B** - Items **2**, **4**, **5**, **7** are fixed together as a single body
- Group **B** is connected to Group **A** with Item **6**
- Group **B** is free to deflect along x axis measurements are taken in relation to Item **8** and **9**

Figure 4.2: Simplified mechanical schematics of the direct compensation EMFC balance force measurement setup.

In order to maintain simultaneous operation with two different circuits, the second channel from the current source is used. Both channels have relatively small output impedance; therefore, when one channel is programmed to stay out of operation in the electric circuit, some parasitic flow of the electric current remains. Furthermore, during motion of the magnet system in the coils, some eddy currents can be generated that can also influence the measurements. In order to avoid this redundant interference, one of the circuits should be physically disconnected from the unused channel while the second channel is operating, or some additional electronic components should be integrated. Otherwise, this small electric current produces some parasitic electromagnetic force that acts on the magnet system or the magnet of the EMFC balance dependent upon the specific coil which is connected through the electric circuit to the passively operating channel. However, the dynamic characteristics of the compensation measurements are analysed extensively for both connection states (connected and physically disconnected) in order to facilitate further precision measurements and ensure the accuracy of the calibration measurements. Later in this chapter (cf. figures 4.8 and 4.9 in section 4.3.1), it is shown that because of this passively connected electric circuits in the FMS, an additional amount of dumping factor is introduced that is far to be influential on the measurement accuracy or precision (under the scope of interest considered in the current work). Figure 4.1 presents the images of the actual mechanical construction of the direct compensation EMFC balance FMS arranged on the prototype channel (left) and the sample of the rectangular coil (right). In the mechanical construction image, the item designated as (4) is the main channel where the electrolyte flow interacts with the magnetic field of the magnet system, whereas (5) is the bypass channel which is blocked when the Lorentz forces are measured. Conversely, it is possible to block the main electrolyte channel by redirecting the electrolyte flow only through item (5).

Figure 4.2 illustrates the simplified mechanical schematics of the direct compensation EMFC balance FMS. The corresponding designations of the main components are presented in the right side of the figure. The physical principle of the measurements is formulated by the equations provided in the left side of the figure. Several mechanical parts are given in simplified form in order to highlight only the main operational characteristics of the setup.

Note that the design of the direct compensation EMFC balance FMS is the geometrical counterpart of the direct compensation Pendulum FMS to some extent; in particular, the rectangular coils and their arrangement within the reference frame of the magnet system are completely identical to the design presented in Figures 3.2 to 3.5 and 3.8. Thus, the theoretical expressions derived in section 3.2 can be used similarly in order to calculate the produced compensation forces that act on the magnet system (cf. equations 3.11 and 3.12).

4.3 Measurements

This section presents the measurement results on the direct compensation EMFC balance FMS using the internal positioning sensor of the EMFC balance. In addition, laser interferometer measurements are obtained to determine the stiffness of the system. In order to identify the performance and dynamic behaviour of the direct compensation EMFC balance FMS, a reference electric current is applied to the internal coil of the EMFC balance and the rectangular coils adjacent to the magnet system in various operational regimes. Initially, the open-loop operation mode is employed, based on which the closed-loop system is set up.

4.3.1 System identification and open-loop

Setting up the measurements. In order to identify the system characteristics, a DC current is applied to the rectangular coil and the coil integrated in the EMFC balance. Measurements from the positioning sensor and interferometer are recorded in the open-loop mode. A typical measurement made in this open-loop operation mode is presented in figures 4.3*c)* and 4.3*d)*.
Data obtained from the interferometer is shown in nm. The measurement signals (cf. figure 4.3 *c)* and *d)*) are symmetrically opposite because the interferometer measures the deflection of the magnet system directly, whereas the positioning sensor measures the deflection of the magnet system proportionally and in opposite direction because the force is exerted on the opposite side of the lever arm of the EMFC balance. Similar measurements are made for the coil of the EMFC balance and for the case where the rectangular coil is connected to the electric circuit by 7 and 29 turns. The mean values and standard deviations are computed at each step once the settling time of the EMFC balance is reached, similar to the computational scenario presented in section 3.4.1. In addition, for the same amount of applied electric current, the effective force is higher when the number of turns is large. The characteristic slope of the measured voltage over the applied electric current or the measured deflection over the applied electric current is larger when the coil is connected by 77 turns. Sensitivity of the direct compensation EMFC balance FMS against the applied electric current for each number of turns is presented in figure 4.4.

Table 4.2: Mean values and standard deviations of the measured sensitivity constants of the direct compensation EMFC balance FMS. In reference to figure 4.4.

coil	V/I in V A^{-1}		relative	x/I in mm A^{-1}		relative
	mean	std	error	mean	std	error
rectangular						
n=7	61.641	6.87	11.1 %	0.2260	0.0177	7.8 %
n=29	268.493	4.214	1.6 %	1.0328	0.0275	26.6 %
n=77	790.09	8.81	1.1 %	3.0126	0.0021	0.07 %
internal of the EMFC balance	128 563.754	1487.01	1.2 %	489.3830	79.969	16.1 %

Figure 4.4 shows the force constant factor $(l \cdot B)$ of the direct compensation EMFC balance FMS for each number of turns in the coil in terms of V/I and x/I quanti-

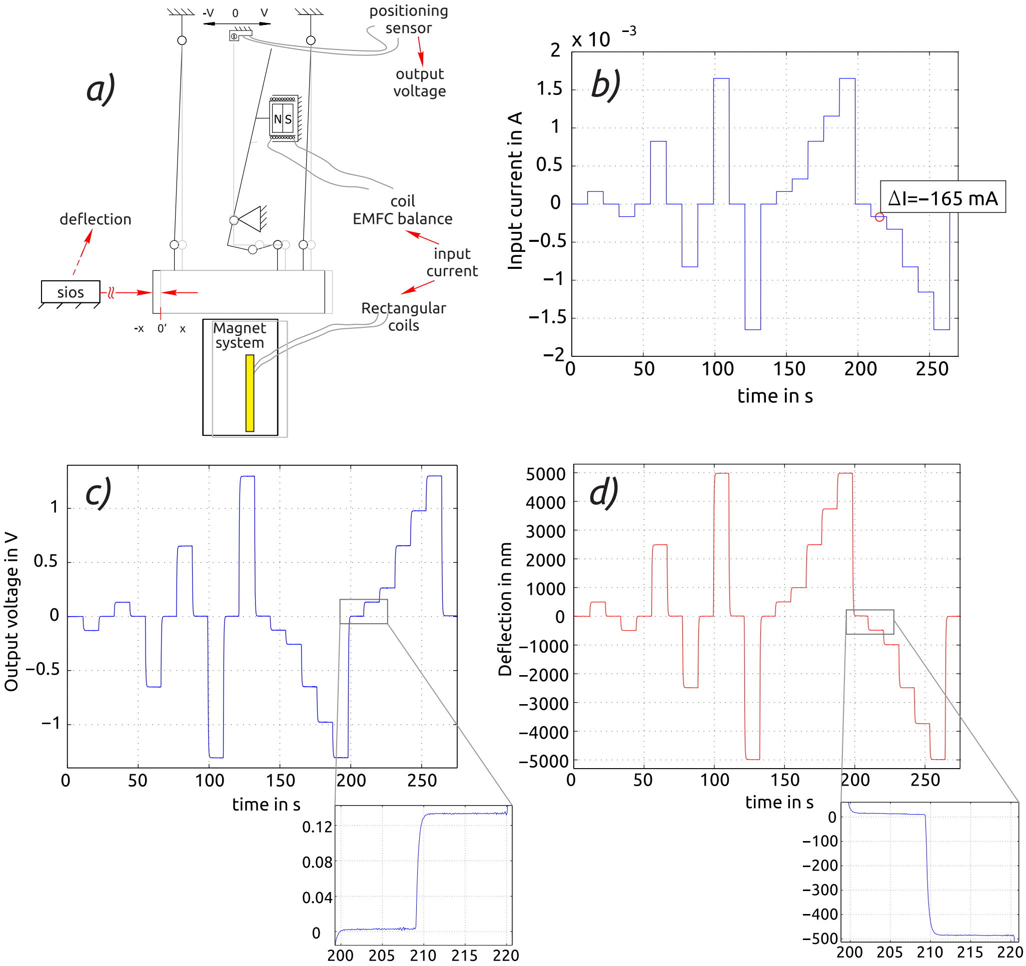

Figure 4.3: Typical response of the direct compensation EMFC balance FMS against the electric current applied to the coils. In this example, the coil is connected by 77 turns. a) Measurement schematics, b) electric current applied to the coil, c) deflection measured by the positioning sensor, and d) deflection measured by the interferometer.

ties. In terms of SI units, these expressions read as $\mathrm{V\,A^{-1}}$ (left) and $\mathrm{m\,A^{-1}}$ (right). Figure 4.5 presents the calibration factor of the deflection measurements by the positioning sensor over the same deflection measurements by the interferometer.

Note that figure 4.5 presents the calibration factor of the deflection measurements, measured directly by the interferometer and positioning sensor as a result of the proportional deflection of the lever arm. Based on the approximate value of the proportionality factor of the lever arm (1:≈5.41), the calibration factor of the positioning sensor can be determined by dividing the values presented in figure 4.5 over ≈5.41, approximately.

In figure 4.6 the simplified schematics of the deflection measurements is presented. According to the measured results in the approximate value of the calibration factor of the positioning sensor can be determined. The deflection measurements of the

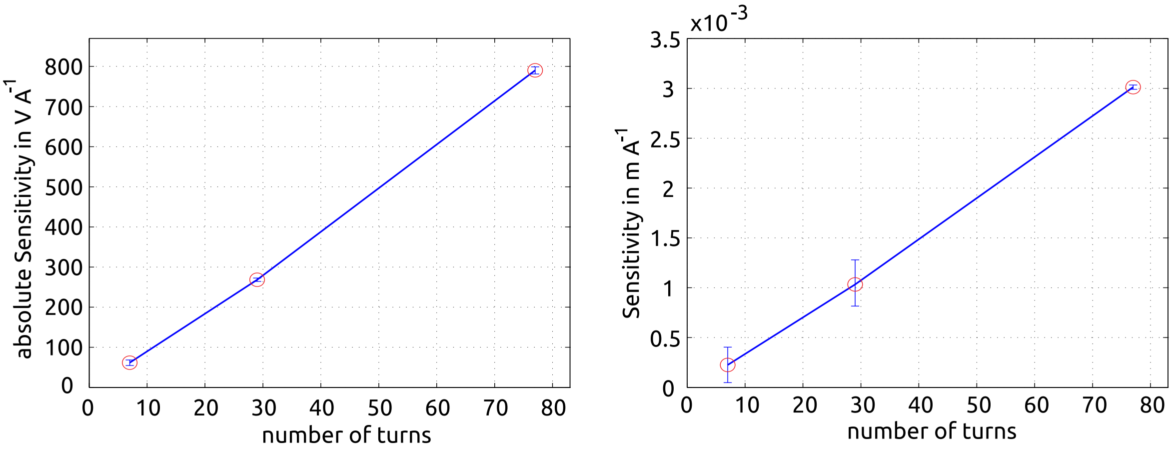

Figure 4.4: Measured sensitivity constant of the direct compensation EMFC balance FMS for each number of turns in the rectangular coil. Measurements are obtained by the positioning sensor (left) and interferometer (right).

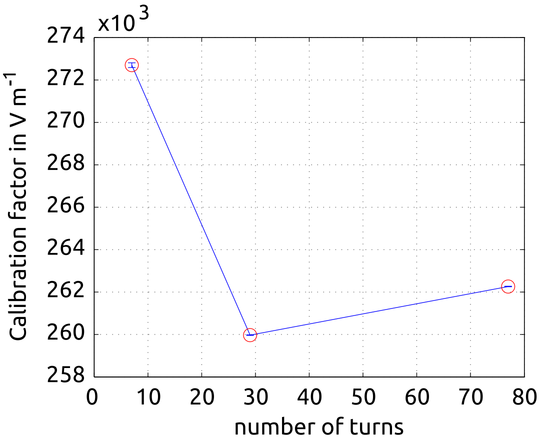

Figure 4.5: Calibration factor of the deflection measurements (cf. figure 4.4).

lever arm are made by interferometer on its shorter side; therefore, the measured value should be multiplied by the proportionality factor of the lever arm to obtain x_2. Thus, the V/x_2 represents the unknown calibration factor of the positioning sensor.

$$\frac{y_2}{x_2} = \frac{y_1}{x_1} \tag{4.1}$$

$$x_2 = x_1 \cdot \frac{y_2}{y_1} \approx x_1 \cdot 5.41 \tag{4.2}$$

Thus, based on values given in table 4.2 and figure 4.5 the calibration factor of the

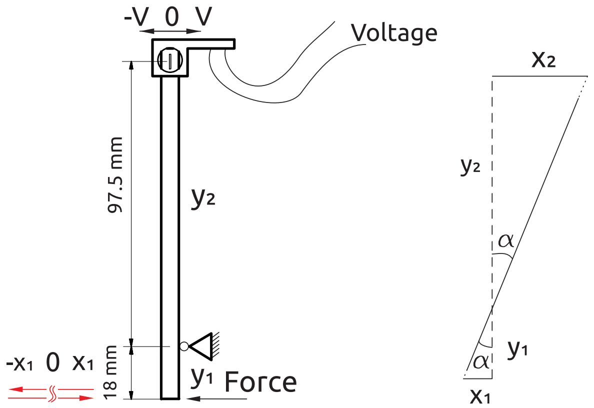

Figure 4.6: Simplified schematics of deflection measurements on the proportional lever arm, showing the calculation principle of the calibration factor for the positioning sensor in terms of V/m. (cf. figures 4.4 and 4.5).

positioning sensor results

$$\frac{V}{x_2} = \frac{V}{x_1 \cdot 5.41} \approx 48.876\,\mathrm{kV\,m^{-1}} \tag{4.3}$$

The combined uncertainty is computed by equation 4.4 based on the values given in table 4.2.

$$\frac{uc(C_{Vx})}{C_{Vx}} = \sqrt{\left[\frac{uc(V)}{V}\right]^2 + \left[\frac{uc(x)}{x}\right]^2} \tag{4.4}$$

In these measurements, the interferometer is fixed on a separate mechanical ground, whereas the positioning sensor, lever arm, and rectangular coils are fixed together on the other mechanical ground. Therefore, in equation 4.4, the combined relative uncertainty of the calibration factor is computed by the method of summation in the quadrature for division. In the future, these values and the mean values, both presented in figure 4.5, can be potentially improved when *a)* the positioning sensor and interferometer are fixed on the same mechanical ground, and *b)* the sampling frequencies of both measurements are sufficiently high to apply filtering or complete data analysis techniques.

Estimation of the transfer function. In order to estimate the transfer function of the direct compensation EMFC balance FMS, a different approach is chosen compared with the analyzes provided in section 3.4.1. In that section, the system response is analyzed against the electric current applied to the rectangular coils as a step-wise function; furthermore, the transfer function of the direct compensation Pendulum FMS is obtained based on theoretical computations. In this section, for the direct compensation EMFC balance FMS, the system response is analyzed against the electric current applied in the form of a sine wave. A set of measurements is made for each coil, and the frequency spectrum is specified similarly for all cases within the range of interest (on logarithmic space by 500 bins within f=10^{-2} Hz to 10^2 Hz).

For this procedure, a necessary algorithm is developed in order to guide the measurements in scrupulous manner, and respectively, to analyze the sequence of the resulting measurement data. Initially, the following parameters are defined in order generate the sine wave function: the frequency range f_0 to f_{end}; separation between the grid points within frequency range Δf, peak-to-peak amplitude of the applied electric current to the coil ΔI; signal length Δt_i. Subsequently, an electric current is generated through the digital current source by the following function:

$$I_i(f_i) = \Delta I \sin\left(2\pi f_i \; \Delta t_i\right) = \Delta I \sin\left(2\pi\left[f_0 + i \cdot \Delta f\right] \Delta t_i\right) \tag{4.5}$$

and it is applied to the coil. Furthermore, the voltage of the positioning sensor is measured during Δt_i time, which is related to the f_i frequency in order to provide at least 4 to 5 full oscillation periods. After one cycle of such measurements, a new function is generated for the next frequency components $f_{i+1} = f_0 + (i+1) \cdot \Delta f$ (increasing values of the frequency along the grid line specified initially). At each subsequent (i) iteration, FFT of the measured response (voltage) is obtained, and from this, the magnitude at the given f_i frequency component (during the i-th iteration) is averaged within ±3 % accuracy. From the series of such measurements, one of the typically measured data sets is presented in figure 4.7 for the frequency of approximately 1 Hz. Finally, once all iterations are finished, the complete magnitude diagram of the Bode plot can be obtained.

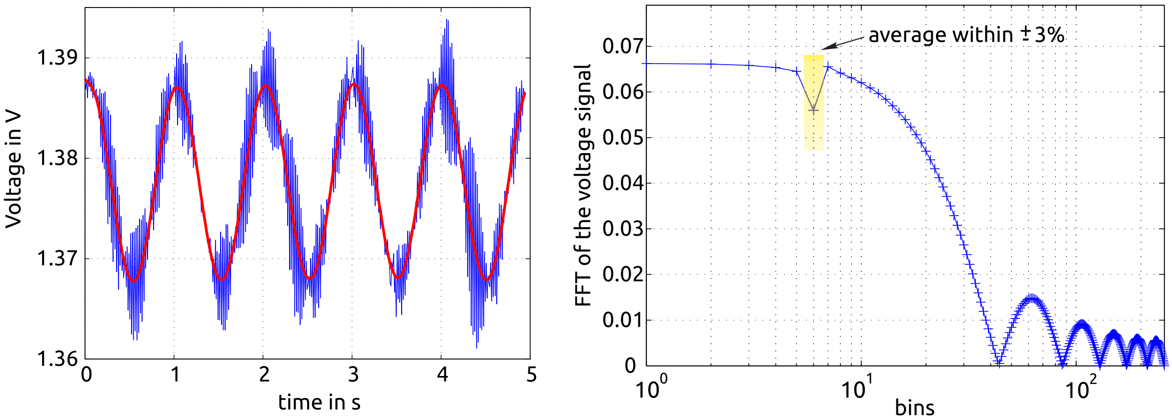

Figure 4.7: An example of the system response of the direct compensation EMFC balance FMS when the electric current in sine wave form is applied to the coil with 77 turns. The parameters of the applied electric current are Δt=5 s, f_{i+n}=1.0093 Hz and ΔI=$50 \cdot 10^{-6}$ A. Measured voltage signal from the positioning sensor (left) with 1.378 V offset voltage and FFT of the filtered voltage signal (right).

Thus, the characteristic Bode magnitude diagram is obtained for all connection cases (rectangular coils n=7, 29, and 77 and internal coil of the EMFC balance). Figure 4.8 shows the magnitude spectrum of all four configurations, and computations are performed based on the ratio of the measured voltage of the positioning sensor over the peak-to-peak amplitude of the electric current applied to the coils, as $20 \cdot \log(V/I)$. The amplitude of the applied electric current is chosen as 50 µA for all four cases. However, an additional test measurement is conducted for 5 mA with rectangular coil n=7.

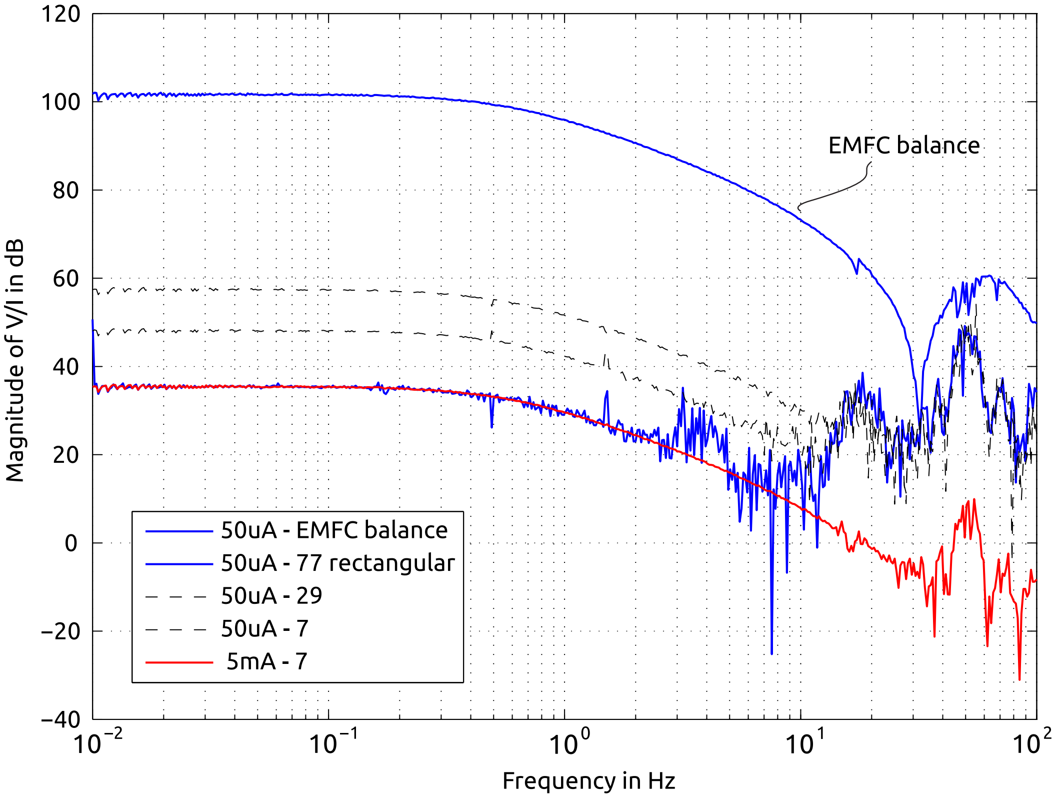

Figure 4.8: Bode magnitude diagram of the EMFC balance FMS.

As expected, the gain of the EMFC balance coil is higher than that of the rectangular coils; the difference between the rectangular coil with n=7 turns and the coil of the EMFC balance is approximately 65.9 dB. Notice that at the higher frequencies rectangular coils have a similar noise characteristic for the same amplitude of the applied electric current (50 µA), whereas for different amplitudes (50 µA-blue and 5 mA-red line), the measurements on the same n=7 coil shows slightly different characteristics. In general, the measurements obtained for each coil show a similar dynamic characteristic, and more importantly, at the main plateau up to 0.56 Hz, the Bode magnitude diagrams are the counterparts of each other and only differ by their gain factors.

As noted earlier, when one of the rectangular coils or the coil of the EMFC balance is connected to the current source, all other electric circuits should be physically disconnected. That which is not operating, but is still connected to the common circuit (passively), can influence the measurements because of some parasitic electric currents that flow in the electric circuit. In particular, in the measurement scheme, an additional amount of dumping factor is introduced. To estimate this dumping factor, the same measurements are repeated while one of the unused coils is connected to the second channel of the current source. Figure 4.9 presents the results of the system response, similar to figure 4.8, but normalized together to the zero gain.

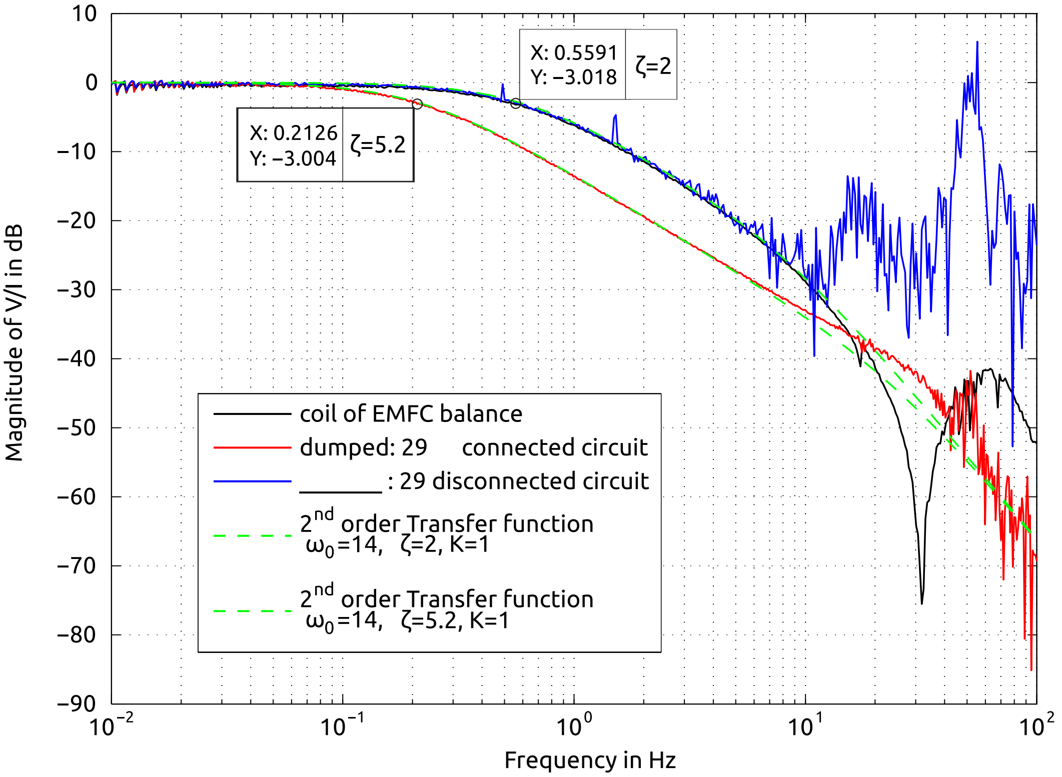

Figure 4.9: Comparison of normalized Bode magnitude diagrams between the coil of the EMFC balance and rectangular coil with n=29 turns (solid), and corresponding transfer functions (dashed).

The results presented show three different measurements, when:

1. only the coil of the EMFC balance is connected to the circuit (black),
2. only the rectangular coil with n=29 turns is connected to the circuit (blue), and
3. both coils are connected simultaneously (coil of the EMFC and rectangular coil with n=29 turns), but the measurements are obtained for the rectangular coil with n=29 turns (red).

It is tested all combinations of simultaneously connected coils; however, as figure 4.9 shows, the combination of any of the rectangular coils with the coil of the EMFC balance has the most largest variation compared with the single-coil operation regime. This is conditioned by the fact that the coil of the EMFC balance has the largest gain factor (cf. figure 4.8).

4.3.2 Closed-loop and calibration

The **closed-loop** operation of the direct compensation EMFC balance is maintained similarly to that developed for the Pendulum FMS. The operational schematic remains the same as described in detailed in section 3.4.2. The only differences concern the control parameters (K_i, K_d, and K_d) of the PID controller, which are tuned separately and are slightly different for each coil (n=7, 29, 77); the gain factors are also different for each coil. Based on the results presented in figure 4.8, the gain factors are summarized in table 4.3.

Table 4.3: Gain factors of the transfer function for each coil used in the direct compensation EMFC balance FMS.

coil	Gain, K
rectangular	
n=7	59
n=29	255
n=77	745
internal of the EMFC balance	121000

The values in table 4.3 are obtained by averaging the data of the Bode magnitude diagram for 10^{-2} Hz to 0.5591 Hz frequency range (cf. figure 4.8). In general, these values agree with the results presented in table 4.2; however, some numerical discrepancy still exist, which can be analyzed in details in the future.
A simulation model is used in order to generate the necessary control parameters (cf. figure 4.10).

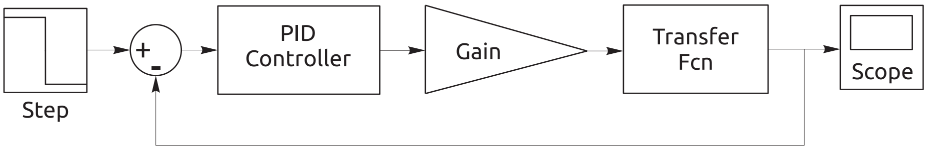

Figure 4.10: Simulink block scheme for the direct compensation EMFC balance FMS.

The cutoff frequency of the EMFC balance is f=0.5591 Hz, obtained in section 4.3.1 from the open-loop operation regime. To be conservative, the settling time of the EMFC balance in the open-loop operation regime is estimated at 2 s, (for example see figure 4.3). Because of the low sampling frequency of the closed-loop operation scheme, random mechanical vibrations, and high inertial forces of the system, the best-achieved value of the settling time during the closed-loop measurements results approximately ≈ 1.4 s.

Calibration of the direct compensation EMFC balance FMS is performed based on comparative measurements against the internal coil of the EMFC balance. The value of the calibration factor of the EMFC balance was determined earlier, and it is known from [15] to be equal to $5.1075\,\mathrm{mA\,N^{-1}} \pm 0.0023\,\mathrm{mA\,N^{-1}}$; however, in later analyzes it was redefined to $5.01\,\mathrm{mA\,N^{-1}}$ by C. Diethold. From this value and that value obtained from the open-loop calibrations using the interferometer measurements (cf. table 4.2: $489.3830\,\mathrm{mm\,A^{-1}} \pm 07.9969\,\mathrm{mm\,A^{-1}}$), the stiffness of the EMFC balance FMS can be determined to by $407.861\,\mathrm{N\,m^{-1}} \pm 24.959\,\mathrm{N\,m^{-1}}$, or in other units, $1.5525\,\mathrm{mN\,V^{-1}} \pm 0.0013\,\mathrm{mN\,V^{-1}}$, which is determined from the measurements by the positioning sensor.

Thus, by applying a known electric current to the internal coil of the EMFC balance, it is possible to generate a known reference calibration force. From here, by compensating this reference force to the zero position with an applied electric current to the rectangular coils it is possible to determine the calibration factor of the rectangular coils. Numerically, the calibration constants can be calculated based on the values provided in table 4.2 for the open-loop operation regime.

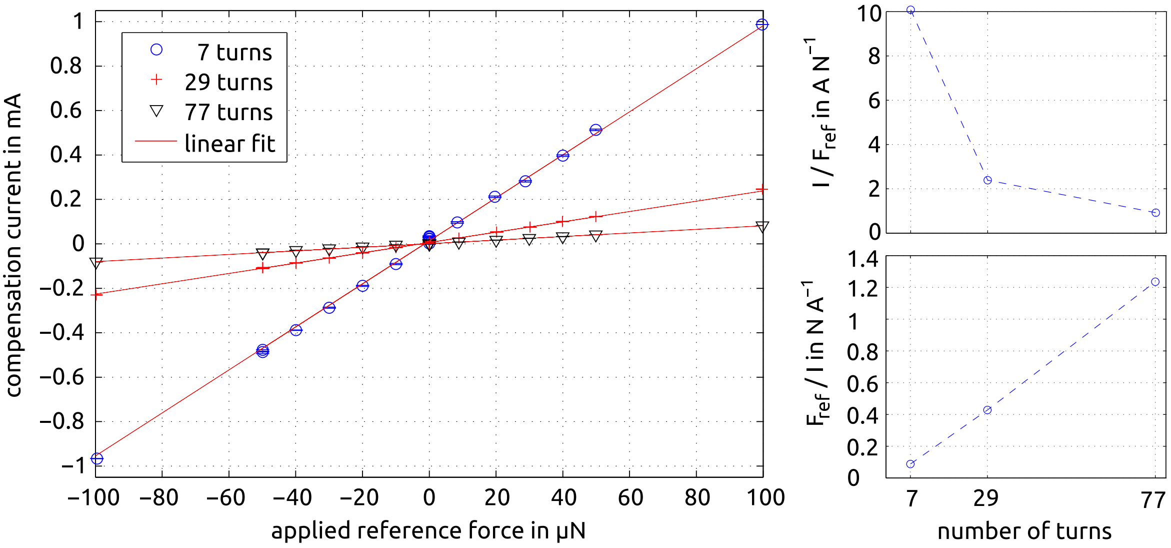

Figure 4.11: Calibration measurements of the direct compensation EMFC balance FMS for each rectangular coil (n=7, 29, 77) against the reference forces applied by the coil of the EMFC balance. Compensation current as a function of the applied reference force (left) and calibration factor in terms of compensation current over the reference force (or reference force over the compensation current) as a function of the number of turns in the coil (right). Figure 4.13 presents an example of the actual measurements for all rectangular coils.

However, a new set of measurements is made in order to provide a full sensitivity

slope of the calibration measurements (compensation currents) against the reference currents (forces) applied to the internal coil of the EMFC balance. The procedure for the calibration measurements in the closed-loop operation regime is as follows: a known electric current is applied in step-wise form to the internal coil of the EMFC balance, thereby generating a reference force that acts on the longer side of the lever arm. The resulting deflection of the lever arm is compensated back to the zero position by an electric current applied to the rectangular coils. The mean values, and respectively, the standard deviations, are collected once the settling time at each step is reached. Measurements are obtained for each coil (n=7, 29, 77) and all obtained results are summarized in figure 4.11.
Table 4.4 compared the results obtained by the calibration measurements in the closed-loop operation regime with the values of the numerical calculations. The numerical calculations are performed using the mean values of the positioning sensor and interferometer measurements in the open-loop operation regime (cf. table 4.2).

Table 4.4: Calibration factors of the direct compensation EMFC balance FMS for each rectangular coil (n=7, 29, 77) in N A^{-1}. Comparison of the results obtained from the closed-loop calibration measurements with the numerical calculations based on the open-loop measurements.

rectangular coil	measured in closed loop	numerically calculated from open-loop by Positioning sensor	interferometer	mean
n=7	0.0983	0.0957	0.0922	0.0939
n=29	0.4275	0.4168	0.4212	0.419
n=77	1.2375	1.2266	1.2287	1.2276

In addition, these results are compared in figure 4.12 with the full analytical solution similar to figure 3.18. Here, it will not be repeated the relevant theoretical argumentation discussed and derived in detail in chapter 3, section 3.2. The computation method remains valid and similar computations for the $F_C^{2\alpha+1}/I_z$ term by equation 3.12 should be considered for an increased amount of turns. This leads to an increased amount of computations of the $\int_{l_0}^{l_{end}} dz \sum_{\alpha=0}^{n} B_y^{\alpha}$ term for each n-th $(n = 2 \cdot \alpha + 1)$ turn of the rectangular coil, also in respect to different geometrical coordinates.
The percentage difference is calculated as

$$\frac{\text{Analytic} - \text{Experiment}}{\frac{1}{2} \cdot \sum(\text{Analytic} + \text{Experiment})} \times 100\% \tag{4.6}$$

According to this comparison between the analytical solution and measured results, some discrepancy still exists. However, the difference between these values decreases once the number of turns in the coils increases, and eventually, in accordance with their linear fits, converges for a higher number of turns (above 1000 turns cf. figure 4.12). In addition, another important conclusion can be drawn here. In terms of

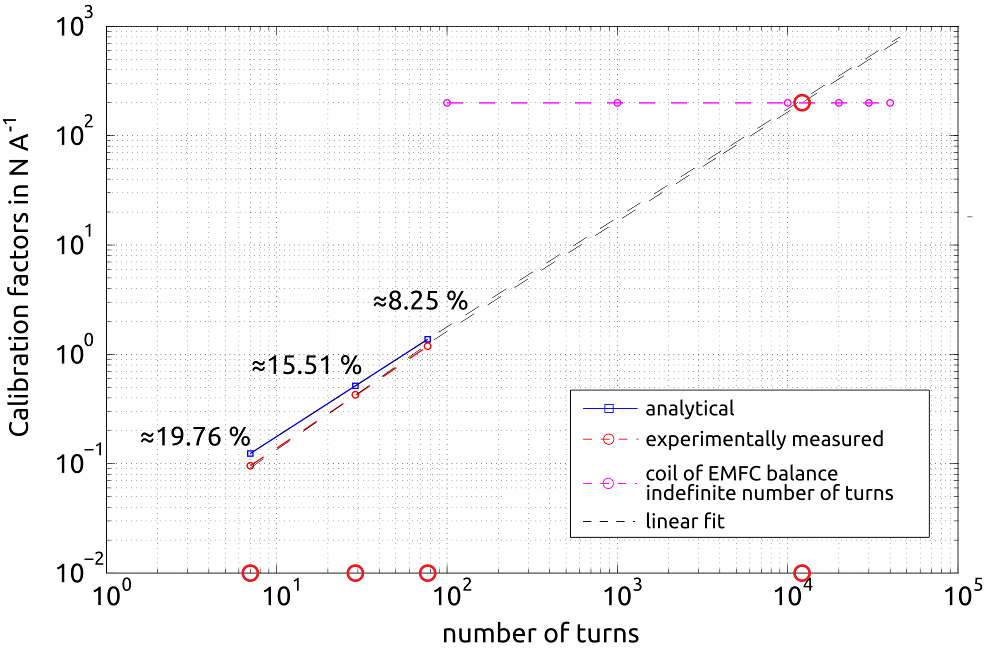

Figure 4.12: Comparison of the calibration factor obtained from an analytical solution and calibration measurements.

these established geometric conditions of the rectangular coil, approximately 11000 to 12000 turns is required in order to reproduce the performance characteristics of the coil of the EMFC balance (cf. red circles and convergence of linear fits with the calibration factor of the EMFC balance in figure 4.12).

In all further practical measurements (cf. figure 4.13), the mean values of the calibration factors obtained from the open-loop calibration measurements are used (cf. table 4.4 column "mean") with a generalized value of combined relative uncertainties $\pm 0.004\,\mathrm{N\,A^{-1}}$ for every coil.

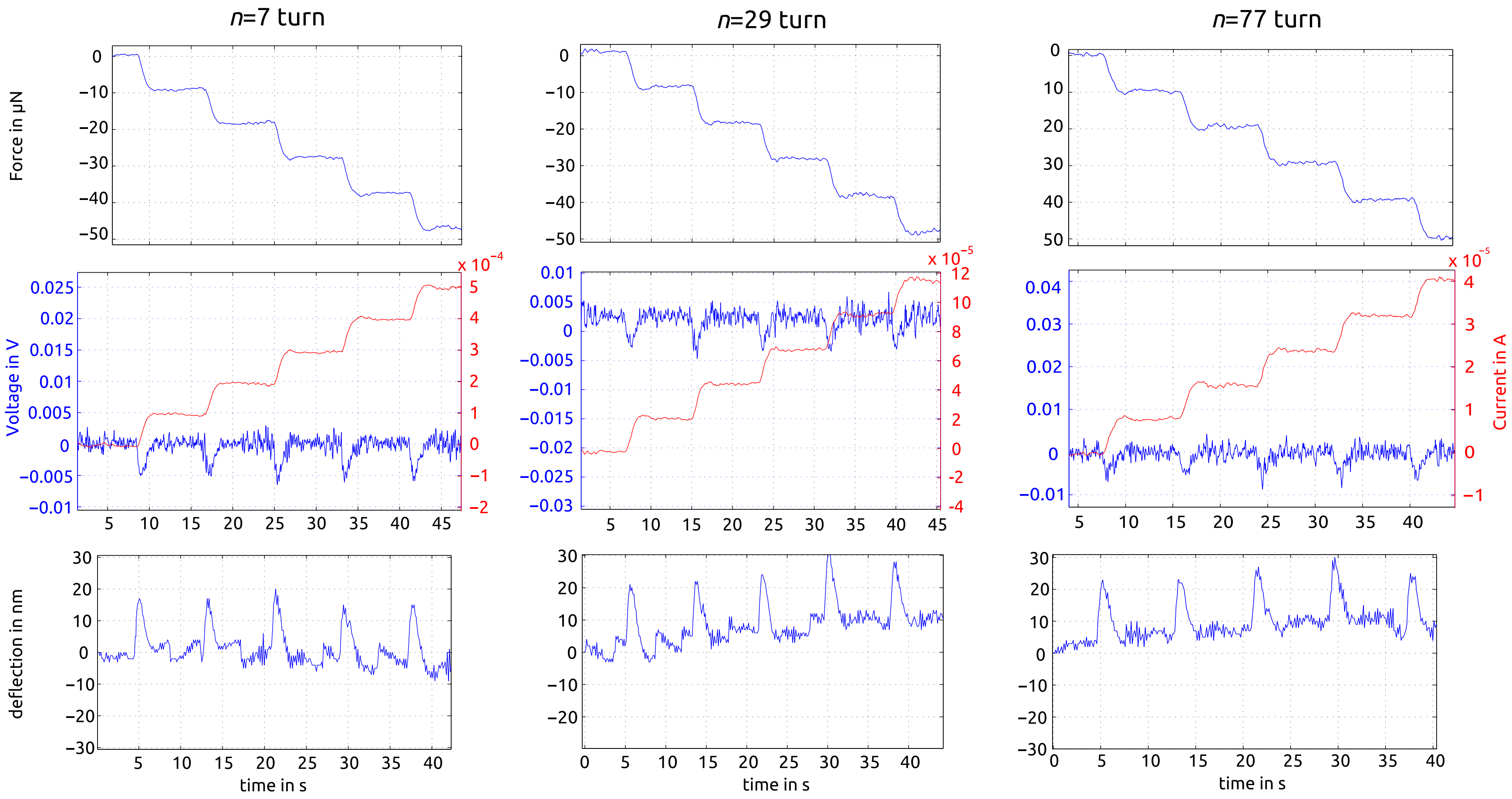

Figure 4.13: A set of calibration measurements in closed-loop. 1st raw is the force values, 2nd measured voltage by positioning sensor (left axis) and the compensation current (right axis) applied to the coils to balance the lever arm at the zero position, 3rd reference measurements of the zero point by interferometer. Each column corresponds to a single measurement process for each of rectangular coils n=7, 29 and 77 turns.

4.3.3 Double coil operation and Fuzzy controller

The summary in section 3.5 indicates that the direct compensation Pendulum FMS has several limitations. In particular, the sensitivity of the compensation measurements is small and the operation range is conditioned by a numerically predefined limit of the electric current applied to the coils. This programmable value of ±1 mA leads to the maximum compensation forces of approximately ±250 µN for the maximum available turns (n=15) in the coil. By the new design presented in this chapter for the direct compensation EMFC balance FMS, the rectangular coil with increased amount of turns (n=77) compensates approximately 1.2276 mN forces for the same 1 mA of applied electric current. Thus, by the new measurements with the newly developed coils (n=7, $\mathbf{29}$, $\mathbf{77}$) on the EMFC balances, an obvious improvement follows as an extended range of compensation force measurements, while the magnitude of the applied electric currents is the same. However, in some cases, there is a necessity to find a tolerable balance between the magnitude of the applied electric current and maximum number of turns in the coil. For this reason, a measurement concept is designed where two different rectangular coils (with a different number of turns) are combined simultaneously during one measurement process. It is proposed to demonstrate the practical implementation possibilities of applying two rectangular coils in the compensation measurements; such coils are switchable and have two different operation ranges for the same range of applied electric current. The concept is illustrated in figure 4.14.

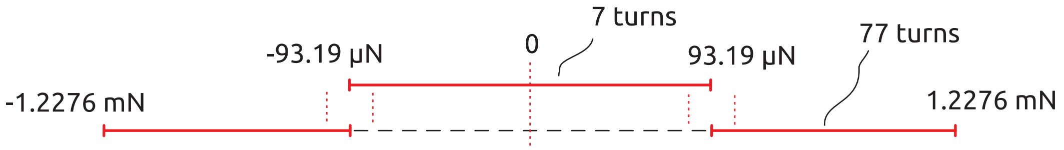

Figure 4.14: Representation of merged ranges while operating with two rectangular coils simultaneously.

This is called the double-coil operation regime or double-force compensation method [62]. The validity of the measurements when two rectangular coils are connected to the circuit simultaneously is shown in section 4.3.1 (cf. figure 4.9). In order to maintain continuous measurements, a relatively simple fuzzy PID controller is developed based on fuzzy logic [63–65]. A single logical condition is set within the controller as a threshold electric current of I_{lim}=1 mA to switch the control loop between the electric circuits of different rectangular coils. Both rectangular coils are tailored similarly, but connected independently to the current source in the electric circuits, and similar control schematics are employed as described in section 4.3.2. There are various different possibilities to set a threshold condition, for instance one of the other practical conditions of interest can be chosen as the value of the absolute error of the position sensor.

The full block diagram of the controller is presented in figure 4.15.

In following, one possible strategy of the fuzzy controller operation is described: the custom-developed (MATLAB) function checks whether C1 controller generates I_{coil}

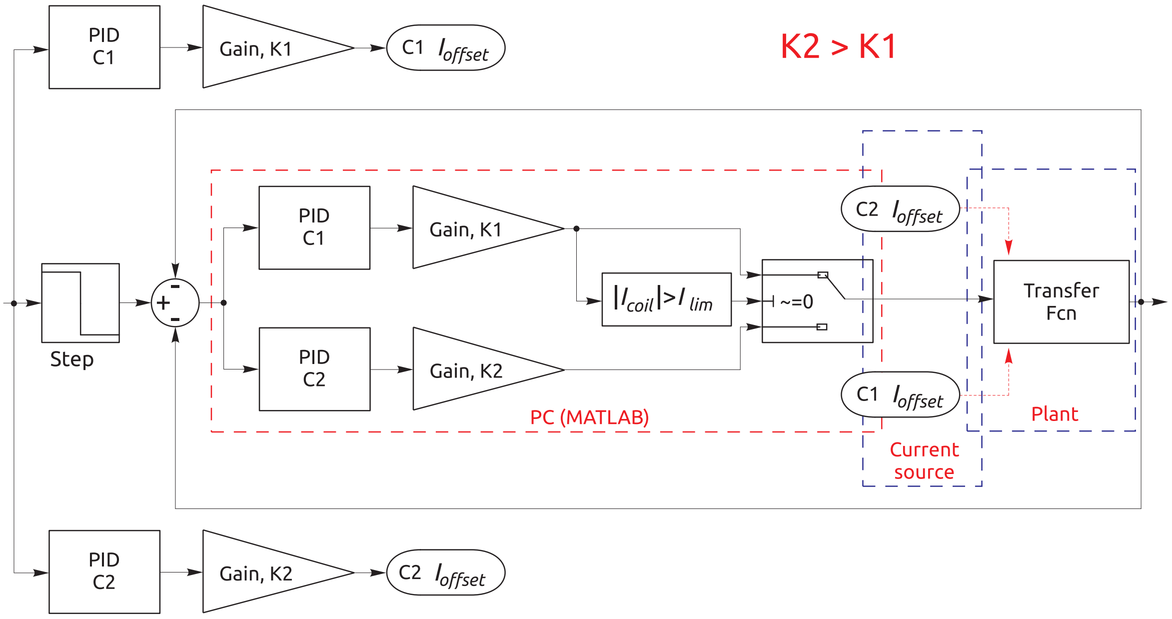

Figure 4.15: Block diagram of the implemented fuzzy controller.

electric current (controller output) that is lower than the allowed boundary I_{lim}. If I_{coil} is greater than I_{lim}, it switches to the second channel connected to the second (larger) coil. The second coil has the same dynamic characteristics but a higher $l \cdot B$ factor, and thus a higher range of measurements. This provides continuous measurement of the process with a larger coil, which means that several orders of magnitude lower electric current are required. Before changing to the bigger coil, a constant electric current is applied to the smaller coil equal to the initial offset value.

The switching process is reversed, so that during the operation with a larger coil (with C2 controller), C1 controller simultaneously computes the output values. Once the computed value is again below the predefined limit value, the process is switched to C1 controller.

This condition of the fuzzy controller, which is a comparison between the $I_{lim}<$(or $>$)I_{coil} values during each iteration of the control loop, is further defined as a floating boundary in order to provide stable and bumpless transition from C1 to C2, and *vice versa* from C2 to C1. For example, after switching to C1 controller (only before the first iteration), a value of the offset current generated by C2 controller is applied to the coil used earlier; meanwhile, the boundary condition is set to 130 % of the I_{lim} value after the control loop with C1 controller continues the compensation process. In the case of switching from C1 to C2, the offset current is similarly applied to an earlier coil, but the boundary condition is set to 70 % of the I_{lim} value. The illustration of the floating boundary condition is provided in figure 4.16.

Thus, figure 4.17 presents the measurement process where the compensation of forces is perform with two different coils. In the measurement scheme, the coils with the smallest (rectangular coil n=7) and largest force constants (coil of the EMFC

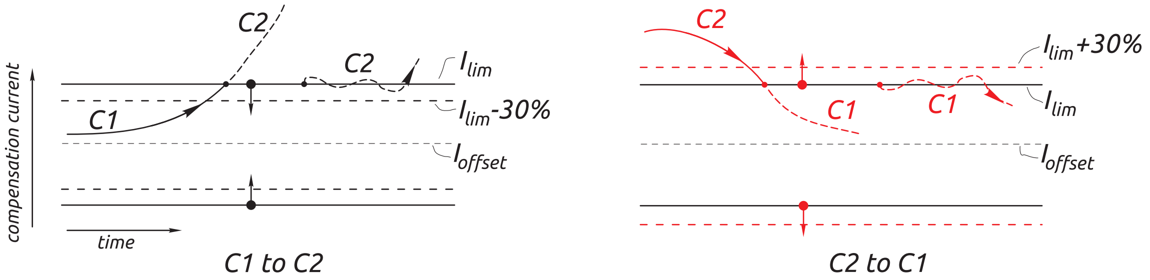

Figure 4.16: Principle of the floating boundary condition employed in fuzzy controller. See figure 4.15 for reference.

balance) are used. In this measurement example, an arbitrary disturbance is created and the effort of the controller is plotted. This is made in order to show a quantitative difference between the magnitude of the applied electric currents to two different coils, and to ensure measurement visualization. Figure 4.17*b)* depicts the controller effort in terms of the values of the applied electric current from the current source to the two different coils. In particular, this shows the use of each individual coil separately and the switching process between them when the value of the generated electric current for the coil with n=7 turns exceeds the limiting predefined border of the controller for the electric current (±1 mA). Because the coil of the EMFC balance compensates the same deflection (force) using the deflection indication of the lever arm in the opposite direction (as an inverted pendulum, cf. figure 4.6), the value of the electric current is inverted from that of the rectangular coil. However, to convert the values of the electric current to the force values, the negative sign of the calibration factor for the coil of EMFC balances should not be missed during multiplication.

From here, the continuous indication of the force signal can be obtained by multiplication of the applied electric current for each coil with the values of their individual calibration factors (cf. figure 4.17*a)*). In 4.17*c)* is presented the measurements of the positioning sensor that show the controller effort in balancing the lever arm of the EMFC balance on the zero point. This also indicates one of the improvements that may be done in the future, particularly when increasing the speed of the control loop (currently it is approximately 50 s to 100 s) the position error can be diminished. In turn, the position error can be considered as a useful means to include it to the fuzzy controller as an additional condition parameter. In generally, the choice of a relevant condition in fuzzy controller is based on practical necessity, and therefore depends explicitly on the possibilities of its practical implementation, as is the case of most common PID controllers.

4.4 Summary

In this chapter, the direct compensation method for measurements of the Lorentz forces is reappraised. In particular, a reexamination of the method was performed on a newly developed system using a different force measurement setup (old EMFC

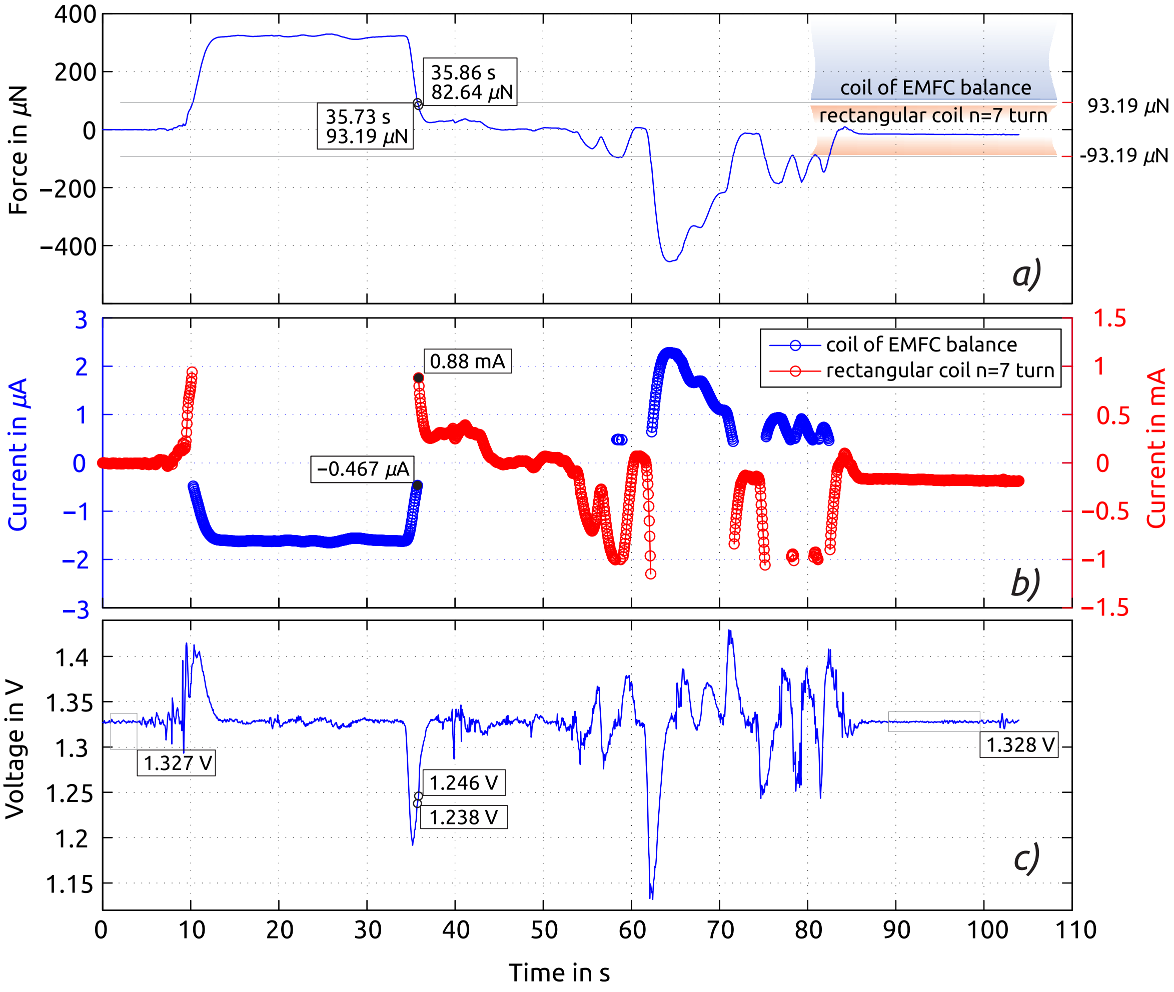

Figure 4.17: An example of the compensation measurements when two different coils are combined in PC-based fuzzy controller. *a)* Force signal, *b)* applied electric current to the coil of the EMFC balance in the left axis (blue) and to the rectangular coil with n=7 turns in the right axis (red), and *c)* measurements by the positioning sensor that show the zero position disturbances.

balance) and different rectangular coils with increased number of turns, compared with the system developed and presented in chapter 3. The foundation for developing the new system evolved as an organic continuation of the results presented in chapters 2 and 3, namely, a combination of the single EMFC balance discussed extensively in chapter 2 and the direct compensation method introduced in chapter 3. In this regard, the primary objective was to set up a robust and relatively simple operating FMS for LFV applications. As discussed in the introduction (cf. section 4.1), the EMFC balance is treated as a 1DoF linear guide in order to provide higher measurement accuracy compared with the Pendulum FMS, which has 3DoF (x, y, xy), but is considered a 1DoF linear guide. In addition, the rectangular coils ware newly manufactured with an additional number of turns in order to provide a higher range of the force measurements and avoid several of the limitations identified during initial development of the Pendulum FMS. Comparison of the measured and theoretically calculated sensitivity factors[2] (cf. figure 4.18) and between the direct compensation Pendulum FMS and direct compensation EMFC balance FMS, shows one of the main improvements achieved when using the EMFC balance and modified coils.

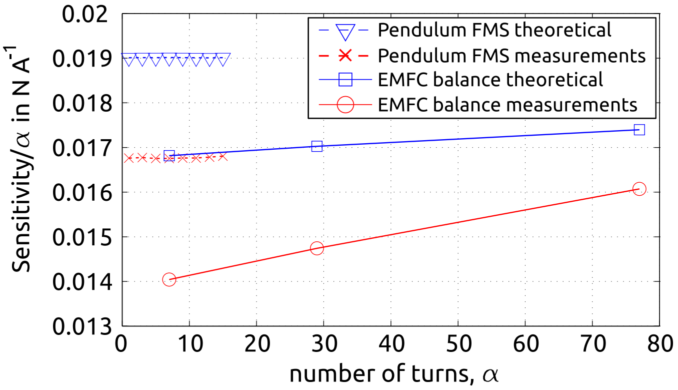

Figure 4.18: Comparison of the sensitivity factors. Refer to figures 3.18 and 4.12.

Compared with the direct compensation Pendulum FMS, resolution of the compensation force measurements is increased from approximately 2 µN to under 1 µN owing the performance of the EMFC balance, which is actually the same value of the old EMFC balance that was reported in [21]. This value can potentially be improved down to approximately 20 nN when considering reference measurements as that presented in chapter 2 during the measurements of the difference signal by dFMS (cf. section 2.3.1) to suppress significant vibration noise. Because of the mechanical arrangement of the new setup, the thermal-drift error is negligible in relation to the magnitude of the mechanical noise. However, several µN force drift still exist during the long-term measurements (approximately 24 hour and longer) at a moderate rate, which was estimated experimentally as being Δ1 µN per 6 hours, or Δ1 µN per 100 mK per 5 to 10 minutes. Here, an important consideration is the possibilities of increasing the resolution of the measurements by decreasing the applied electric current. Measurements made by existing FMSs under existing laboratory conditions show that this consideration does not necessarily lead to an increased resolution of the force measurements because of high mechanical vibration. The second reason is the insufficient accuracy and precision of the voltage measurements from the positioning sensor, which limits the sampling speed of measurements therefore leading to limitations for the controller performance.

Compared with the Pendulum FMS, the range of compensation force measurements increased from ±250 µN to ±1.2273 mN, thus also providing proof of an earlier proposal where an increased in the number of turns in the rectangular coils also in-

---

[2] Throughout the text of this work, this term is variously referred to as calibration factor, force constant and $l \cdot B$ factor. However, its general meaning is the same as the flux integral by the terminology used in development of the *watt balances*. (See for example [36].)

creases the force measurements (almost with a linear relationship cf. figure 4.18). The main non-linearity appears to be caused by the non-uniform distribution of the magnetic field and the choice of geometrical arrangement (parameters) of the rectangular coils.

In addition, a measurement scheme was proposed in section 4.3.3 where two different coils operate simultaneously within a single PC-based fuzzy controller. This digital controller is created by a combination of two standard PID digital controllers, each of which employs the compensation measurements by two different coils. The main intention is to combine two different coils with different ranges of operation during the single and continuous measurement process. The algorithm for the fuzzy controller provides a logical condition in order to check the limiting electric current (to be applied to the coil) upon which one of the coils is switched from the compensation scheme, and the second coil with a different operation range takes the advantage and continues the compensation measurement routine. In order to provide a stable and bumpless transition between these standard PID controllers, the switching condition was extended as if this logical boundary condition is floating once it is being crossed, such as widening upon entering the smaller measurement range or decreasing upon leaving it (cf. illustration in figure 4.14 for the nominal ranges of the rectangular coils with n=7 and 77 turns, figure 4.16 for floating boundaries, and figure 4.17 for the actual measurements results).

In general, the range and resolution of the compensation force measurements (or the measurements of the applied electric current) are strongly subject to the design of the particular setup. In this regard, a detailed parametric study that reveals this dependency can be performed. The study is part of future research whose main goal is to provide optimal configuration for the rectangular coils in the magnetic field of the magnet system (cf. figures 3.3 to 3.5 where the main parameters to be considered are indicated, and equations 3.3 to 3.12, where the starting point of the potential investigation is drawn). Nonetheless, the shape of the magnet system and the magnetization properties (temperature dependency and B-H curve) of each individual permanent magnet have to be considered for complete analyzes, if considering magnet system of Halbach Array type then additional considerations also should be taken in account. Based on these factors and the assumptions made while deriving the analytical expression of the F/I term (equal to $l \cdot B$), some discrepancy is observed between the theoretically calculated values and those obtained from the measurements (cf. figures 3.18, 4.12, 4.18, and table 4.4).

5 Practical Measurements of Lorentz Forces

> the any decision you make will have a
> percentage of regret attached to it
> (own reformulation of the “either/or” —
> conundrum).
>
> Søren Kierkegaard

This chapter is intended to summarize the performance of all developed FMSs when they are applied on the electrolyte channels for practical measurements of the Lorentz forces. The measurements of the Lorentz forces, which are generating in the electrolyte flow (F_L=-F_R), is the ultimate objective for the development of the FMSs. As mentioned in the introduction, in order to characterize the velocity or the electrical conductivity of the electrolyte flow, the Lorentz forces should be measured in sufficient accuracy and precision. Besides of the importance to improve the foundation of such kind of noncontact flowmeters, it is objectively important to extend the practical measurement limits further, as drawn by the theory of the LFV [4, 5]. Thus, in this chapter will be presented the actual measurements with the developed FMSs targeting to fulfill both objectives, that is *a)* to improve the accuracy and the precision of the Lorentz force measurements on electrolyte flows for already tested values of flow velocity and electrical conductivity, *b)* to provide confirming measurements that the LFV theory is also valid for the lower ranges of conductivity (below $2\,\mathrm{S\,m^{-1}}$).
The results of flow measurements are shown in the chronological order as they was obtained during research project. It is started by the earlier obtained result on the small electrolyte channel using the direct compensation Pendulum FMS (cf. chapter 3). Next, extensive measurements on the extended channel using dFMS system (cf. chapter 2, section 2.3) for the values of electrical conductivity $10\,\mathrm{S\,m^{-1}}>\sigma>0.06\,\mathrm{S\,m^{-1}}$ will be presented, showing improved measurement error and the extension of the LFV measurements for almost 2 orders of magnitude smaller values of electrical conductivity which were not measurable previously [13–16]. Further, it will be presented measurements (with same dFMS) for a special case of the electrolyte flow which has lower electrical conductivity than the ordinary tap water $0.06\,\mathrm{S\,m^{-1}}>\sigma>0.005\,\mathrm{S\,m^{-1}}$. The smallest value achieved for the electrical conductivity is the practical limit of the filter which was used to purify the ordinary tap water. However, it will be shown by measurements that even before reaching those levels of purification of the electrolyte (water) flow, that is right below the values of

$0.06\,\mathrm{S\,m^{-1}}$, the linear dependency of the LFV theory does not holds, detailed description will be provided in the corresponding section 5.3.

5.1 On Prototype Channel: Direct Compensation Pendulum FMS for $2\,\mathrm{S\,m^{-1}} < \sigma < 20\,\mathrm{S\,m^{-1}}$

The introduction of the measurement facility (**Prototype Channel**) is presented in chapter 3 (also in figure 5.1) with all available characteristics and calibration measurements.

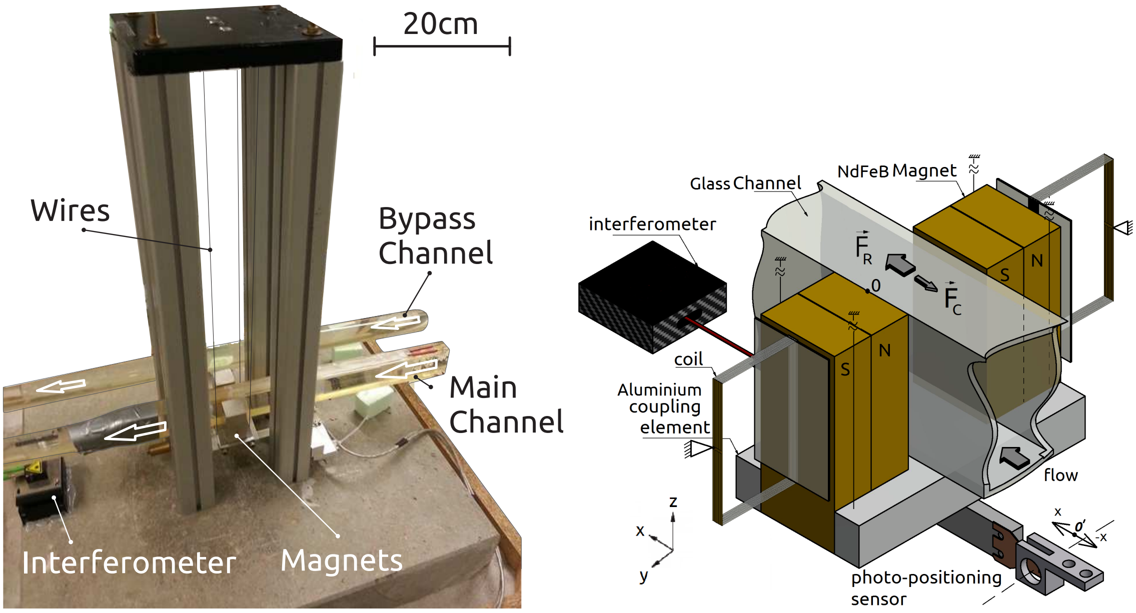

Figure 5.1: Prototype channel (left) and the simplified sketch of the setup direct compensation Pendulum FMS (right).

An example of short-term measurements are exemplified in the figures 3.19 earlier, showing the performance and the typical procedure of the Lorentz force measurements by the direct compensation Pendulum FMS (for coil with n=15 turns). Particularly, in figure 3.19*a)* is shown the given flow velocity which is referenced by a UDV flowmeter, in figure 3.19*b)* the compensation current applied to the coils, which is required to keep the Pendulum FMS at the zero position. The value of the electric current should be multiplied by sensitivity factor of the coil (cf. figure 3.18) in order to obtain the actual force signal.

This measurement procedure is made for different values of the electrical conductivity σ =[2.7, 4.35, 10.01, 17.86, 20.11] $\mathrm{S\,m^{-1}}$ and for different values of the electrolyte flow velocity. In figure 3.19*a)* can be seen the applied velocity in step-wise form and respectively in figure 3.19*b)* the corresponding responce of the Pendulum FMS, as discussed in terms of the applied electric current. The mean values and the standard deviations of all data are collected once the settling time is reached at each

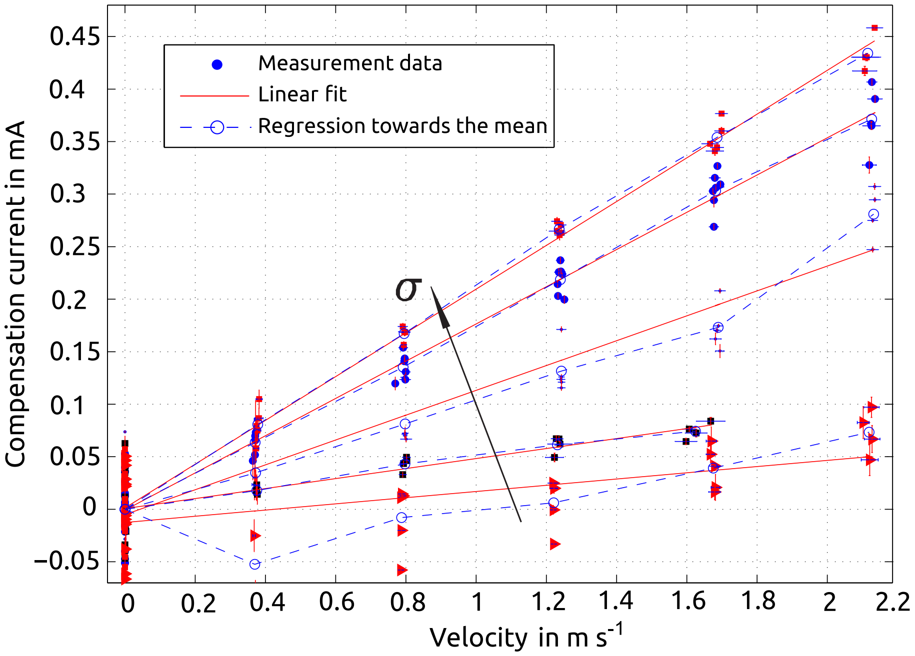

Figure 5.2: Compensation current I in coil as a function of electrolyte (σ=[2.7, 4.35, 10.01, 17.86, 20.11], [$\mathrm{S\,m^{-1}}$]) flow velocity v_0, during the compensation measurements of the Lorentz forces with coil n=15 turns.

step (τ=2.4 s, for electric current the signal is filtered by standard running average filter with last 25 measured data). Additionally, all measured results from the one set of measurements are processed in a way to eliminate a typical linear drift, which is shown for instance in figure 3.22*(bottom)*. Also a compensation measurements are made for the case of thin sheet of conductor. The thin sheet of conductor is attached to the channels, and the compensation forces are produced from the inner side of the magnets (cf. figure 3.3). For the last set of measurements an additional rectification and smoothing of the obtained results with a low-pass filter is performed. Because the mechanical vibration of the electrolyte channel are directly transmitting to the thin sheet conductor, it is leading to a change of the predefined coordinates of the mechanical arrangement, therefore, the compensation forces also will change.

Thus, the mean values of the compensation current at each step is plotted over the mean values of the flow velocity. In figure 5.2 the full set of measurements made by rectangular coil with n=15 turns are presented. It can be seen the linear dependency between the compensation current (that is $I \sim F_L = -F_C$) and the reference velocity in accordance with equations 1.2 and 1.3. Next, all data are combined together in order to concretize the characteristic of the flowmeter in terms of the most relevant parameters showing the sensitivity of the flowmeter (cf. equations 1.2 and 1.3). In figure 5.3 the sensitivity of flowmeter is presented as the necessary compensation current per velocity per electrical conductivity of the electrolyte flow. The force transfer factor is approximately 250 µN mA^{-1}.

In similar manner the results obtained form measurements of the Lorentz forces with

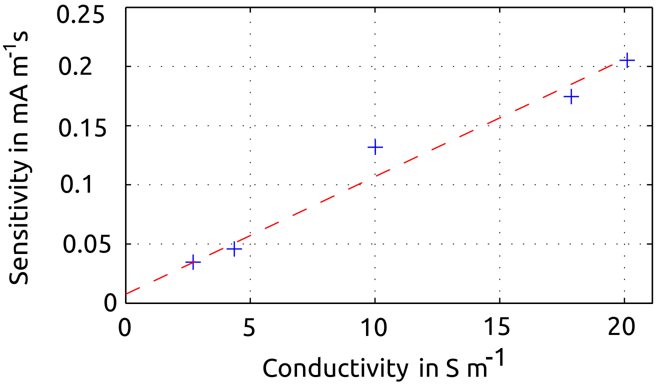

Figure 5.3: Sensitivity of flowmeter for coil with n=15 turns (from linear fit of I/v_0, cf. figure 5.2) as a function of electrical conductivity of the electrolyte flow. The force transfer factor is ≈ 250 µN mA^{-1}.

the thin sheet in figure 5.4 are presented.

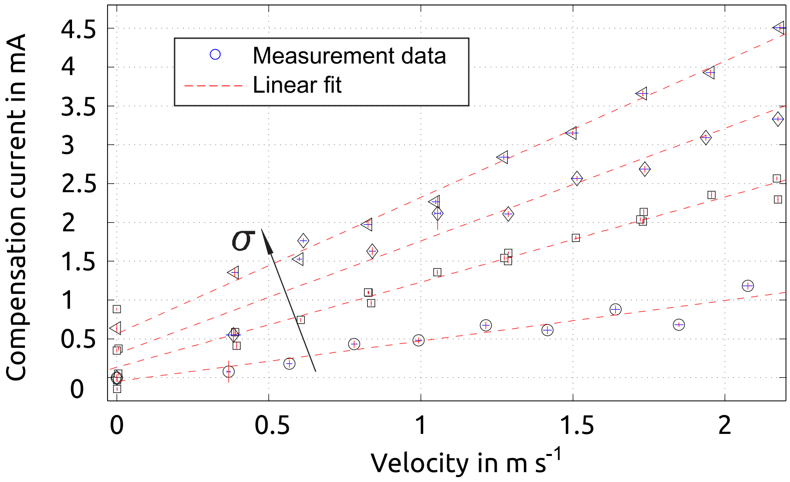

Figure 5.4: Compensation current I in thin sheet of conductor as a function of electrolyte flow velocity v_0, similar to figures 5.2. σ=[6.7, 12.42, 15.4, 19.72], [S m^{-1}].

Note that the calibration factor of the thin sheet of conductor is different than that of the rectangular coils with n=1, 3, . . ., 15. The transfer factor to convert the compensation electric currents to the force values is obtained during the calibration measurements, which is approximately 24.75 µN mA^{-1} with ±2.6 % accuracy, whereas in terms of the voltage measurements from the positioning sensor is obtained 50.2 mV mA^{-1} with ±12 % accuracy (cf. figure 3.11 in section 3.4.1). Following from the compensation measurements by the rectangular coil with n=15 turns and by the thin sheet of conductor, two different sensitivities of flow measurements are obtained. In figure 5.5 the sensitivity of the flow measurements by the thin sheet of conductor is presented based on the results shown in figure 5.4.

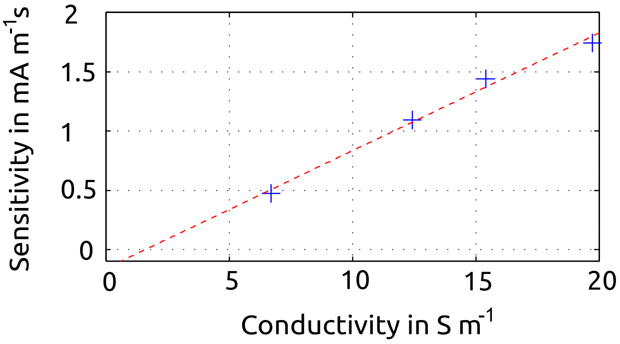

Figure 5.5: Sensitivity of flowmeter for thin sheet of conductor (from linear fit of I/v_0 cf. figure 5.4) as a function of electrical conductivity of the electrolyte flow, similar to figure 5.3. The force transfer factor is $\approx 24.75\,\mathrm{\mu N\,mA^{-1}}$.

The performance of measurement system for both configurations (rectanguilar coil and thin sheet of conductor) is different, since the force factor (F/I) in case of the figure 5.3 is conditioned by involvement of the rectangular coil (n=15) in compensation schema, whereas in case of the figure 5.5 the same amount of electric current in the thin sheet of conductor compensates less effective forces than coil by 15 turns, in other words a higher magnitude of electric currents are required to apply to the thin sheet of conductor to achieve the Lorentz force measurement. In future, the performance of the flowmeter have to be tested by additional measurements. For the same value of the electrical conductivity two identical measurements (at least) should be made with two different coils (different number of turns in coils for each set of measurements) to obtain a better agreement. These additional measurements are important to confirm that the performance characteristics of the direct compensation method is independent from the number turns of the coil or from the general structure of the current conductor, but rather dependents only from the amount of the electric current that is flowing in it. This was one of the motivation in developing the new direct compensation EMFC balance FMS where the several parallel working rectangular coils with different number of turns (n=7, 29, 77) may allow these measurements.

5.2 On Extended Channel: *d*FMS for $0.06\,\mathrm{S\,m^{-1}} < \sigma < 10\,\mathrm{S\,m^{-1}}$

[1]In this section, enhanced flow rate measurement by applying the contactless Lorentz Force Velocimetry (LFV) technique is present. Particularly, it is show that the LFV is a feasible technique for metering the flow rate of salt water in a hori-

---

[1] A significant portion of the results obtained in this section are compressed in the peer-reviewed journal publication [66] **S. Vasilyan et al. Towards metering tap water by lorentz force velocimetry. Measurement Science and Technology, 26(11):115302, 2015.**

zontally aligned rectangular channel. The measurements of the Lorentz forces as a function of the flow rate are presented for different values of electrical conductivity of the salt water (electrolyte). The main interest is to extend the feasibility of the LFV technique to the flow rate measurements of salt water with low electrical conductivity. Based on the results previously reported in [13–16], improvements of the experimental facility and the force measurement setup were implemented in order to enable flow rate measurements of salt water with an electrical conductivity below 2 S m^{-1}.

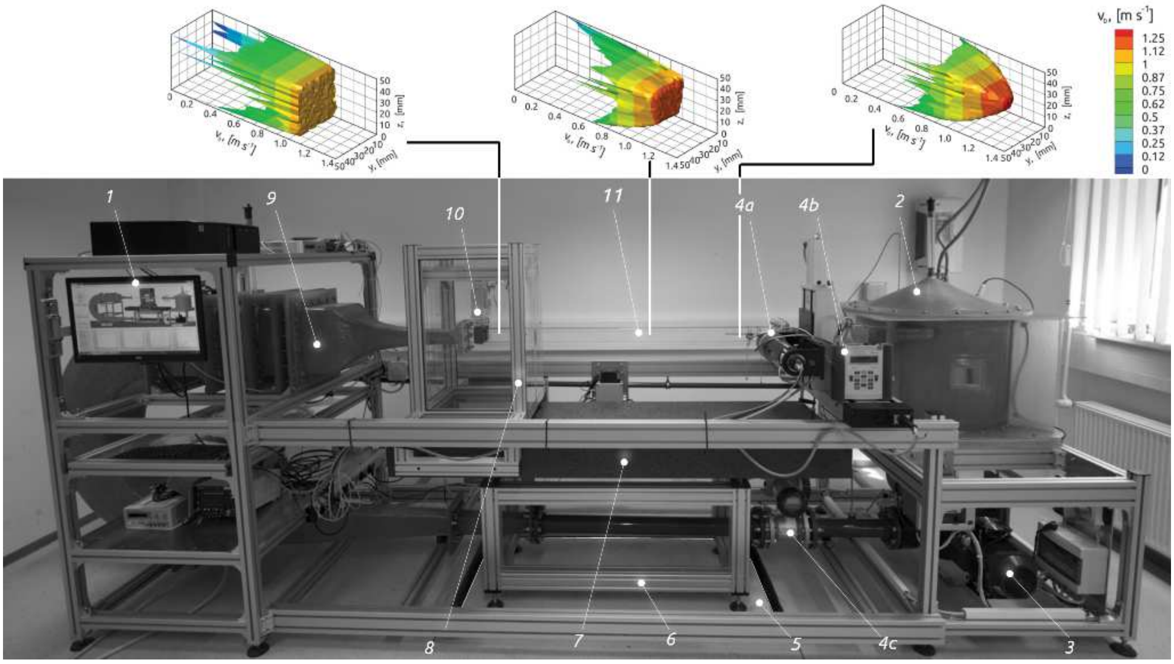

Figure 5.6: Photograph showing the complete LFV experimental setup of extended electrolyte channel-loop with force measuring setup. Above, typical flow profile distributions which are measured by 4a at 3 different locations of the test section are shown, (left - inlet, center and right - outlet of the test section) [22]. 1 - Control PC, 2 - Reservoir of fluid with conductivity meter, 3 - Pump, 4 - Reference flowmeters (a) Laser Doppler anemometer with traverse system, (b) Ultrasonic and (c) Magneto inductive flowmeter, 5 - Decoupled block of basement, 6 - Main supporting frame, 7 - Granite-stone (800 kg), 8 - Supporting frame of the LFV, 9 - Diffusor, dumping and nozzle sections, 10 - Force measuring system with magnets, 11 - Flow measurement test section.

The smallest value of electrical conductivity where the LVF is applicable is achieved at 0.06 S m^{-1}, which corresponds to the typical value of tap water. In comparison with previous results, the performance of LFV is improved by approximately 2 orders of magnitude by means of a high-precision dFMS. Furthermore, the sensitivity curve and the calibration factor of the flowmeter are provided based on extensive

measurements for the flow velocities ranging from $0.2\,\mathrm{m\,s^{-1}}$ to $2.5\,\mathrm{m\,s^{-1}}$ and conductivity ranging from $0.06\,\mathrm{S\,m^{-1}}$ to $10\,\mathrm{S\,m^{-1}}$.
The section is organized as follows: First, the flow measurement facility and its working principle are introduced, and details of the salt water loop characteristics and magnet systems are presented. Then, the dFMS (presenting a force measuring resolution which is about 2 orders of magnitude better than that of the previous setup [21]) is presented with the magnet systems (instead of dummy weights, cf. chapter 2, section 2.3) which are suspended from EMFC balance; further the flow measurements for different values of electrical conductivity are presented. Finally, the sensitivity curve of the LFV flowmeter and the uncertainty consideration of the measurements are provided.

5.2.1 The channel and the electrolyte

The entire facility is designed in a way to provide constant flow in the test section of the channel (cf. figure 5.6) [15, 22]. For experimental convenience salt water is chosen as a working fluid. The fluid used is ordinary tap water that has an electrical conductivity of $4 \cdot 10^{-2}\,\mathrm{S\,m^{-1}} \pm 0.5 \cdot 10^{-2}\,\mathrm{S\,m^{-1}}$. The variation of this value depends on the season of the year and on the temperature of the laboratory $293.15\,\mathrm{K} \pm 2\,\mathrm{K}$. The rate of conductivity is set ($\sigma = [0.059, 0.09, 0.099, 0.32, 0.62, 1.01, 2.31, 10.05]\,\mathrm{S\,m^{-1}}$) by mixture of the tap water ($\approx 300\,\mathrm{l}$) and salt (sodium chloride). The electrical conductivity value for saltwater is measured with reference conductivity meter (Indumax CLS50/CLS50D, Endress+Hauser AG) [67] by 1 Hz sampling frequency. During the typical operation period (2-3 hours) of the experimental facility, this value is stable within the accuracy of the device in use (0.5 % of measured value). In case of existing setup, the standard deviation of the conductivity measurements is resulting to $2 \cdot 10^{-3}\,\mathrm{S\,m^{-1}}$.
The flow is driven by a rotary pump (item 3) providing a maximum velocity of $4\,\mathrm{m\,s^{-1}}$ in the test section of the channel (item 11 in figure 5.6) with an inner constant cross section of $50\,\mathrm{mm} \times 50\,\mathrm{mm}$ that corresponds to a flow rate of $10\,\mathrm{l\,s^{-1}}$.
The horizontally aligned test section of a length of 1500 mm is made of transparent polycarbonate material and has an outer rectangular cross section with a height of 80 mm and a width of 54 mm. The 15 mm thick top/bottom walls diminish the vertical deformation of the channel whereas the thickness of the side walls amounts to 2 mm only. This allows to minimize the distance between the magnets to 56 mm also providing close-fitted configuration for interaction of the magnetic field with the flow. Thus, the volume between the magnets encompasses the channel with a minimal air gap of <1 mm from both sides as depicted in figure 5.9 (left).
The flow in the channel is turbulent and the range of the Reynolds number is from $Re \approx 1 \cdot 10^4$ to $2 \cdot 10^5$ as a result of relative insignificance of viscous forces compared to the inertial forces in the system. The Lorentz force measurements are considered for steady flows that is in our case is when the flow reaches a statistically steady state. By this scenario, the fluid flow characteristic meets the requirements of the kinematic theory of LFV which are discussed in details in *Thess et al.* [68]. As a part of contribution of the current measurements is to verify this theory for the val-

ues of electrical conductivity well below earlier discussed cases. Hence, the flow rate can be computed from the mean velocity.

To validate the velocity measurement results and to obtain information about the flow characteristics, two independent reference flowmeters are used (cf. item 4b and 4c in figure 5.6). Particularly, the flow rate is cross-checked by an ultrasound flowmeter (USD - Fluxus F601, H. Hermann Ehlers GmbH) [69] which is installed at the outlet of the channel against the magneto-inductive flow meter (MID - Optiflux 2000, Krohne Messtechnik GmbH) [70] installed after the pump. The result is used to design the measurement procedure in such a way as to avoid detected delays in the settling time of the flow rate at different points of the loop. Furthermore, the MID device (also 1 Hz sampling rate) is used for the direct referencing of the measured Lorentz force.

In addition, some measurement results made by the 1D laser Doppler anemometer from [22, 71] (cf. figure 5.6 item 4a) are supplied, to order to gather the necessary information of the velocity field distribution at different positions of the test section. In figure 5.6, measured flow profiles are illustrated at different positions of the test section **a)** inlet x=30 mm away from nominal 0 entrance point of channel, **b)** center x=750 mm, *c)* outlet x=1470 mm. All measurements were made at a constant mean flow velocity of v_0=30 m s^{-1} (cf. Ref [22] for more details). At the inlet of the test section, the fluid profile has a piston-like shape which further develops into a parabolic-like shape at the outlet of the channel.

As a magnetic field source assemblies of permanent magnets are used. The magnets are directly suspended from the force measuring system without contact to the test section (item 10 in figure 5.6). The mass of the magnet systems ($m_0 \approx$1 kg) represents an unavoidable dead load applied to the force measurement system.

5.2.2 Magnet systems of LFV for extended channel

Following the scaling behavior as given in equations 1.2 and 1.3, the flux density of the magnetic field could be increased in order to generate higher magnitudes of Lorentz forces. In spite of the possibility to generate necessary orders of magnitudes of the magnetic fields with solenoids, the use of such electromagnets yet remains problematic. The main reasons are the high weight of such systems which should be suspended from mechanically highly sensitive force measurement systems and unavoidable contact of cables for high power supply currents. Other limitations are the consideration of energy consumption (to generate the magnetic field and to cool the coils) and the stability of the system in relation to power losses due to high power supply currents, as well as possible electrical noise and heat production. In case of this work, however, the magnetic field is generated by a custom-built systems based on rare-earth permanents magnets (cf. table 5.1, figure 5.7). It can be used two different configurations of magnet systems. The first conventional system consists of two rectangular bars of permanent magnets, whereas the second is constructed from 10 rectangular bars in two blocks, 5 in each side of the test section. The last, is arranged in a so-called Halbach array structure that was earlier designed to fit to the channel [23, 24]. When using permanent magnets, the magnitude and the distribution of the magnetic flux density are dependent on the volume, dimensions and magnetic properties of the used material, therefore the stability of the flux density depends only on the operating temperature. The influence of the temperature on the magnetic flux density can be consider with the temperature coefficients for the remanence and coercivity of the used magnetic material (see table 5.1 and Ref. [23]).

Table 5.1: Parameters of magnet structures, NdFeB (grade N52).

Parameter	Units	Halbach	Conventional
Dimension of single magnet, a×b×c	mm	15×18×46	30×40×47
Total mass, m_0	kg	1.008	1.048
Remanence, B_r	T	1.5	1.4462
Coercivity, H_{cB}	$\mathrm{A\,m^{-1}}$	0.98×10^6	1.11×10^6
Temperature coefficient, α	$\mathrm{K^{-1}}$	0.011	0.06

Both configurations are magnetically coupled by a carbon fiber lightweight material with a separation distance of 56 mm.

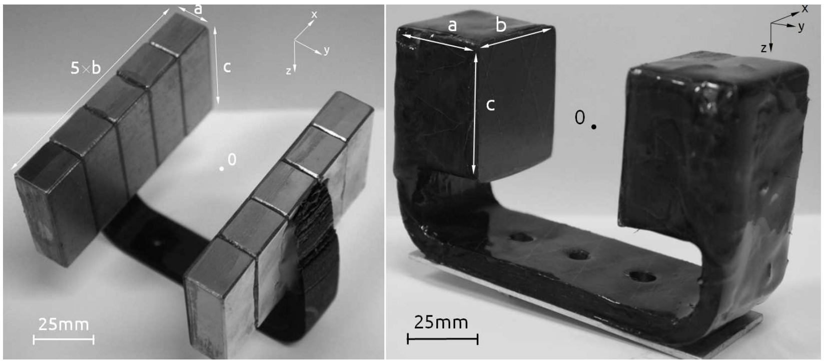

Figure 5.7: Magnet system configurations for extended channel; left - Halbach array, right - Conventional magnets [22–24].

For handling convenience and depending on the initial choice of the mechanically highly sensitive force measurement systems, the total mass of the magnets is limited to $m_0 \approx 1$ kg. The Halbach array was designed and built by means of a special optimization algorithm based on the initial performance of the conventional configuration (see Ref. [24] for details). Although the magnetic flux density of the conventional magnet configuration at the symmetry point $B(0,0,0)=299$ mT is bigger than that for the Halbach array $B(0,0,0)=160$ mT, the proposed numerical simulations in [24] together with earlier obtained confirming experimental results in [23, 24] showed an increased F_L by a factor of 2.8 when using the Halbach magnet system. This is due to directing straying of magnetic field to the internal volume of the magnets thereby reducing interactions and losses of the magnetic field in external part, so that the magnetic field penetrates the flow in the channel with the same magnitude approximately. Comparative examples of magnetic field measurements of conventional and Halbach array systems are presented in figure 5.8.

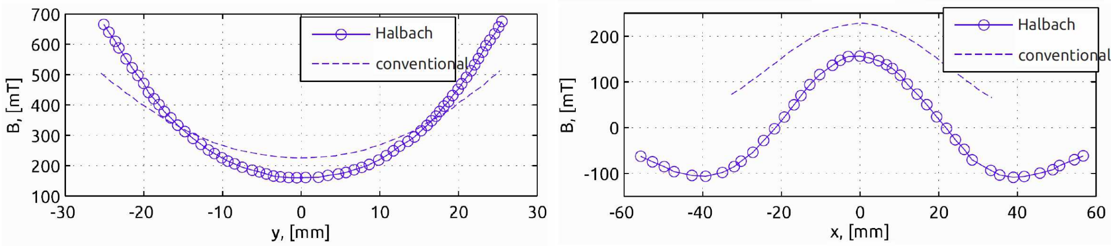

Figure 5.8: Measured magnetic flux density of Halbach array (∘ —) and conventional (– – –) magnet [22, 23] along the y-axis (left) - $B(x=0,y,z=0)$, and x-axis (right) - $B(x,y=0,z=0)$.

The magnetic field distribution of the magnet systems was measured with a three-axis Hall probe (AXIS-3, Arepoc S.R.O.) which was fixed to the three-dimensional positioning system (8MT175-200, STANDA) with a step resolution of 2.5 µm. The Hall probe has an active area of 50 µm × 50 µm; the linearity error is lower than 0.2 %. The measurements of the magnetic flux density in the volume between magnets were made at a resolution of 1 mm in all three directions[2].

5.2.3 *d*FMS with magnets

Earlier, in [13, 14], the main principle and the implementation method of LFV measurements by using a pendulum-like system were described. For continuous and stable measurements, based on the same setup a measurement method with reduced complexity was proposed by applying a direct force compensation scheme [16] in chapter 3 and section 5.1. In [15], more accurate and precise flow measurements were presented using single EMFC balance. In [15], the single EMFC balance is introduced in details separately as a stand-alone system (see Ref. [21]). In Table 5.2, a short summary of the main details described in previous reports (see also Ref. [13–16, 21]) is presented.

The development of a special force measuring system is primarily dictated by the technical complexity of the LFV application. The setup (cf. item 8 and 10 in figure 5.6) is designed to focus attention on the horizontally directed channel flow, which is the common flow scenario met in research and industry [5]. As described in theory [4], the LFV measurements are considered when the flow reaches the so-called statistical steady state regime that is for the case of acting stationary forces (dF_L/dt = constant). Since the Lorentz force develops instantaneously according to the temporal variations of the velocity (dv/dt), there is a demand to resolve the quasi-dynamic force in order to optimize the measurement process and to reach

---

[2] Results of the magnetic field measurements for Halbach array system were obtained in collaboration with Markus Weidner.

Table 5.2: Details of LFV measurements reported previously.

	Units	Pendulum [13, 14, 16]	EMFC [15, 21]
Force measurement			
Resolution	µN	2 – 3	1
Response time	s	11 [13], 2.4 [16]	1.4
Electrolyte flow			
Conductivity	$\mathrm{S\,m^{-1}}$	≥ 2.3	≥ 2
Velocity	$\mathrm{m\,s^{-1}}$	1 – 4	0.2 – 4
Settling time	s	> 5	> 30
Total Volume	l	≃ 11	≃ 300

higher temporal resolution. Particularly for the force measurements the limit of $t \to 0$ is considered as a minimal time when the flow develops through an early stage. In order to realize gravity free measurements of F_L the dFMS is used.

For the noise reduction as discussed in section 2.3 the dFMS is developed, particularly to compensate the vibration and tilt influences. The first EMFC balance carries the magnet structure and is intended to measure the F_L, whereas the second EMFC is carrying an equivalent dead weight made of a non-ferromagnetic material (copper), compared with the ferromagnetism of the permanent magnets the diamagnetism of copper is negligible. In the simultaneous measurement mode, the EMFC balance that carries the dummy weight is recording signals of non-ferromagnetic origin - that is for this purposes - represent undesirable external disturbances. Figure 5.9 shows the image of the force measurement setup and the functional diagram of the measurement principle.

In the working mode the EMFC compensates the deflection by balancing it at zero offset position using the compensation current of the voice coil which is integrated inside the EMFC. This electric current drives the measurements and is proportional to the deflection and, therefore, to the mean flow velocity. The EMFC balances are equipped with factory electronics that performs the compensation procedure with a well-defined cycle of the PID controller. Both EMFC balances are aligned along the common x axis by their offset zero positions. The F_L measurements assume the following calculation principle:

$$F_{1M} = F_{err}, \tag{5.1}$$

$$F_{2M} = F_{err} + F_L, \tag{5.2}$$

$$F_L = F_{2M} - F_{1M}. \tag{5.3}$$

Here, F_{2M} is the measurement signal from the EMFC balance that carries the mag-

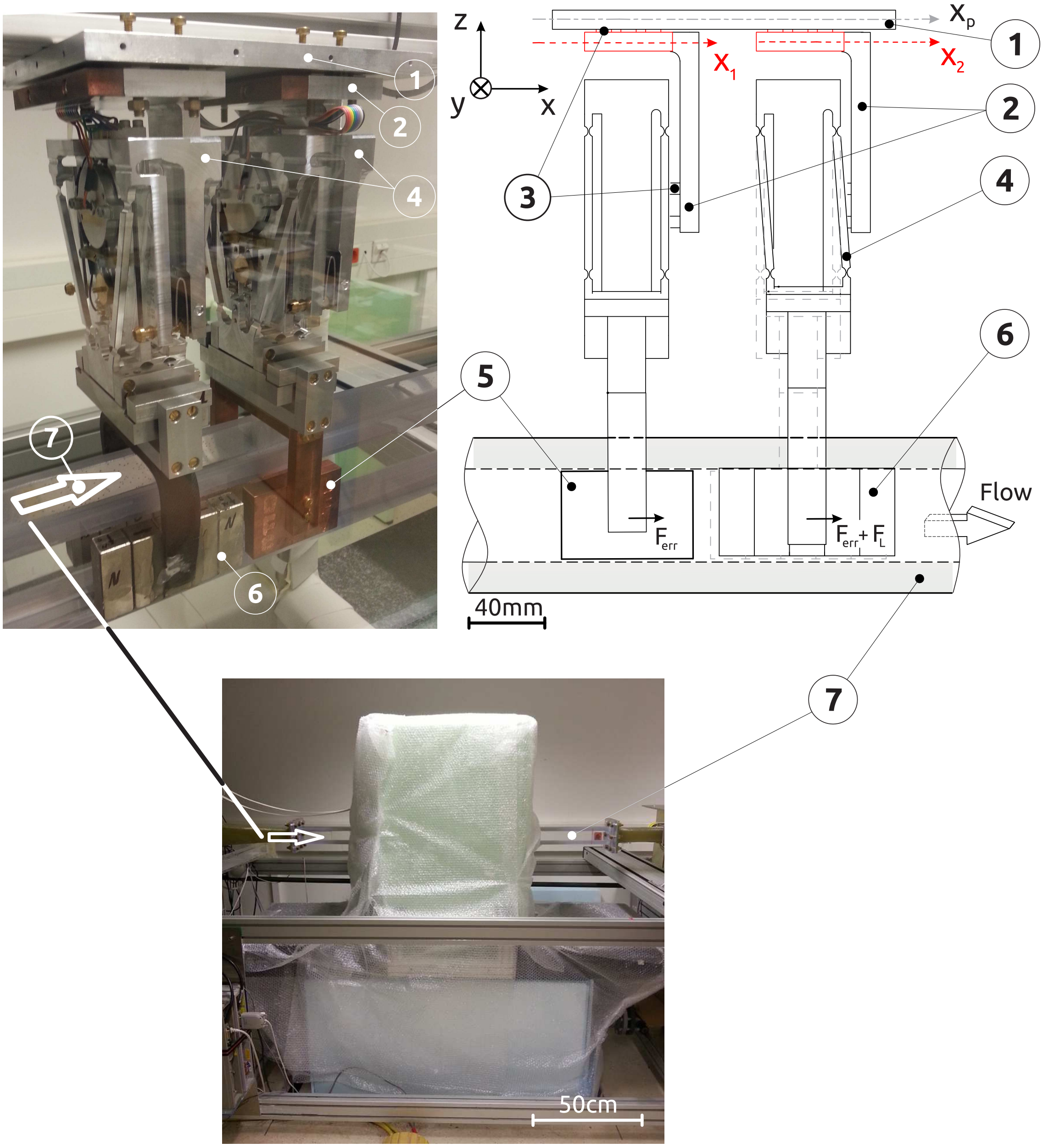

Figure 5.9: Left - Image of the differential force measurement system with two EMFC balances, (6) Halbach array magnet and (5) dummy weight. Right - Functional diagram and geometrical configuration of the system presented in side view and can be simplified as two swinging pendulums; dashed line on the right EMFC indicates the actual state whereas the deflection is represented in the exaggerated state to indicate the measurement principle. (1) hanging common plate, (2) two separate suspension parts (in form of elbow) for fine tuning both EMFC in horizontal plane, (3) clearance holes for fixing EMFC balances, (4) EMFC balance, (5) dummy weight, (6) Halbach array magnet, (7) channel. The sequence of (5) and (6) in the flow direction can be chosen optionally. The positions of (5) and (6) are interchangeable due to their equal masses and the identic EMFC balances. The *d*FMS under the cover of the passive thermo-insulation (bottom).

net, F_{1M} the measurement signal from EMFC balance with dummy weight, and F_{err} the noise in both signals. Hence, the difference of signals obtained from both EMFC balances is the target signal, and thus should refer to it in the measurements of the salt water flow simply as Lorentz force (F_L). The filtering is done after the raw signal of F_L is obtained by equation 5.3. The filtering is made similar as described in section 2.3.2. This low pass filter provides 6 s settling time.

For calibrating the force measurement system, the second dummy weight (item (5) in figure 5.9) instead of magnets is used. In this configuration the force measurements by both EMFC balances are sensitive only to noise effects (tilt and mechanical vibrations). Furthermore, to mimic the Lorentz force measurements a linear voice coil actuator is used to generate horizontally directed forces to be measured by one of the EMFC balances. The examples of such calibration measurements of forces are represented in figures 2.16 and 2.17. Notice that each of the EMFC balances alone has clearly observable noise with several hundreds of nN resolution. This noise is purely mechanical and occurs also in the raw signals of both EMFC balances. The difference signal is shown in the lower plots in both figures, where the raw and filtered signal of the force measurements are plotted. For case of small calibration forces it can be seen that the resolution of the unfiltered signal is approximately 0.1 µN while that of the filtered one is 20 nN. More detail about the calibration is presented in section 2.3.3.1 and section 2.3.4.

Thus, the nominal capabilities of the dFMS are, a resolution of $20 \cdot 10^{-9}$ N over the working range of $\pm 10^{-4}$ N (potentially it can be extended up to ±55 mN) and a response time of 6 s. An analysis shows that the stability of the measurements mainly depends on the tilt error of the force measurement setup which is greatly restricted by the temperature stability of the surrounding environment and during this work is is estimated below ΔT=20 mK (for more detail see chapter 2). This advance in force measurements provides means for further investigations in the actual application of interest the flow rate measurements by LFV technique. The experimental procedure and the measurement results of the salt water flow velocity for different values of electrical conductivity down to 0.06 S m^{-1} are presented next.

5.2.4 Results of flow rate measurements

In this section, it is present a collection of flow rate measurements by means of LFV for constant conductivity values σ=[0.059, 0.09, 0.099, 0.32, 0.62, 1.01, 2.31, 10.05] S m^{-1}. For each set of conductivity a step-wise function of velocity from 0.2 m s^{-1} to 2.5 m s^{-1} (cf. figure 5.10a) with ≈ 0.011 Hz frequency is applied. The magnitude and the standard deviation of the Lorentz force are measured by differential force measurement system (cf. figure 5.9), when the settling time of the flow in the test section is reached. The values are obtained by collected them in relation to the velocity signal measured by a reference MID flowmeter. The control of the measurement procedure and the data acquisition are done in LabVIEW environment by unifying each individual element of the electrolyte channel loop within custom developed software [15, 22].

The typical settling time (≈ 10 % overshoot) to observe a stable signal of the flow ve-

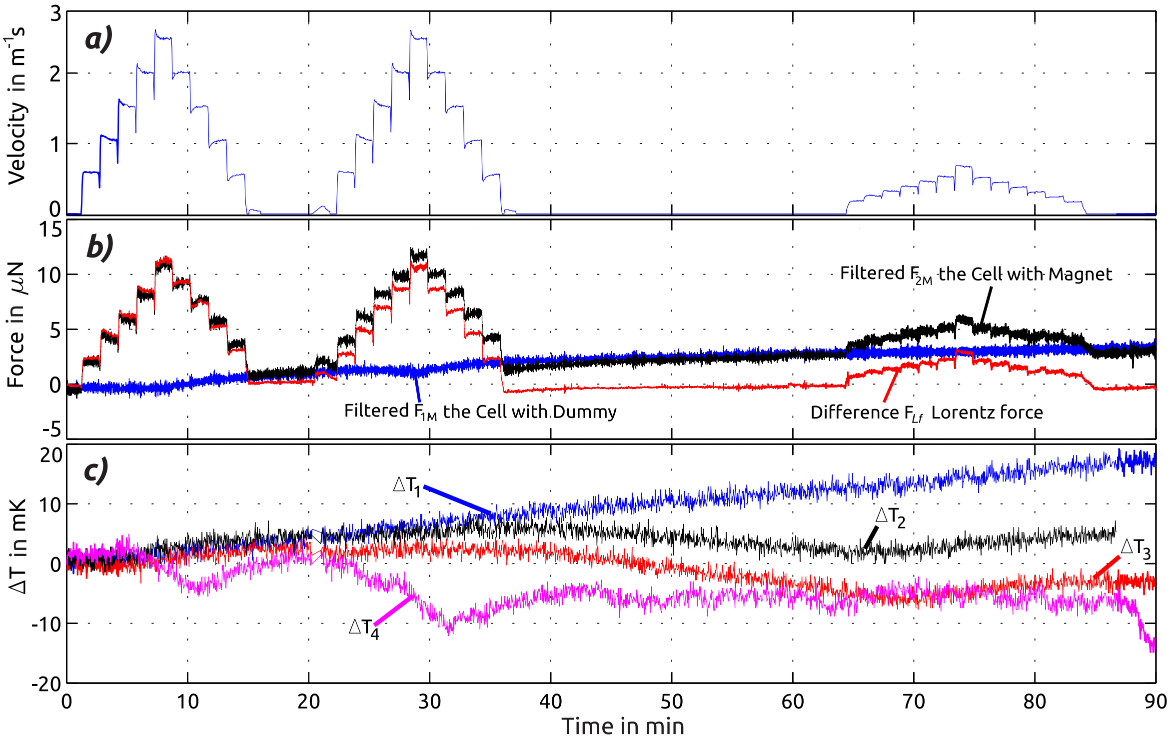

Figure 5.10: Measurement results of the LFV for a low conductive fluid. The provided example represents a continuous measurement of the Lorentz force in accordance with the changing flow velocity over a 90 minute period, the conductivity is σ=1 S m^{-1}. a) The step-wise velocity signal recorded by reference MID velocity meter, b) filtered force signals of each EMFC and the filtered difference, c) temperature change of the surrounding environment; inside the housing: top ΔT_1 and bottom ΔT_2 parts, outside the housing ΔT_4 is the room temperature and ΔT_3 of the stone.

locity with the reference MID flowmeter is 30 s. This fact allows to take F_L measurements with a differential force measurement setup as a raw signal ($F_{diff}\approx$ 150 nN) and further to process it in a software based external filter with considerable integration time as discussed in the previous section. The drift in both signals of the EMFC balance force measurements originates from the thermo-mechanical stresses existing in the supporting construction, due to the temperature change in the laboratory which is estimated as energy dissipation from the pump. In the example shown in figure 5.10, it is provided measurements over a 90 minute period when the change of the temperature is below the predicted ΔT <20 mK value. In this particular example the force drift is entirely eliminated, thus providing around 3.5 µN force correction of drift error, whereas the resolution of F_{Lf} remains below 70 nN.

Figure 5.11 shows the results of the Lorentz force measurements at the inlet of the channel as a function of saltwater flow velocity for different values of electrical conductivity.

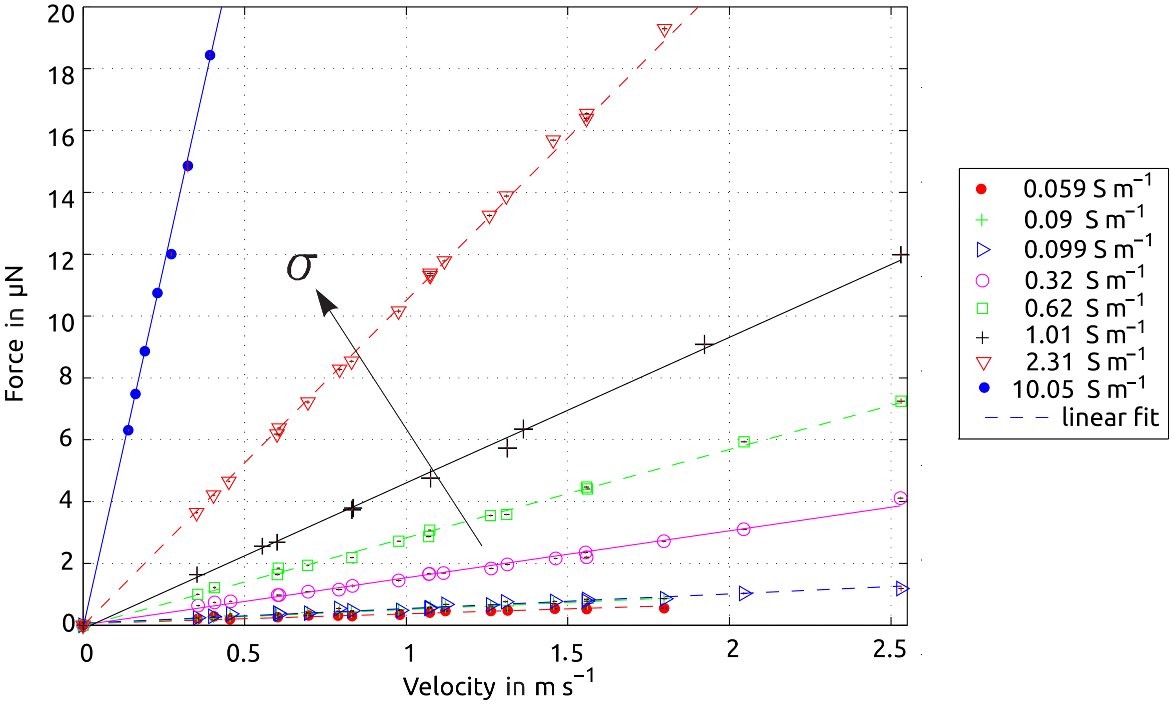

Figure 5.11: Measured Lorentz force F_L as a function of flow velocity for different values of the electric conductivity (markers) and linear fit (line).

In previous studies [15, 21], the stability of the force signal was undefined, and the resolution of the measurements was limited to ≤1 µN (cf. Table 5.2). In particular, the accuracy was obstructed by a systematic error defined as force drift due to the tilt of the setup, whereas the resolution was limited due to random error originating from mechanical vibrations. In this work, as shown by the measurements (cf. figure 5.10), both sources of errors can be significantly reduced by introducing the second EMFC balance on the same measurement axis, thus obtaining in Lorentz force measurements in maximum 70 nN standard deviation.

The accuracy and the resolution of the measurements are obtained on the basis of uncertainty considerations of the devices and the actual measured values. The results are analyzed in accordance with the GUM [51] recommendations. The combined relative uncertainty is computed on the basis of the velocity data measured by the MID flowmeter and the force signal which is measured by the differential force measurement system. Both values are calculated in percentage as $\sqrt{[uc(v_0)/v_0]^2 + [uc(F_{Lf})/F_{Lf}]^2} \cdot 100\%$, where $uc(v_0)$ and $uc(F_{Lf})$ are the measurement uncertainty of the mean flow velocity and filtered Lorentz force F_{Lf} as one standard deviation. It can be seen from figure 5.12 that measurements above $0.06\,\mathrm{S\,m^{-1}}$ electrical conductivity are conducted within 6 % of a combined relative uncertainty for velocities as small as $0.2\,\mathrm{m\,s^{-1}}$ to $2.5\,\mathrm{m\,s^{-1}}$.

The accuracy of the flowmeter, which is given for the electrical conductivity in 3 different orders of magnitude, increases from <6 % to <1 % as the value of the conduc-

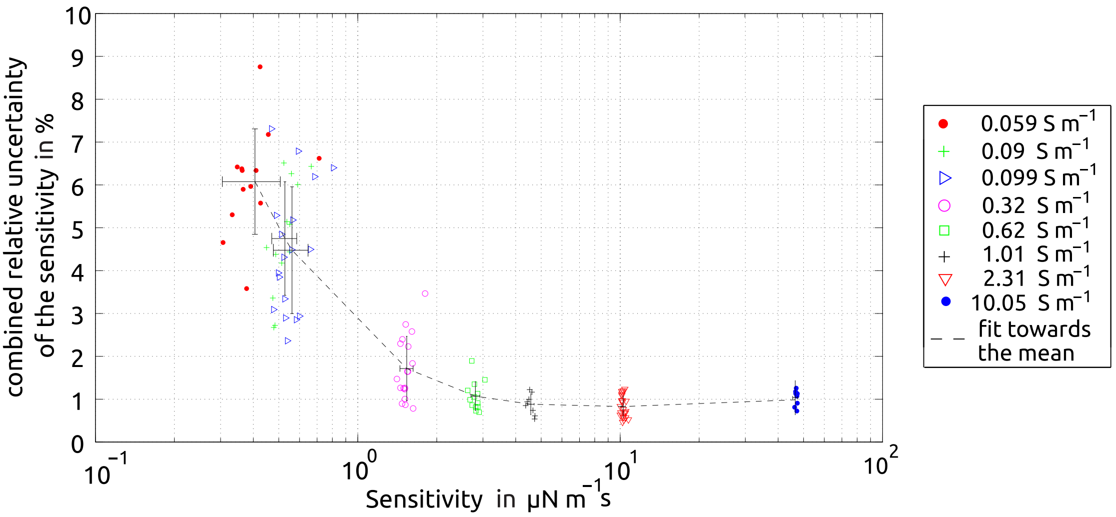

Figure 5.12: Combined relative uncertainty of measurements as a function of the sensitivity $F_L \cdot {v_0}^{-1}$.

tivity increases from 0.06 S m^{-1} to 10 S m^{-1}. The reason is described as follows: At the high values of electrical conductivity the magnitude of the induced F_L is more than 2 orders of magnitude higher than the resolution of the differential force measurements, therefore, only the resolution of reference flowmeters (MID) contributes to the 1 % value, whereas at the low values of electrical conductivity the magnitude of the induced F_L is much closer to the actual resolution of the differential force measurements, therefore, both uncertainties contribute significantly to the development of 6 %. This inaccuracy further increases as the electrical conductivity of the salt water decreases towards the value of electrical conductivity of tap water and below.

Besides this, hydrodynamic characteristic of the electrolyte flow should be considered, such as distribution of flow velocity profile, geometry and scale of the electrolyte channel, etc. For instance, test measurements of Lorentz force response to change of flow profile are shown in figure 5.13. Measurements were done by changing the position of LFV setup to different positions of the channel in correspondence to same measurements positions of flow profile which were done by A. Wegfrass by LDA (cf. figure 5.6). Thus, the measurements of the Lorentz forces at different positions along the test section of the channel is presented in the figure 5.13 for inlet, center part and outlet of the test section. The value of the electrical conductivity in these measurements is 2.31 S m^{-1}.

Results of these comparative measurements at different positions show ≈ 4 % difference in Lorentz force response between inlet and outlet of the channel, whereas combined relative uncertainty only at the inlet have been estimated only ≈ 1 % (cf. figure 5.12). This result may be verified in future by extensive measurements of Lorentz forces when influencing the flow profile in more vivid forms.

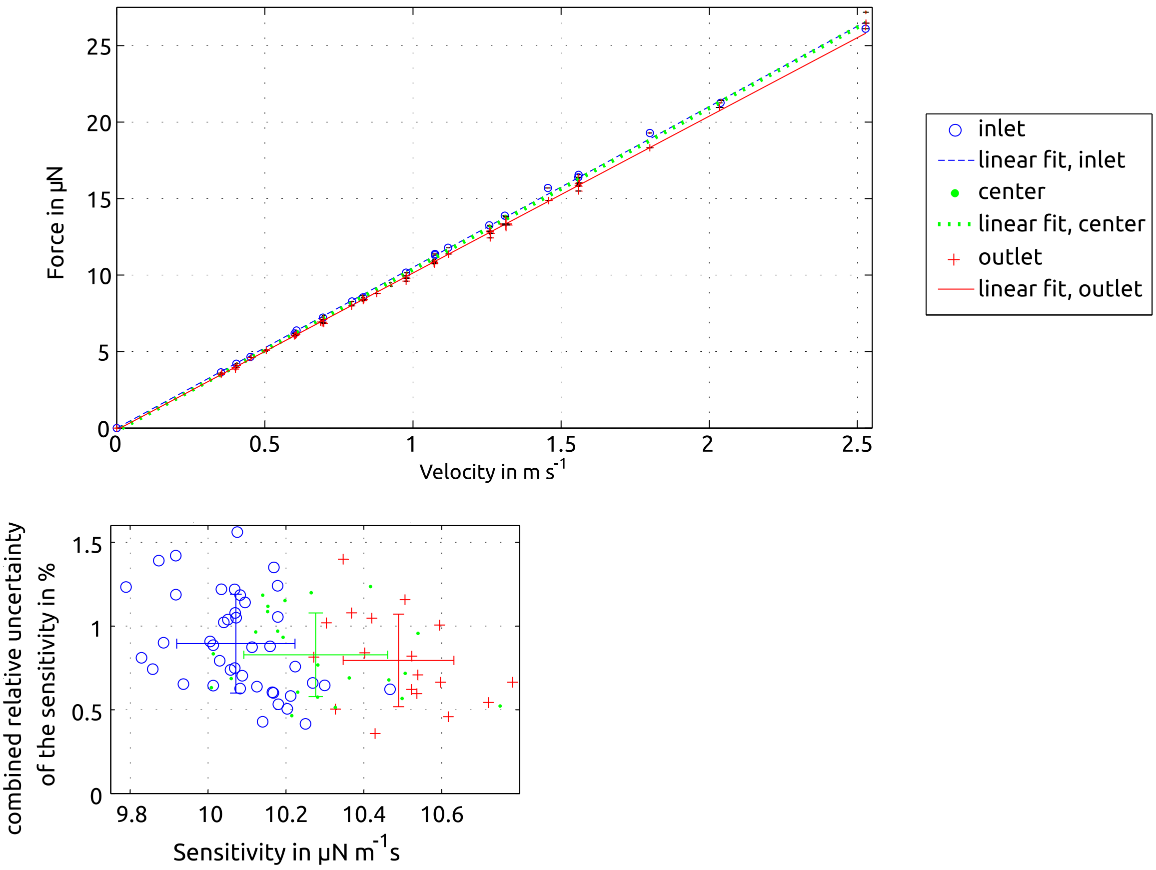

Figure 5.13: Measurements of the Lorentz forces at different positions along the channel (top), and relative uncertainty of the sensitivity (bottom). The value of the electrical conductivity is σ=2.31 S m^{-1}.

5.2.5 Sensitivity and calibration factor

Based on the results presented here, the linear dependency is obtained as it is predicted in the LFV theory (cf. equations 1.2 and 1.3). The sensitivity of our system is presented as a function of the electrolyte conductivity (cf. figure 5.14). From this sensitivity diagram of the LFV flowmeter it is possible to define the range of the expected force measurements when the value of the electrical conductivity is given. Furthermore, according to equation 1.3, it is possible to determine the missing calibration factor by combining the whole measurement data together from the sensitivity curve in the form of the ratio of sensitivity and conductivity $F_L \cdot v_0^{-1} \cdot \sigma^{-1}$. The value of $c_{cf} \cdot B^2$ estimates as 4.8 with ≈ 8 % accuracy (cf. figure 5.14 inset) for conductivities above 0.1 S m^{-1}. This value only represents the calibration factor for our particular design of the flowmeter and may vary for each individual system differently, with some general considerations being discussed in [72, 73]. Therefore, depending on the parameters of each individual system, it should be calibrated exper-

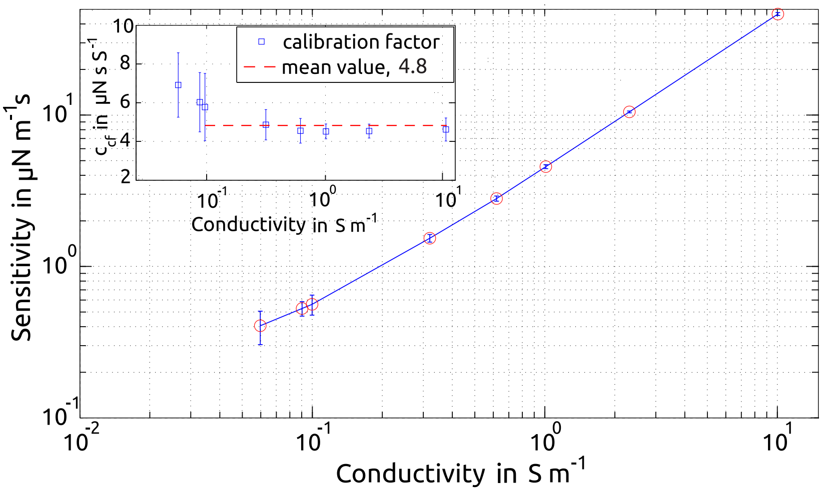

Figure 5.14: Sensitivity of the setup as a function of the electrical conductivity of the salt water (based on data from figure 5.11), fitted towards the mean values (marker). Inset, calibration factor given in µN s S^{-1}. The calibration factor includes the constant value of magnetic flux density.

imentally. Also this value contains the product of the magnetic flux density in the second power, which is in our case constant and non-uniformly distributed in the interaction volume of the moving flow in the test section. Note that here the B is not the measured or numerical calculated value but should be interpreted as the force weighted effective value of the real spatial distribution of the magnetic flux density within the interaction volume of the moving flow. However, once the position of the flowmeter is set at the certain location of the test section and the magnetic field is defined, the calibration factor $c_{cf} \cdot B^2$ can be determined as it is presented in this subsection.

5.2.6 Discussion and summary

The results of flow measurements illustrated in figures 5.10-5.14, and the nominal measurement capabilities of the differential force measurement system show that the accuracy of Lorentz force measurements may still be improved. It is evident that for the given range of force measurements ±100 µN down to ≤100 nN and with a measurement resolution of 20 nN, the flow measurements may address the cases when the electrical conductivity of salt water is $\sigma \leq 0.06\,\mathrm{S\,m^{-1}}$. For example, the resulting force produced by the saltwater flow with v_0=1 m s^{-1} mean flow velocity and σ=0.06 S m^{-1} electrical conductivity (cf. figures 5.14 and 5.12) is $F_L \approx 400\,\mathrm{nN}$. A comparison of the single EMFC balance FMS [15, 21] and of the current work with differential EMFC balance is presented in table 5.3.

Although significant improvements (cf. table 2.1) were achieved in this work compared with previous results [13–16, 21], some remaining aspects still need to be investigated critically. So, the future work is classified as follows;

Table 5.3: Comparison of measurement results between previous [13–16, 21] and current work. Evolution of the LFV applications in measurements of the low electrically conductive saltwater flows.

Measured parameters	Units	Pendulum [13, 14, 16]	Old EMFC balance [15, 21]	New EMFC balances, *d*FMS (current work)
Force measurement				
Resolution	µN	2 – 3	≤ 1	≈ 0.02
Response time	s	11 [13], 2.4 [16]	1.4	1.2 (filtered 6)
Electrolyte flow				
Conductivity	$\mathrm{S\,m^{-1}}$	≥ 2.3	2 - 20	0.06 - 10.05
Velocity	$\mathrm{m\,s^{-1}}$	0.4 – 4	0.2 - 4	0.2 - 2.5
Stable period [§]	min	-	-	30
$std(F_L)/F_g$	ppb	≈300	≈75.93	1.47

[§] Otherwise is given as temperature stability within 20 mK, e.g. in figure 5.10 presented measurements over 90 minutes.

- The long-term stability problem may be investigated in terms of strong thermal fluctuations exerting a big influence. The temperature fluctuations primarily affect the supporting construction, thus leading the system to drift due to thermal deformations. Therefore, a supporting construction is desirable with reduced complexity and negligible coefficient of thermal expansion. The change of the temperature may also affect the stability of the magnetic flux density. Under the scope of this work it is considered within the combined value of the calibration factor.

- The spatio-temporal dynamics of LFV in low ranges of conductivity and velocity. A set of measurements is desirable to explore the limits of the frequency response of the LFV.

- In this work, it is present only measurements on a flow profile with piston-like shape (cf. figure 5.6, left side) at the inlet; however, some further measurements are necessary to ensure universality of the performance of the flowmeter independently of the local characteristics of the flow profile. This will be verified (and published soon) by extensive measurements of the Lorentz force response when influencing the flow profile in more vivid forms compared to cases presented in figure 5.6.

Another major limitation for the current facility is the magnetic field generating system. The magnet structures were preliminary chosen in such a way as to not exceed the mechanical limits of EMFC, because the gravity force causes unavoidable vertically directed mechanical stresses. To avoid this effect and to refine measurements further, a several method can be applied to compensate the gravity force.

In order to reduce the cost of this kind of flowmeters, one can consider an alternative to State-of-the-Art EMFC weighing systems by using the magnetic field of the magnets to compensate the Lorentz forces directly [16]. This can be done by applying an additional electromagnetic force produced by custom made coil systems.

Thus in summary, the results presented in this section focuses on improving a contactless flow rate measurement technique (LFV) for low conductive fluids by means of a differential force measurement system. This is particularly achieved by reducing the noise effects of non-ferromagnetic origin (ground vibrations and the force drift) which occur in the measured force signal. The force measurement system uses two identical high-precision state-of-the-art weighing balances whose working principle is based on zero point balance by means of electromagnetic force compensation (EMFC).

The dFMS shows a remarkable improvement in the relative Lorentz force measurement resolution, which is by a factor of 50 is improved in comparison with that from previous results [14, 15]. In the current work, the relative Lorentz force measurement resolution reach to $std(F_L)/F_g \approx 1.47\,\mathrm{ppb}$. A comparison of the results of current and previous work is presented in table 5.3.

The flow rate measurements are made by measuring horizontally induced Lorentz forces in the salt water channel due to the interaction of the stationary magnetic field and of the flow of the electrically conducting fluid. The Lorentz force is linearly dependent on the electrical conductivity of the fluid and the velocity of the flow and on the magnetic flux density in the second power. It is show that the LFV technique is applicable for fluids with electrical conductivities below $2\,\mathrm{S\,m^{-1}}$. In figure 5.11, Lorentz force measurements for a salt water flow with an electrical conductivity in the order of magnitude of ordinary tap water (0.06) and up to $10\,\mathrm{S\,m^{-1}}$ are shown.

Based on the performance of the flow measurement facility and a differential force measurement system, the sensitivity slope of the flowmeter (cf. figure 5.14) is obtained. Figure 5.12 shows the combined relative uncertainty of the flow measurements with an accuracy of 6 % for the case of σ=$0.06\,\mathrm{S\,m^{-1}}$, and a further increase to 1 % as the electrical conductivity of the salt water is increased to $10\,\mathrm{S\,m^{-1}}$. Finally, a combined value as a product of the calibration factor/constant of the flowmeter and the real spatial distribution of the magnetic flux density from equation (1.3) is obtained.

5.3 On Extended Channel: *d*FMS for $0.005\,\mathrm{S\,m^{-1}} < \sigma < 0.06\,\mathrm{S\,m^{-1}}$

As discussed in section 5.2.6 and presented in section 5.2.4 (particularly by figure 5.14) the dFMS has capabilities to perform LFV measurements at the lower ranges of the electrical conductivity of the saltwater flow. Here, in this section it will be shown some extensive measurements of the Lorentz forces for the values of the electrical conductivity below $0.06\,\mathrm{S\,m^{-1}}$. Although, the measurements are made on the basis of initially developed procedure, which was used in all previous cases presented in section 5.1 and section 5.2, several changes in the configuration of the measurement process were made in order to gather some understanding on untypical results obtain during the LFV measurements for values of the electrical conductivity of $0.005\,\mathrm{S\,m^{-1}}$ to $0.06\,\mathrm{S\,m^{-1}}$. However, a more systematical approach in making these measurements at these ranges of electrical conductivity is yet required in order to grasp the complete picture of physical effects and characterize them on the adequate level, or oppositely, to identify the errors and/or the incompleteness of the experimental facility in use.

5.3.1 Estimation and probing the limits of LFV sensitivity

Taking in consideration the linear dependency of the generated Lorentz force (F_L) from the value of the electrical conductivity (σ) and the velocity of the flow (v_0) by equations 1.2 and 1.3, and the measured results presented in figure 5.14, it is possible to estimate the expected values of generated Lorentz forces well below the $\sigma = 0.06\,\mathrm{S\,m^{-1}}$. Thus, the rearranged representation of the figure 5.14 in log-log scale for $10^{-4}\,\mathrm{S\,m^{-1}}$ to $10^{1}\,\mathrm{S\,m^{-1}}$ and $10^{-2}\,\mathrm{\mu N\,m^{-1}\,s}$ to $10^{2}\,\mathrm{\mu N\,m^{-1}\,s}$ ranges with linear fit and shape-preserving fit is given below in figure 5.15.

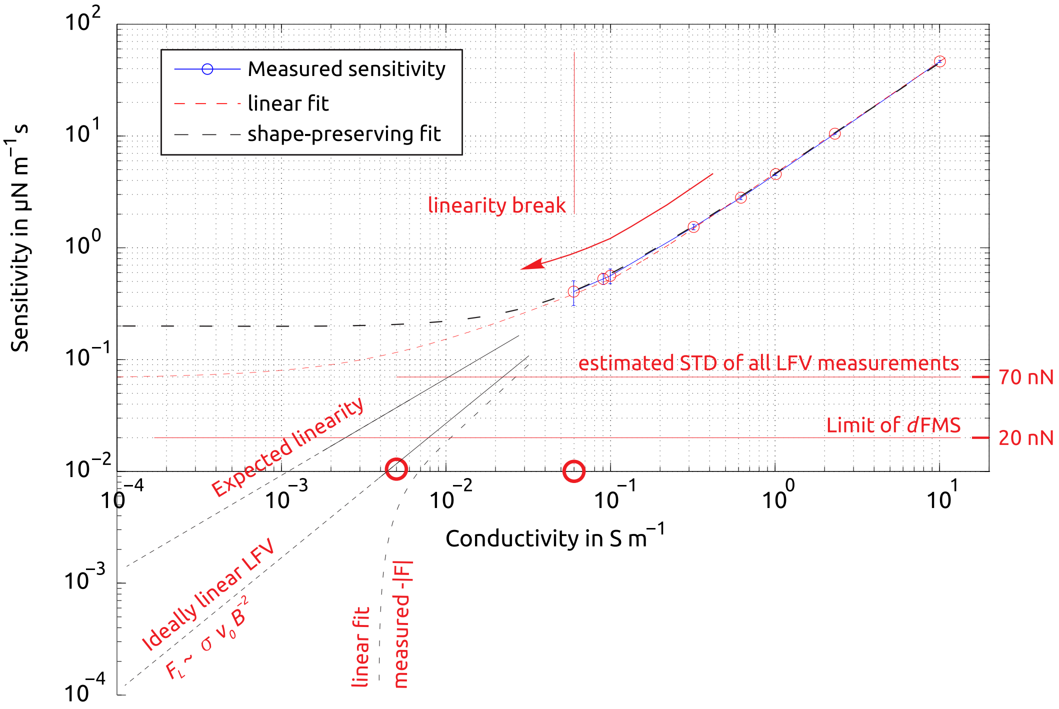

Figure 5.15: Measured sensitivity of the LFV on extended channel for $10^{-4}\,\mathrm{S\,m^{-1}}$ to $10^{1}\,\mathrm{S\,m^{-1}}$ and $10^{-2}\,\mathrm{\mu N\,m^{-1}\,s}$ to $10^{2}\,\mathrm{\mu N\,m^{-1}\,s}$ ranges. Illustration of the limits of *d*FMS and LFV measurements, based on all measured data the linear dependency breaks below $0.06\,\mathrm{S\,m^{-1}}$. This estimation is done based on all available measurement data for velocities of $0.2\,\mathrm{m\,s^{-1}}$ to $2.5\,\mathrm{m\,s^{-1}}$ (see figure 5.11).

As it can be seen from figure 5.15 the shape-preserving fit and the linear fit diverge after the value of electrical conductivity of $0.06\,\mathrm{S\,m^{-1}}$. For this reason an additional

Lorentz force measurements are made to test the character of the measured results below this value.
The resolution of the dFMS is 20 nN, whereas the LFV measurements are made with combined uncertainty of about 70 nN, which is resulting to ≈ 6 % relative uncertainty for the lowest $0.06\,\mathrm{S\,m^{-1}}$ value. However, this relative uncertainty is valid only under the assumption that the measured process is linear.

5.3.2 Measurements of the negative forces

The value of electrical conductivity of the ordinary tap water is about $0.04\,\mathrm{S\,m^{-1}}$. To obtain even lower values of electrical conductivity a spacial water purification filter is used. The minimally achievable electrical conductivity by this filters for 300 l water is $0.005\,\mathrm{S\,m^{-1}}$ which is one order of magnitude lower than that of the unfiltered ordinary tap water. At several different values of electrical conductivity σ=$[0.005, 0.037, 0.08, 0.1]\,\mathrm{S\,m^{-1}}$ the full set of Lorentz force measurement are repeated as shown in section 5.2 (particularly by figure 5.10).
Additional measurements with the conventional magnet system are made (instead of the Halbach array) to highlight the main differences of all electromagnetic interactions. The following electromagnetic interactions are possible during the measurement process of Lorentz forces which all may lead to and may originate systematic or random errors in force measurements

- between the environment and the conventional magnet system,
- between the environment and the Halbach magnet system,
- between the electrolyte flow and the conventional magnet system,
- between the electrolyte flow and the Halbach magnet system,

Here, the term "environment" should be understood as the all possible magnetic and electromagnetic disturbances (existing in the laboratory) which are interfering with the stray of LFV magnet systems. It is obviously evident that due to the structures of both magnet systems the conventional magnet system should be attributed to such an error interactions more than the Halbach array (cf. section 5.2.2). In contrary to the environmental effects, the interaction between the electrolyte flow and magnet systems is expected to show the opposite behavior, since the stray of the Halbach array is concentrated towards the electrolyte flow and the LFV interaction is estimated to be 2.8 times higher than that of the conventional magnet system (cf. section 5.2.2 and Ref. [23, 24]).
Besides of these preparations it should be also considered the change of the temperature in the laboratory during the full measurement period. The estimated value of maximally allowed temperature change is Δ20 mK, as it is discussed earlier in chapter 2, otherwise both EMFC balances are misaligned and the difference signal will by corrupted with high thermal (force) drift, therefore the calibration results (linearity, accuracy, range and resolution) will be invalid.

In figures 5.16 and 5.17 are given two representative set of measurement which are showing the measured **unexpected negative forces** (F_U), when the Halbach array magnet is used. The measurements are done at the inlet of the channel.

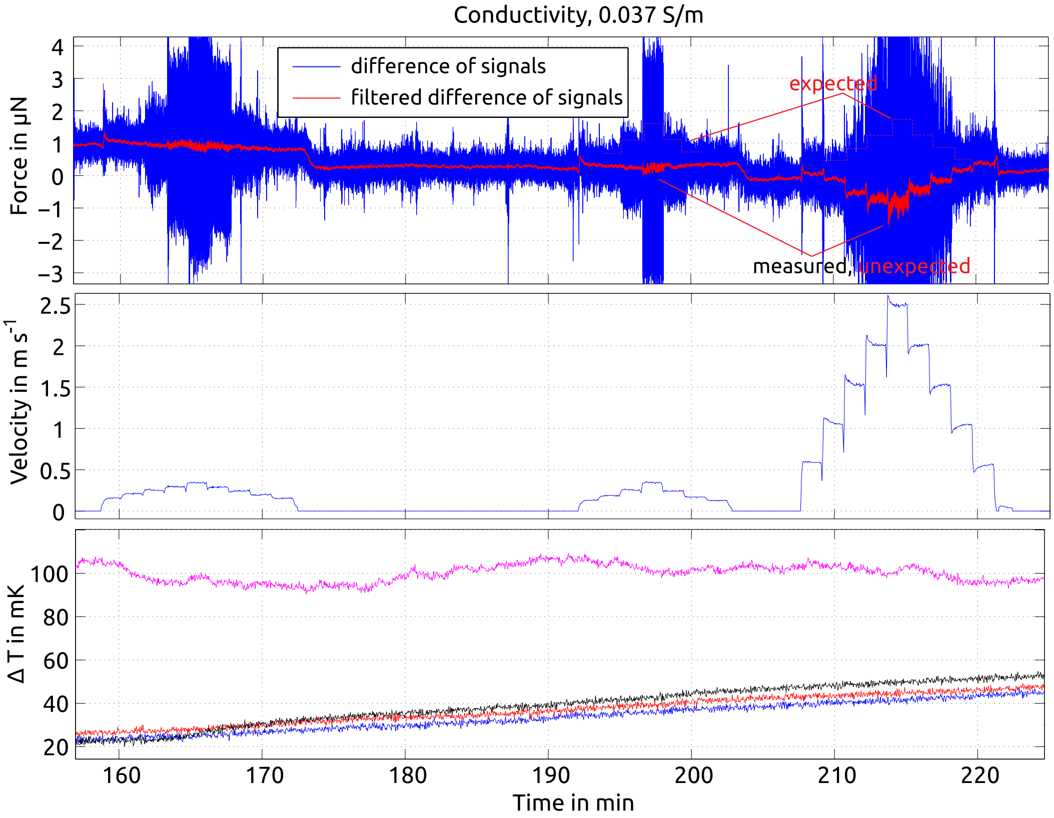

Figure 5.16: Measurement results of the LFV for the electrical conductive of σ=0.037 S m^{-1} (tap water). Description is similar as in figure 5.10.

From measurements by dFMS the measured Lorentz forces can be referenced with the velocity of the electrolyte flow, which is measured by a MID flowmeter. Similar to the figure 5.11 the new measured data for values of electrical conductivity of σ=[0.005, 0.037, 0.1] S m^{-1} and various different mechanical configurations of the dFMS are presented in figures 5.16 to 5.22.

In case of measurements when the positions of dFMS is at the different locations along the channel, the behavior of the force signal more nonlinear. Closer to the outlet part of the channel the shape of the measured forces becomes similar to the shape of the force highlighted in the figures 5.22 and 5.21. Generally, the results show that for the range of electrical conductivity below 0.06 S m^{-1} the typical hysteresis of measurements does not hold in similar way as observed in figures 5.10, 5.16 and 5.17. It is evident that certain systematic characteristic of the electrolyte flow or some unknown error factor of the whole facility is yet hidden. Since, the total response of the measured forces is sufficiently high in relation to the actual resolution (limit) of the dFMS measurements, in future, it could be potentially arrange more systematic approach in these measurements. In the current work the results shown

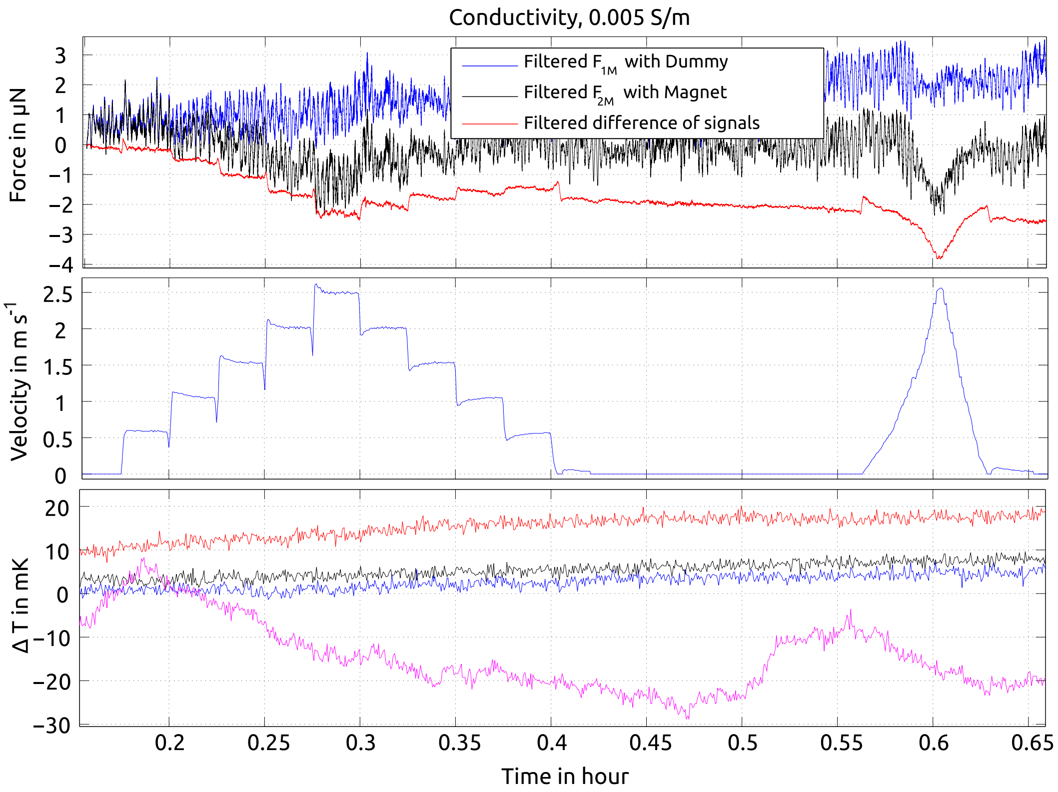

Figure 5.17: Measurement results of the LFV for the electrical conductive of σ=0.005 S m^{-1} (purified water). Description is similar as in figure 5.10.

in figures 5.16 to 5.22 were obtained based on initial guess of the relevant parameters for cross-check. It was mainly driven by the necessity of continuous verification of the measurement procedure and results in comparison with the estimation presented in figure 5.15.

5.3.3 Summary and open problem

Although the results presented in this section are far to be complete for drawing a definite conclusions, it is clear that more research is now needed to establish a number of things

- generally, are these **measured negative forces** $-|F| = F_L + F_U$ due to a systematic/random error that is originating from the particular design of the current facility or it is a clearly distinguishable effect which may be described by physical law ?
- what other evidences there can be brought up in order to systematize the findings on the adequate level ?
- what was the assumptions that were considered during the theoretical derivation of the LFV theory and how they relate to this case of measurements when

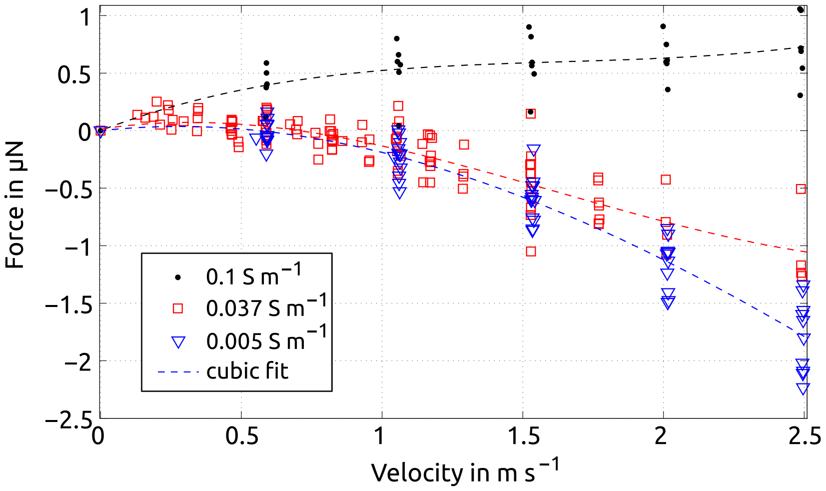

Figure 5.18: Comparison of measured negative forces for different values of electrical conductivity σ=[0.005, 0.037, 0.1] S m^{-1}. Position of dFMS - inlet, magnet system - Halbach array, position of the magnet system in relation to channel is arranged in full height.

the electrical conductivity is very low, which is $\approx 10^{-7}$ times smaller (and below) than the original theory was discussing ?

- and how can such a feature be used or avoided on the practical bases ?

All these questions are in equal basis sharing the importance to be considered in both, theoretical and experimental, disciplines.

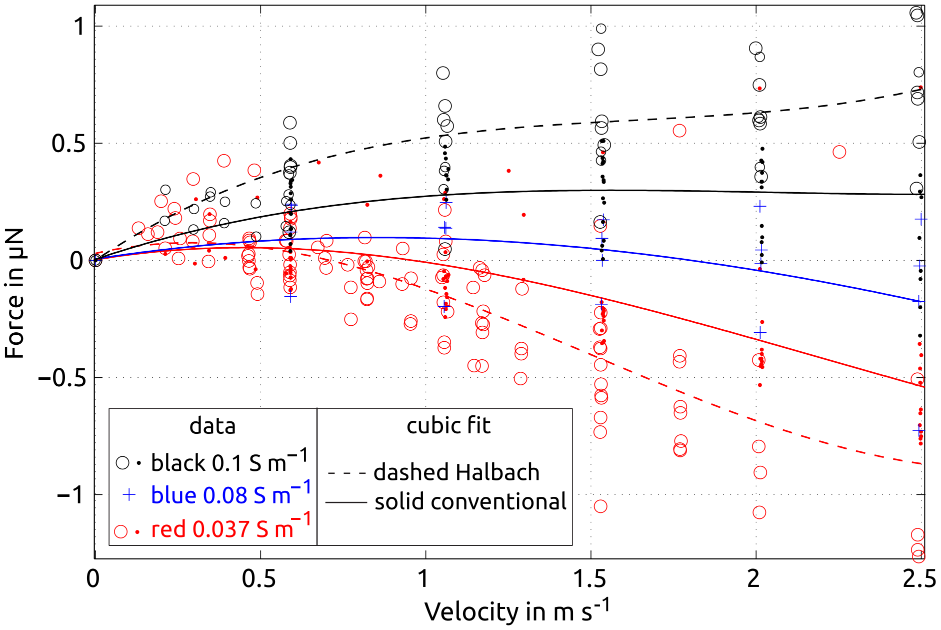

Figure 5.19: Comparison of measured negative forces for different values of electrical conductivity with different magnet systems. Position of *d*FMS - inlet, magnet system - Halbach array and conventional, σ=[0.037, 0.08, 0.1] S m^{-1}, position of the magnet system in relation to channel is arranged in full height.

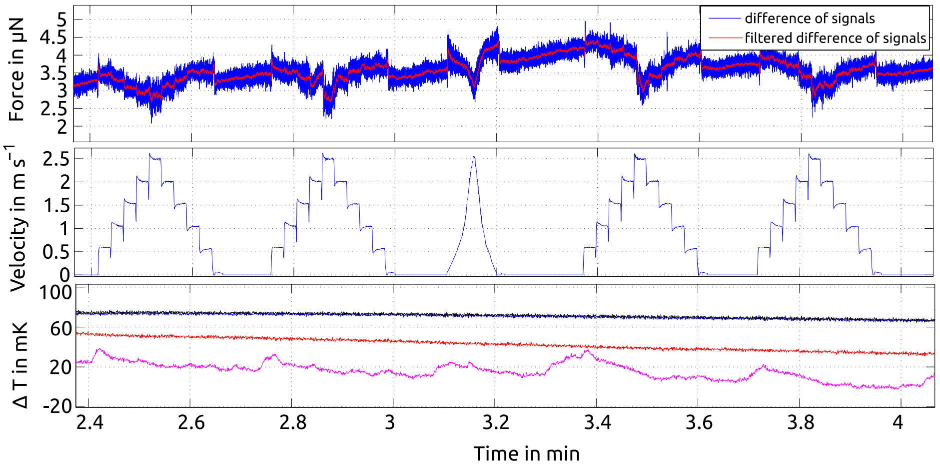

Figure 5.20: Measured forces when the position of the *d*FMS is at the center of the channel. Magnet system - Halbach array, σ=0.005 S m^{-1}, position of the magnet system in relation to channel is arranged in full height.

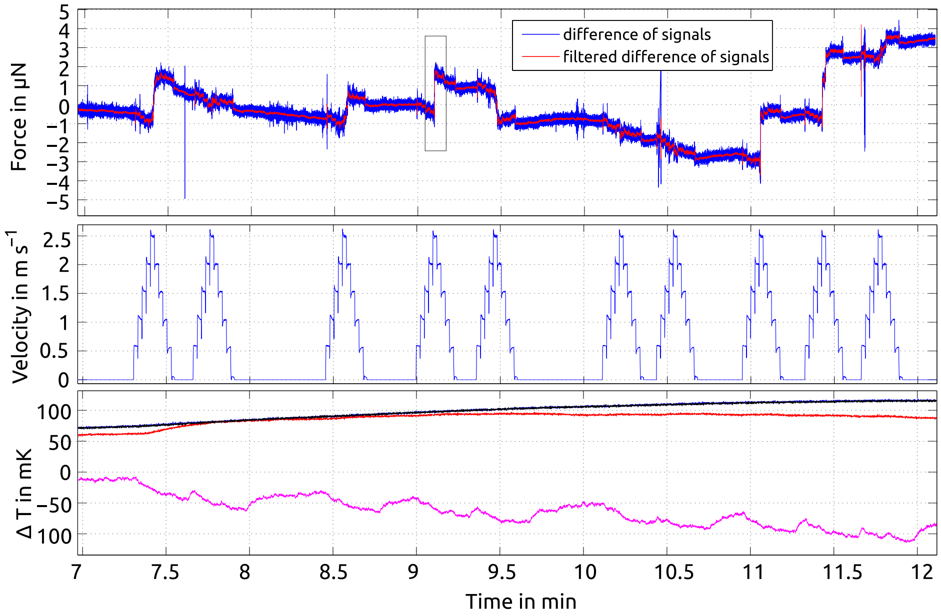

Figure 5.21: Measured forces when the position of the dFMS is at the outlet of the channel. Magnet system - Halbach array, σ=0.005 S m^{-1}, position of the magnet system in relation to channel is arranged in full height.

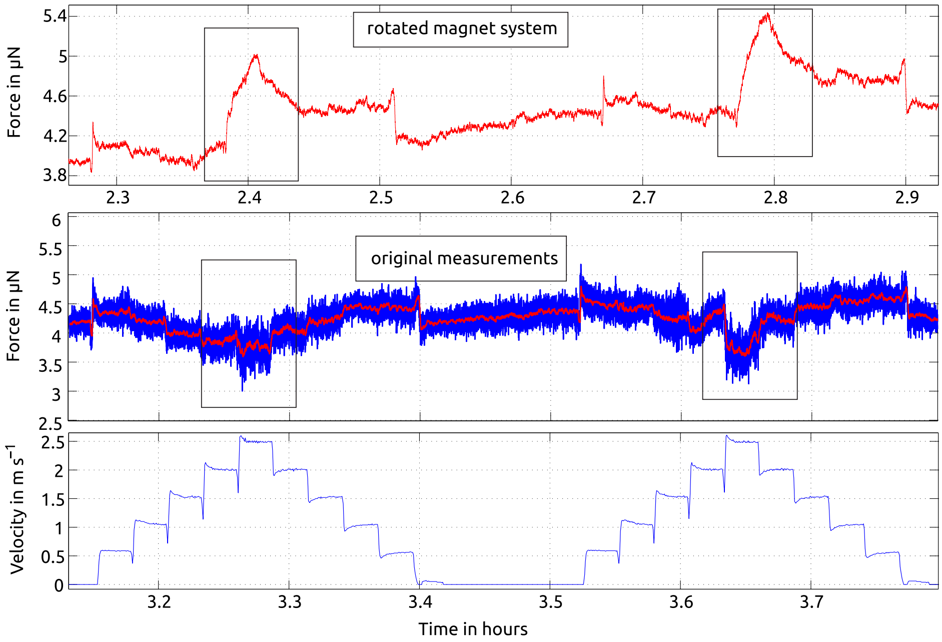

Figure 5.22: Comparison of measured forces when the magnet system is rotated. Position of dFMS - center, magnet system - Halbach array, σ=0.047 S m^{-1}, position of the magnet system in relation to channel is arranged in full height.

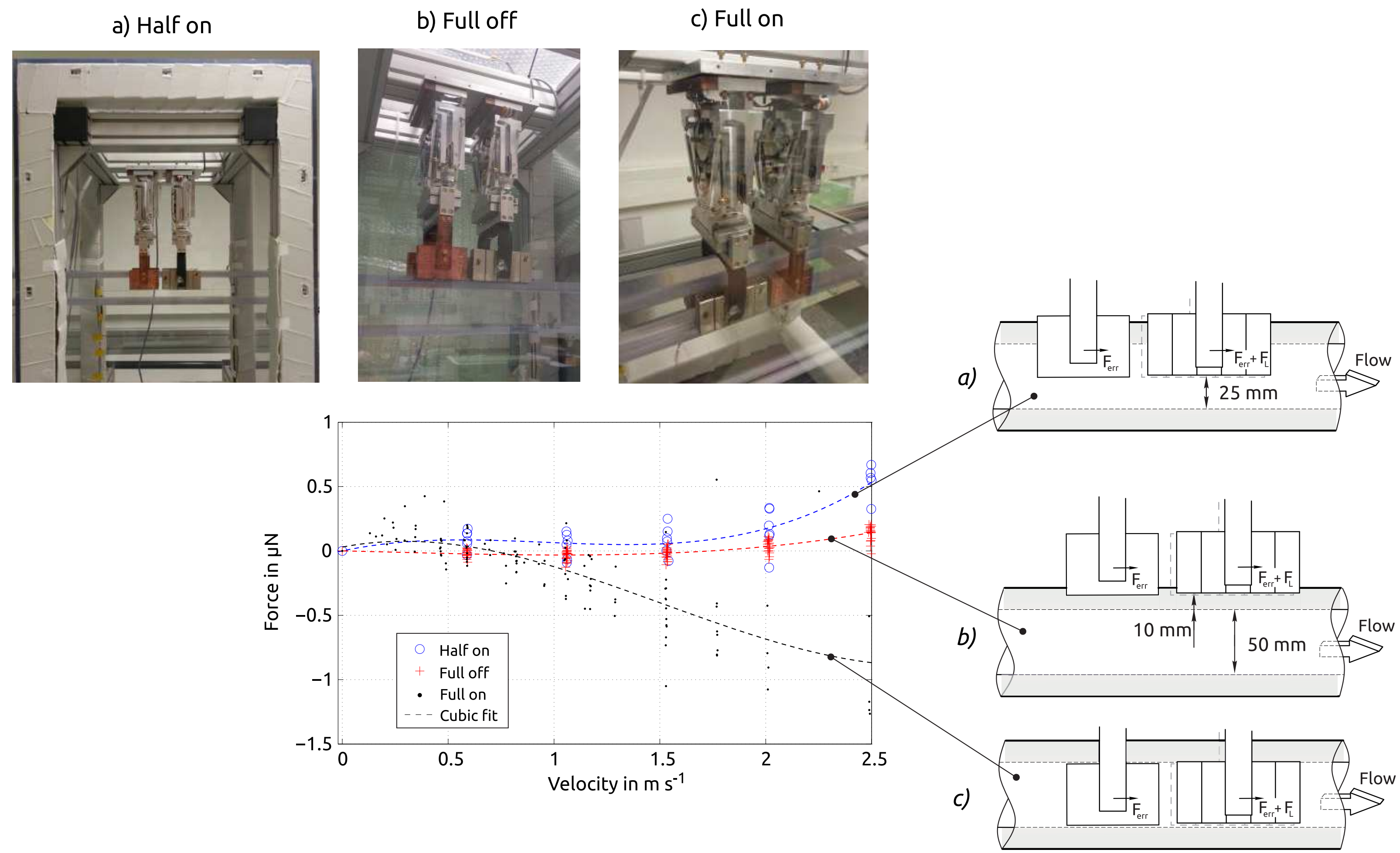

Figure 5.23: Comparison of measured negative forces for same values of electrical conductivity at different height arrangements of the magnet system in relation to the channel. Arrangements of the magnet system are - *a)* in half height of the channel, *b)* fully lifted above the channel and *c)* in full height. Position of *d*FMS - inlet, magnet system - Halbach array, σ=0.037 S m^{-1}.

6 Conclusion and discussion

This work is about *i)* the development of single axis (1DoF) force measurement systems for high-precision horizontally directed force measurements (FMS) and *ii)* the measurements of Lorentz forces on the practical application of interest, the Lorentz Force Velocimetry (LFV). It is also discussing the general instrumentation requirements and the practical measurement problems for both; the measurements of the single axis arbitrary forces and the measurements of Lorentz forces in electrolyte flow channels. Eventually, based on earlier developed technical framework and results achieved in current work, some additional and more significant measurements are made in the light of newly achieved results when the values of the electrical conductivity is below $0.06\,\mathrm{S\,m^{-1}}$. These, newly achieved results in flow measurements and some general open problems are presented in the last part of the work.
The key element of the novel noncontact LFV flowmeters is the Lorentz force measurements, which are generating in the flow due to certain arrangement of the magnet systems in relation to the flow of an electrically conducting fluid. In fact, the magnitude and the direction of the Lorentz force are associated with the velocity and the electrical conductivity of the flow. In accordance with the theory described by *A. Thess et al.* [4], the generated force is linearly proportional to the mean flow velocity, the electrical conductivity of the fluid and the magnetic field in the second power that interacts with the flow. In case of relatively low electrical conductivity, such as the electrolytes $\sigma \approx 10^{-6}\,\mathrm{S\,m^{-1}}$ to $10^{2}\,\mathrm{S\,m^{-1}}$, and flow characteristics which are typical in the industry and in the research, the forces to be measured are in the ranging of $10^{-5}\,\mathrm{N}$ down to nN. For complete industrialization of the flowmeters as well as to ensure their high accurate and high precision performances, the Lorentz forces at these ranges should be resolved with adequate accuracy and precision. The main problem in such measurements is the relatively high precision of the required Lorentz force measurements in horizontal direction (gravity free). These forces in fact are acting to the magnetic field generating source as a result of oppositely directed reaction forces. As a magnetic field generating source an assemblies of permanent magnets are typically used. These magnet systems are directly suspended from the FMS without contact to the electrolyte channel. The mass of the magnet systems ($m_0 \approx 1\,\mathrm{kg}$) represents an unavoidable dead load applied to the FMS. Thus, the crucial parameter in Lorentz force measurements is the ratio between the resolution of the horizontally directed force measurements and the gravity force of the magnet system acting to the FMS in vertical direction.
The aims of this work were investigations and improvements of the existing FMSs, development of new types of FMSs, and their laboratory tests. The new FMSs are intended for measurements of the actual Lorentz forces which are generating in the electrolyte channel flows, for the values of electrical conductivity below $2\,\mathrm{S\,m^{-1}}$. In

order to fulfill these general objectives it was initially analyzed the performance of the earlier developed single EMFC balance FMS and the Pendulum FMS (by Diethold et al.). These FMSs were providing only force measurements for very narrow operational conditions and was developed for the first time, therefore they serve as a basis of the current investigations and developments. The Pendulum FMS, in accordance with result presented in [13, 15, 22, 23], has measurement range of about ±100 µN and resolution of about 2 µN to 3 µN by which the electrolyte flow measurements on the prototype channel was achieved above 2.3 $\mathrm{S\,m^{-1}}$ values of electrical conductivity and for velocity of 1 $\mathrm{m\,s^{-1}}$ to 4 $\mathrm{m\,s^{-1}}$. The single EMFC balance FMS, in accordance to [13, 15, 21–23], has measurement range of about ±100 µN, resolution of ≤ 1 µN and settling time of ≈ 1.4 s by which the electrolyte flow measurements on the extended channel was achieved above 2 $\mathrm{S\,m^{-1}}$ values of electrical conductivity and for velocity of 0.2 $\mathrm{m\,s^{-1}}$ to 4 $\mathrm{m\,s^{-1}}$. Thus, to enable LFV measurements for electrolyte flow with the value of electrical conductivity below 2 $\mathrm{S\,m^{-1}}$ a force measurements with better resolution is required. Initially, the goal was set to enable the force measurements at least by 100 nN resolution by the use of new type of commercially available state-of-the-art EMFC balances.

The necessity of the additional investigations were motivated by the fact that the force measurements and therefore the flow measurements were greatly attributed to unknown/random force drifts (not discussed elsewhere), which were suppressing any possibility for continuous and stable measurements. In these regards, the starting point of the current work was analysis of the existing FMSs. By extensive (short- and long-term) measurements the suitability of the FMSs was reexamined and several critical points were identified (see from chapter 1 up to section 2.1.3).

On the basis of those FMSs and after identifying the main errors involved in the measurements, further in this work, a three different FMSs was developed by which an improvements on the force measurements were achieved in several respects. They are presented in chapters 2, 3 and 4 as *a)* dFMS, *b)* direct compensation Pendulum FMS, *c)* direct comensation EMFC balance FMS, respectively.

a) The innovation, which is considered in the *d*FMS (cf. chapter 2) for measurements of the horizontally directed force, is the introduction of the second EMFC balance on the same axis for the reference force measurements. Thus, by constructing a FMS with two identical EMFC balances, it is achieved a remarkable resolution of horizontally directed force measurements of approximately 20 nN (even better than the initial goal was set), particularly by reduction of the thermal drift and vibration noise. However, certain methodological requirements should be met for performing these force measurements on the adequate level, for instance, the temperature stability during the measurements.

Since, the technical and maintenance requirements of the advanced *d*FMS becomes increasingly complex it is required to develop some FMS with reduced complexity.

b) The innovation considered in the direct compensation Pendulum FMS (cf.

chapter 3) is the introduction of the new method for making the force measurements in LFV applications with simplified measurement schematics. The new method is based on the well known electromagnetic force compensation principle which is widely used in variety of different fields, industrial and academical. Driven by the necessity to eliminate undesirable magnet system used in EMFC balances from the all LFV measurements scheme, it was decided to perform similar compensation measurements on the LFV magnet system directly, by creating electromagnetic force with – an additional – custom manufactured coils. During the initial developments, carried out on the Pendulum FMS, several advantages and disadvantages of the adapted method were revealed, which were serving as apparent strategies underlying in the development of the last, *c)*, third version of FMS.

c) In the chapter 4 the direct compensation method was reevaluated for different FMS (EMFC balance) and modified coils. It was decided to combine the EMFC balance with the newly manufactured coils to reappraise the practical limits of the direct compensation method. Apparently, the finer mechanical structure and the sensitivity of the EMFC balance provides a suitable means for single axis guidance and deflection measurements. Based on extensive calibration and test measurements, various improvements in comparison with the Pendulum FMS are presented and some proposals for improving the method further are discussed.

Finally, in chapter 5 a collection of the practical flow measurement results on both salt water channels are presented. The results in the chapter is structured in a way to highlight the order of their relevance in terms of LFV measurements. Initially, it is shown measurement results obtained from prototype channel. These results are verifying the performance of the direct compensation method, providing also full set of two different LFV measurements for two different measurement configuration. Then, the Lorentz force measurements are presented for the extended channel, where the values of the electrical conductivity of the salt water ranges $0.06\,\mathrm{S\,m^{-1}}$ to $10\,\mathrm{S\,m^{-1}}$. Finally, the results of similar kind of measurements are presented for the values of the electrical conductivity $0.005\,\mathrm{S\,m^{-1}}$ to $0.06\,\mathrm{S\,m^{-1}}$. In this latter measurements some unexpected but clearly distinguishable negative forces are measured, in opposite direction to the expected Lorentz forces. Summarizing diagram of most relevant results obtained for LFV measurements are presented in the last section, see figure 5.15.

Understanding on the future works can be garnered from the summaries of each individual chapter. Throughout this work it can be found several minor proposals for further investigations and developments, which may still improve the general objectives to some extent. However, in the future one of the major improvement should concern the mechanical arrangement of any of the FMSs, particularly in case of dFMS the mechanical supporting construction should be redefined to achieve negligible temperature influences. In case of direct compensation EMFC balance FMS, it is practically requires the same improvement. However, due to the simplicity of the measurement scheme it is more desirable to develop an independent flowmeter having completely unique mechanical, electrical and magnetic structure.

Bibliography

[1] E. J. Williams. The induction of electromotive forces in a moving liquid by a magnetic field, and its application to an investigation of the flow of liquids. *Proceedings of the Physical Society*, 42(5):466, 1930.

[2] J. A. Shercliff. *The Theory of Electromagnetic Flow Measurement.* Cambridge University Press, 1962.

[3] P. A. Davidson. Magnetohydrodynamics in materials processing. *Annual Review of Fluid Mechanics*, 31(1):273–300, 1999.

[4] A. Thess, E. Votyakov, Y. Kolesnikov. Lorentz force velocimetry. *Phys. Rev. Lett.*, 96:164501, Apr 2006.

[5] Y. Kolesnikov, C. Karcher, A. Thess. Lorentz force flowmeter for liquid aluminum: Laboratory experiments and plant tests. *Metallurgical and Materials Transactions B*, 42(3):441–450, 2011.

[6] C. Weidermann. *Design and laboratory test of a Lorentz force flowmeter for pipe flows.* PhD thesis, Ilmenau University of Technology, 2013.

[7] A. Viré, B. Knaepen, A. Thess. Lorentz force velocimetry based on time-of-flight measurements. *Physics of Fluids (1994-present)*, 22(12):125101, 2010.

[8] D. Jian, C. Karcher. Electromagnetic flow measurements in liquid metals using time-of-flight lorentz force velocimetry. *Measurement Science and Technology*, 23(7):074021, 2012.

[9] J. Priede, D. Buchenau, G. Gerbeth. Single-magnet rotary flowmeter for liquid metals. *Journal of Applied Physics*, 110(3):–, 2011.

[10] D. Buchenau, V. Galindo, S. Eckert. The magnetic flywheel flow meter: Theoretical and experimental contributions. *Applied Physics Letters*, 104(22):223504, 2014.

[11] C. Heinicke, A. Thess. Electromagnetic force on a magnetic dipole inside an annular pipe flow. *Physics of Fluids (1994-present)*, 25(9), 2013.

[12] C. Heinicke, A. Thess, I. Rahneberg. Towards local resolution measurements in turbulent liquid metal duct flows. *Journal of Physics: Conference Series*, 318(7):072029, 2011.

[13] A. Wegfrass, C. Diethold, M. Werner, C. Resagk, T. Fröhlich, B. Halbedel, A. Thess. Flow rate measurement of weakly conducting fluids using lorentz force velocimetry. *Measurement Science and Technology*, 23(10):105307, 2012.

[14] A. Wegfrass, C. Diethold, M. Werner, T. Fröhlich, B. Halbedel, F. Hilbrunner, C. Resagk, A. Thess. A universal noncontact flowmeter for liquids. *Applied Physics Letters*, 100(19):194103, 2012.

[15] B. Halbedel, C. Resagk, A. Wegfrass, C. Diethold, M. Werner, F. Hilbrunner, A. Thess. A novel contactless flow rate measurement device for weakly conducting fluids based on lorentz force velocimetry. *Flow, Turbulence and Combustion*, 92(1-2):361–369, 2014.

[16] **S. Vasilyan, T. Froehlich. Direct Lorentz force compensation flowmeter for electrolytes. *Applied Physics Letters*, 105(22), 2014.**

[17] A. Thess, E. Votyakov, B. Knaepen, O. Zikanov. Theory of the lorentz force flowmeter. *New J. Phys.*, 9(8):299, 2007.

[18] B. Hartmut, K. Porzig, J. Mengelkamp, M. Carlstedt, M. Ziolkowski, H. Toepfer. Lorentz force eddy current testing: a novel nde-technique. *COMPEL - The international journal for computation and mathematics in electrical and electronic engineering*, 33(6):1965–1977, 2014.

[19] R. Uhlig, Z. Mladen, M. Ziolkowski, B. Hartmut, A. Thess. Lorentz force sigmometry: A contactless method for electrical conductivity measurements. *Journal of Applied Physics*, 111(9):094914, 2012.

[20] I. Sokolov, Y. Kolesnikov, A. Thess. Experimental investigation of the transient phase of the lorentz force response to the time-dependent velocity at finite magnetic reynolds number. *Measurement Science and Technology*, 25(12):125304, 2014.

[21] C. Diethold, F. Hilbrunner. Force measurement of low forces in combination with high dead loads by the use of electromagnetic force compensation. *Measurement Science and Technology*, 23(7):074017, 2012.

[22] A. Wegfrass. *Experimentelle Untersuchungen zur Anwendbarkeit der Lorentzkraft-Anemometrie auf schwach leitfähige Fluide.* PhD thesis, Ilmenau University of Technology, 2013.

[23] M. Werner. *Design, Optimierung, Realisierung und Test von passiven Magnetsystemen für die Lorentzkraftanemometrie an Elektrolyten.* PhD thesis, Ilmenau University of Technology, 2013.

[24] M. Werner, B. Halbedel. Optimization of ndfeb magnet arrays for improvement of lorentz force velocimetry. *Magnetics, IEEE Transactions on*, 48(11):2925–2928, Nov 2012.

[25] N. Dubovikova, C. Karcher, Y. Kolesnikov. Electromagnetic flow control in liquid metals using lorentz force techniques. *PAMM*, 14(1):721–722, 2014.

[26] D. B. Newell, J. A. Kramar, J. R. Pratt, D. T. Smith, E. R. Williams. The NIST microforce realization and measurement project. *IEEE Transactions on Instrumentation and Measurement*, 52:508, 2003.

[27] J. R. Pratt, J. A. Kramar, D. B. Newell, D. T. Smith. Review of SI traceable force metrology for instrumented indentation and atomic force microscopy. *Measurement Science and Technology*, 16(11):2129, 2005.

[28] S. Chen, S. Pan, Y. Yeh, Y. Lin. Measurement of cantilever spring constant using an electrostatic sensing and actuating force measurement system. *Measurement Science and Technology*, 25(11):115006, 2014.

[29] V. Nesterov, M. Mueller, L. L. Frumin, U. Brand. A new facility to realize a nanonewton force standard based on electrostatic methods. *Metrologia*, 46(3):277, 2009.

[30] H. V. Parks, and J. E. Faller. Simple Pendulum Determination of the Gravitational Constant. *Phys. Rev. Lett.*, 105:110801, Sep 2010.

[31] T. Quinn, C. Speake, H. Parks, R. Davis. The BIPM measurements of the Newtonian constant of gravitation, G. *Philosophical Transactions of the Royal Society of London A: Mathematical, Physical and Engineering Sciences*, 372(2026), 2014.

[32] D. Frollani, M. Coletti, S. B. Gabriel. A thrust balance for low power hollow cathode thrusters. *Measurement Science and Technology*, 25(6):065902, 2014.

[33] A. N. Grubišić, S. B. Gabriel. Development of an indirect counterbalanced pendulum optical-lever thrust balance for micro- to millinewton thrust measurement. *Measurement Science and Technology*, 21(10):105101, 2010.

[34] M. Thomas, P. Espel, D. Ziane, P. Pinot, P. Juncar, F. Pereira Dos Santos, S. Merlet, F. Piquemal, G. Genevès. First determination of the Planck constant using the LNE watt balance. *Metrologia*, 52(2):433, 2015.

[35] S. Rocca, C. Menon, D. Nicolini. Feep micro-thrust balance characterization and testing. *Measurement Science and Technology*, 17(4):711, 2006.

[36] D. Haddad, F. Seifert, L. S. Chao, A. Cao, G. Sineriz, J. R. Pratt, D. B. Newell, S. Schlamminger. First Measurements of the Flux Integral with the NIST-4 Watt Balance. *IEEE T. Instrumentation and Measurement*, 64(6):1642–1649, 2015.

[37] H. Baumann, A. Eichenberger, F. Cosandier, B. Jeckelmann, R. Clavel, D. Reber, D. Tommasini. Design of the new METAS watt balance experiment Mark II. *Metrologia*, 50(3):235, 2013.

[38] T. J. Quinn. The beam balance as an instrument for very precise weighing. *Measurement Science and Technology*, 3(2):141, 1992.

[39] E. Jäger, E. Manske, H. Wurzbacher, R. Grünwald, H. J. Büchner, W. Schott, W. Pöschel. Novel microoptical fibre coupled laser interferometers for various applications in precision engineering and nanotechnology. In *Proceedings of the International EUSPEN Conference 3*, 26 - 30 May 2002 Eindhoven.

[40] *Sartorius Lab Instruments, Datasheet WZA26-NC, www.sartorius.de (last accessed on 02.08.2015).*

[41] T. Fehling, T. Fröhlich, D. Heydenbluth, and French College of Metrology. *Design and Performance of the New Sartorius 1kg-Prototype Mass Comparator for High Precision Mass Determination and Research Applications*, pages 657–668. ISTE, 2010.

[42] T. Fröhlich, T. Fehling, D. Heydenbluth. Mass Dissemination using a Robot System. Massevergleiche mittels eines Robotersystems. *tm - Technisches Messen Plattform für Methoden, Systeme und Anwendungen der Messtechnik*, 76(7-8):382–387, 2009.

[43] B. Andreas, Y. Azuma, G. Bartl, and et. al. Determination of the Avogadro Constant by Counting the Atoms in a ^{28}Si Crystal. *Phys. Rev. Lett.*, 106:030801, Jan 2011.

[44] H. Weis, F. Hilbrunner, T. Fröhlich, G. Jäger. Mechatronic FEM model of an electromagnetic-force-compensated load cell. *Measurement Science and Technology*, 23(7):074018, 2012.

[45] **S. Vasilyan, M. Rivero, J. Schleichert, B. Halbedel, T. Fröhlich. High-precision horizontally directed force measurements for high dead loads based on differential electromagnetic force compensation system. *05.10.2015 submitted to Measurement Science and Technology*.**

[46] M. Kühnel, M. Rivero, C. Diethold, F. Hilbrunner, T. Fröhlich. Dual axis tiltmeter with nanorad resolution based on commercial force compensation weigh cells, In 58th Ilmenau Scientific Colloquium. 2014.

[47] *Leica Geosystems, Datasheet Nivel210-220 www.leica-geosystems.com (last accessed on 02.08.2015).*

[48] S. Schlamminger. *Determination of the Gravitational Constant Using a Beam Balance.* PhD thesis, Universität Zürich, 2002.

[49] *Physikalisch-Technische-Bundesanstalt 2007. Schwereinformationssystem SIS. http://www.ptb.de/cartoweb3/SISproject.php (last accessed on 04.03.2016).*

[50] *Agilent HP 3245A Universal Source, Hewlett-Packard/Agilent Technologies, first Edition Update 2, Manual Part no. 03245-90001, USA, 1994.*

[51] BIPM, IEC, IFCC, IUPAC, IUPAP and OIML 2008 Evaluation of Measurement Data-Guide to the Expression of Uncertainty in Measurement Joint Committee for Guides in Metrology JCGM 100:2008 www.bipm.org/utils/common/documents/jcgm/JCGM_100_2008_E.pdf.

[52] *dSpace, model DS1006. www.dspace.com (last accessed on 02.08.2015).*

[53] J. Schleichert, M. Carlstedt, R. Marangoni, I. Rahneberg, T. Fröhlich. Dynamic characterization of a multi-component force transducer using a Lorentz force load changer. In 58th Ilmenau Scientic Colloquium, 2014.

[54] T. Klügel. Bestimmung lokaler Einflüsse in den Zeitreihen inertialer Rotationssensoren. Technical report, Schlussbericht zum DFG-Forschungsprojekt LOKROT, Fundamentalstation Wettzell, 2003.

[55] Bundesanstalt für Geowissenschaften und Rohstoffe. Seismic waveform data requests www.bgr.bund.de, (last accesed 09.08.2015).

[56] B. Halbedel, M. Klaiber, M. Weidner. Hochtemperatursupraleiter als Magnetfeldquelle für die Lorentzkraft-Anemometrie von schwach leitfähigen Fluiden. In: Proceedings Workshop Elektroprozesstechnik, Technische Universität Ilmenau, 12.-13. Sept. 2013.

[57] T. Fröhlich and A. Thess. Verfahren und Vorrichtung zur berührungslosen Messung des Massen- oder Volumenstromes eines elektrisch leitfähigen Fluids, Application number: **DE 10 2013 012 616 A1** 2015.01.29.

[58] E. P. Furlani. *Permanent Magnet and Electromechanical Devices: Materials, Analysis and Applications.* Academic Press, 2001.

[59] *Magnetometer Series/Model: KOSVAHA 5, www.wuntronic.com/ .../Magnetometer-Teslameter-Gaussmeter-Handbuch.pdf, (last accessed on 27.09.2015).*

[60] *Agilent Technologies 3458A Multimeter, fourth edition, Manual Part no. 03458-90014, USA, 2000.*

[61] A. Wegfrass, C. Diethold, M. Werner, and et al. Lorentzkraft - Anemometrie für die berührungslose Durchflussmessung von Elektrolyten. *tm - Technisches Messen Plattform für Methoden. Systeme und Anwendungen der Messtechnik*, 79(9):399–402, 2012.

[62] I. Choi, D. Choi, S. Kim. Double force compensation method to enhance the performance of a null balance force sensor. *Japanese Journal of Applied Physics*, 41(6R):3987, 2002.

[63] J. Jantzen. *Foundations of Fuzzy Control: A Practical Approach, Second Edition.* John Wiley & Sons, Ltd, Chichester, UK., 2007.

[64] K. M. Passino, S. Yurkovich. *Fuzzy Control.* Addison Wesley Longman, Inc., 1998.

[65] W. S. Levine. *Control System Advanced Methods, The Control Handbook Second Edition.* CRC Press, Taylor & Francis Group, 2010. ISBN: 978-1-4200-7364-5.

[66] **S. Vasilyan, R. Ebert, M. Weidner, M. Rivero, B. Halbedel, C. Resagk, T. Fröhlich**. **Towards metering tap water by Lorentz force velocimetry**. ***Measurement Science and Technology***, **26**(11):**115302**, **2015**.

[67] *Indumax CLS50/CLS50D, www.endress.com.*

[68] A. Thess, E. Votyakov, B. Knaepen, O. Zikanov. Theory of the lorentz force flowmeter. *New Journal of Physics*, 9(8):299, 2007.

[69] *Fluxus F601, H Hermann Ehlers, www.ehlersgmbh.com.*

[70] *OPTIFLUX 2000, KROHNE, www.krohne.com.*

[71] *DANTEC DYNAMICS, The original model have been several time upgrated. Consist of: Fiber Flow optics (60x24), Manipulator, Spectral-Physics Lasers generator, BSA F60 Flow processor, isel-automotion traverse system...*

[72] X. Wang, Y. Kolesnikov, A. Thess. Numerical calibration of a lorentz force flowmeter. *Measurement Science and Technology*, 23:045005, 2012.

[73] V. Minchenya, C. Karcher, Y. Kolesnikov. A. Thess. Calibration of the lorentz force flowmeter. *Flow Measurement and Instrumentation*, 22:242 – 247, 2011.

Acknowledgments

This work was supported by the DFG (Deutsche Forschungsgemeinschaft) - funded project in the framework of the RTG/1567. The work was carried out at the Institut für Prozessmess- und Sensortechnik of the Technische Universität Ilmenau within the sub-project B/2 in Research Training Group "Lorentz Force Velocimetry and Lorentz Force Eddy Current Testing".

My sincere gratitude and appreciation is dedicated to Herrn Univ. Prof. Dr.-Ing. habil. Thomas Fröhlich who enabled me in his role as a director of the institute and as an academic adviser to make this work possible. I would also like to thank Prof. Dr. rer. nat. habil. André Thess for all stimulating and constructive discussions at the earlier stages of the work.

The appreciation is also extended to Andre Wegfrass, Christian Diethold, Michael Werner, Christian Resagk, Bernd Halbedel for their invaluable efforts in building up the earliest state of the research infrastructure.

The employees of the Institut für Prozessmess- und Sensortechnik I thank for the working environment which they have developed throughout many years and made me to be a part of it in both aspects of — personal and professional — activities. Particularly, Gunter Krapf — allows access to the laboratory for calibration of the temperature sensors. Helge Mammen — borrowed the water purification filter used to purify more than 300 liters of tap water. Mathias Röser — manufactured several pieces of mechanical components. Cordula Höring — backed me up in most of administrative and paper works which were popping out quite randomly. Uwe Gerhardt — provided various electronic components.

Thanks also to all members of the mechanical workshop of the Department of Mechanical Engineering (especially to Jürgen and Marco) for smooth and very prompt cooperation to deliver all requested mechanical components during past 3 years.

Special thanks to my very close research collaborators — Michel Rivero and Jan Schleichert — for their invaluable support, which were mostly done on a voluntary bases. Moreover, their joyful willingness to cross-check some of my ideas are greatly acknowledged. The last part of this appreciation implies for one other dude — Konstantin Weise (Porzig) — as well.

Very special thanks to my parents (Jeanne and Zohrab) and brother (Davit) in helping me continuously to keep up the main path of the life, and also, to identify among all relevant and irrelevant issues the most critical ones at each particular period of time.

… Thanks to all those who, for whatever reason, give me a smile …

Erklärung

(gemäß Anlage 1 der Promotionsordnung der TU Ilmenau — Allgemeine Bestimmungen)

Ich versichere, dass ich die vorliegende Arbeit ohne unzulässige Hilfe Dritter und ohne Benutzung anderer als der angegebenen Hilfsmittel angefertigt habe. Die aus anderen Quellen direkt oder indirekt übernommenen Daten und Konzepte sind unter Angabe der Quelle gekennzeichnet.

Bei der Auswahl und Auswertung folgenden Materials haben mir die nachstehend aufgeführten Personen in der jeweils beschriebenen Weise unentgeltlich geholfen:

- Christian Diethold — Vorstellung der beiden FMSs (in seinem Werk — “Pendulum” und “old EMFC balance”) im Jahr 2012 beim Beginn dieser Arbeit.
- Michel Reviero — Zusammenarbeit bei den numerischen Simulationen für die Abb. 2.3.
- Jan Schleichert — Zusammenarbeit beim Aufbau einer Messeinrichtung für Abb. 2.23.
- Markus Weidner — Messungen der Magnetfeldverteilung des Halbach Array Magnetsystems, welches in der Abb. 5.8 teilweise dargestellt ist.

Weitere Personen waren an der inhaltlich-materiellen Erstellung der vorliegenden Arbeit nicht beteiligt. Insbesondere habe ich hierfür nicht die entgeltliche Hilfe von Vermittlungs- bzw. Beratungsdiensten (Promotionsberater oder anderer Personen) in Anspruch genommen. Niemand hat von mir unmittelbar oder mittelbar geldwerte Leistungen für Arbeiten erhalten, die im Zusammenhang mit dem Inhalte der vorgelegten Dissertation stehen.

Die Arbeit wurde bisher weder im In- noch im Ausland in gleicher oder ähnlicher Form einer Prüfungsbehörde vorgelegt.

Ich bin darauf hingewiesen worden, dass die Unrichtigkeit der vorstehenden Erklärung als Täuschungsversuch bewertet wird und gemäß § 7 Abs. 10 der Promotionsordnung den Ab-bruch des Promotionsverfahrens zur Folge hat.

Ilmenau, den March 23, 2016 Suren Vasilyan